

Multi-Scale Detection, Mapping, and Modelling Geomorphic Change in Gravel- Bed Rivers with UAV Remote Sensing

Rory Scott

Ecosystems and Environment Research Centre
School of Environment and Life Sciences
University of Salford
Salford, M5 4WT
UK

Submitted in Partial Fulfilment of the Requirements of the Degree of Doctor of

Philosophy, July 2019

Rory Scott

Multi-Scale Detection, Mapping, and Modelling Geomorphic Change in Gravel-Bed Rivers
with UAV Remote Sensing

Supervisors:

Dr Neil S. Entwistle

Prof. F. Mark Danson

Contents

List of Tables.....	vi
List of Figures	vii
Acknowledgments	xii
Abstract.....	xiii
Chapter 1: Introduction.....	1
1.1. Research Context.....	1
1.2. Research Motive.....	2
1.3. Thesis Structure	6
Chapter 2: Literature Review.....	8
2.1. Introduction.....	8
2.2. Remote Sensing.....	9
2.2.1. Background	9
2.2.2. Remote sensing platforms.....	10
2.3. UAV Systems.....	13
2.3.1. System types.....	13
2.4. Photogrammetry.....	14
2.4.1. Computer Vision and Image Processing	14
2.4.2. Structure from Motion (SfM).....	15
2.5. Fluvial Geomorphology.....	18
2.5.1. River Forms and Controls.....	18

2.5.2.	Artificial Influences on River Form.....	21
2.6.	Applications for UAV remote sensing.....	26
2.6.1.	Ecology and Vegetation Monitoring.....	26
2.6.2.	Earth Sciences.....	27
2.6.3.	Glacial Applications.....	29
2.6.4.	Fluvial Sciences.....	29
Chapter 3:	Research Questions.....	32
Chapter 4:	Field Site & UAV Campaign.....	35
4.1.	Introduction.....	35
4.2.	Pre-flight survey planning.....	36
4.2.1.	Earth Observation Background.....	37
4.2.2.	Methodology Construction.....	38
4.2.3.	Validation.....	43
4.2.4.	Workflow.....	44
4.3.	UAV Flight Operations.....	48
4.3.1.	Field Methodology Overview.....	48
4.4.	Wooler Water Study Location.....	52
4.4.1.	Existing Structures and Features of Interest.....	56
4.4.2.	Historic Change Analysis.....	57
4.4.3.	Recent Change Analysis.....	60
4.5.	Survey Details.....	62

4.5.1.	July 2016 (Survey 1)	63
4.5.2.	November 2016 (Survey 2)	64
4.5.3.	September 2017 (Survey 3)	66
4.5.4.	April 2018 (Survey 4)	67
Chapter 5: Methodology and Data Processing Approaches		69
5.1.	Introduction	69
5.2.	Noise Filtering and Vegetation Removal	72
5.3.	Topographic Model Construction	77
5.3.1.	Common Workflow	77
5.3.2.	Survey 1 Processing	79
5.3.3.	Survey 2 Processing	82
5.3.4.	Survey 3 Processing	83
5.3.5.	Survey 4 Processing	84
5.4.	DEM and DoD error analysis	86
5.4.1.	Independent Error Analysis	87
5.4.2.	Absolute vs Relative Error	94
5.4.3.	Limitations and implications	96
Chapter 6: Surface Comparison and Geomorphic Change Detection		98
6.1.	Introduction	98
6.2.	Channel Evolution – Full Site	100
6.2.1.	Cross-sectional Analyses	100

6.2.2.	Planform Evolution	106
6.2.3.	Gradient Adjustments	112
6.3.	Geomorphic Evolution – Reach Scale Analyses	113
6.3.1.	Error Considerations and implications	129
6.3.2.	Budget Segregation	131
6.3.3.	Sediment Budget - Volumetric Statistics	132
6.3.4.	Sediment Budget - Area Statistics	136
6.4.	Internal Bed Dynamics and Inter-reach Geomorphic Change	139
6.5.	Clast Scale Geomorphic Change Analysis	147
6.5.1.	Critical Evaluation and Limitations	155
6.5.2.	Grainsize evolution at Wooler Water	157
Chapter 7:	Discussion & Conclusions	159
7.1.	Sediment Budget and Flow Regime.....	159
7.1.1.	Planform Response	163
7.2.	Error Considerations and Limitations.....	175
7.3.	Conclusions.....	176
7.3.1.	Research Question 1	177
7.3.2.	Research Question 2	178
7.3.3.	Research Question 3	180
7.3.4.	Future Works.....	183
References	185

Appendix 1 – Final Data Products	214
Appendix 2 – Geomorphic change Tables	221
Appendix 3 – Agisoft Photoscan® Processing Reports.....	225

List of Tables

Table 2.1 – Summary of the effects of modification of discharge (Q) and sediment load (Q _s) Note: * = indirect effect.....	22
Table 4.1 – Breakdown of various parameters, conditions, and results from all surveys	62
Table 5.1 – Compared RSME values of this study against similar works.....	96
Table 6.1 – Respective offset factors for each sub-reach when compared to the respective preceding survey.....	113
Table 6.2 - LODs and net propagated error in volume calculations for inter-survey epochs.	130
Table 6.3 – Ground sampling distances and minimum resolvable grainsized for all surveys.....	149
Table 6.4 – Reported grainsizes (cm) from Sear and Archer 1998, and estimated distributions for 2016 and 2018 by this study. (2016 error ±1.75cm, 2018 error ±1.31cm)	157
Table 7.1 – Comparison of inter-survey peak flows and respective volumetric change.	162
Table 7.2 – Source: Janes et al., (2018), modelled bank retreat rates for UK rivers.....	166

List of Figures

Figure 1.1 – Scales of application for various remote sensing platforms.	4
Figure 4.1 – Ground resolution target.	37
Figure 4.2 – Diagram to illustrate proportionality of angular and distant parameters within a camera and subject environment.	42
Figure 4.3 – Linear relationship between survey altitude, resolution (GSD) and Coverage (FOV).....	43
Figure 4.4 – An example workflow to allow users to calculate optimal survey flight parameters according to coverage and resolution requirements	44
Figure 4.5 – Study location map, (A) The town of Wooller, Northumberland and (B) An overview of the study reach, including Wooller Water, which is fed by Colgate Water and other upland streams.	52
Figure 4.6 – Powerline pylon, south of the town of Wooller. Paleo-channel marks. (Image dated July 2006)	54
Figure 4.7 Weir remnants (top) and Haugh Head Ford respectively (bottom), within Section C of the Study Site.	56
Figure 4.8 - The previous courses of Wooller Water, as traced from historical maps.	58
Figure 4.9 - (A) River course in circa. 1920, encroaching railway embankment and (B) newly adjusted river course in circa. 1970.....	59
Figure 4.10 – from Sear and Archer (1998), looking upstream at Haugh Head following a flood resultant incision in 1971. The concrete ford is destroyed, and footbridge piers exposed.	61
Figure 4.11 - Painted GCP marker within river channel.....	66
Figure 5.1 – Progressive filtering and cleaning of vegetated point-cloud.	75

Figure 5.10 - Locations of GPS observations utilized for error checking.....	88
Figure 5.11 – Mean absolute error in $\pm m$, of independent GPS checkpoints.....	90
Figure 5.12 – Cross section transect on Haugh Head Ford.....	91
Figure 5.13 – Cross sectional profiles of Haugh Head ford.....	92
Figure 5.14 – Worst case histogram offset of Haugh Head Ford (Survey 1-3 Raw DoD).....	92
Figure 5.15 – More ideal inter-survey histogram offset. (Survey 2-3).....	93
Figure 5.16 – Offset of histogram peak from zero reflects mean vertical error between DEM surfaces.....	95
Figure 6.1 – Locations of cross sections CS1-7 at the Wooler Water field site.....	101
Figure 6.2 – Cross sectional profile CS1.....	102
Figure 6.3 – Cross sectional profile CS2.....	102
Figure 6.4 – Cross sectional profiles CS3 - 5.....	104
Figure 6.5 – Cross sectional profiles CS6 and CS7.....	105
Figure 6.6 – Planform adjustment to the right bank in the proximity of CS2.....	108
Figure 6.7 – Planform adjustments and bank collapse in the downstream end of the Study Site.....	109
Figure 6.8 – Shaded relief closeup of left bank in the proximity of CS6.....	110
Figure 6.9 – Map and longitudinal profile of the river section leading upto Haugh Head Ford.....	112
Figure 6.10 – CloudCompare screenshot displaying “cloud of difference” histogram offset.....	114
Figure 6.11 – Locations of sub-reach splitting, based on a compromise between size and morphological continuity.....	116
Figure 6.12 – Geomorphic change analyses for Sub-reach A.....	117
Figure 6.13– Geomorphic change analyses for Sub-reach B.....	119

Figure 6.14– Geomorphic change analyses for Sub-reach C.	122
Figure 6.15 – Geomorphic change analyses for Sub-reach D.....	124
Figure 6.16 – Geomorphic change analyses for Sub-reach E.	126
Figure 6.17 – Geomorphic change analyses for Sub-reach F.	128
Figure 6.18 - Bed/bank segregated volumetric statistics for Survey 1-2.	132
Figure 6.19 - Bed/bank segregated volumetric statistics for Survey 2-3.	133
Figure 6.20 - Bed/bank segregated volumetric statistics for Survey 3-4.	134
Figure 6.21 – Total volumetric comparison for all inter-survey periods. Lighter shading represents erosion.....	135
Figure 6.22 – Area statistics for erosion (red), stability (grey) and deposition (blue) between Surveys 1 and 2.	136
Figure 6.23 - Area statistics for erosion (red), stability (grey) and deposition (blue) between Surveys 2 and 3.	137
Figure 6.24 - – Area statistics for erosion (red), stability (grey) and deposition (blue) between Surveys 3 and 4.	138
Figure 6.25 – Internal Bed dynamics occurring in Sub-reach A.	139
Figure 6.26 – Continuation of chute channel in Figure 7.8.....	140
Figure 6.27 - Internal Bed dynamics occurring in Sub-reach E.	142
Figure 6.28 – Detail view of bar formation and migration in Sub-reach E.....	143
Figure 6.29 – Detail view of the left bank within Sub-reach F. DoDs for Survey 1-2 and 2-3.	144
Figure 6.30 – Orthomosaic images for Survey 1, 2 and 4 of the left bank within Sub-reach F.	145
Figure 6.31 – Close up of left bank within Sub-reach F. Mass failure and bed scour visible	146

Figure 6.32 - Estimated portion of grains unable to be sized by image based analysis methods (6.3%) based on reported D ₁₆ , D ₅₀ , and D ₈₄ from Sear and Archer (1994)....	149
Figure 6.33 – Area of Interest for coarse clast analysis (sub-reach B	151
Figure 6.34 - Detected clasts (grey) for 2016 and 2018 based upon clast/pore contrast definition.....	152
Figure 6.35 – Detected clasts (grey) for 2016 and 2018 based upon clast/pore contrast definition	152
Figure 6.36 – Comparison of image sieving methodology against manual measurement of resolved clasts from aerial imagery. The former underestimates grainsize by approximately 23%.....	153
Figure 6.37 – Linear regression between manual and image analysis clast measurements	154
Figure 6.38 – Mis-classifications (red) of individual clasts as multiple due to surface contrast variations.....	155
Figure 6.39 – Region of interest for grainsize change analysis and detected clasts for 2016 and 2018.....	157
Figure 6.40 – Grainsize distributions for 1998 (Sear and Archer, 1998), and error corrected (+23%) data for 2016 and 2018.....	158
Figure 7.1 - Daily River level record at Coldgate Mill.	160
Figure 7.2 - Gauged flow record 2009-2016 from Coldgate Mill gauging station. Maximum gauge = 20 m ³ /s.....	160
Figure 7.3 – Flow levels within cross section at Coldgate Mill.....	161
Figure 7.4 – Scatter graph of sedimentary response to different flow magnitudes.....	162
Figure 7.5 – Diagrammatic representation of a widening mechanism in an incised river.	164

Figure 7.6 – Cross sectional transect location.	165
Figure 7.7 – Cross sectional profile of right bank in Sub-reach B.	165
Figure 7.8 – Upstream half of full-scale DoD for 2009 LiDAR against 2016 UAV Dataset.	169
Figure 7.9 - Downstream half of full-scale DoD for 2009 LiDAR against 2016 UAV Dataset.	170
Figure 7.10 – Cross sectional profile along the same transect as in Figure 7.6, including LiDAR DEM	171
Figure 7.12 – Example selection of easily identifiable clasts which remain imobile throughout the field campaign.	173
Figure 7.13 – A mechanism for in-situ construction of a bed armour layer by lateral expansion.	174
Figure A1.1 – Survey 1 Channel DEM result.	214
Figure A1.2 – Survey 1 Orthomosaic Result	215
Figure A1.3 - Survey 2 Channel DEM result.	216
Figure A1.4 - Survey 2 Orthomosaic Result	217
Figure A1.5 - Survey 3 Channel DEM result.	218
Figure A1.6 - Survey 3 Orthomosaic Result	219
Figure A1.7 - Survey 4 Channel DEM result.	220
Figure A1.9 - Survey 4 Orthomosaic Result	220

Acknowledgments

I would like to extend my thanks to my supervisors, Neil Entwistle and F. Mark Danson. Their continued support and guidance has not only facilitated the completion of this Thesis, but a great deal of personal development over the past 3 years. Dr George Heritage has also been instrumental in the forming of my research. Without his mentoring solving many problems along the way. Additional thanks are extended to the UK Environment Agency and Tweed River Forum for their provision of data, and to the various landowners who gave permission for UAV surveys on their land. I am particularly grateful to Dr Entwistle and Dr Heritage for not letting me go hungry by providing me with the opportunity to work alongside them in a commercial capacity in the recent months, facilitating my “flowery” ramblings and ability to send them 20 Thesis drafts per day.

I also am grateful to Professor Dan Parsons, of The University of Hull, who initially recognised me as a PhD candidate and set in motion my research journey. Him and my other mentors at the University of Hull are responsible for sparking my interest in geomorphology. To Dr Rob Williamson, I extend thanks for his support, friendship and dependability. Dr Williamson is among the most approachable people I have ever known, and I’ve enjoyed working alongside him. Cheers to Stuart Robertson, Sam Browett and everyone else in the various ELS PhD offices, who have provided the much-needed social relief over many lunches and Friday evenings (afternoons) in the New Oxford. To my Dad, Dr Martyn Scott, thank you for helping me with this “homework”. To Grace Bishop, you can’t really know how much you’ve really contributed to this PhD, but I can tell you. It’s a lot. Lastly, I’d like to thank myself for finally finishing this thing so I can get a real job like the rest of functioning society.

Abstract

Fluvial science is in particular need of surveying tools which can rapidly and accurately capture topographic data. The use of low-cost, consumer grade UAV (unmanned aerial vehicle) systems and Structure from Motion (SfM) processing methods has seen successful adoption by many other earth surface processes sub-fields however their use for monitoring within the field of fluvial geomorphology remains limited. This study tests the applicability of UAV photogrammetry to fluvial surveying, capturing centimetric resolution data across kilometric scales, providing an ideal perspective for geomorphic process interpretation. For a historically modified UK case study, four series of very high resolution DEMs (digital elevation model) and orthomosaic imagery are produced for a 2km reach of quasi-wandering gravel-bed river. Comparative analyses of DEMs between 2016 and 2018 reveals widening of the incised margin and significant geomorphic evolution characteristic of re-naturalization following the termination of gravel mining, channelization, and resultant aggressive incision. Whole reach volumetric analysis reveals a negative sediment budget approximating a net loss of 250m³/year. Budgetary segregation shows 22% of eroded material is sourced from the banks of the inset wandering margin and is a possible cause of a general fining (30% reduction in mean b axis) of bed material within active channels, detectable by grain scale analysis of high-resolution orthomosaic imagery. Vertical scour is seen to be prevented, even under extreme flows ($\sim 100 \text{ m}^3/\text{s}^{-1}$), by a bed armouring effect which is sustained by liberation of coarse clasts from the floodplain via lateral erosion and bank collapse. Woody debris dynamics, gravel bar creation and migration are intricately modelled throughout the site, their presence seen to be affecting flow-prioritization of sub-channels inside the incised margin. UAV surveying workflows and processing protocols are also developed for fluvial science: A means to neutralize and filter out surface error caused by vegetation occlusion in the SfM workflow, and a method to correct for geo-referencing error in large DEMs. Geomorphic findings at this UK case study hold valuable and transferable insights to river re-naturalization in the context of gravel extraction and channelization.

Chapter 1: Introduction

1.1. Research Context

The three-dimensional recording of landscapes and features is one of the foundations of geomorphological study. Reliable and accurate capture and later reconstruction of spatial data is central to interpretation of landscape processes. The scale of feature of study is important to consider when selecting a suitable method for capture of such data. This naturally leads to a degree of constraint when approaching larger scale features (+1km) if specialist equipment is not available to the researcher. Since features at the kilometric scale and above cannot be measured by contact measurement (by hand), remote sensing equipment must be employed. The main limitation when using such sensors is the associated relatively high cost and loss of spatial resolution. The capability to survey large scale features is a huge advantage however. LiDAR systems have to an extent closed the scale gap between traditional contact measurement and less resolved, but wider scope remote sensing instruments over the past decade. Cost remains a significant barrier to widespread use of LiDAR for geomorphology studies however (Hummel *et al.*, 2011).

The suitability of data collection systems to certain scales, subjects and applications makes selection of the appropriate sensor critical if end data products are to be fit for purpose. Lack of options in this respect, whether due to constrained capital and support equipment or technical expertise and personnel, can dictate a reduction in the survey coverage, resolution or overall quality. Ideally, the subject of study should always control which type of sensors are employed, never the other way around. Access to a wide choice of suitable surveying tools is conducive to production of high-quality geomorphology studies. Systems and sensors which remain competitive at a wider variety of scales thus

provide increased options to the user, permitting greater methodological flexibility and ultimately studies of higher quality. Access to extra data collection methods promises most advantage to smaller working groups or individuals who might not otherwise have the capability to perform landscape research at the scales relevant to their specific sub-field of study.

1.2. Research Motive

Management of rivers, in terms of the hazards they present, resources they provide, and how they affect the surrounding physical and human environment is becoming of increasing importance, both in the UK and worldwide. Enabling and informing protection of people, property, and infrastructure from flooding and erosion is central to academic study of fluvial systems. This paradigm is unlikely to change as multiple climate models predict an increase in extreme rainfall events resulting in shorter return periods for large floods, particularly in the North-West of the UK in the coming decades (Huntingford *et al.*, 2003; Ekström *et al.*, 2005; Kay *et al.*, 2006). Monitoring and prediction of flood events and other river dynamics is facilitated by numerous tools and methods. Stream gauge and precipitation data allow for effective interpretation of the status of fluvial systems. Used in conjunction with spatial interpolation and the use of numerical modelling, prediction of possible discharge values and subsequent implementation of appropriate mitigation strategies is possible. The capture and digital reconstruction of river landscapes in a modelling capacity similarly allows for more detailed interpretation and forecasting of potential flood heights and geomorphic changes (Cobby *et al.*, 2001).

Tools for collection of geospatial data in the physical environment have seen considerable evolution and improvement concerning the information density such systems are able to deliver. Contact methods including manual logging of elevation points with highly

accurate differential GPS (dGPS) require relatively advanced equipment, are labour intensive, and may present operational risks to fieldworkers. Whilst interpolative processing methods can render a good degree of spatial information from such surveys, remote sensing methods are safer and offer greatly increased data collection rates (Brasington *et al.*, 2000). LiDAR and Structure from Motion (SfM) interpreted photogrammetry each have their own advantages and drawbacks when executing and analysing surveys of fluvial landscapes, however in terms of equipment accessibility, image based remote sensing methods are currently more desirable

Unmanned aerial vehicle (UAV) based photogrammetric surveying provides a relatively cheap yet very effective means for rapid collection of spatial data. As such, UAV surveying methods hold enormous potential for capturing geomorphic change, expedited by their ease of deployment and operation. Variations to channel and floodplain morphologies because of high discharge events, both subtle and dramatic, influence the surrounding population and may facilitate more fluvial evolution upstream or downstream. Induced fluctuations to sediment dynamics and flow regime may compromise existing flood defences and proximal infrastructure, however foresight of such variability can enable more informed planning or mitigation implementation. This project intends to predict, detect, and assess the wider impact of geomorphic readjustment for a UK case study. Data used will be primarily collected with UAV based photogrammetric surveying. Openly available LiDAR data will secondarily be utilized for dataset validation and to provide context to data collected by the UAV method. It is expected that such research will benefit local infrastructure planning additionally developing the understanding of fluvial dynamism and analysis using UAVs as a universal tool.

Modern UAV systems are capable of carrying suites of highly specialised sensors and equipment, including multi-spectral and hyper-spectral imagers and even compact LiDAR systems (Chisholm *et al.*, 2013). The flexibility and agility afforded by the UAV platform complements the high data quality these sensors provide. Access and employment of these sensors is often prohibitively costly to the majority of workers; however, consumer grade systems below £1000 have become widespread. Contemporary camera sensors have reached a sufficiently high level of pixel density that extremely capable systems are compact and light enough to be mated to similarly lightweight aerial platforms. This has broadened the scales at which geomorphological research can be carried out whilst not sacrificing survey resolution.

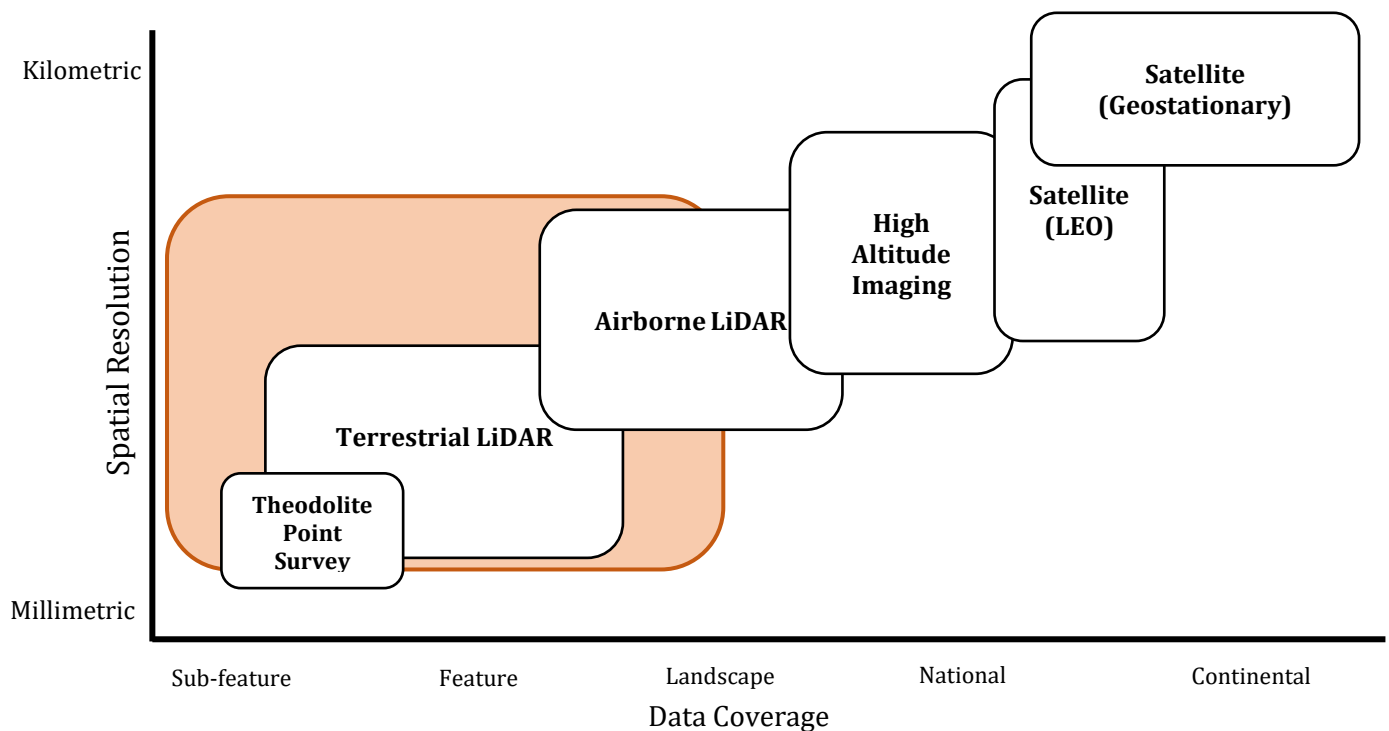


Figure 1.1 – Scales of application for various remote sensing platforms.

Different remote sensing platforms have an associated optimal scale of operation. Sensor and platform selection are usually dictated by the size of the subject of study. For geomorphology, this can be highly variable, between the order of centimetres and kilometres. For workers with limited access to expensive high-end remote sensing

equipment this may prevent their desired study. Accessibility to sensors and platforms which broaden the spectrum of study available to a user has the potential to expedite research in the field of geomorphology and environmental science. Figure 1.1 illustrates the approximate coverage and resolution footprints of the most common remote sensing methods in use today, as well as UAV photogrammetry. When temporal sampling rate and cost are considered, the type of end-users are identifiable, with the highest coverage systems being exclusive to government and space agencies. The intermediate platforms traditionally utilised by larger institutions, and the lower end by sub-institutions and individuals.

One of this study's aims is to test the applicability of UAV photogrammetry data collection and analysis at the centimetric and kilometric scales utilising a single dataset; the ability to capture data over a kilometric scale at the centimetric resolution. Fluvial systems present the ideal case study. Rivers are subject to rapid geomorphic changes at a wide variety of scales (Richards, 1987). Repetition and comparison of multiple surveys under variable conditions will permit detection of changes to the bed, banks and floodplain of the river. In parallel to this aim, the project will employ novel data processing techniques to further improve topographic reconstructions provided by the UAV. Surveying of fluvial settings presents its own unique set of challenges and drawbacks inherent to UAV photogrammetry. Original circumventions and solutions to these problems are presented in tandem.

This project's field campaign will utilize Wooler Water, Northumberland, UK as its primary case study. This gravel-bed river is a good but rare example of a quasi-stable channel in the British Isles. Previous examinations of this site include that by Sear and Archer, (1998), who record incision of up to 9m following intensive gravel extraction which ceased in 1970. The work identifies high-discharge flood pulses and sequencing

of gravel extraction sites as the main catalyst for vertical scour within the channel. This was characterised by metamorphosis from multi-threaded sinuous to single-threaded. Vertical instability is geologically inherent to a limited degree (Tipping, 1994) at Wooler Water, however it is clearly exacerbated by and proportional to the intensity of local gravel extraction. Over twenty years on, the channel's morphology remains in flux, most notably with very large avulsion events during 2013 and the "Boxing Day Floods" of 2015. The presence of some management structures, some abandoned, some maintained, adds further complexity to the local geomorphology. Wooler Water is at an important phase of its physical history. This study will effectively record and analyse the ongoing shifts within this system, at the reach, sub-reach, feature, and clast scale, with the UAV platform at its core.

1.3. Thesis Structure

This project combines two highly prolific disciplines of environmental science; fluvial geomorphology and remote sensing. It is intended that by doing so, each respective field will benefit from the tools developed and insights they provide. A degree of segregation between each will exist when discussing the respective backgrounds, methods and challenges specific to each field. This will be most visible within the Thesis' literature review and methodology sections. The Thesis includes a comprehensive literature review, encompassing the backgrounds and contemporary research into remote sensing systems and fluvial geomorphology. This will be followed by laying out of the Project's research aims in the form of three research questions intended to discreetly illustrate the investigative path. An increasingly focused approach will be taken when describing of the UAV field campaign. This will include general UAV operation and pre-flight planning, as well as the detailed recounting of each survey performed within the course of this PhD.

Data processing and analysis descriptions will be comprehensive throughout but will however be split into their respective relevant sections (namely according to their scale). Finally, the project's three research questions will be considered with the data, each receiving their own summary.

Chapter 2: Literature Review

2.1. Introduction

Technological developments during the twenty-first century have allowed for an expedited growth in the field of Earth observation and subsequent monitoring applications. Remote sensing systems have become far more capable, as have processing methodologies. The variety of platforms available on which to base such technologies have allowed workers to study a wider range of environments, in more detail, at reduced cost. The use of unmanned aerial vehicles (UAVs) has seen considerable development in academic and industrial research within the last decade due to technological advances in onboard global position system (GPS) technology and associated ease of post-processing using photogrammetric software. In addition, the use of UAV photography to generate 3D models of objects and landscapes at high resolutions has proved an easily accessible alternative to expensive, cumbersome laser scanning systems. Spatial coverage and resolution can be easily adapted to suit survey parameters. The recent explosion in the use of unmanned aerial platforms within a research capacity has been supplemented by developments in camera sensors and mounting systems, as well as computing and post-processing power. According to UAV Global's listings there are 241 standalone commercial UAV manufacturers, as of May 2016 (UAVGLOBAL, 2016). The market itself has an estimated worth of \$10 billion with projected 20% growth in the civilian sector (Business Insider, 2015). As such it is becoming increasingly hard to deny the accessibility afforded to consumer grade drone platforms. Their use in remote sensing and environmental science has found them to outperform more traditional platforms such as LiDAR, especially in terms of cost and ease of deployment.

The need for an inexpensive means to collect data about river environments is high, particularly in less developed nations, where reliance upon, and hazards posed by rivers are more prevalent. Rapid and accurate data collection is essential for water resource management and environmental monitoring. Small UAV systems suit this role well due to their low cost and ability to deploy quickly. The information provided by aerial imaging can find application in a multitude of modelling and analysis suites, aiming to inform risk managers and developers. A concise review of literature encompassing developments in remote sensing systems, associated platforms, and data processing is presented here alongside examples of studies which have employed such technologies.

2.2. Remote Sensing

2.2.1. Background

Earth observation has seen the much of its development in military or surveillance applications. Initially used to effect during World War I, aerial photography, reconnaissance and intelligence gathering have become central to strategic decision making. As cameras became more compact and ruggedized, imaging systems were mounted onto smaller, faster aircraft during the Second World War and improvements in developing methods allowed for more ease of processing, resulting in an improved information output rate. Smaller cameras also opened up the availability of other platforms other than manned aircraft, including rockets, balloons, and kites. The majority of the early development of earth observation systems took place during the Cold War, driven by generous funding. Advanced rocketry and aerospace development additionally saw an increase in the number and variety of sensing systems and platforms on which to mount them.

The U-2 high altitude imaging aircraft was possessed extreme imagery coverage and resolving power. Vulnerabilities in the system however led to the need for the development of a space-borne platform, resulting in the CORONA satellite programme. With global coverage at good resolution, the platform was highly capable. Spaceborne imaging systems of the time, whilst capable of data collection at extreme coverages with acceptable resolutions, were severely limited by the lack of an information transmission system, necessitating the physical recovery of film canisters from satellites. These technologies soon found application in civil research and laid the groundwork for a new generation of remote sensing systems. The U-2 aircraft platform continues to see service under NASA for meteorological research (Goldhagen *et al.*, 2003). CORONA satellites also saw non-military application for resource exploration (McDonald, 1995).

2.2.2. Remote sensing platforms

Improvements in data return methods enabled civilian use of remote sensing platforms for routine collection of data. Platforms such as Landsat providing regular data collection for previously unmapped areas. Digitally available data encouraged development of processing and analysis methodologies. Having been previously only accessible to large institutions with the necessary capital and equipment, the standardization and increasing availability of digital datasets positively impacted the field of environmental science by attracting more researchers and developers. Operating since 1972 a total of eight Landsat satellites have been produced. The principle instrumentation aboard Landsat missions 1-5 (1972-1984) consisted of a multispectral scanning system (MSS) capable of providing imagery to a ground resolution of approximately 80m (Mika, 1997). Whilst missions 1-4 carried the return beam vidicon (RBV) to accompany the MSS, Landsats 4 and 5 utilized a thematic mapping (TM) instrument. The RBV was capable of capturing imagery across a 185 km by 170 km area in three spectral bands (green, red and near infrared). The MSS

could provide multispectral data, however in four bands and at higher detail (with less regard for positional accuracy) (Campbell, 2011). Despite the relatively advanced abilities of satellite remote sensing, routine application was recognised to be difficult. Four of the seven Landsat missions (pre-1999) failed or malfunctioned in some way (Campbell, 2011) the reliability of spaceborne remote sensing platforms could be questioned. Some studies openly recognise the limitations of the data provided by such systems, naming noise and a lack of pre-processing as two distinct disadvantages of the Landsat platforms (Maxwell, 1976).

On the other hand, the repetitive provision and extensive coverage of the data provided by the first Landsat missions expedited not only extension in the quantity of studies utilizing remote sensing to develop understanding of earth surface processes, but also the diversity of environments now available for remote exploration. Alpine and glacial systems, previously difficult to study due to equipment access limitations became of particular interest, especially in the advent of initial glacial retreat studies around the sixties and seventies (Terasmae and Hughes, 1960; Edwards, 1975; Dreimanis, 1977). Studies involving mass balance and inventories (Rundquist *et al.*, 1980; Scambos *et al.*, 1992) as well as reflectance and albedo (Hall *et al.*, 1987, 1989; Dozier, 1989) were well explored during this period. Contemporary Landsat missions are aimed toward continuity of data collection by preceding operations (Zanter, 2016).

As more applications were found for the updated technologies, technical limitations were uncovered. Perhaps the most basic and persistent problem associated with spaceborne optical sensors is the need for cloud free imagery if ground features are of interest. Whilst cloud screening algorithms utilizing a variety of methodologies have existed since the eighties (Ebert, 1987; Gutman *et al.*, 1987; Saunders and Kriebel, 1988; Derrien *et al.*, 1993) cloud cover often restricted the abilities of spaceborne remote sensing systems to

detect and monitor short-term or temporally acute events (Moran *et al.*, 1997). Cloud obscuration frequently hinders observations of tropical environments (Wright and Van Schaik, 1994; Mulkey *et al.*, 2012). Snow detection algorithms such as SNOMAP (Hall *et al.*, 1995) are also made problematic by some cloud obscuration due to the similar reflectance values of snow and ice-containing clouds (Dozier, 1984; Marshall *et al.*, 1993). The abilities of some contemporary satellite systems to provide ground resolutions down to 0.4 cm (Fraser and Ravanbakhsh, 2009) and to correct for atmospheric effects (Richter, 1996) make them extremely powerful platforms for provision of remote sensing data, however the issue of cloud obscuration remains un-circumvented without use of synthetic aperture radar sensors, which are not competitive in terms of resolution. Manned aircraft have not seen a considerable amount of evolution geared towards improving aerial photography since the cold war era. Development of cameras and sensors which are universally mountable to such platforms has taken precedence. With the first patents for the digital camera emerging in 1970s (Lopes and Thomas, 1973; Barrett, 1978) progression in the field of optics and image analysis has arguably led to the evolution of modern photogrammetry.

2.3. UAV Systems

2.3.1. System types

The concept of a pilotless, self-propelled aerial vehicle was conceived, as a result of wartime innovation. An “aerial torpedo”, the Hewitt-Sperry Automatic Airplane (1918) may be considered autonomous to a degree, containing a gyroscope flight stabilization system. Radio control technologies had been demonstrated (Tesla, 1905) before the Automatic Airplane’s development. The first radio controllable and reusable aircraft was developed in 1935 by the British Royal Navy; the DH.82B Queen Bee training target. A modified version of the US Air Force Ryan Firebee supersonic aerial target drone, outfitted with a film camera and recovery parachute, was utilized for reconnaissance over during the 1960s and 70s. Further iterations on reconnaissance systems such as the Israeli “Scout” drones saw improved digital sensors and greatly reduced operational costs (Edwards Jr, 1990). These were used in the 1986 Yom Kippur War for gathering intelligence. (Miller, 1988; Cai *et al.*, 2010). Further improved versions of the Scout (Pioneer) were also employed with during the Gulf War (Polmar, 2013).

Methods of controlling and directing UAV platforms is central to their usefulness. Guidance for the first reusable drones was based upon inertial guidance systems alone (Shima *et al.*, 2006). The most significant improvement to this area is however the use of the global positioning system (Campa *et al.*, 2004). Combined with on-board inertial measurement units (IMU) and accelerometers, algorithmic implementation of GPS can allow for precise and reliable manoeuvring and positional feedback (Kaminer *et al.*, 1998; Kim *et al.*, 2006). Additionally, vision-based guidance systems exist for situations where GPS may be denied (Ahrens *et al.*, 2009; Cesetti *et al.*, 2009; Lange *et al.*, 2009). Such guidance systems are vital to operation of rotary-wing UAVs, especially multi-rotors,

where a lack of control surfaces necessitates attitude control through differential thrust and torque balancing alone. Certain advantages exist for rotary systems however, perhaps most explicitly their vertical take-off and landing (VTOL) abilities. Conversely, the increased speed, range and payload capabilities of fixed-wing platforms are an advantage.

Small-form computers, rapid manufacturing, and improved materials have boosted availability of technology to consumers (Hopkinson et al., 2006). Concurrently, the proliferation of UAV systems within military, commercial, and domestic applications has seen the new manufacturers and development groups. In the USA alone over 90 such companies have been in operation since 2015 (Canis, 2015). Aided by the relative ease of manufacturing, requiring few components and using well proven techniques, the cost of UAV production can be kept down. Furthermore, the integration of ubiquitously available technologies including smartphones, tablet computers, WiFi receivers, and GPS integration has permitted elevated levels of control and consumer accessibility.

2.4. Photogrammetry

2.4.1. Computer Vision and Image Processing

In an earth observation context, the role of digital image processing has developed in tandem with the development of sensors and platforms. Applications were found in the form of weather observation, initiating in the 1970s. Caveats of equipment expense and availability remained into the 1980s however (Kümmerlen *et al.*, 1999). Continued computer miniaturisation and cost reduction eventually allowed the public to access such technologies. Today, digital image processing is important within industry and research, for a diverse range of applications. Optical systems and associated postprocessing have multiple applications within assembly line quality control for a plethora of industries,

including food (Gunasekaran, 1996), automotive and aerospace (Vernon, 1991). Critically, such practices enable low-cost, non-contact methods for consistent quality control. Computerised image processing is also used for medical applications (Tavares *et al.*, 2009). Aerially captured images are automatically interpreted by McKeown, Harvey, & Wixson (1989), who use rudimentary object based image analysis (OBIA) to classify variable land use and features; differentiating roads, houses and airport taxiways and hangars. OBIA is well used within environmental sciences literature, where rapid classification of large datasets is made easy and quick (McKeown *et al.*, 1989; Yu *et al.*, 2006; Blaschke, 2010; Myint *et al.*, 2011; Arvor *et al.*, 2013; Hussain *et al.*, 2013).

For DEM generation, images must be captured with a degree of coverage overlap, the extent of which may be defined by the application. Registration is achieved through identification of pixels in multiple images which correspond to a common point on the ground. Assignment of an absolute spatial reference for each image should be sought, however interpretation can be achieved with relative or arbitrary coordinates only, provided location can be identified through context (Schowengerdt, 2007).

2.4.2. Structure from Motion (SfM)

Image registration forms the initial step of the Structure from Motion (SfM) workflow. A multitude of computational methods exist, some more suited to certain applications than others. Brown, (1992) discusses several of these, identifying those best suited to multi-sensor and multi-temporal data, as well as the applications of three-dimensional information extraction and model-based object recognition. For spatial reconstruction, point-mapping may be considered the primary approach for image registration. First, spatial features are computed or manually chosen for each image. These features, control points or tie-points, are then corresponded to common images across the data set. Finally, an image transformation is applied according to a function to best overlay common

control points, such as least squares regression. Tie points may be assigned manually, i.e. by reference of landmark or another static feature, or automatically through computer vision. Successful processing is however subject to all tie points being assigned a relative spatial reference so that image transformation may be applied. Collinearity equations rendezvous the 2D coordinates in the sensor plane to the 3D coordinate in the real world (Schenk, 1994; Schindler, 2015). These equations form the basis of the algorithms utilized by processing packages (Maas, 1995; Schenk, 2005). Further matching algorithms such as the Lucas-Kanade tracker (Lucas and Kanade, 1981) give additional means for initial tie-point generation. Modern processing packages include means for distortion compensation through camera calibration models, ultimately improving data densities and reducing error.

For the purpose of forwarding the field of environmental science, the abilities of aerial platforms to provide parametric values coupled with detailed imagery make them ideal instruments for reconstruction of landscapes and their physical characteristics. This allows workers to go beyond image interpretation alone, enabling a wide scope of modelling techniques. This in turn facilitates analysis of processes within the environment. Systems such as the CORONA satellite imaging platform, operating with dual cameras, were capable of producing stereo-photographic images, permitting interpreters to perceive depth (Barnard and Fischler, 1982). More recent studies have been able to reconstruct digital surface models from CORONA imagery (Schmidt *et al.*, 2001; Altmaier and Kany, 2002; Casana and Cothren, 2008). The principle is easily transferable to aerial photography and best suited to urban environments, where straight edges and predictable geometries ease interpretation (Baillard and Maitre, 1999). Stereo-photogrammetry is a means for three dimensional interpretations to be made through combination of individual images, which by themselves, cannot convey true 3D structure.

LiDAR provides further means for constructing three dimensional models from land based (TLS) or air based (ALS) platforms. By utilizing the time of flight principle, the instrument detects points with relative coordinates in the environment. The system captures many millions of points from an environment to create a point cloud which with further processing can be used to produce a polygonal mesh and DEMs. The resolution of such systems is effectively controlled by the specified field of view and scanning time. Whilst laser range finding systems had existed for a time before their mapping applications (Stickley and Gingrande, 1967; Hamilton, 1969) their use as a means for capturing feature morphology was initiated around the 1980s (Krabill *et al.*, 1984). Its application to the physical environment was particularly noted in forests at the beginning of the millennium and many contemporary studies favour the use of LiDAR based methodologies (Dubayah and Drake, 2000; Lim *et al.*, 2003; Popescu *et al.*, 2003). LiDAR scanning systems may often be used from a terrestrial base, particularly suited for capturing vertical features, such as cliffs and outcrops (Bellian *et al.*, 2005; Lato *et al.*, 2010; Young *et al.*, 2010). The instrument can also operate in an aerial capacity (Verma *et al.*, 2006), however the bulk of LiDAR devices often limits accessibility to such platforms.

2.5. Fluvial Geomorphology

2.5.1. River Forms and Controls

The relationship between form and flow in river systems gives rise to numerous and varied feature types. The field of fluvial geomorphology aims to quantify, categorise and monitor these features to learn how they might be formed and maintained. This could inform artificial modification of the physical world. The introduction of human actions may disturb the equilibrium that exists to maintain the geomorphic “status-quo”, leading to removal, alteration or creation of new features within the main river channel or floodplain. Long understood in Europe, the Middle and Far East (Burke, 2009) this fact has aided hydraulic engineering throughout history. Observing changes in river systems and identifying the underlying causes for such evolution form the basis of many studies. Schumm & Lichty (1963) rationalise ongoing channel widening and floodplain accretion through accounting the effects of variable precipitation and its subsequent effect upon peak flows and the affinity for vegetation to stabilize features within the system; channel widening is associated with low-precipitation periods which produce higher peak flows due to the intermittent nature of rainfall. Conversely, floodplain accretion is associated with more consistent rainfall, making for lower peak discharges and permitting vegetation to grow within the channel margins, arresting the flow and allowing for deposition. Channel response may alternatively be due to alterations in a river’s sediment load as in Smith & Smith (1984) who identify similar channel widening to Schumm & Lichty (1963), but by different mechanisms. The former work finding that the channel widening could be explained by the influx of extra bedload material by aeolian processes upstream. The additional sediment decreases channel depth, therefore flow the river

increases in channel width to accommodate the same flow. This study classically highlights the relationship between river load and form.

Alluvial systems provide the most diverse array of river forms, centrally dependent upon sediment type and quantity. According to Leopold & Wolman, (1957) planform channel patterns may be generally classified to be either (relatively) straight, meandering or braided, with increasing sediment load and lateral instability respectively. Sub (or super) classification is afforded by other works which account for additional effects such as variable flow regime, vegetation and geology (Schumm, 1985; Rosgen, 1994; Nanson and Knighton, 1996). These works serve to categorise river form in a spectral manner, where sediment size and quantity along with water velocity and stream power fundamentally shape a river channel's final form. The distinctness of different channel types is afforded by the existence of intrinsic and extrinsic geomorphic thresholds, whereby if exceeded, a new mechanic process arises. An extrinsic threshold may be identified as one which requires forcing by an external variable for exceedance to occur. For example, the stripping of vegetation leading to river-bed scour. An intrinsic threshold however does not require forcing by an external variable to be exceeded. An example of an intrinsic threshold exceedance might be slope failure under gravity following steepening by sediment accretion.

Basic forms are identified by Leopold & Wolman, (1957), naturally maintained straight channels are very rare under fully natural condition since any lateral asymmetry will inevitably lead to flow deflection and creation of more variable roughness downstream. This lateral instability forms the basis for meandering channels whereby pools and riffle sequences provide the embryonic disturbance for sinuosity to increase. The meandering pattern is synonymous with a higher ratio of fine sediment (suspended) to coarse (bed load) and exists at a quasi-stable level. Meandering systems can additionally be identified

when the ratio of a sinuous channel's wavelength to its width is maintained between 5 and 7 (Whiting & Dietrich, 1993). Braided systems are found when sedimentary load is higher (Murray & Paola, 1994), the splitting and reconnection of sub-channels becoming more common when sediment load is coarser (Doeglas, 1962). Structural processes that give rise to the braids are fundamentally similar to those which aim to increase sinuosity in straight channels, albeit with more verticality due to increased sediment load. Additional mechanics exist where channels bifurcate and converge; bars are subject to migrate downstream through erosion at their head and deposition at the tail within the pool caused by flow confluence (Bristow & Best, 1993). Sediment bars are laterally unstable since any minor shift in flow direction, power or load can lead to flow deflection, actioning geomorphic processes to occur upon the flanks of any bar (Ferguson, 1993). Anabranching river systems are recognisable by the presence of channel splitting and reconnection around bars or islands which are more stable than their braided system counterparts (Tooth & Nanson, 1999). Such stability is afforded by a relatively low stream power despite these rivers often carrying a relatively coarse sediment load (Latrubesse, 2008).

Despite large number of categorized river forms, the classification of system types should be considered to exist on a spectrum, where a continuum of morphologies exists. System type is, at the most basic level, defined by the interaction between flow and sediment load/type, any change (beyond extrinsic threshold levels) in such inputs should lead to a lateral or vertical modification to the river's general profile. This is the basis for river metamorphosis; whereby the complete morphology of a river is altered (Schumm, 1969). Natural variability in precipitation and sediment loading processes are well documented to affect channel dimensions and sinuosity under human timescales (Erskine & White, 1996; Erskine, 1986; S. Schumm & Lichty, 1963). Channel metamorphosis has been

observed to occur even under very slight environmental forcing (Brizga & Finlayson, 1990), usually when the systems exists in a pseudo-stable state. That is, a river may flip flow regime under some circumstances, for example where paleo-channels are available for reactivation or geology serves to deflect flows or alter sediment load/type. The fragility of stasis to mild environmental forcing within fluvial systems follows that artificial influences will affect river planform and channel dimensions.

2.5.2. Artificial Influences on River Form

The role of human actions which alter flow regime along with sediment quantity and type should be slated to have an equivalent effect as natural analogues, however artificial influences are not so limited. Conversion of natural landscapes for industry or settlement inevitably will affect drainage, if not the riparian margin directly. Development within the catchment is associated with rivers transitioning to more stable types often through reduction in sediment supply. Marston *et al.* (1995) establish a strong link between increasing floodplain clearance for industry and settlement which served to lower the water table leading to channel incision. The metamorphosis from braided to single channel system is further fulfilled by stasis of abandoned channels by vegetation. Artificial changes to the equilibrium that exists to maintain the present form are the fundamental driver of river metamorphosis. A qualitative summary of such changes is well summarised by Chang (1986):

Table 2.1 – Summary of the effects of modification of discharge (Q) and sediment load (Q_s) Note: * = indirect effect

	Channel Width	Channel Depth	Width/Depth Ratio	Meander Wavelength	Channel Slope	Sinuosity
Q^+	+	+	+	+	-	*
Q^-	-	-	-	-	+	*
Q_s^+	+	-	+	+	+	-
Q_s^-	-	+	-	-	-	+
$Q^+ Q_s^+$	+	*	+	+	*	-
$Q^- Q_s^-$	-	*	-	-	*	+
$Q^+ Q_s^-$	*	+	-	*	-	+
$Q^- Q_s^+$	*	-	+	*	+	-

Each scenario described by Table 2.1 can be caused by natural variation, however artificial analogues exist. An increase in discharge along with bedload is characteristic of deforestation, conversely a decrease in each may be attributable to dam or weir construction. A rise in discharge and decrease in bedload is symptomatic of flow diversion from elsewhere by canals, irrigation and potentially climate change. Vice-versa, a decrease in discharge and increased sediment loading might be caused by over exploitation of water resources.

Gregory, Davis and Downs (1992) link ongoing urbanisation within the margins of a UK floodplain to localised channel widening by more than double with an associated slight increase in depth (0.4m). Channel enlargement is similarly observed by Brookes, (1987) who documents channel incision and widening to variable degrees at 14 sites downstream of channelization works. The effects investigated by these works are linked by the symptomatic increase in peak discharge and thus stream power due to increased hydraulic input within an unchanged given period, by landscape impermeability and flow acceleration respectively. The control and relationship between flow and channel dimensions is known to vary between case examples. Proportionality between change in

peak flow and associated channel expansion is seen to be inconsistent by Booth (1990). Some cases exhibit modest channel adjustment in response to alterations in peak discharge, whereas some channels are observed to “catastrophically” incise out of proportion to the change in discharge that has occurred. Examination of this non-linearity is undertaken through prioritised analysis of the controls upon basal shear stress (τ_b), specifically slope (S). When considered that the action of channel incision serves to decrease gradient, idealistically all the way between source and local base-level, a negative feedback cycle is identified; reduction of slope by incision serves to reduce shear stress thus limit further incision. The initial slope conditions in a channel however are what source the non-linear relationship between change in peak flow magnitude and incision. In channels of initial low gradient, any incision that occurs acts to reduce slope as a greater percentage of the initial gradient. Contrastingly, in streams of high initial slope, the negative feedback is less pronounced since vertical scour does not decrease slope to the same relative degree that it would in a shallow-gradient system. This presents an obvious discourse in the expected channel response between upper stage, headwater streams, and lower to middle course channels.

Landscape context aside, human influences upon the factors which define fluvial form are diverse and often widespread in developed countries. Artificial effectors to discharge, most pervasively land-use, and sediment type and quantity have varying levels of disturbance to river systems. Such disturbance may be spatially or temporally inconsistent, with wide-ranging magnitude. Direct interference with sedimentary throughput by human installations or processes both in-channel and within the wider catchment gives rise to channel adjustments throughout the long-profile. Deforestation and subsequent soil erosion as in Restrepo, Kettner and Syvitski (2015) may serve to increase a river’s sediment load resulting in aggradation of in-stream habitats (Brookes,

1990). Conversely sedimentary cut-off by dam or weir can almost invariably lead to vertical scour, bank failure and stripping of riparian vegetation (Barclay, 1980) and thus it's stabilising effect. The connotations of such effects lend significance to the understanding of channel adjustment. Increased channel depth as a result of clearwater erosion due to sedimentary cut-off upstream, often defined as incision or degradation, may progress upstream or downstream depending on the nature of the initial disturbance (Galay, 1983). In the former case, an adjustment to the local base-level such as a lake level or meander cut-off can introduce an adverse change in gradient or knick-point, conducive to an increase in velocity and thus shear-stress. Downstream progressing incision is synonymous with in-channel installations which disrupt sedimentary throughput, reservoir dams being the most prevalent example; retention of material within the main reservoir affords outflow water to have a higher affinity to erode.

The proliferation of river bed lowering whilst confined to a singular direction in the case of base-level adjustment or sediment cut-off may process both up and downstream in certain cases. A localised and sustained removal of bed material introduces a spatially discreet area of lowered channel, which can affect equilibriums upstream and downstream. In-channel gravel mining presents the most obvious artificial process that fits these conditions. Effects identified by Kondolf, (1994) and Rundquist, (1980) namely incision occurring up and downstream are attributable to the localised abrupt change in slope at the start and terminus of an extraction pit. Two fundamental effectors arise: the creation of a knick point at the upstream end of the site, and the retention of bed material within the extraction pit (Erskine, 1990; Petit *et al.*, 1996; Harvey and Smith, 1998). In accordance with the shift in equilibrium this causes, vertical scour is to be expected upstream as the head-cut migrates, and downstream as clearwater erosion takes place

due to sediment capture within the pit. Gravel extraction industries are rarely confined to the channel alone and often utilize the entire riparian margin, mining the floodplain. Whilst this may initially prevent direct channel incision channel avulsion to a floodplain pit can have more violent consequences than in-channel mining alone. "Pit capture" as referenced in Mossa and Marks, (2011) introduces not only a slope anomaly to the river system, but additional lateral instability, potentially exaggerating downstream effects (Kondolf, 1998).

2.6. Applications for UAV remote sensing

2.6.1. Ecology and Vegetation Monitoring

Image-based UAV remote sensing is highly applicable to monitoring of plant health parameters. Vegetation distributions and crop plots are often multiple hectares in area, thus ground sampling operations are unfeasible for acquisition of big datasets (Kaneko and Nohara, 2014). The use of UAVs for surveying of crops has enabled producers to maximise yields (Anthony *et al.*, 2014) through provision of higher spatial and temporal resolution data (Bendig *et al.*, 2013), for comparatively little cost (Lelong *et al.*, 2008; George *et al.*, 2013). The use of near infrared sensors mounted to UAV platforms has been demonstrated as capable of providing data for vegetation biomass (via reflectance interpretation), which when combined with crop height data, provided by visible light (RGB) imagery, can provide a great deal of information (Berni *et al.*, 2009; Bendig *et al.*, 2015). Calibration of such sensors is critically important, and even slightly variable lighting conditions between surveys may skew results (Berni *et al.*, 2009). Implementation of other sensors such as thermal imaging systems are able to provide data for plant coverage and soil moisture, through use of temperature as a proxy both (Turner *et al.*, 2011; Baluja *et al.*, 2012). Data processing methods such as object based image analysis (OBIA) methodologies make effective use of the high quality data provided by UAVs to enable capacities such as distinction between vegetation and bare soil (Torres-Sánchez *et al.*, 2015) and more informed weed control (Meyer and Neto, 2008). Such processing methods however require imagery where objects of interest are comprised of at least several pixels and not occluded (Blaschke, 2010).

UAV remote sensing for forest applications draws multiple parallels to that of agriculture. Whilst aerial LiDAR has been noted as an effective tool for measuring tree height and

crown size (Drake *et al.*, 2002; Brandtberg *et al.*, 2003; Patenaude *et al.*, 2004; Andersen *et al.*, 2005) risks are presented to aircraft flying low over densely forested landscapes by subsequent lack safe landing options in an emergency (FAA, 2004). The use of unmanned systems thus represents a bypassing of such risks, whilst still retaining operational capabilities. Small platform feasible LiDAR systems have been evaluated to be feasible for forestry surveying (Lin *et al.*, 2011) however there are implications for the range of UAVs carrying such systems (Wallace *et al.*, 2012), thus the overall survey coverage. All literature involving the use of UAV based LiDAR systems appears to have so far exclusively used rotary-wing systems and hence been limited in survey coverage. Rotary systems are however undoubtedly more feasible for sub-canopy operations, although range and battery life implications persist (Chisholm *et al.*, 2013) especially when carrying heavy LiDAR scanners. The role of UAVs for insight to forest parameters draws many obvious inferences to correlating physical variables, including those of wider local biotope. An example being the relationship between forest structure heterogeneity, biodiversity and gross primary production (Turner *et al.*, 2003; Gitelson, 2004; van Leeuwen and Nieuwenhuis, 2010).

2.6.2. Earth Sciences

Photography and other imaging systems have been well used to analyse both modern and historic geological subjects (Arnot *et al.*, 1997; Wickliff, 1997). Reconstruction of photo-realistic 3D models has traditionally been made possible through LiDAR scanning (Bellian *et al.*, 2005; Buckley *et al.*, 2010; Lato *et al.*, 2010; Burton *et al.*, 2011), which also allows inference of rock properties through variable wavelength reflectance measurement (Burton *et al.*, 2011). Such studies often involve use of ground-based scanners, which are limited when capturing particularly wide or tall outcrops. To circumvent this problem, helicopter mounting of scanning systems has been suggested

(Buckley *et al.*, 2008), however cost and accessibility to such assets rules out such methodologies to most workers. Photogrammetric employment of UAVs offers a means for modelling of large-scale geological structures with greatly reduced cost, perhaps at the expense of LiDAR's property sensing abilities. However, it may be possible to infer rock properties through use of multi-spectral imaging systems such as near-infrared photography. The use of drone-based photogrammetry and thermal imagery is immensely applicable to the volcanic sciences, where access limitations, even for manned aircraft, make study problematic (Saiki and Ohba, 2010). For hazard surveillance, UAV platforms offer a wide array of sensing possibilities including landform monitoring (Saggiani *et al.*, 2007; Nakano *et al.*, 2014; Clapuyt *et al.*, 2016) gas sampling (Caltabiano *et al.*, 2005; Patterson *et al.*, 2005; McGonigle *et al.*, 2008), and temperature mapping (Amici *et al.*, 2013).

For management of earth resources, remote sensing facilitates extensive landscape modelling and management implementation options. UAVs have proven useful within the coal industry for resource management and exploration to a limited degree. For monitoring and detection of possible sub-surface combustion events, UAV based thermal imaging allows for hazard mitigation and resource preservation (Vasterling *et al.*, 2010; Malos *et al.*, 2013). As platforms for resource exploration and mapping, UAVs equipped with gravimetric sensors and magnetometers would be feasible for cheap, rapid terrestrial mineral exploration (Barnard, 2010). Deurloo, Bastos, & Bos, (2012) however note the limitations relating to the bulk of more conventional gravimeters, thus their suitability for mounting to manned aircraft more exclusively. Aeromagnetic surveying with UAV based instrumentation similarly limits sensor dimensions and mass, however Funaki *et al.* (2008) demonstrates the successful use of such systems with decent accuracy in fair conditions (Funaki and Hirasawa, 2008). UAV based magnetometers have

additionally been found feasible for unexploded ordnance (UXO) detection (Versteeg *et al.*, 2007).

2.6.3. Glacial Applications

Glacial retreat as a result of recent climate forcing is ubiquitously identified throughout the scientific community (Bond *et al.*, 1993; Zwally *et al.*, 2002; Howat *et al.*, 2007; Kulkarni *et al.*, 2007; Joughin *et al.*, 2008), thus an increase in the means to study such systems, especially with UAVs, has followed. Photogrammetric and structure from motion (SfM) applications include investigation of terminus calving dynamics in marine glaciers, where temporally critical DEM generation is of importance (Ryan *et al.*, 2014, 2015). High temporal resolution data collected via UAV based photogrammetry makes these systems ideal for measuring rapid morphological change including that of glacier mass balance. Immerzeel *et al.* (2014) utilize drone photography for investigation of ablation and velocity patterns in Himalayan glaciers. The survey does offer great insight into sub-feature scale morphological variations, however changes at the scale of the entire system are not wholly presented. Other photogrammetric glacier studies include a terrestrial based survey; Piermattei, Carturan, & Guarnieri (2015) find photogrammetric interpretation of glacier mass balance is achievable, performing similarly to TLS, however care must be taken where the presence of shadows and variable contrast may lead to less reliable point cloud generation.

2.6.4. Fluvial Sciences

Landscapes and features which demonstrate dynamic morphological variability are particularly well suited to capture and reconstruction via UAV photogrammetry and SfM, especially when such changes may often have a direct effect upon their surrounding environment, be it physical or human. Rivers are invariably subject to morphological evolution at a wide range of spatial and temporal scales, thus timely data collection is

paramount if such variability is to be utilized in modelling and analysis processes. Morphological study of rivers employing UAV surveys has drawn significant attention. For shallow rivers Bagheri, Ghodsian, & Saadatseresht (2015) and Bangen, Wheaton, Bouwes, Bouwes, & Jordan (2014) utilize UAV imaging and ALS respectively, returning very comparable yet high quality DEM data. When compared to a work, such as Javernick, Brasington, & Caruso (2014), who use a combination of DEM data collected via helicopter photogrammetry, and manual GPS referencing of channel bathymetry and water surface elevation, rather similar results and accuracies are observed. The obvious implication that the former studies offer data quality alike to the latter, whilst having vastly simpler methodologies further demonstrates the applicability of UAVs for rapid, effective collection of morphology data. Channel bed bathymetry does however present a challenge to aerial remote sensing methods, especially image-based ones, where surface glare and water visibility negatively affect DEM quality. An interesting approach is taken by Storlazzi, Dartnell, Hatcher, & Gibbs (2016) albeit in a marine capacity, who use replace the drone mounted method with a housed camera designed to capture georeferenced nadir imagery floating on the surface, reconstructing bed bathymetry with SfM for waters of good visibility between 4m and 12m depth. Such conditions are rarely observed within fluvial systems, although it is not entirely implausible that a hybrid aerial-water drone could fulfil both roles. Imaging and interpretation of sub-aerial and immersed topography has been demonstrated to be possible using airborne photography methods alone, however sonar and LiDAR based methods have been found to provide more complete data (Feurer *et al.*, 2008).

Works which seek to improve facilitation of river restoration through increasing ecological integrity whilst maintaining flood protection often include the use of UAV imaging. Flynn & Chapra (2014) utilize UAS for detection of algal blooms, a characteristic

indicator of organic pollution, at a watershed scale. Such a scale is yet to become feasible for SfM methods. Mancini, Frontoni, Zingaretti, & Longhi (2015) work at a similar scale to characterize land use for riparian and estuarine environments, interestingly including an unmanned ground vehicle (UGV) for additional imaging viewpoints and the use of a change detection algorithm to map temporal variability. Jensen, Hardy, McKee, & Chen (2011) utilize a fixed wing UAV to generate orthomosaics imagery for assessing habitat homogeneity for several miles of river over the course of a year. The results of their surveys well show the dynamic nature of the riparian environment, as flow rates fluctuate throughout the year. The resolution of imaged areas could have been improved however by executing surveys at lower altitudes. The works described above do not utilize 3D processing as it is not necessarily required, however for monitoring instream and floodplain vegetation heights, a means to gauge elevation is invaluable. Such studies as Van Iersel, Straatsma, Addink, & Middelkoop (2016) accomplish this using SfM, however whilst their level of accuracy is deemed sufficient for detecting vegetation height change, the work does not utilize GCPs and thus includes significant error within the generated DEMs.

Chapter 3: Research Questions

1. How are existing channel and bed morphologies influenced by the current flow regime and how might they be affected by future variability?

The primary aim of this project is to carry out concise recording and mapping of sedimentary processes within the study reach will be carried out. Research question 1 intends to utilise this data in order to track and extrapolate upon the geomorphic evolution of Wooler Water. The role of UAV surveying is most central to this, as timely and high-resolution measurement of surface variability is essential in order to build the most complete picture of river variability. Volumes of sediment transported during even short periods of high flow may exceed those moved during an entire season of low flow however, potentially leading to channel avulsion or potential for further change by other processes. Flood events represent such periods and have historically led to significant morphological change within the study reach. The project aims to generate fine resolution mapping of erosional and depositional patterns, allowing for precise tracking of the volumes of water and sediment which enter and leave the system, thus permitting interpretation of how downstream areas might be affected. Understanding the role of flooding and its influences upon local geomorphic change and the wider sediment flux of the Wooler Water field site will aid the project by improving transferability of the observations made throughout its course as well as developing the capabilities and applications for UAV surveying and wider remote sensing.

2. What present evolutionary trajectories exist for the channel and bed morphology of Wooler Water.

As a study location example, the Northumbrian river; Wooler Water provides a suitable case for geomorphic change analysis. Recent and historic channel variability at this

location provides basis for prospect of future change which may be studied as part of this project. Furthermore, good quality LiDAR data, detailed historical maps as well as other surveys by various organisations are available for interpretation of past conditions and will aid the project through provision of secondary data. Historical evidence and recent observations have concluded that in the case of Wooler Water, approximately 2km south of the village of Wooler significant channel adjustment has occurred. More recent investigations, such as those carried out following the December floods of 2015, found significant portions of the channel and floodplain were morphologically distinct from previous configurations, whilst longer term records indicate the main active channel have laterally migrated by up to 200m in some places.

For the purpose of prediction of possible fluvial evolution, contextual interpretation of geomorphic alteration is possible from data already available on the study reach. Additionally, options for prediction of possible geomorphic change scenarios exist within modelling applications. Volumetric sediment budget calculations can provide estimations of how a system has and may evolve over time. Using data already available for the study site, a range of possible outcomes will be investigated.

3. How extensively and effectively can UAV photogrammetry be applied for multi-scale (kilometric to centimetric) fluvial surveying?

The relatively low cost and accessibility of UAV based data collection and photogrammetric processing when compared to alternatives such as LiDAR scanning, manifests such methods as a reliable alternative to traditional systems. As has been the case for a multiplicity of past technologies cost reduction has been among the first steps to wider dissemination and proliferation within society. High detail, large scale fluvial surveying is alike in this regard, inaccessible to the majority of organisations and individuals. This may stand to change however. Aerial LiDAR surveying (ALS) has been

the primary means for such surveying, requiring specialist equipment and tools accessible only with generous funding. Aircraft cost and operational fees combined with expensive instrumentation and correspondingly costly maintenance make ALS a tremendously niche operation. In the UK, the data from many such surveys carried out by the Environment Agency is openly available, however in a temporally succinct availability. The need for a rapidly repeatable, low-cost alternative, that does not compromise on data quality thus exists. If found to be successful, the use of UAV imagery for fluvial surveying stands to open a new front for commercial and private applications. Indeed, this has been the case in many other fields and industries, including the geosciences, mining, and construction industries, who seek to keep costs down, whilst obtaining reliable topographical data.

Chapter 4: Field Site & UAV Campaign

4.1. Introduction

This project's three-year field campaign began in July 2016, when the first survey of Wooler Water was carried out. The gap between this and the commencement of the PhD (January 2016) is attributable to the time necessary to source equipment and be trained regarding specific operation. Acquisition of a Phantom 3 Pro UAV system occurred early on, and flight training was carried out. Specific operation in relation to field surveying of the case site took more time however. Training for operations at Wooler Water included a series of test flights near the Peel Park Campus of the University of Salford. During these tests, the basis for a pre-flight planning workflow was developed alongside the relevant field skills required to effectively gather data at the field site in Northumberland. These included the practical skills of manually flying the UAV without GPS assistance if the situation required as well as study of existing aerial photographs (Environment Agency, 2009) in order to scout good locations for GCP placement.

This section of the thesis will recount the details of the necessary pre-flight workflow as well as how it was specifically developed for use with fluvial settings. This workflow was utilised in the course of each river survey to preserve data continuity and integrity. In practice, conditions at the case study site will of course vary, and the survey workflow is intended to normalise this to a degree. Similarly, some equipment was updated between surveys. These changes are not deemed to negatively affect the data, since they all constitute upgrades over previous equipment. Finally, user proficiency was certainly increased between surveys, as experience was gained.

4.2. Pre-flight survey planning.

Use of unmanned aerial vehicles (UAV) has enriched surveying in the environmental sciences. Technological advances in onboard GPS technology and ease of data post-processing using photogrammetric software such as Structure from Motion (SfM). In addition, the use of UAV photography to generate 3D elevation models of objects and landscapes at high resolutions has proved an easily accessible alternative to often expensive, cumbersome laser scanning systems (Flener *et al.*, 2013). Survey spatial coverage can be increased simply through an increase in flight altitude, although resolution is sacrificed. Finding a balance between these two factors is key to producing high quality data, quickly, yet to date a protocol for deployment of UAVs to establish optimal spatial coverage, flight height to resolution ratio has not been documented. This section intends to establish a simple, repeatable methodology, based on a standard UAV platform, to provide information to optimize flight plans according to their requirements for resolution and coverage.

Affordability and extensive choice of Unmanned Aerial platforms along with improvements in on-board systems have allowed for a recent exponential growth of their use within academic and industrial use. Results have been applicable to a multiplicity of scientific fields, from volcanic surveys (Nakano *et al.*, 2014) riverine research (Woodget *et al.*, 2016) and studies of vegetation (Mathews and Jensen, 2013). Among the most powerful applications of UAV photography is the ability to rapidly generate digital elevation models and high resolution orthomosaics of large scale subjects (Siebert and Teizer, 2014). This process is however limited by the conventional restraints of coverage and resolution, which are so often present in nearly every form of remote sensing and data collection system. Whilst literature exists regarding the applicability of UAV field

deployment, there is yet to be a study that defines and examines the relationship between spatial coverage and image resolution when surveying in the field. This is often a critical element for researchers or industry to both understand this relationship and ensure the level of detail in the results. In addition, the protocol presented here provides information on how to best plan and manage flights. Fundamentally, this protocol will allow surveyors to work more efficiently and produce quality results within their personal constraints.

4.2.1. Earth Observation Background

As earth observation technologies developed, a means for testing the resolving power and quantifying the spatial resolution of imaging systems was pioneered by the United States Air Force, who established a standardised measure of spatial resolution: ground resolved distance (GRD), referring to the dimensions of the smallest distinguishable objects in the image. The 1951 standard remains in use today and is shown in Figure 4.1. The significant recent use of unmanned aerial platforms within a research capacity has been supplemented by developments in camera sensors and mounting systems, as well as computing and post-processing power (Turner *et al.*, 2012). According to UAV Global's

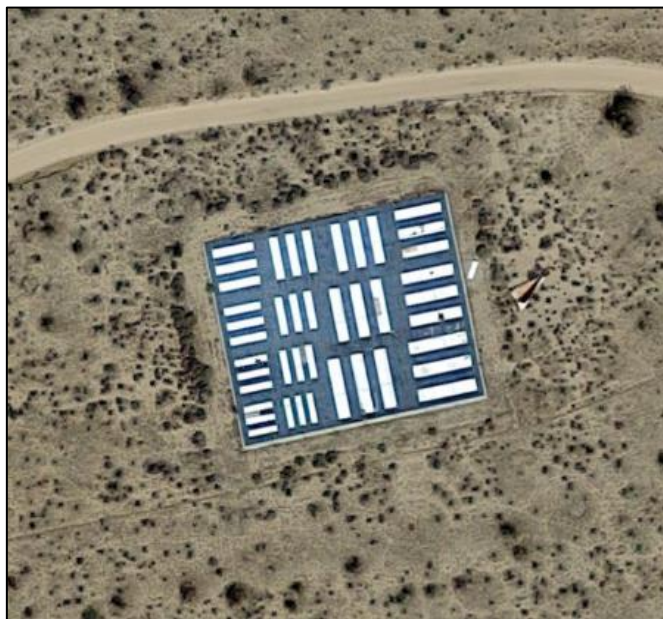


Figure 4.1 – Ground resolution target.

listings, there are 241 standalone commercial UAV manufacturers, as of May 2016 (UAVGLOBAL, 2016), with an estimated worth of \$10 billion and a projected 20% growth in the civilian sector by 2024. The use of UAVs as a field of remote sensing and environmental science has found them to outperform platforms such as LiDAR, especially in terms of cost and ease of deployment (Hodgson, 2013). This section will inform practitioners seeking to optimise the data collection process for UAV derived 3D DEM generation, allowing for the acquisition of highest quality imagery in the most efficient time period.

4.2.2. Methodology Construction

4.2.2.1. Field of View and Ground Sampling Distance.

Image resolution is the most important factor when it comes to overall quality of the texture of generated DEMs and level of detail in orthophotos (Nex and Remondino, 2014). Ground details are often more easily resolved at higher resolutions, by imaging at lower altitudes. Doing so however limits the field of view (FOV) for each image and as such, requires more individual images to be captured during the survey, necessitating increased flight times, battery usage, data storage and processing time. Whilst higher resolutions are more desirable if small landscape details are of interest, they are not always feasible for surveys of large extent (where coverage is the more favoured factor). In this study, survey resolution will be referred to as ground sample distance (GSD). This parameter represents the real-world scale of one pixel or the distance between the centres of two pixels i.e. the size of the smallest feature that the user wishes to detect in their survey. For example, for an image with a GSD of 5cm, one pixel would represent 5cm on the ground. Simply flying for the highest possible resolution, (smallest possible GSD) is not always feasible, even if users are not limited by processing time constraints or computing processing power. For generation of the highest quality, blur free

orthophotos, image calibration and alignment error must be reduced through employment of ground control points (GCPs). To utilize GCPs effectively however, they must be present in numerous overlapping images. Placing and recording the position of GCPs using high accuracy GPS can be the most laborious part of executing a UAV survey, particularly in the field of environmental science where difficult conditions may compromise workers' ability to access ideal GCP placement or compromise the durability/survivability of the UAV. By flying with absolute favour for resolution, resulting image FOV can be so narrow that the number of GCPs that would need to be placed, recorded and during the course of the survey would be much higher. Image overlap is also particularly important when generating DEMs using SfM processing methods, specifically when generating 3D point clouds (Neitzel and Klonowski, 2011). SfM software commonly identifies three-dimensional structures by recognising common points in multiple images. The more images in which a specific point in the surveyed environment is documented, the more accurate the resulting point clouds and DEMs will be (Fonstad *et al.*, 2013).

The role of data quantity management and storage capacity also become apparent in such situations. For subjects of particularly wide extent, thousands of images may be captured per flight. This has implications for surveyors using SfM tools to generate DEMs as well as those using only orthophotos. Whilst modern data storage is relatively inexpensive and accessible for those working in developed areas, workers who might be operating in remote field conditions with limited resources for prolonged periods should carefully consider their data capacity and processing capabilities. Users must consider limiting their survey resolution in such situations in order to increase coverage and reduce processing times. Equations that allow users to calculate an optimal surveying altitude

for a GSD or FOV of their choice are given by (Hernandez-Lopez *et al.*, 2013). Using simple camera parameters, the methodology is universally applicable to nearly any imaging platform:

Equation 4.1

$$H = (Fl \times FOV)/Sw$$

Equation 4.2

$$H = (Fl \times GSD \times Iw)/Sw$$

Where: H is distance to subject (altitude) in meters, Fl is camera focal length in millimetres, Sw is camera sensor width in millimetres, FOV is image field of view (width) in meters, GSD is image ground sampling distance in meters and Iw is Image width in pixels

4.2.2.2. Equation Operation

Equation 4.1 and Equation 4.2 operate on the proportional nature of angular and distant parameters inside the camera and in the imaged environment. This allows for trigonometrical calculation of an unknown parameter when others are known. Figure 4.2 illustrates the identifiable angles and distances, which are used to calculate appropriate flying height and image field of view. The upper portion of the diagram shows a highly simplified camera (existing as only a lens and sensor), whilst the lower part illustrates the field of view for the camera. Values for sensor width (S_w) and focal length (F_l) are usually available within manual documentation or image metadata. It should be noted that Equations 4.1 and 4.2 use data for width of FOV and camera sensor (in the X-axis), and operate in one dimension, thus width can be substituted for height of FOV and sensor (in the Y-axis).

Ultimately, FOV and GSD dictate the overall quality of resultant outputs and processing time required to obtain them. Rearranging Equations 4.1 and 4.2 can be particularly helpful for users whose survey altitudes are restricted but wish to calculate FOV or GSD in order to identify whether their survey is feasible or not. GSD or FOV can also be calculated as a product of one or the other through use of the width or height of the image in pixels, depending on which dimension (X or Y) was initially selected, as shown in Equations 4.3 and 4.4:

Equation 4.3

$$GSD = \frac{FOV}{I_w}$$

Equation 4.4

$$FOV = GSD \times I_w$$

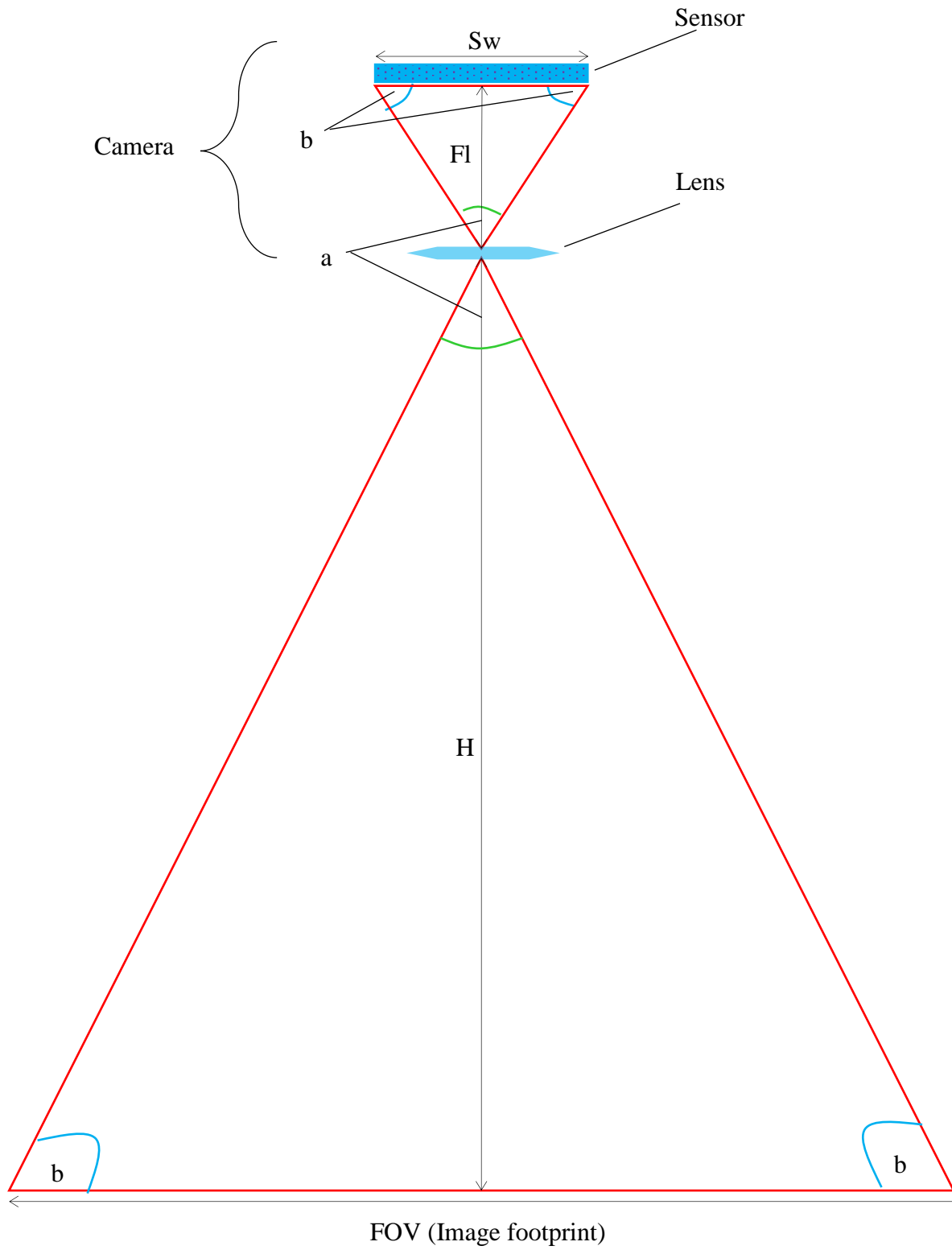


Figure 4.2 – Diagram to illustrate proportionality of angular and distant parameters within a camera and subject environment.

4.2.3. Validation

Workflow development and error estimation is possible by working in reverse with Equation 4.1 or 4.2 to calculate known, fixed parameters such as focal length, sensor width or image width, whose values can be found from manual documentation and image metadata. Equations 4.1 and 4.2 were tested via reverse calculation using data collected during experiment flight with a DJI Phantom 3 Professional UAV. The drone was ascended to a height of 120m over a fixed point, capturing nadir images at intervals of 5m. A tape measure laid to a length of 20m positioned directly below the UAV allowed for gauging of scale and thus calculation of FOV width for 18 images. Use of Equation 4.2 then permitted calculation of GSD for each image using the image width in pixels (4000). The inferred measurements of FOV in all captured images are shown plotted against their respective capture altitude in Figure 4.3. Calculated values for GSD are also plotted on the secondary

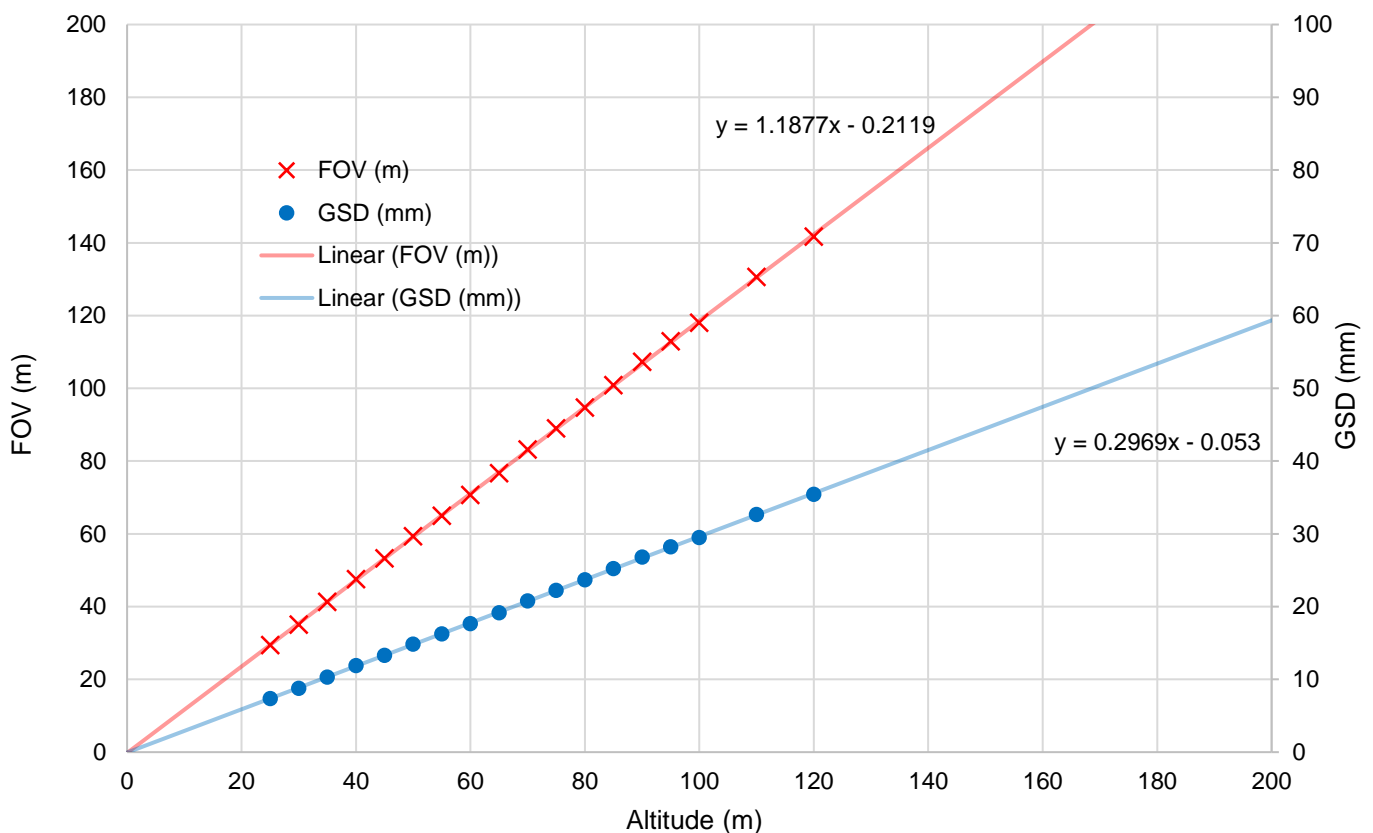


Figure 4.3 – Linear relationship between survey altitude, resolution (GSD) and Coverage (FOV)

axis of Figure 4.3. Focal length and image width (4mm and 4000 pixels respectively for Phantom 3) were reverse calculated using Equations 4.1 and 4.2, returning values with $\pm 0.3\%$ deviation. This error may be attributed to the $\pm 0.1\text{m}$ accuracy in the UAV's altimeter and marginal error when measuring image FOV.

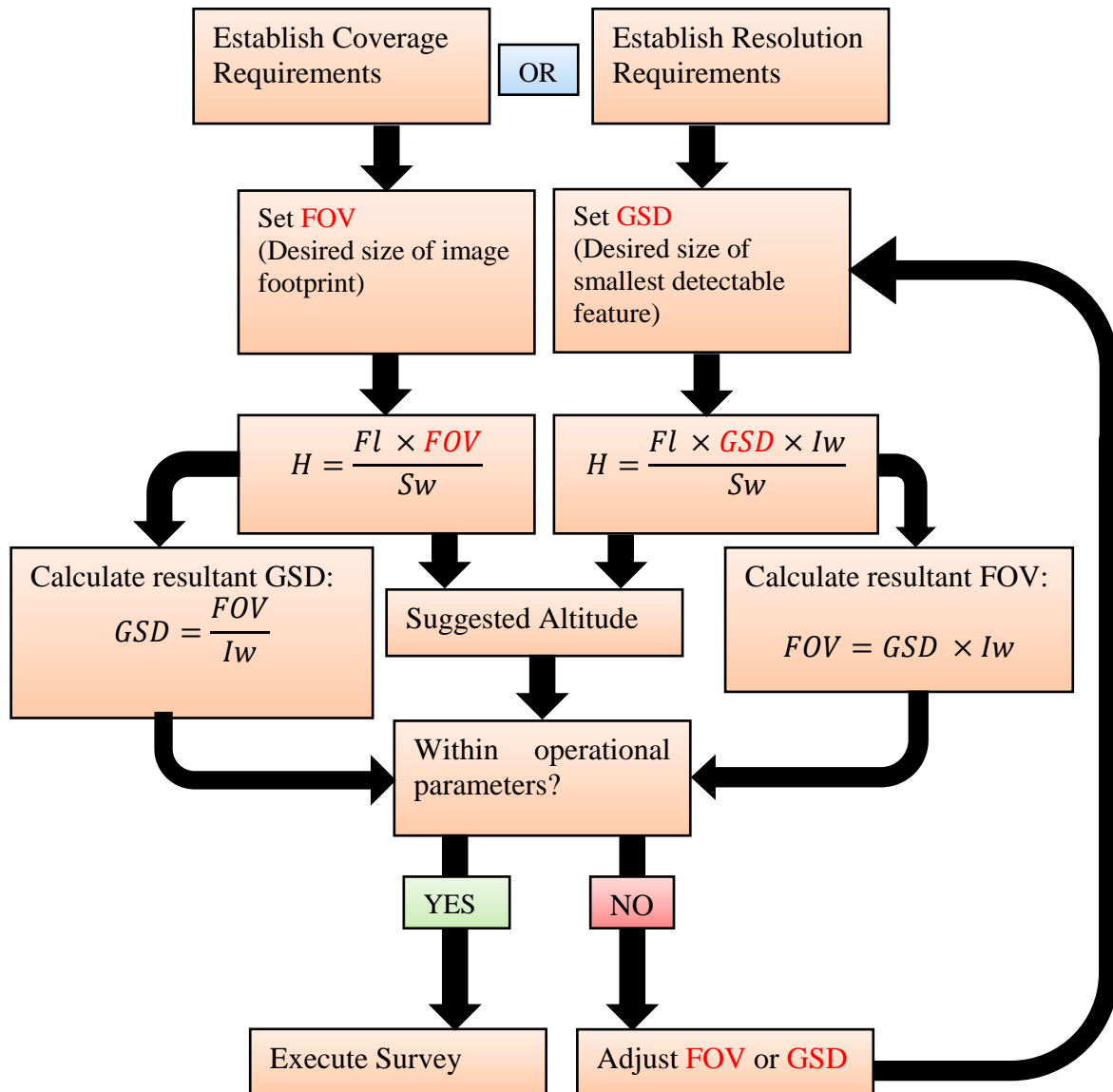


Figure 4.4 – An example workflow to allow users to calculate optimal survey flight parameters according to coverage and resolution requirements

4.2.4. Workflow

4.2.4.1. Flight Planning

Whilst no methodology is universally applicable to all UAV surveys due to the differing natures of and problems presented by environments of interest and imaging subjects, the

equations outlined above can however offer a degree of transferability with regard to planning for possible survey altitudes. As the primary control upon the variables of image FOV and GSD, survey altitude may be considered the most immediately favourable factor to be known when flight planning. It may however be favourable to calculate FOV, GSD or even focal length as the primary control for a survey, especially in situations where one or more parameters may be constrained (altitude being the most common). In such circumstances, the above equations remain capable of providing valuable information. If altitude is restricted, tuning of FOV and GSD is still possible through adjustment camera focal length, calculable via rearrangement of Equations 4.1 and 4.2. Similarly, if users wish to restrict survey GSD in order to save data capacity and improve image overlap, or constrain FOV in order to maximise orthophoto and DEM detail, suitable employment of the above equations can facilitate bespoke flight planning and information feedback.

Figure 4.4 shows a suggested workflow for flight planning with regard to controls for FOV and GSD using Equations 4.1 through 4.4. The initial step is to establish the operational requirements for coverage or resolution for the survey. Coverage requirements should be favoured if users are particularly constrained in terms of their data storage or processing power. Contrastingly, identification of resolution requirements should be of more concern to workers who wish to set specific limits for the scales of detectable features in their surveys. Once the user has established the required resolution and extent of their survey, they may choose a primary control variable (GSD or FOV) from which to begin the necessary calculations to find a suitable flying height. Desired values for image FOV or GSD are utilised in Equation 4.1 or 4.2 in order to calculate a suggested survey altitude. Users may also calculate the resultant counter-variable of their chosen control through employment of Equation 4.3 or 4.4. Once values for H, FOV and GSD have all been named or calculated, they must be checked to ensure they are within the

operational capacity of the UAV platform, camera system, as well as the user's own abilities. For altitude, users must be responsible for not exceeding regulatory limits (Watts *et al.*, 2012). If calculated H, FOV or GSD are not within desirable limits, the surveyor may wish to adjust their quoted values for step 2 in order to improve coverage or resolution of their investigation. Once the user is satisfied that all parameters are within operational limits, the survey may be executed at the calculated altitude.

4.2.4.2. *Limitations*

The equations and protocols presented here, whilst easily applicable to a wide range of UAV imaging systems, cannot circumvent constraints of hardware limitations or altitude restrictions, however they are capable of aiding users in making the most of their available resources. Whilst FOV and GSD may be calculated as absolute values, the amount of error between the desired and actual values observed in survey outputs is dependent upon the accuracy of the UAV platform's altimeter or vertical autopilot (or the pilot's ability, if flying manually). Furthermore, GSD may not necessarily reflect the exact scale of distinguishable objects and is not a perfect proxy for resolution due to the effects of contrast and other variables. If users are concerned that landscape details or morphology of interest may not be detected in their survey because of this, slightly decreasing GSD beyond their desired value as a buffer may be advisable.

4.2.4.3. *Conclusions*

The ability for workers to identify the ideal survey altitude for their projects should not be understated, as it is the defining factor for the level of detail and volume of data captured during the survey. The use of UAVs for environmental surveying allows users to overcome the various difficulties and limitations of systems such as LiDAR or satellite-based sensing. Moreover, with adequate planning and implementation of the methods discussed in this section, users are offered a good deal of flexibility (within their

operational limits) to find an ideal compromise between survey resolution and data volume. Although designed for speed and simplicity of operation, UAV surveying can often involve complex techniques and processing methods. The diverse range of environments and conditions in which surveyors and researchers may find themselves operating leads to great variability in the challenges faced and requirements for gathering high quality data. As the field of environmental UAV surveying develops, it is likely that different environments and survey subjects will develop specific methodologies suited to their particular traits and characteristics. The workflow described is intended to act as a strong foundation on which for researchers and surveyors to base their own methodologies, tailored to circumvent challenges posed by their particular environment of interest. By understanding the relationship between, altitude, coverage and resolution, the most important controls on the quality of survey output data, users are able to better plan around other factors such as the required battery and data storage capacities. Planning carried out well in advance of field operations will similarly allow workers to select (and if necessary, purchase) the most suitable hardware for their survey such as UAV platforms, cameras, or simply lenses. Overall, the protocols and workflows described in this paper are not a “one-size-fits-all” solution, however they can provide a substantial base from which users can individually plan methodologies for the particular conditions of their project.

4.3. UAV Flight Operations

4.3.1. Field Methodology Overview

As a utility for rapid and high-resolution recording of surface features, UAV technology offers a unique standpoint in terms of equipment accessibility and operation. The abilities of consumer grade platforms to deliver data of academic quality makes UAV surveying an attractive option for those without access to laser-based surface scanning equipment due to prohibitive costs, especially in the case of aerial LiDAR scanning (ALS). UAV based photogrammetric surveying and structure from motion (SfM) processing enables collection and handling of data more quickly and cheaply than LiDAR based methods. This may be attributed to the ease of UAV deployment with reliable operation and faults requiring less technical expertise to repair. Data quality and density is also not subject to compromise, as survey resolution is entirely controllable by the operator and only limited by available processing power. Generation of high-resolution digital elevation models (DEMs) and orthomosaic photos enable precise and repeatable tracking of landscape variability at a variety of scales.

To collect data, the UAV is flown across the survey reach, either manually or by autopilot along a plotted course, saving usually vertical nadir images with a large degree of overlap between each frame. For standard flight operation, the UAV is fitted with inertial and GPS based guidance systems, the data for which is additionally utilized during SfM processing. Extraction of approximate surface geometry is possible through use of image georeferencing (provided by UAV GPS), enabling SfM processing software to detect the locations of each imaging point, thus permitting reconstruction of a three-dimensional point cloud. The cloud is generated via computer vision algorithm, detecting points common to multiple images and giving them a specific 3D position extracted from the

geo-referenced data in the images themselves. Further processing enables production of a polygonal mesh and ultimately an entire 3D model of the landscape, complete with orthomosaic texture. One drawback of image-based surface surveying over systems like LiDAR is the inability to provide data beyond occluding structures, such as leaves. Whereas data concerning the number of beam returns permits filtering of such obstructions for LiDAR methods, the process is more problematic for photogrammetry, leading to lack of data for particularly occluded areas. Fortunately, this can be mitigated to a degree through extra processing of the point cloud, by selective use of detected points when generating the DEM mesh.

The method of inferring surface geometry via the geo-referencing method described above, whilst extremely easy and fast to carry out and process, cannot produce DEMs with sufficient 3D accuracy, as the consumer grade GPS unit in the UAV used for point cloud is rarely accurate to within <50cm. This can result in significant spatial inaccuracies in DEMs and mismatched image stitching in orthophotos generated using this method alone. Other artefacts may also be present in output products, such as a doming or a rippling effect towards the edge of DEMs. Reduction of this error is central to the accurate detection of geomorphic change as part of this project, thus the methodology will employ the use of ground control point (GCP) referenced DEMs and orthophotos. The use of GCPs referenced with highly accurate differential GPS (dGPS) enables more precise point cloud generation and reduction of error in resultant DEMs. In practice, the area to be surveyed is first populated with physical ground markings, detectable within UAV imagery. A3 size white cards or spray paint is often sufficient to show up in images, however lighting and ground colour conditions should be considered for optimal, ground/marker contrast. The exact coordinates of these markers are then recorded using dGPS in the field and utilized during SfM processing create DEMs with spatial errors of <5cm. This error may be

reduced through further optimisation of GCP placement and equipment accuracy. For the purposes of this project, a DEM error of <10cm would be acceptable as geomorphic change below this scale is too continuous and universal to reliably predict and map.

Four surveys of the Wooler Water have been carried out. The first on the 28th of July 2016 (Survey 1), the second on the 27th of November 2016 (Survey 2), the third on the 7th of September 2017 (Survey 3), and most recently on the 29th of April 2018 (Survey 4). The four surveys have been conditionally distinct from each other, in terms of ground and vegetation conditions and weather, requiring variable approaches for surveying. All surveys were executed with the intended resolution of at least 5cm. Depending on the platform being used for that survey this dictated the chosen flight survey altitude between 50m and 60m according to the pre-flight planning workflow. All four surveys took approximately half a day to complete, including placement, recording, and recovery of all ground control points (GCPs). The survey area, extending approximately 2km, was imaged on all occasions with GCPs spread on either side of the channel.

The survey is initiated with placement and reference of all GCPs with high accuracy dGPS. Initially, large white padded envelopes staked into the ground were used for Survey 1, however this required them to be recovered at the end of the survey. As such, Surveys 2, 3 and 4 instead used white marking spray paint, which had been tested as a suitable alternative to the preceding method, enabling more rapid placement, and eradicating the need for recovery. Once all GCPs had been placed in suitable locations and their coordinates recorded flight operations could commence. Current FAA regulations advise that consumer UAV's be operated in the presence of two people. One, the pilot, ready to assume control of the aircraft if any hazards or loss of autonomy arise. The other on hand to observe the surrounding conditions, acting as a lookout for potential hazards such as flocks of birds or errant branches extending above canopies. Some possible threats within

the survey area were identified, including a large power pylon and associated cables spanning the northern section of the reach. Following this, the pilot and observer then proceed to survey the reach, maintaining visual contact with the UAV at all times. The scale of the study site necessitates multiple battery changes as depending on wind conditions the consumer grade platforms can sustain 10-20 minutes' worth of flight time. Approximately 3 batteries were used on each occasion. The UAV proceeds to capture images in rapid succession, criss-crossing the channel from top to bottom.

4.3.1.1. Platform Parameters

Given that different sensors were utilised between Surveys 1 and 2 and Survey 3 and 4, survey altitude was altered slightly in order to maintain data consistency. The first two surveys used a DJI Phantom 3 Professional model, however the third and fourth made use of the updated Phantom 4 Pro. The latter platform included a higher resolution sensor, but slightly reduced field of view (FOV). Despite this the Phantom 4 was still able to capture images from a higher altitude, thus larger FOV, without sacrificing resolution. This enabled reduced raw data quantities but increased data density and an overall decrease in survey time and battery use. The effective employment of different UAV models between the earlier and later surveys was possible due to a robust pre-flight planning workflow, which informed the selection of the most optimal surveying altitude for each respective UAV survey flight. Using the specific internal parameters of the camera; focal length, image width and sensor width, the maximum altitude for sub 5 cm survey resolution was calculated for each survey.

4.4. Wooler Water Study Location



Figure 4.5 – Study location map, (A) The town of Wooler, Northumberland and (B) An overview of the study reach, including Wooler Water, which is fed by Colgate Water and other upland streams.

The study area of interest is an approximately two-kilometre-long stretch of the Wooler Water which is fed by watersheds within the Cheviot Hills to the west. Wooler Water is a tributary of the River Till, which itself feeds into the Tweed. The drainage area within the Cheviot Hills is approximately 18km² and is primarily composed of managed moorland and grassland, with sparse low vegetation and trees beside drainage channels and valley floors. Some artificial plantations (coniferous) are present within the wider catchment and border the channel in some places along Wooler Water. Two road fords are present within the study reach, one at Colgate Cottage and another at Haugh Head. These two roads have seen significant lateral migration of the point where they are crossed by the river over the past 150 years. The Wooler Water, flowing north, proceeds through the village of Wooler itself before joining the Till, its floodplain traversing multiple land uses including high and low value residential (cottages and a large caravan park), industrial and recreational. The river channel is crossed by three bridges within the built-up area and is also traversed by major powerlines, a pylon for which lies within the meander belt, just south of the village (Figure 4.6).

The channel of the River is flanked by steep banks on its left side, increasingly so on approach to the village of Wooler. The right of the channel is more low-lying and is almost exclusively pastoral use, with the exception of some coniferous plantations and a house, near Haugh Head ford. Aerial images depict paleo-channel marks (Figure 4.6), which are most visible within the grass of the pastoral fields and appear to cover much of the valley floor. These markings are evidence of significant historic channel migration, suggesting the river's wetted channel has migrated by as much as 400m in places. The timescale over which such adjustment may have occurred is more uncertain however. Historical maps accurately show the previous course of the channel, even depicting the presence of in-channel islands and bars. In order to gauge the rate at which the river channel may have

migrated the distance suggested by paleo-channel markings, tracing of the wetted channel is possible for maps available from as far back as circa. 1860. Polygon tracing was carried out in ArcGIS for four historical maps (1860 – 1970) and an aerial photograph from 2009. The overlaid river courses are visible in Figure 4.8.



Figure 4.6 – Powerline pylon, south of the town of Wooler. Paleo-channel marks. (Image dated July 2006)

Historic records from before 1945 detail flood damages by Wooler Water. The bridge in the settlement being swept away on at least two occasions and flood embankments being washed away north of the town during a flood in 1839. One record from October 1949

describes a “trebling” of channel width and creation of a new channel south of Wooler (Sear and Archer, 1998). Further erosion and channel avulsion is described in 1981 and 1984, resulting in weirs becoming circumvented by auxiliary channels which then laterally erode the structures (Wilson, 2010) Such actions are manifestations of Wooler Water’s naturally active regime, as a transport dominated system, facilitated by the great availability of sediment from the river’s catchment in the Cheviot Hills.

4.4.1. Existing Structures and Features of Interest

The 2km long stretch of Wooler Water which will be the subject of this study has numerous features of interest which make it particularly suited as a candidate for the project. A highly dynamic system with a history of artificial modification, Wooler Water shares many similarities with other rivers in the UK, the majority of which are designated as being artificially modified in some way. The presence of a set of 10 iron and concrete weirs within sections B and C in the Upper Reach are manifest to the local history of man's



Figure 4.7 Weir remnants (top) and Haugh Head Ford respectively (bottom), within Section C of the Study Site.

involvement. The channel in Section C is also forded by a small road at Haugh Head (Haugh Head Ford). The weirs installed during channel straightening works sometime after 1920 are now considerably degraded and buried, increasingly so in an upstream direction.

4.4.2. Historic Change Analysis

The variation in position of the wetted channel seen in Figure 4.8 appears to suggest some sections of the study reach are more laterally mobile than others. Whilst some short stretches appear to have moved by nearly 100m, others have not strayed for nearly 150 years. The scale and rate at which channel course change occurs also appears to be inconsistent, with certain sections remaining stable for up to a century, then abruptly straying from the established path. Historical maps from circa 1920 show the river channel encroaching closer to a railway embankment, a potential hazard which must have been recognised at the time. We know this as the next available historical maps (circa. 1970) show the section of channel has been dramatically adjusted to a much straighter path, far from the railway embankment, and contains 10 weirs, presumably as a means for maintenance of the new, almost completely straight channel. The course realignment is in fact rather extreme, appearing to cut through ground which is marked as a steep embankment on previous maps. Such a course adjustment may have been warranted by protection of the railway, but also in the interest of local gravel mining operations which are discussed as part of this project.

Whilst interpretation of lateral migration of the channel is made relatively easy through use of historical maps, inference of vertical variability within the system is less accomplishable with such resources. Fortunately some past studies, specific to Wooler Water, provide data concerning bed elevations; Klingeman (1998) and Sear & Archer

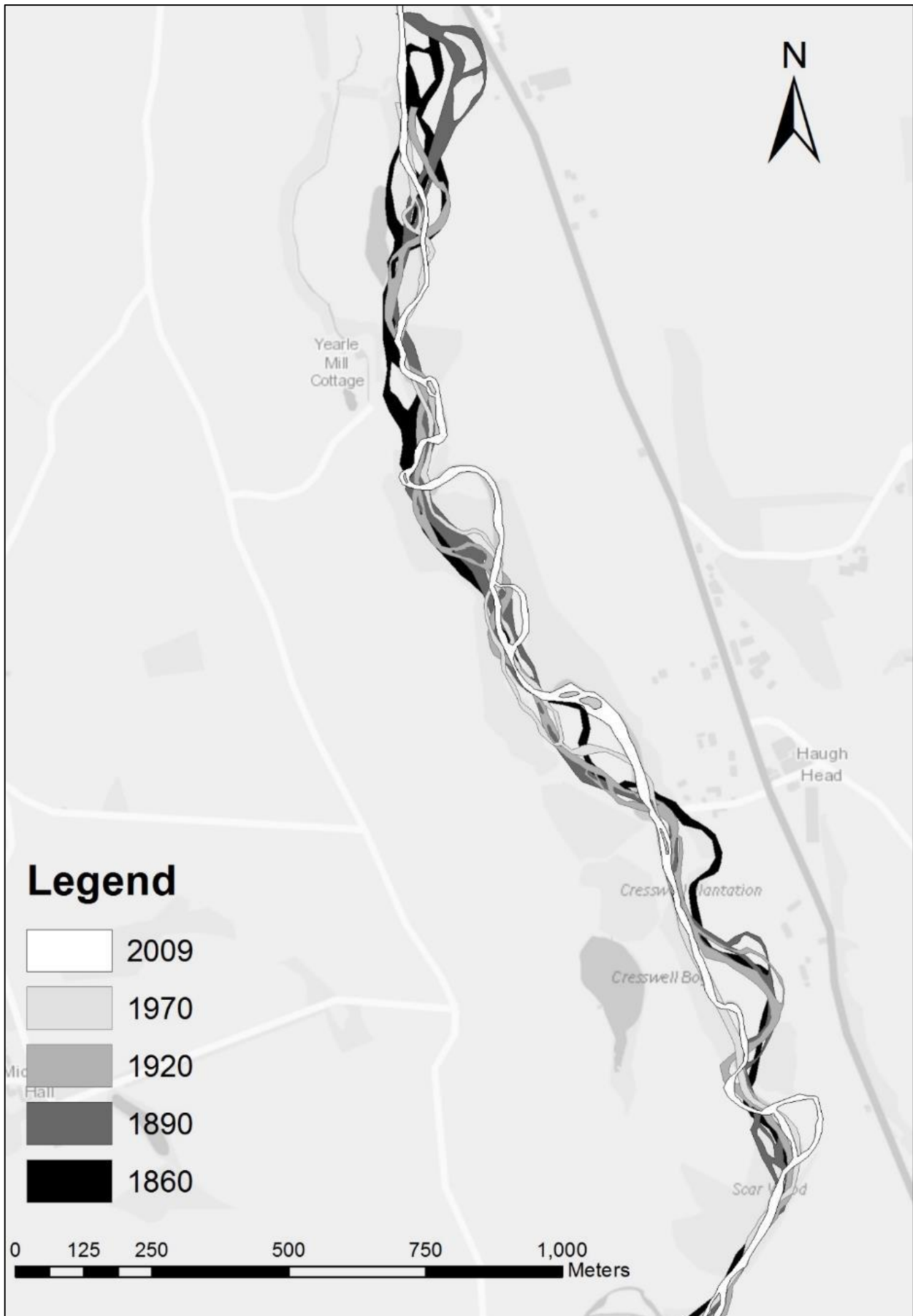


Figure 4.8 - The previous courses of Wooler Water, as traced from historical maps.

(1998). The former provides details regarding the locations of gravel extraction, identifying one site near the Haugh Head ford, further suggesting that lateral platform changes were more prevalent during the river's pre-mined phase and triggered by larger, low-frequency flood events. Whilst gravel mining operations were found to cause significant channel scour, the effect upon lateral stability was variable depending on net sediment budget. In any case, gravel extraction has not occurred at the Haugh Head site for a number of decades and as such, any lateral stability induced as a result of down-cutting can be expected to be annulled as the river's naturally high sediment throughput is restored.

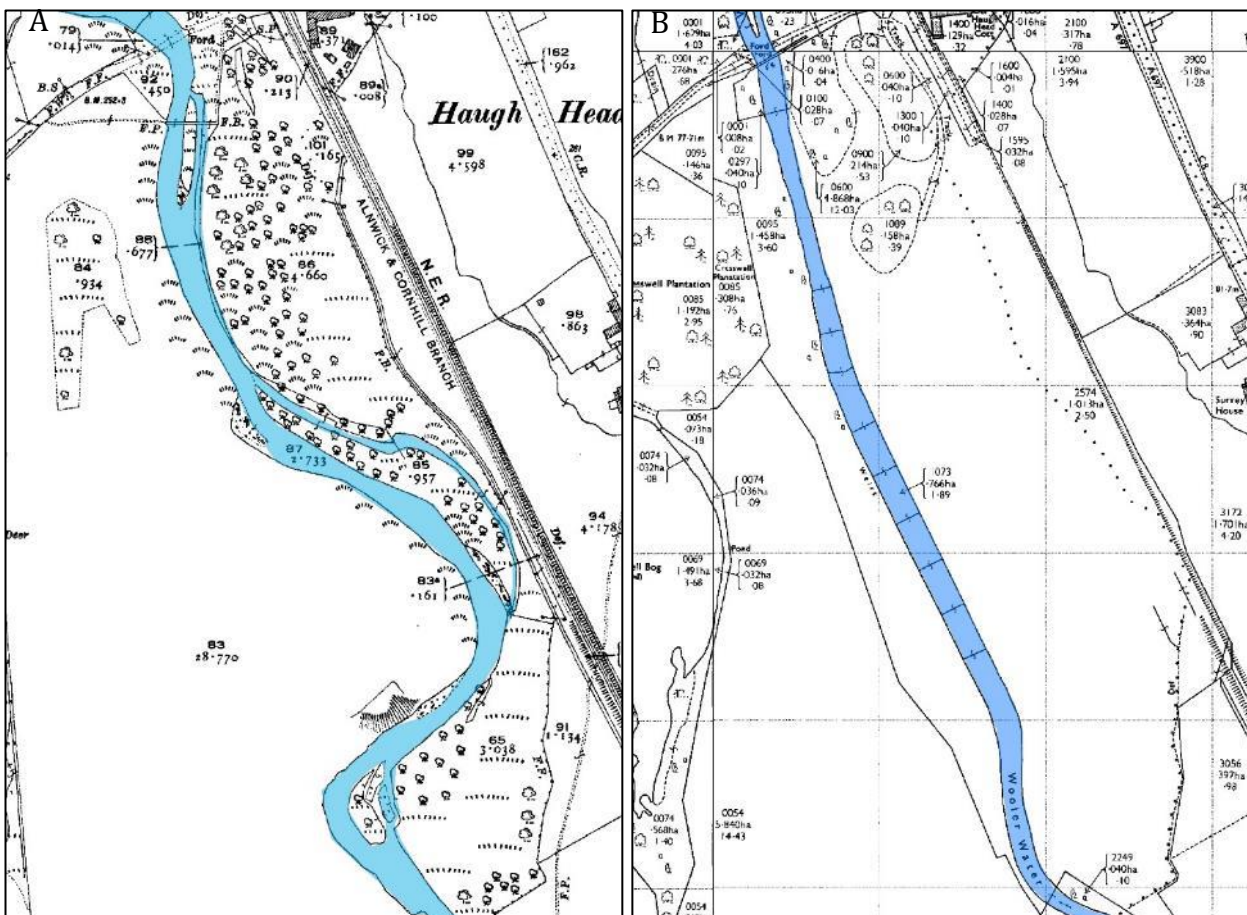


Figure 4.9 - (A) River course in circa. 1920, encroaching railway embankment and (B) newly adjusted river course in circa. 1970.

4.4.3. Recent Change Analysis

Analysis of how Wooler Water has evolved in the long term is valuable to development of a wider understanding of the chosen field site, however detecting and mapping geomorphic change within the river system at much smaller timescales is the primary premise of this project. The context and information provided by historical map analysis and review of past studies specific to this site permit for more focused data collection for sections which might be subject to particularly dramatic change, such as the section of weirs, just upstream of Haugh Head ford. This area is of particular interest as the river appears to be re-adjusting into its old course, away from the artificial channel layout adopted following 1920. It is expected that the river will attempt to increase sinuosity in response to an increase in local gradient caused by the shortening of the channel length by straightening (Schumm, 1993). It is not known how the weirs in place throughout the channelized section will affect the restoration of natural course, thus the section is of particular attention. What is more, the history of gravel extraction in this reach and its subsequent cessation, may lead to further channel variability as the system's sediment budget is replenished (Sear and Archer, 1998).

Sear and Archer, (1998) estimates the sediment yield of per year of Wooler Water to be 145 m³/year. During the gravel extraction phase an estimated 32,000 m²/year was extracted, a yield/extraction ratio of over 200. Similar gravel extraction works on Northumbrian rivers are far more conservative, the rivers Wear, Tyne and Coquet having yield/extraction ratios of 64, 14, and 54 respectively. The effect upon Wooler Water was the introduction of major vertical instability leading to incision and the undermining of the ford and footbridge pier at Haugh Head (Figure 4.10)

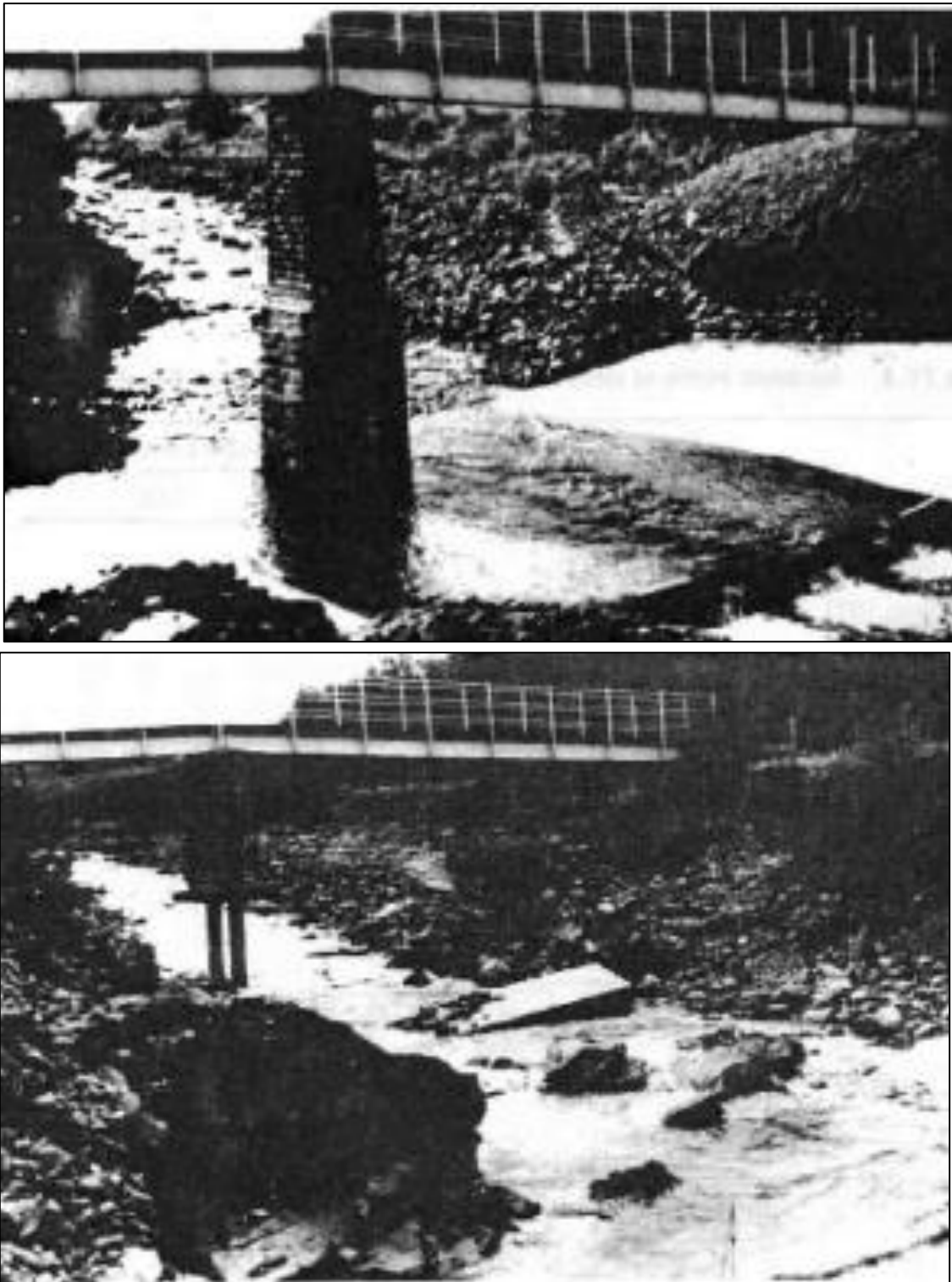


Figure 4.10 – from Sear and Archer (1998), looking upstream at Haugh Head following a flood resultant incision in 1971. The concrete ford is destroyed, and footbridge piers exposed.

1 4.5. Survey Details

2 Table 4.1 gives a description of the various parameters and conditions of each of the four field surveys. Also presented in this section is a
3 description of on-site activity, followed by the specific processing steps that were taken for each respective survey.

4 *Table 4.1 – Breakdown of various parameters, conditions, and results from all surveys*

	Date of Survey	Platform	GSD (cm)	RSME (cm)	Max Error (cm)	Images Captured	GCPs Used	Number of points generated	Weather and lighting conditions
Survey 1	July 28th 2016	Phantom 3 Pro	1.75	4.65	9.78	1513	24	45 Million	Light cloud and breeze. No shadows, good light.
Survey 2	November 27 th 2016	Phantom 3 Pro	2.17	2.02	4.04	929	26	69 Million	Light cloud, strong breeze. No shadows, fading light.
Survey 3	September 7 th 2017	Phantom 4 Pro	1.50	2.55	5.92	553	30	82 Million	Clear sky, direct sun. Calm. Shadows present in places.
Survey 4	April 29th 2018	Phantom 4 Pro	1.31	3.54	7.84	815	80	116 Million	Light cloud, light wind. Good light, minimal shadows.

4.5.1. July 2016 (Survey 1)

This study's first survey of Wooler Water was undertaken in July 2016. Being in summer, vegetation at the field site was in full leaf. Accurate reconstruction of topography by SfM is subject to consistent ground visibility in multiple images, where occlusion is as low as possible. The presence of large shrubs and vegetated bars within the river channel thus leads to some gaps appearing in the data, where inference of ground level is either too unreliable to be considered or impossible due to complete occlusion. A degree of vegetation filtering is possible through implementation of a moving-window point selection process, which effectively "picks" the points with the lowest elevation in a cell, assigning them the designation "ground points". This processing step is discussed in more detail in Section 5.2. Such methods are able to return data of reasonable density and reliability for lightly vegetated zones, however for areas of dense canopy cover, no data can be discerned. The densest vegetation was however limited to beyond the incised channel margin.

This survey made use of large white padded envelopes as GCPs, which had to be placed and affixed to the ground, then collected upon conclusion of the survey. This proved laborious, requiring the entire reach to be walked over, twice. Totalling 4-5 km of walking in waders. The GCPs were however easily identifiable and remained secured for the duration of the survey. Regarding conditions in the field, lighting conditions were very consistent with very few shadows or overly bright areas which might lead to errors during SfM processing. Water conditions were also favourable for SfM processing, being no more than approximately 60cm deep and with little suspended load. The majority of the channel was thus successfully captured by SfM, with few areas of submerged topography being too deep to image. Even so, the banks of the channel were not

submerged due to relatively low flow encountered during the survey. This enabled very good quality data collection of the banks.

Flow conditions on the day were low, with the entire channel margin safely accessible with thigh high waders. Once GCPs had been placed the UAV was prepared for flight. Flight time was approximately 35 minutes, requiring three returns to the home-point for a battery change once the level reached approximately 30%. Being the first survey of the site, a much wider initial coverage was flown for reconnaissance purposes; approximately 150m either side of the main channel as well as an extra kilometre downstream, above a recreational holiday caravan park, for which overflight permission had been pre-approved. This resulted in attaining many more images than would otherwise be used for SfM processing. This would allow return surveys to have better informed access and GCP placement route planning. A total of four out of eight available batteries were employed on this occasion, with the final being only partially used, retaining 75% of its charge upon termination of the survey.

4.5.2. November 2016 (Survey 2)

The second survey, carried out 4 months after Survey 1, almost immediately following Storm Angus (Met Office, 2018), was subject to conditions fairly distinct from that of the first. Most notably the flow within the channel was high and had to be considered when seeking potential crossings to access GCP placement zones. Seasonal vegetation had mostly either died back or was not in leaf. Many of the sparsely vegetated areas were now able to be captured by SfM given the reduced occurrence of occlusion afforded by the leafless conditions. Conversely, the zones more dominated by vegetation remained inaccessible to data collection as the density of branches alone was enough to occlude the ground. The preceding storm had caused significant vegetation stripping, and recent high flow was evident by trash-lines and torrential flattening of more resilient vegetation.

Light conditions were not optimal due to delays in arriving at the field site. Conditions were not too dark however, and image blurring was minimised by manually piloting the UAV, ensuring that horizontal velocity had been wiped before the capture of each image. This technique was more laborious but was highly effective at mitigating the effects of lower than optimal light. This flight pattern was more energy intensive however and resulted in a higher drain and change rate of batteries. A total of 6 out of 8 available batteries were used for this survey. Whilst the platform and sensor utilised were identical to Survey 1, the methodology for GCP placement differed slightly. On this occasion, to circumvent the need to secure and recover the large white envelopes used as GCPs in the preceding survey, semi-permanent white and yellow survey marker spray paint was used instead such as in Figure 4.11. The colour of paint was selected based on the surface colour in order to provide best visibility. This provided more reliability as there was no risk that the GCPs could be moved by the wind, which was relatively high on that day, or other factors during the survey and would be washed away overtime, thus removing the need for recovery at the end of the survey. The painted GCPs were as identifiable as their paper counterparts proving the ideal means for ground control marking.

Given the time of year this survey was executed and time constraints regarding travel and other external factors, the flight itself was executed in the mid-afternoon. As a result, near the end of the survey, fading light lead to a number of the images captured being blurred somewhat. A contingency for such an issue might have been to reduce the exposure time of the sensor (shutter speed), however this instead resulted in images being under-exposed, with features too dim to be discerned within SfM processing. Fortunately, by ensuring the aircraft was stable and not moving at the time of image capture when using



Figure 4.11 - Painted GCP marker within river channel

a longer exposure time this problem could be circumvented. In the cases where images were significantly blurred, they were excluded from the SfM processing, justifiable by the desire for data reliability over sheer density. This accounts for the lower number of images and overall data density in Survey 2 when compared to Survey 1.

4.5.3. September 2017 (Survey 3)

Survey 3 made use of the updated Phantom 4 platform, with an improved sensor over the Phantom 3, permitting an increase in survey altitude and wider field of view. This in turn enabled a reduction in the number of images for the whole survey, without reducing resolution. The Phantom 4 also includes a suite of infrared and ultrasonic proximity sensors which prevent collision with environmental obstacles, which would certainly permit safer operation at extremely low altitudes or amongst vegetation. Conditions at Wooler Water do not require such operation, but it is plausible that the methodology could be transferred to a situation which does. Lighting conditions were less favourable upon the outset of the survey, where a cloudless sky lead to some shadows falling from larger rocks and boulders within the channel. Consequently, lighting conditions are

somewhat inconsistent. Some images captured at the beginning, of the survey, when the sun was strongest have a high level of contrast. Winds on the day were particularly calm. Flow conditions were typical of summertime low-flow as minimal precipitation had occurred in the preceding days. Observations at the site did not suggest much in the way of significant bank collapse or channel avulsion, however an increased amount of large woody debris (LWD) was present, which had caused some flow redirection and scour through gravel bars constructed during Storm Angus.

The painted GCPs were again used, as they had significantly expedited Survey 2. In this case however the GCPs were placed on notable landscape features such as gravel bars or near fence posts in positions where the overly bright conditions risked over-exposing the camera sensor resulting in the markers being “washed out” and indiscernible from the surrounding ground. Furthermore, the direct sunlight introduced many shadows on protruding features. Intense light and shadow is known to induce noise within SfM (Thomas and Oliensis, 1999) and should be limited where possible. A degree of image post-processing can mitigate this, however any contingency which can be implemented at the data collection stage will cut down on later processing workload. To do this, the UAV flight was extended to capture two auxiliary sets of very slightly oblique images (approx. 5-10 degrees off-nadir), opposite to the bearing of the sun. This minimises the appearance of shadows within images to a degree and ensures more consistent lighting, at the expense of a longer survey duration, larger data quantity and processing time. The slightly extended survey used five out of eight available batteries despite the calm flying weather.

4.5.4. April 2018 (Survey 4)

The most recent survey in April of 2018 also utilised the Phantom 4 platform and the “sprayed” GCPs. Lighting conditions were more optimal than the preceding survey, where

direct and bright sunlight led to exceedance of the camera's dynamic range resulting in areas of over-bright and over-dark pixels which risks data loss without post-processing. In this scenario, light cloud cover provided more diffuse lighting, thus a lower overall range of brightness within the environment. This reduced the need for any post-processing once data collection had been completed. Ground control was intended to be more exhaustive. A total of 80 GCPs were sprayed and an additional 78 GPS points taken within the river bed, atop large boulders or significant in-channel features as an extra independent validation dataset. The position of 158 GPS points was recorded throughout the survey. For a sub 2cm GSD a maximum survey ceiling of 55m was calculated using the pre-flight planning workflow according to the internal camera parameters of the Phantom 4 platform.

Flow conditions were more medial on this occasion. Recent springtime rainfall events had induced some high flow events in the preceding week. The trailing end of the flood event was still present at the time of the survey. This level of flow was not deemed to affect access requirements or GCP placements during the survey. "Sprayed" GCPs were georeferenced alongside the independent checkpoints. GPS points were also taken at the base of some low in-channel vegetation, mainly gorse. This was done as a means to later validate the accuracy of post-processing vegetation filtering in the SfM workflow. The vegetation and ground point filtering details are discussed further in Section 5.2. GPS sample points were assigned either GCP (ground control point), HB (hard bed), VEG (vegetation base), WR (weir) or BR (bridge deck) coding for ease of differentiation in post-processing. Multiple cross-sectional profiles of the wetted channel were also recorded by GPS for later validation purposes. As to fit with the research project's timeline, this survey marked the conclusion of field operations at the case study site, Wooler Water

Chapter 5: Methodology and Data Processing Approaches

5.1. Introduction

The data processing path from plain RGB images to a full scale, high resolution digital elevation model (DEM) and orthomosaic image involves intensive application of computer vision algorithms. Users have a wide choice of software packages suited to this type of data processing. This section of the research will discuss how these processing tools were applied throughout the project and how their use might be optimised when used for wider study of fluvial geomorphology. For SfM processing this study made use of Agisoft Photoscan Professional 1.4.2 (Agisoft), which has some interface improvements over previous versions, but whose SfM processing algorithms have remained consistent and among the best performing in the industry (Agisoft, 2011, 2018). Use of this software package has been widespread in geomorphology (Fonstad *et al.*, 2013; Javernick, Brasington and Caruso, 2014; Westoby *et al.*, 2015; Woodget *et al.*, 2016), however competitive open source alternatives such as Mic Mac (Ouédraogo *et al.*, 2014; Rupnik *et al.*, 2017) exist. Free alternatives provide those without the necessary capital, to still deliver high quality SfM products (Jaud *et al.*, 2016).

Each survey will receive its own processing summary and all software reports generated by Agisoft will be available in Appendix 3. General processing steps will be discussed in following. Developmental processing steps, such as vegetation removal and DEM correction will additionally be discussed in their own respective sections. These steps constitute part of what specialises this project to the field of fluvial-geomorphology, as they are implemented as a means to side-step the niche problems associated with the

conjunction of rivers science and UAV remote sensing. These complications can be summarised thus:

a. The linearity of fluvial features

River systems are unique in their general morphology in-contrast to other natural features. Most notably, their linearity. No other landscape feature retains such a disparate ratio of width to length. This fundamental aspect of rivers presents unique challenges when surveying them at kilometric scales. GCP placement configuration, which is known to critically affect error distributions in SfM DEM products (James *et al.*, 2017) can be complicated if key areas are inaccessible, or are outside the survey bounds. Much of the existing literature which reviews the accuracy of UAV photogrammetry does include variable ground control geometry (Barry and Coakley, 2013; Ruiz *et al.*, 2013; Tahar, 2013; Leitao *et al.*, 2016), however the general scaling of such studies is more static. Limited work exists surrounding accuracy reviews of larger scale surveys.

b. The presence of in-channel vegetation

Barren channels are not common in the UK. The majority of managed and un-managed river systems worldwide, poses vegetation at their margins if not in the channel. UAV photogrammetry exclusively uses RGB imagery as its data source, rendering it as susceptible to object occlusion as the human eye. Whereas LiDAR systems are able to “see” through even dense vegetation cover to a degree (Chasmer *et al.*, 2006), photogrammetric methods cannot. The spindly structures and partial ground occlusion present in vegetated environments can interfere with SfM processing, producing noise and point cloud artefacts. A means to correct errors like this must be developed if UAV remote sensing of river and associated large scale sediments analysis are to truly mature.

c. The need for extremely low vertical error when sediment budgeting at large scales.

As part of Research Question 1, this study will investigate the large-scale geomorphic evolution of Wooler Water. The 2km long study channel is one of the most extensive ever surveyed by a UAV platform. The problems previously brought to attention are part of a number of complications which compound vertical uncertainty within final DEMs. These uncertainties are preserved when producing a DEM of difference (DoD); subtracting the elevations of one DEM from the another as a means to detect geomorphic changes. Even if error in the Z axis is apparently low, $\pm 10\text{cm}$ for example, over the course of a 2km stretch of river this can induce inaccurate volume calculations potentially leading to misinterpretation of geomorphic processes (Milan *et al.*, 2011). The case study channel of Wooler Water is approximately 2km long, with a mean width of 25m constituting a surface area of roughly 50,000 m^2 . If each input DEM has a vertical error of $\pm 10\text{cm}$, the resultant raw DoD will have $\pm 20\text{cm}$, representing a potential volumetric uncertainty of 10,000 m^3 within the river's sediment budget. Loosing track of that much material is not acceptable for effective channel management. The RSME values for each of this project's survey DEMs are considerably lower than $\pm 10\text{cm}$ however and in reality, simple addition of surface error is not suitable for calculation of combined error. Rather propagated error is used as a measure of DoD uncertainty. This propagated error may then be used as a detection threshold, permitting differentiation of signal from noise. More discussion of error propagation is given in Section 6.3.1 and 7.2. The data capabilities of UAV SfM has been validated to be reliable at intermediate scales and where the survey site is approximately square/rectangular (Caroti *et al.*, 2015; Cook, 2017; Sanz-Ablanedo *et al.*, 2018), however for larger, laterally extensive features, the literature is less supportive. If this project's aims (detection of fine geomorphic shifts across very wide scales) are to be met, a means to reduce DEM uncertainty as much as possible must be developed.

5.2. Noise Filtering and Vegetation Removal

The need for removal of all non-ground points is critical to ensure accurate sediment budgeting. LiDAR surveying traditionally overcomes this by filtering points according to the return number, utilizing only points which exist on the ground surface. No such method is available to photogrammetry, which relies on ground remaining un-occluded. The standard SfM workflow will reproduce everything it “sees”, resulting in all environmental features being reconstructed in the model, including vegetation. This is undesirable for the purposes of detecting geomorphic change with UAV photogrammetry, especially in the context of fluvial systems, where in-channel vegetation is common. For models of smaller scale, vegetation can be easily identified and manually removed, however the process is time-consuming and a relatively blunt, risking data loss at the margins of vegetated areas. Furthermore, the natural structure of vegetation makes it particularly problematic for SfM to accurately discern. If generalised as a surface, shrubs, trees and bushes possess extreme roughness, where thin limbs and branches extend vertically. This is characterised as noise and within the reconstructed point-cloud, increasing local spatial uncertainty. Fortunately, a degree of fine geometric post-processing is available to circumvent this issue.

Agisoft Photoscan’s filtering method relies on detection of points which exceed statistical thresholds, namely their relative angle and distance from the lowest point in a moving window. This can be imagined as a virtual terrain mesh, triangulated from the lowest existing point in a given cell size. Each point in the dense cloud is tested relative to this virtual mesh. If the tested point exceeds an angular and distant threshold it is classified as a non-ground point. Points which lie within the given maximum angle (θ_{max}) and distance (D_{max}) are designated as “ground points”. The selection of these parameters is

dependent upon the spatial properties of the cloud being filtered. The parameter for θ_{max} should not exceed the maximum slope of the ground within the model. Similarly, D_{max} should not be greater than the maximum height of ground elevation variations. The cell size of the virtual mesh should also be specified and will be similar to the size of the largest object which must be removed from the model. In the case of Wooler Water, a high degree of both ground slope and elevation is present due to the very steep banks. Filtering must therefore be carried out iteratively in order since filter tolerance will initially be relatively low. Single pass filtering would result in inclusion of too much non-ground data in the form of low vegetation for sediment budget outputs to be meaningful. Initial filtering is able to remove trees and continuous canopies, a large moving window cell size of 18m was selected, with a maximum angle of 15 degrees and a maximum distance of 2.2m; approximately the height of tree leaves above the ground. These filter settings are more suited to removing groups of trees proximal to the river banks. Larger groups of trees can be removed by manual selection and re-classification. The first filtering pass did not however remove small shrubs and low vegetation below 2m. A second filtering pass was therefore necessary. For this purpose, a smaller cell size of 10m was selected for the moving window. Representing a higher resolution virtual terrain mesh. A reduction in θ_{max} to 6 degrees and D_{max} to 0.5m was also required in order to remove objects such which may have been mis-classified as ground points during the first filtering pass.

The lack of detected ground points underneath occluding vegetation presents an additional problem. Points that are detected through denser vegetation are often of erroneous due to the local high-noise environment and may not be caught by filtering in Photoscan. This leads to vegetated areas being essentially eliminated from the dataset and replaced with “no data” cells in the final DEM. Small holes may be patched via interpolation of edge cells, however this method is not suitable for larger “NoData”

patches without secondary data. A means to mitigate this was tested during Survey 4, where many GPS ground points were recorded within areas of vegetation in the upper section of the Study Site, for the purpose of providing additional data to improve hole-filling interpolations. The highly accurate GPS observations provide a less uncertain means for data interpolation when compared to using intermediate points within vegetation clusters reconstructed by normal SfM. Ground points calculated to occur beneath, or in-between dense vegetation are often indistinguishable from seemingly random noise points induced by the visually complex features; overlapping branches, leaves and shadows.

Separation of ground points from vegetation noise is problematic for the geometric filtering method. This presents a significant drawback for photogrammetric surveying of rivers with UAVs. A potential solution may be to make use of the variable colouring of points. Each point within the UAV cloud is assigned its own RGB value. Whilst this value is considered a generalisation of the pixels which were used during SfM calculations, the extremely high resolutions afforded by UAV photogrammetry limit this dilution. Here then lies a means to differentiate darker ground points from differently coloured vegetation. Supervised application of point reclassification according to colour provides a method to segregate ground points from vegetation noise. In-leaf vegetation is most easily detected due to the contrast in colour between the green plant surfaces and the often beige/brown hue of the ground. For vegetation not in-leaf, the method is more limited, however a degree of colour contrast usually remains between plant material and the ground. In such cases, a more refined approach is necessary, utilizing lower tolerance when selecting points of a certain colour, as well as more intensive manual inspection

that the re-classified points are consistent with erroneous vegetation noise, and not correctly computed ground points.

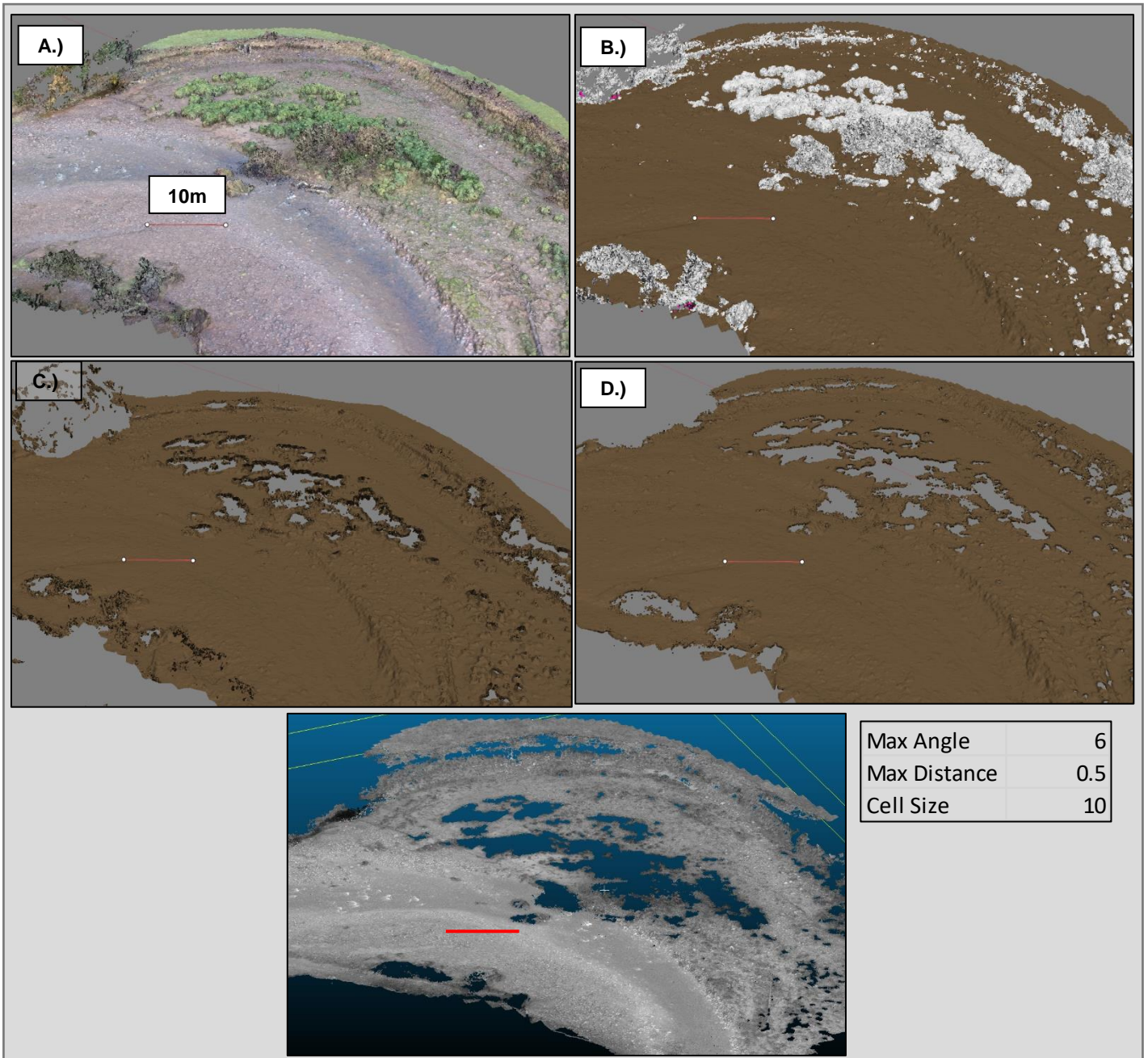


Figure 5.1 – Progressive filtering and cleaning of vegetated point-cloud.

Figure 5.1 displays the multi-step process used to remove non-ground point data from the point cloud. Figure 5.1 A represents the raw point cloud to which no post-processing has been applied. Non-ground data present includes gorse bushes to the right of the channel and trees which overhand the banks of the incised margin. Figure 5.1 B presents

first pass result of Agisoft Photoscan's ground point classification algorithm. Figure 5.1 C illustrates the re-application of the ground point classification filter using less tolerant settings to remove outlying points which were not captured by the first pass. Following visual inspection that no erroneous points, obvious by their significant elevation disparity from the river bed, the point cloud is transferred to cloud compare for additional filtering. The vegetation filtering phase is not exhaustive however and some isolated noise points may persist. These are particularly common within "no data" patches, where vegetation was so dense as to completely occlude the ground. This may manifest as a "lip" at the edges of holes where vegetation has been removed. This is visible in Figure 5.1 C and D. Such points should be removed as they do not represent any valid ground data which might be used for sedimentary budgeting.

Manual removal of such points is too time-consuming and inconsistent for application at the data scales present in this project. Further semi-automatic filtering is therefore required. CloudCompare's statistical outlier removal (SQR) tool operates similarly to the classification filtering in Agisoft Photoscan but is less constrained by the relative verticality of points from each other, and more so the raw distance of a point from its neighbours. Instead of testing against a cell on a virtual terrain mesh, pure point-to-point comparisons are made. This limits generalisation, making the SQR method more suited to clean-up of more discreet groups of points. Mechanically, the SQR filtering operates by calculating the mean distance of a point from a set number of its neighbours, then accepts or rejects points based on that distance plus a set number of times its standard deviation. This permits fine tuning of the size of point groups to be removed, as the number of neighbours selected closely controls the standard deviation to be used as part of the calculation. The result of this process is displayed by Figure 5.1 E which contains fewer potentially erroneous points around the edges of gaps where sections of vegetation and

individual shrubs have been removed. The complete vegetation and noise filtering workflow makes use of multiple classification and removal methods, beginning with a coarse approach and becoming more focused. In the case of Wooler Water, a high variability of ground conditions (slope and elevation) and heterogenous vegetation types necessitate the multiple stages of filtering. Survey subjects of more consistent conditions (low slope, low terrain undulation, and low vegetation diversity) do not require such iterative filtering, since

5.3. Topographic Model Construction

5.3.1. Common Workflow

Following image acquisition and recording of ground control points data was transferred to the processing computer with an active Agisoft Photoscan Pro Licence. General image positioning retrieved from the on-board GPS metadata is visually checked, and any anomalous images, such as those accidentally snapped on the ground or for auxiliary viewing of the site were removed. Image quality was visually checked for artefacts and automatically quantified using the quality estimation utility in Photoscan. Low-quality images were removed. Post-processing of differential GPS data used for ground control was carried out in-tandem. Receiver Independent Exchange (RINEX) data for the day of the survey was downloaded from the UK Ordnance Survey website and used to apply differential corrections to all recorded GPS instances. This step is not essential for initial camera alignment, as the integral GPS data of each image can approximate alignment and be optimised later. It is however time critical, as the RINEX files are hosted for just 30 days.

Image tie point computation is the first SfM step and produces a cloud of points with spatial commonality to multiple images. This is referred to in-program as the “sparse

cloud". This step is among the most time consuming of the process, taking between four to eight hours depending on image quantity and density, and the quality setting chosen by the user. Following this, ground control may be added, by "placing" at least three named GCPs within all images in which they appear. Following this, GCP coordinates are imported to Photoscan, which automatically places the remaining GCPs approximately at their real-world positions in-image. Manual correction and refinement are applied to GCPs. As this is done Agisoft automatically updates the rest of the ground control set. This is carried out until all GCPs are verified to be centred on their respective image markers. The model's coordinate system is then formally switched from the on-board image GPS to that of the ground control network. Before alignment optimization, obviously errant tie-points are deleted. These may be caused by vegetation noise or the presence of anomalous photographs. Camera alignment optimisation is executed by Photoscan to minimise misalignments and refine tie-point positioning for the next SfM steps. Dense cloud generation is then carried out, producing a large point-cloud with a point density approximately that of the survey GSD. A degree of depth-filtering is available to the user at this stage and can aid in mitigation of spatial artefacts and noise caused by vegetation or white-water. Dense-cloud calculation is also a hardware intensive and time-consuming step, taking between 6 and 12 hours at higher qualities.

The resultant dense cloud is a true spatial reconstruction of the surveyed ground and if desired a digital surface model (DSM) could be generated. This project however requires a "bare earth" digital terrain model (DTM), alike to that produced by LiDAR, for flawless geomorphic change detection. Ground point detection and vegetation filtering is thus required. The initial steps of this are carried out in Photoscan which possesses a fairly robust point classification suite. In a given cell sample size, the lowest Z point is selected, to create an approximate triangulated terrain mesh. Points are then included to this

classification providing they do not exceed an angular and distant threshold to the virtual terrain mesh. Cell size, max angle and max distance are set by the user. Multiple classification passes may be required to catch different geometries of vegetation. Additionally, verification that the algorithm has not mis-classified steep banks or similar surfaces as “non-ground” points must be done manually.

The semi-filtered dense point cloud may then be triangulated and gridded to attain a draft DEM of the survey area using Photoscan’s in-built algorithm. Orthomosaic generation is also executed at this stage. Users have control to set the blending mode (usually mosaic) and pixel size (as close to the survey GSD as possible). This orthophoto may be draped as a texture on the DEM for visualisation purposes. For additional filtering and refinement in CloudCompare, the processed point-cloud is then exported as a .PTS file. CloudCompare is an open source program for viewing and editing point clouds and possesses an extensive library of user developed plugins, providing a more robust toolkit than can be provided by Photoscan. It is here that fine point cloud adjustments are made. Point clouds undergo “sieving” to improve data contiguity. Additional reduction of vertical error is also applied at this stage, which is described in more detail Section 5.5. Once accomplished, the final refined point-cloud for that survey is converted into a high-resolution DEM, comprising the final data product of the workflow.

5.3.2. Survey 1 Processing

Image data and GPS recordings were transferred to the machine used for processing; a workstation with 16gb RAM and i7 processor but no graphics processing unit (GPU). Over 2000 images had been captured during the course of the survey, however much of these consisted of wider reconnaissance of the site and were not necessary for spatial modelling of the main river channel. Image locations were reviewed and pruned out as necessary, reducing the size of the photoset by approximately half. Image quality was also

assessed, both manually and by Agisoft Photoscan's in-built image quality estimation utility. Manual visual checks did spot a few images in which the landing legs of the Phantom 3 UAV were visible within the photograph. This usually only occurs in high-wind conditions when the aircraft will automatically tilt into the wind in order to maintain positional stability. These images were easily identifiable and uncommon within the dataset, enabling them to be safely excluded from processing. Automatic image quality estimation by Photoscan returns a value between 0 and 1 based on image sharpness. Motion blurred or out-of-focus images generally receive values below 0.5 and are advised to be removed from processing (Agisoft, 2018). Fortunately, this comprised less than 2% of images taken in Survey 1. Whilst camera alignment was running, the relevant RINEX data was acquired and applied to the GPS observations. Camera alignment was initiated, taking a full day to complete due to hardware limitations. Upon completion of camera alignment, GCP locations were imported and checked. Alignment optimization was executed, and dense-cloud construction started, with aggressive depth-filtering due to the abundant vegetation within the channel. Dense-cloud reconstruction took over 3 days to complete, due to the processing machine lacking a GPU. Automatic iterative vegetation filtering was run over the point surface twice. Firstly, with a coarse cell size of 20m and relatively high angle and distance thresholds, to catch larger trees contiguous canopies, then again with a 1m cell size and less tolerant settings for maximum angle and distance, to filter out smaller areas of scrub and lone bushes. Manual checking of the automatic point classification process revealed some sections of steep banks had been misclassified as non-ground points, requiring some manual re-classification corrections to be applied. The semi-processed point cloud was then migrated to CloudCompare.

Vegetation filtering in Photoscan had been successful in removing the majority of points which might be incorrectly included in the bare-earth DTM. Some retention of ground

points below occluding vegetation was observed. Dependent upon in-leaf conditions and vegetation height some capture of ground points is possible. The high-noise environment encountered around vegetation can induce vertical inconsistencies in such points. These points are rarely spatially contiguous however and of dubious vertical accuracy. This is visually obvious upon closer inspection of the point cloud however instances are too numerous to manually select and clean. To automate this process, CloudCompare's statistical outlier removal (SQR) tool was implemented. This utility works in a similar manner to the Photoscan's point classification tool; The distances of a point from a set number of neighbours is calculated. The point is removed if the average distance plus a set number of times the standard deviation is exceeded. ($\text{max distance} = \text{mean distance} + n * \text{std dev.}$) This results in a significantly cleaner point cloud, without errant individual points that might induce artefacts when converting to the DEM. Final preparations to the point cloud included trimming of the extent to just the incised channel. This was done to remove the areas of agricultural field and grassland on the floodplain. When later comparing DEMs for sediment budgeting, inclusion of these areas could lead to errors due to variations in crop height or type. Before clipping the point cloud file size approximated 6 gigabytes. CloudCompare initially did struggle to render the cloud, however removal of many points by clipping to the channel margins greatly smoothed operation. The filtered, clipped point cloud was then grid sampled at a resolution of 5cm to produce the final, full reach DEM. This DEM was exported under the name JulyChannelDEM.tif, since survey numbering had not yet been established. A grid size of 5cm was utilised as it was considered at the time an easily achievable minimum resolution for potential future surveys to also attain, thus ensuring data consistency.

5.3.3. Survey 2 Processing

The special conditions encountered in during Survey 2 dictated a higher degree of image post-processing before the SfM workflow could commence. The lower light conditions increased instances of blurred images. Image improvements were made in Adobe Lightroom, specifically adjustments to image sharpness, contrast and saturation were applied. This had the effect of improving the average image quality estimation score assigned by Agisoft from 0.74 to 0.80. Image locations were also reviewed and pruned as necessary. For SfM processing, an upgraded workstation was used. Specifications included 256GB of RAM, an Intel i9 processor and Nvidia TITAN X GPU. Camera alignment was thus dramatically accelerated, taking just 5 hours. Processing of differential GPS observations took place in-tandem on a separate machine. 24 GCPs were imported and verified to be correctly positioned preceding alignment optimization. Dense cloud construction was orders of magnitude faster than in Survey 1 as the TITAN X GPU significantly accelerates this section of the workflow. The dense cloud was completed in 11 hours. Having taken place in November, what vegetation that hadn't been stripped by recent stormflows was not in-leaf, thus the filtering process returned more optimal results than in Survey 1. The iterative approach was applied as it had been with Survey 1. A coarse, high tolerance point-classification filter was passed over the before a fine, more conservative filter designed to catch both high and low vegetation. A draft DEM was exported at this stage, as well as the semi-processed point cloud. A high resolution orthomosaic was created and saved at this point

Processing in CloudCompare followed a very similar workflow to that of Survey 1, albeit in a different order. In order to speed up SQR filtering, parts of the model unnecessary for sedimentary analysis, such as adjacent fields, were trimmed before the tool was applied. This enabled CloudCompare to run more smoothly under the load of such a large dataset.

Visual inspections were carried out to verify no anomalous points were still present in the dataset. The point cloud was then converted to a 5cm DEM file, designated NovemberChannelDEM.tif, again in the absence of a known number of surveys that would be completed at the time.

5.3.4. Survey 3 Processing

The lighting conditions of Survey 3 additionally required some image post-processing to improve their quality. Adjustments in Adobe Lightroom included a reduction in exposure to many of the brighter image, as well as a slight reduction in contrast. Small sharpening and saturation boosts were applied to all photographs. This did not affect Photoscan's image quality estimations, since the utility primarily assesses image sharpness, not light consistency or colour. If the images had been left unprocessed, an unacceptable risk of SfM artefacts and noise appearing in areas of extreme brightness was present. This had been tested with a small sub-set of particularly bright images beforehand, the results of which were not satisfactory. Image corrections applied, the data was loaded into Photoscan for SfM processing. The upgraded workstation was again utilized, no hardware changes had been made since Survey 2. The more compact dataset afforded by the upgraded UAV used in the instance of this survey additionally reduced processing time. Camera alignment was completed in a little under four hours, 18 times faster than Survey 1. Processed GPS data was inducted to the model and the coordinate system switched from the UAV to the ground control network. Optimization of image alignment was carried out once all 30 GCPs had been placed and verified. Some points in the sparse-cloud were miscalculated, particularly around areas of vegetation, which was at the time of the survey, in-leaf. These points were deleted preceding dense cloud construction.

Dense cloud processing was less accelerated than camera alignment had been since the data resolution was similar to that of preceding surveys, albeit from a lower number of

photographs. Depth reconstruction and cloud generation took approximately 10.5 hours. The increasing number of points between surveys had a noticeable effect on the time taken to complete initial vegetation filtering. This survey possessed nearly double the number of points within the dense cloud than had been generated when processing Survey 1. The coarse classification filter took less time than the fine to run, however total processing time of this step was approximately 4 hours. Sheer data volume dictated unnecessary section of the point cloud be clipped before it could be exported to CloudCompare. The high-performance workstation was a capable of rendering the many millions of points in CloudCompare, however inputs were choppy, and the program ran at a reduced FPS. Trimming the cloud in Photoscan allowed for increased dataset portability and ease of backup. Backing up of datasets became a higher priority at this stage in the project, and multiple copies of the raw images, GCP data, point clouds and DEMs were distributed across backup drives and cloud servers. The trimmed down point cloud was subject to SQR filtering in CloudCompare, which was more extensive than in Survey 2, given the increased vegetation. Final checks verified data continuity and the point cloud was converted to a 5cm DEM, designation SeptemberChannelDEM.tif.

5.3.5. Survey 4 Processing

Survey 4 collected the largest quantity of data attained from any survey to date. No post-processing was required for the images acquired, except for the removal of some images accidentally taken on the ground. Image quality estimations in Photoscan were high, not requiring any photos to be removed. Camera alignment took 12 hours to complete in Agisoft. This survey also utilized the largest number of GPS observations to date. Differential corrections are applied all at once, however GCP placement and checking is slowed the more markers there are. Once camera alignment was complete the 80 GCPs were imported and their placement was checked. Camera alignment optimization was

applied, and construction of the dense cloud started. The immense data density meant this step took longer than previous surveys, despite being run on higher end hardware. At high quality with aggressive depth filtering cloud generation took 17 hours. The resultant cloud was trimmed to the channel margin before applying vegetation filtering in order to reduce the amount of points that needed to be analysed as part of the process. Vegetation conditions were less abundant than in the previous two surveys, however the same level of filtering was applied. Ground points were checked, and any misclassifications were corrected. The orthomosaic image was generated and exported at resolution of 2.6 cm. The clipped, semi-processed cloud was exported to CloudCompare for final clean-up and DEM production. Only limited SQR filtering was applied as automatic classification in Photoscan had worked particularly well on this occasion. Final visual verification of the point cloud was carried out and the final DEM was exported at a resolution of 5cm, designation AprilChannelDEM.tif. An overview of each DEM and orthophoto is available in Appendix 1.

5.4. DEM and DoD error analysis

Spatial error within a DEM can be characterised as the level of departure from the “real world” elevation. This may be characterised in individual dimensions (X, Y, and Z) or as a singular root mean squared error (RMSE) value (Carlisle, 2005). The standard error reporting format given by Agisoft Photoscan includes RMSE for each spatial dimension for both the entire model, as well as for each GCP. All Surveys carried out were reported to have a general RSME below 5cm. Not reported however is the standard deviation of this value. The data scales used by this project are too extensive to take general RSME at face value, combined with the fact that calculations surrounding sedimentary budgeting are highly sensitive to input errors raise the necessity for a more robust error analysis (Milan *et al.*, 2011). This section of the project will recount more the more in-depth approaches to accuracy assurance which should be applied as part of the processing workflow for UAV photogrammetry. This will include modelling spatial distributions of error, and novel corrective processing techniques. Singular error estimations are prone to inflation of uncertainty across planar surfaces and underestimation at slopes or areas of higher relative roughness (Heritage *et al.*, 2009). Modelling of spatial distributions of error and its importance to accurate geomorphic change detection has well covered (Ashmore and Church, 1998; Lane *et al.*, 1998, 2003; Brasington *et al.*, 2000) and powerful tools for detailed inference to error variability are available (Bangen *et al.*, 2014). Fuzzy inference system (FIS) approaches make use of multiple input models to generate an inferred map of DEM error. FIS models, such as that by Bangen *et al.*, (2014) utilises input surfaces of point-density, slope, roughness and others to define error at the cellular level. This type of error modelling is more suited to GPS surveys, where error is more controlled by interpolation uncertainty and 3d point quality. For SfM no “absolute”

error metadata exists for each reconstructed point and densities over ground are ubiquitously high enough to not have a significant interpolation error and effect on DEM uncertainty.

A more in-depth analysis of error distributions than can be provided by GCP level reporting is presented in this section. For conceptual purposes, this is done only using data already gathered in the field during the course of the field campaign. Preservation of methodical transferability is made possible by limiting collection of auxiliary datasets, instead utilizing data which would already be available to users replicating the protocols laid out by this project. In total 160 GCPs are utilised for model construction across all four surveys. This may be used as a self-contained dataset of ground truthing checkpoints. Checkpoints not utilised as GCPs during the construction of a survey model can be considered independent to all other models produced by this project. For a given survey model GCPs from every other survey can be used as independent checkpoints.

5.4.1. Independent Error Analysis

GCP data provides a basic level of information surrounding error distribution in DEMs produced by this research. General roughness analysis may also be of use however, areas of high noise are already removed in final DEM products, making this method somewhat redundant. GCP network quality then represents the primary control over error within the SfM methodology. It is sensible that modelling of error distributions in this project falls partially to multi-epoch comparison of Z levels at static GPS points recorded throughout the field campaign; at points of unchanging elevation between surveys, DEM elevation should vary by less than the 3D uncertainty within the GPS data when that point was logged (typically <0.05m). A review of all GPS points taken during the field campaign

was undertaken in order to source these points. Each entry was rejected or included into the independent checkpoint list provided it satisfied two conditions:

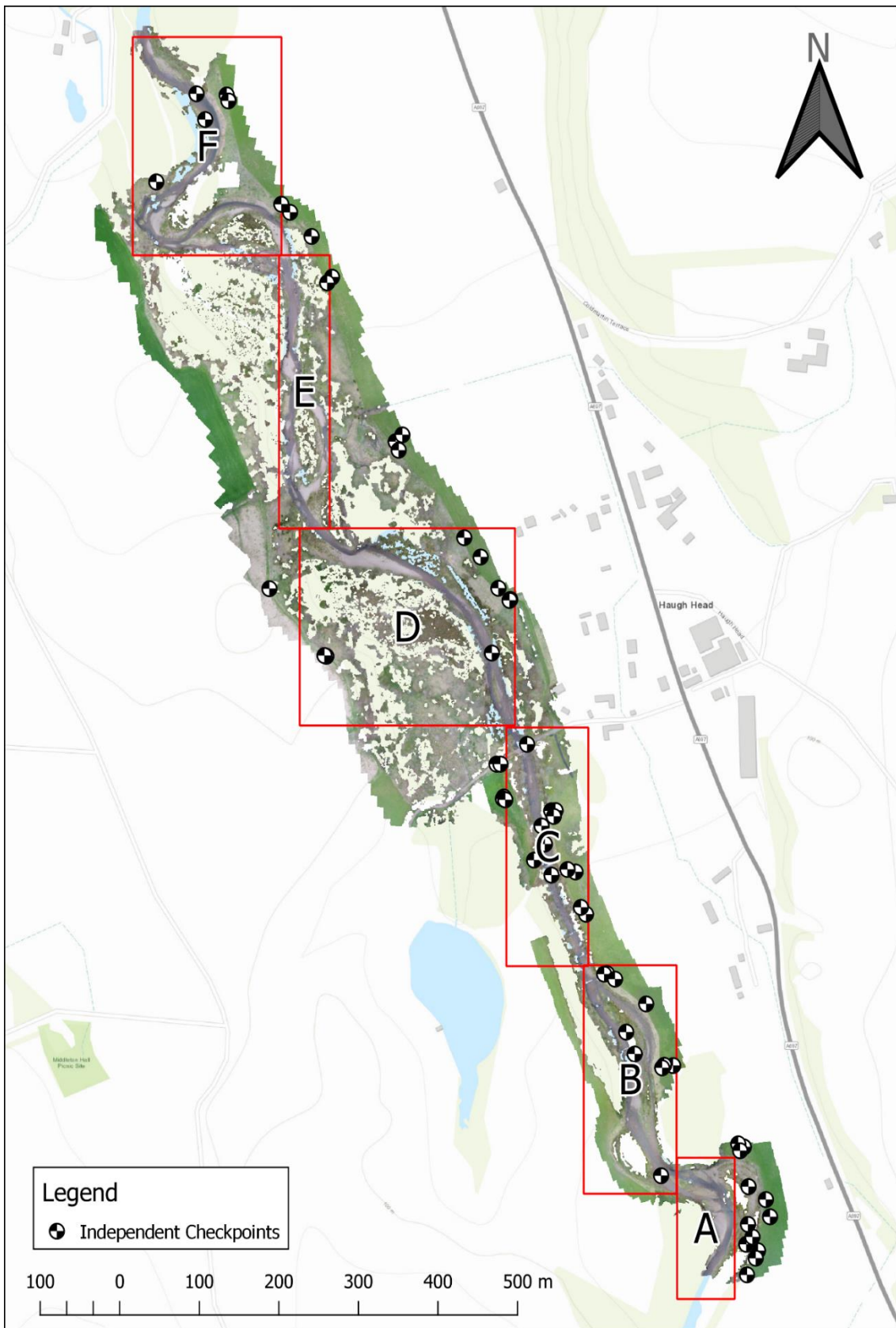


Figure 5.2 - Locations of GPS observations utilized for error checking.

- i. It was within the DEM coverages of all four surveys.
- ii. It existed on a surface which had not undergone elevation change between any survey (floodplain, weir top, bridge deck or un-wetted channel point)

A total of sixty-seven such points were identified, 15 from Survey 1, 9 from Survey 2, 16 from Survey 3, and 27 from Survey 4. Their positions are mapped in Figure 5.2. These points are evenly distributed linearly (along the river), however lateral placements are nearly all on the floodplain next to the channel as this is where the majority of GCPs were placed. Analyses of these points is presented here. Figure 5.3 represents the mean absolute error elevation between concurrent surveys of all three Z values for all 67 checkpoints. Although the mean error for all checkpoints is quite low and within the tolerance for reliable sediment budgeting, there is considerable variation between points. A maximum absolute error of 0.11m is reported at checkpoint 39, whilst the difference at point 11 is practically nil. This outlines how variable error can be across the modelled surface when utilizing UAV photogrammetry and presents a problem for reliable sediment budgeting. Error reporting is most critical at areas of geomorphic change, since any vertical uncertainty will be carried over into volumetric calculations, potentially interfering with management implementations. This problem must be overcome if meaningful geomorphic change detection can be achieved via the UAV photogrammetry method.

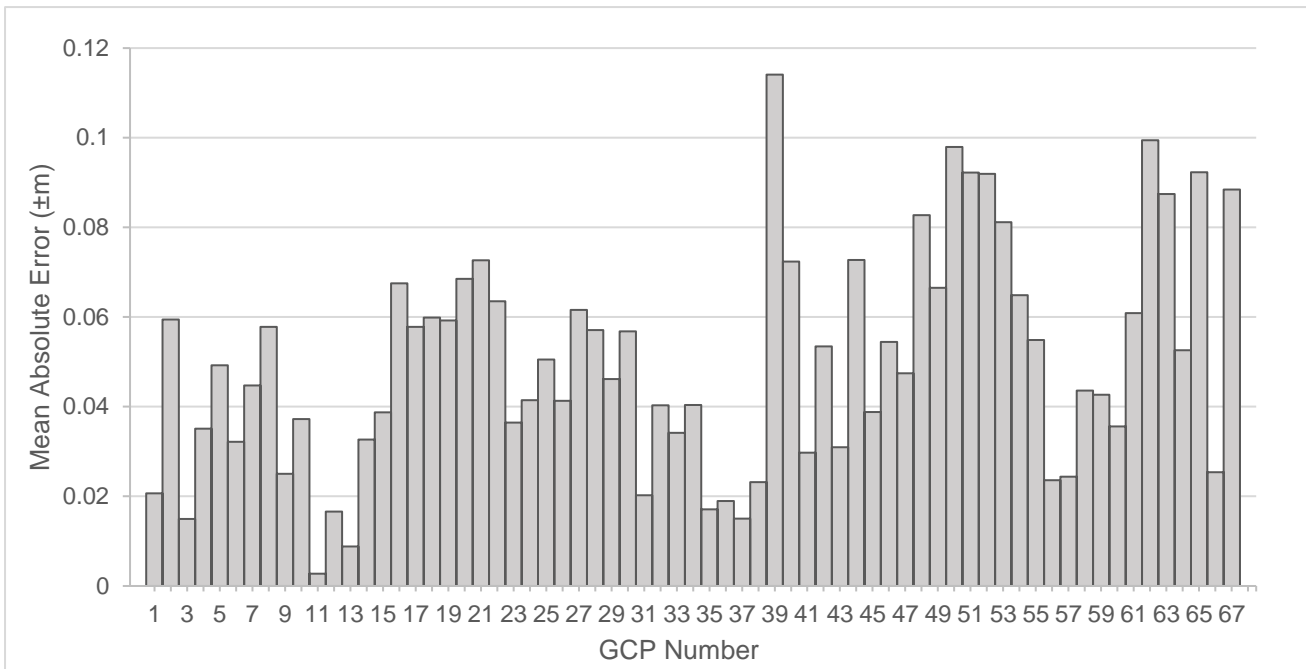


Figure 5.3 – Mean absolute error in $\pm m$, of independent GPS checkpoints.

Any vertical error present within the DEMs produced in this research will be retained as volumetric uncertainty in the DoDs created when subtracting the Z values cells of a more recent model from that of a previous survey. Since the final results in this project are represented by detailed change maps produced from such DoDs, error analysis of these data products is as justified as that of the inputs. This not only ensures data quality at the final stage of the processing and analysis methodology, but additionally provides a proxy for the quality of data inputs used. Error within a DoD product is detectable as significant change being observed where static ground is expected. In the case of this project, such areas are characterised as: Flood plain spaces where grass length is known to be consistent between surveys. Relatively flat areas within the incised channel as-yet untouched by known flows, thus not subject to hydrological morphing or failure under gravity. Artificial surfaces, such as the concrete at Haugh Head Ford. Very large boulders confirmed not to have been shifted between surveys from observation of high-detail orthophotos. GCP markers within the main channel whose paint had persisted between surveys and were re-discovered during orthophoto observation.

Observation of some raw change DoDs produced at the site level indicated significant change over some of these features. This is characteristic of error, since they are known to be static in reality. The detection of a change in elevation on a static surface implies the presence of error within at the input DEMs. This may be illustrated by small-scale DoDs of the Haugh Head Ford. This concrete surface should not have undergone any significant vertical change throughout the field campaign, however the measured elevation does



Figure 5.4 – Cross section transect on Haugh Head Ford

vary within the UAV constructed DEMs. Cross sectional profiles taken along the axis shown in Figure 5.4 are displayed in Figure 5.5.

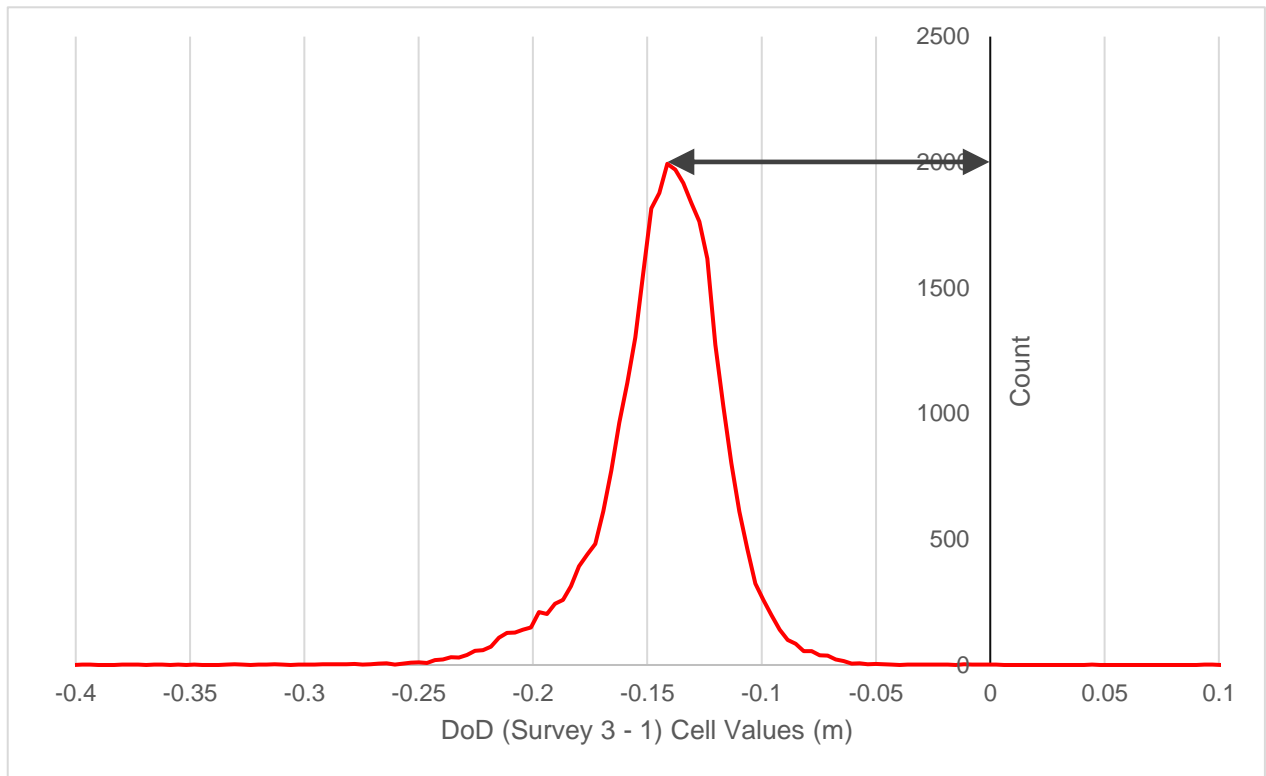


Figure 5.6 – Worst case histogram offset of Haugh Head Ford (Survey 1-3 Raw DoD)

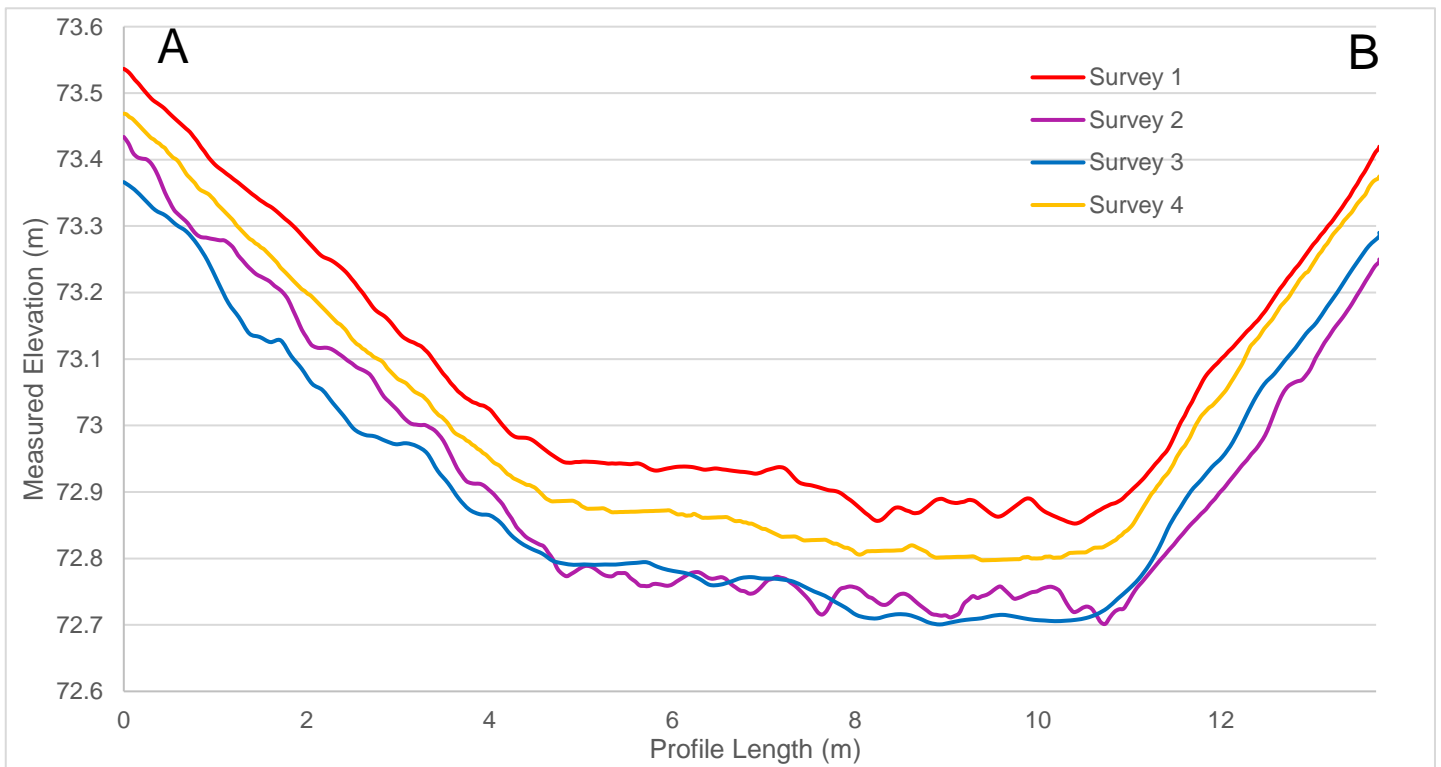


Figure 5.5 – Cross sectional profiles of Haugh Head ford.

Maximum variability is found between the surfaces modelled by Survey 1 and 3, which are separated by a mean distance of about 15cm. Figure 5.6 displays the histogram of the DoD surface produced when these surfaces are compared. For a survey with no error, a single peak at zero would be expected, however in this case the peak is skewed to -15cm, representing the most common cell value and thus relative vertical error. Closest in agreement, are the DEMs for Survey 2 and 3, however these surfaces cannot be considered the most accurate compared to the others and only reflects a relative consistency.

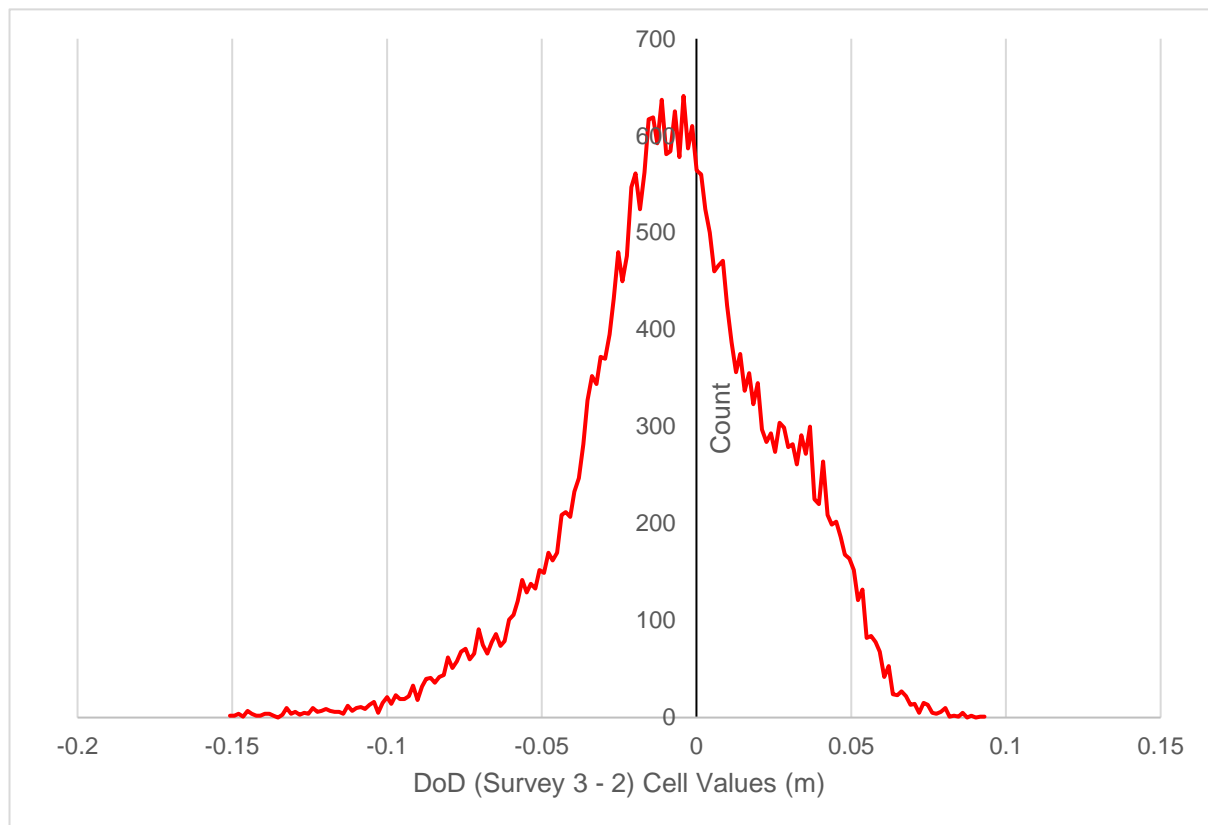


Figure 5.7 – More ideal inter-survey histogram offset. (Survey 2-3)

The histogram for the DoD produced by subtraction of the Survey 3 surface from that of Survey 2 is shown in Figure 5.7. The peak value reads much closer to zero, reflecting the relative local vertical agreement between the two DEMs. Survey 4 represents the most accurate reconstruction of Haugh Head Ford in this case, as GCPs used for model georeferencing were placed on the surface itself and may act as the local benchmark in

this case. The GCPs in question were deemed to have a vertical error of approximately 1.5cm. Knowing this, Survey 1 can be deemed to be too high, and Survey 2 and 3 to be too low, at least in the local context of Haugh Head Ford. Spatial variation of vertical uncertainty prevents this statement from being applicable to the wider survey extent. The information remains valuable however, since the Survey 4 surface in this case can act as a validation dataset, the other models may be manually translated to align with the benchmark. This would essentially negate vertical error in a local context but may exacerbate uncertainty elsewhere. Therefore, any corrections applied must be done so at a scale smaller than that of the full model extent.

5.4.2. Absolute vs Relative Error

The discussed measures and methods of spatial error apply to the uncertainty in the “absolute” reference system. That is, the relative closeness of DEM elevations to that of the “real-world” value. For detection of geomorphic change this makes sense; If both input surfaces are minimally disparate from the absolute frame of reference, resultant DoDs will also have low error. For DEMs of decent coverage, the histogram of these difference surfaces should have its peak at 0. Difference surfaces that have their histogram peak at a non-zero value can be assumed to either have the vast majority of their cells undergone elevation change between surveys, or that the total vertical error of the input surfaces is equal to the value at which the histogram peak is found. If the precise amount of absolute error contributed by each input surface is known, then translative corrections could be applied to each surface, essentially negating vertical error, at least the most statistically significant portion of it. However, knowing the error in each respective input surface is impossible at this point as the DEMs are essentially entangled. The total error is however known (equal to the value at which the histogram peak lies). Applying the inverse of this value as a vertical translation to one of the input DEMs will

cause this peak to fall at 0. This will of course increase error in the absolute reference, however relative error will have been minimised. The data products of geomorphic change detection are themselves relative outputs, thus input data does not necessarily need to be absolutely referenced. This method can be summarised as a probabilistic approach to error quantification and correction. A very precise offset factor is provided for the most common frequency bin of cells in a DoD. For the data utilised here, this should be the “static” cells; those which have not undergone elevation change.

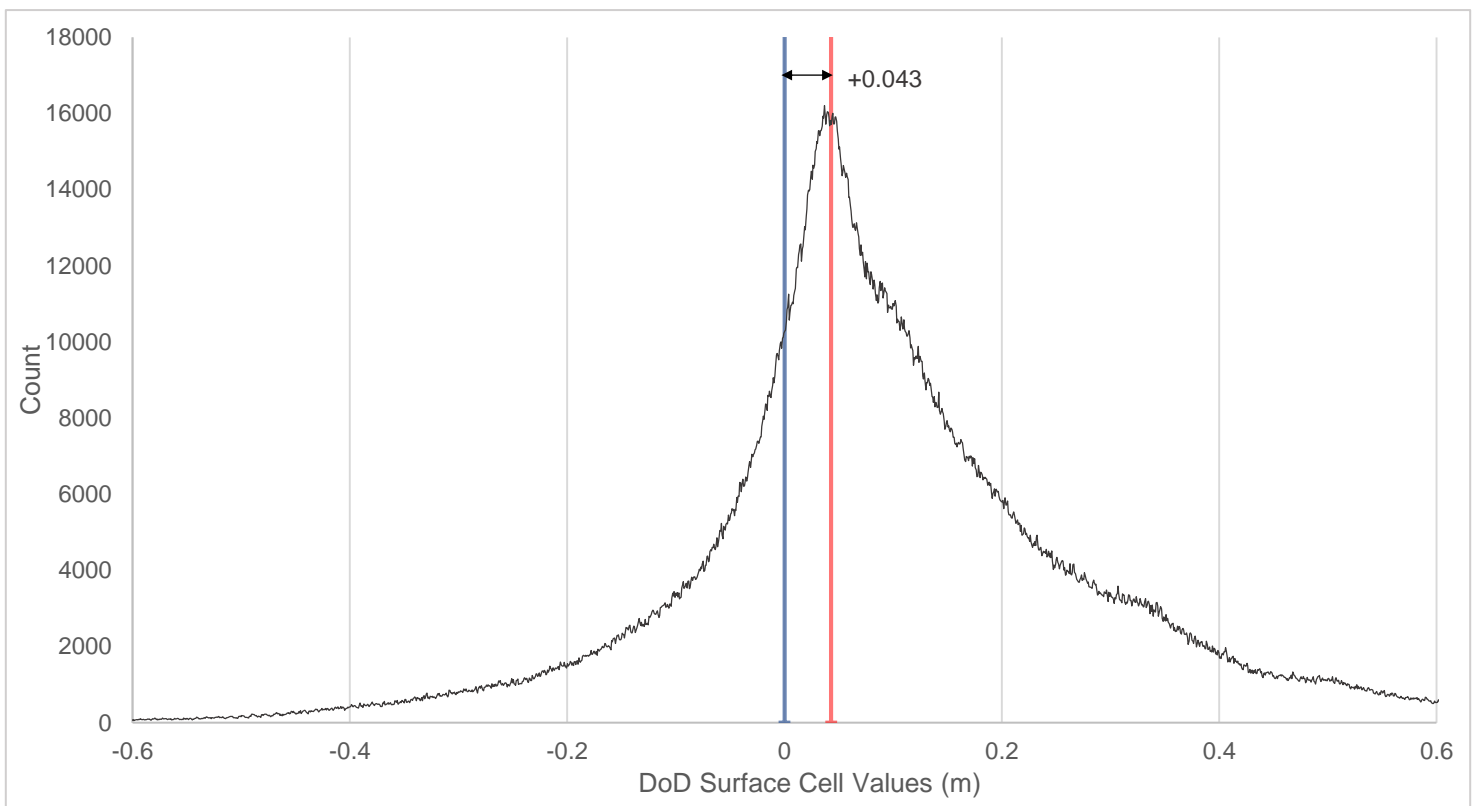


Figure 5.8 – Offset of histogram peak from zero reflects mean vertical error between DEM surfaces.

It should be noted that “offset factor” is not synonymous with error, as the uncertainty for each DEM, relative to the absolute reference, cannot be known. Offset factor refers only to the value at which the peak of the histogram is found. This is characterised by the most probable elevation difference that exists between static cells in each respective input DEM. Translating one of the input DEMs by the inverse of this factor (placing the histogram peak at zero) thus assigns zero to be the most probable vertical difference for

static cells between the two surveys, as it would be if both DEMs possessed the perfect absolute reference. This can be referred to as probabilistic offset error translation (POET).

5.4.3. Limitations and implications

It is intended that this translative approach be applied to the DEMs produced by this project. The caveats should first be cemented however. POET is not suitable for wholesale application to DEMs of large scale, as error is not spatially uniform unlike any translations that might be applied. This is characterised by the histograms of DoDs produced at such scales possessing a wider frequency distribution and lower kurtosis. This results in a higher uncertainty in the translation factor itself, as it is proportional to the “peakedness” of the histogram. It is therefore necessary to divide input DEMs into smaller units. By spatially limiting the inputs the variability of error within them is also limited. In the case of the data presented in this project, splits are applied at the sub-reach level, as illustrated in Figure 6.11 Manual translations of any sort to an absolutely referenced model will void its usefulness as an accurate representation of real-world elevations, suiting it only to use within the relative frame of reference which itself is specific only to surface or surfaces against which it has been relatively corrected. This includes use for development planning and hydrological modelling. It should be noted that spatial distributions of error remain unchanged by application of uniform translations and may in fact be exacerbated if POET is applied too generally.

Table 5.1 – Compared RSME values of this study against similar works.

Author	UAV System	RSME (cm)
This Study	DJI Phantom 3 and 4	2.02 - 4.65
Escobar Villanueva et al., 2019	eBee (fixed wing)	23.0 - 46.2
Hugenholtz et al., 2016	eBee RTK (fixed wing)	5.7-7.2
Langhammer et al., 2017	Mikrokopter Hexa	2.5
Ajayi et al., 2017	DJI Phantom 2	46.87

The error shown by Figure 5.6 and Figure 5.5 represent only a small section of the entire survey extent. Overall surface error as reported in Table 4.1 is higher. Table 5.1 compares reported RSME values for similar works to that present in this study. The surface error in this study is lower than other studies, and is most comparable to Langhammer *et al.*, (2017), who achieve particularly low error and high survey resolution (1.5cm). This is however done over a comparatively smaller area relative to this project (0.14km² vs 0.20km²).

Chapter 6: Surface Comparison and Geomorphic Change Detection

6.1. Introduction

Detection and spatial characterisation of changes to the natural landscape is central to geomorphic study. Understanding how and why landscape features evolve in the way they do is also core to preserving, managing and living alongside dynamic environments (Vita-Finzi and Schumm, 1992). Insight to how future landscapes may evolve is granted by analysis of previous configurations of river systems. This may be done with historical maps (Hooke and Perry, 1976) however workers may encounter data quality and availability issues. Contemporary detection of geomorphic evolution has been empowered by development of surveying tools capable of delivering higher quality data, at more extensive coverages, including aerial photography and LiDAR, which hold advantages over historical map interpretation (James *et al.*, 2012). The UAV platform is among the most recent of tools to be developed for this purpose, and already is recognised as a powerful asset to the general field (Colomina and Molina, 2014). Additional developments in the fields of computer vision and processing have revealed SfM to be the cheapest means for high-detail reconstruction of landscape features, available to more users than ever before, even for those without access to UAV photography (James and Robson, 2012; Prosdocimi *et al.*, 2015).

This section of the research will introduce the data approaches applied to the UAV constructed DEMs for the purpose of detecting geomorphic evolution, between both the landscape and clast scale. A top-down approach will be taken, with largest scale results being presented first and steadily focusing the applied scale of change detection down to the centimetric level. Accuracy of detected changes is key. Many reviews of the accuracy

of UAV imagery are present within the literature, (Brasington *et al.*, 2012; Harwin and Lucieer, 2012; Tonkin *et al.*, 2014; Stumpf *et al.*, 2015; Brunier *et al.*, 2016), mostly citing the good level of accuracy provided by the method. This project will contribute to the understanding of error and uncertainty within UAV photogrammetry, but also present the results of possible corrective methodologies, outlined in the previous section as probabilistic offset error translation (POET). This will enable users who for whatever reason have been unable to attain data with high quality georeferencing to also take part in low-uncertainty geomorphic change detection. This technique is not suitable to application at the site scale, instead being more tailored to improving and reducing uncertainty at the sub-reach level, approximately within the order of 100-200m. These calculations made at the sub-reach level may then be fed into one and other in order to gain a semblance of sedimentary mobility throughout the study site.

This understanding of sediment movement within rivers is crucial to understanding their form and development (Erskine, 1986). Sedimentary quantity and grainsize fractions control not only the planform shape of the system (Leopold and Wolman, 1957), but additionally the types of habitat, niches and communities which inhabit it (Padmore, 1997). Hence, detailed and accurate insight into the parameter, as well as its temporal variance, is a critical fulcrum about which environmental science rotates. This is no exception in the setting of Wooler Water, where artificial manipulation of the sediment regime has been historically present (Sear and Archer, 1998) and the effects of which are present today in the form of a highly-incised channel margin and a system heavily disconnected from its floodplain. Sedimentary flux within the system continues and is prevalent within the data presented here. Research Question 2 will be the primary focus of the work in this section, which presents the maps, volumes and statistics explaining the current state of geomorphic change at the site. From this extrapolative analysis of the

results will permit a degree of prediction regarding the possible evolutionary trajectory of the local configuration and how it may affect flow regime and implementation of future management options.

6.2. Channel Evolution – Full Site

The results of comparative analyses of DEM data and aerial imagery are presented in this section. Cross sectional and planform evolutions also presented, followed by analyses of gradient change and overall sediment budget. In order to provide data context, secondary elevation data acquired by aerial LiDAR survey in 2009 (Environment Agency, 2009) is included in comparative analyses. Examination of broad scale (full-site) changes at Wooler Water are critical to provision of insight to the evolutionary trajectory of the system, but also test the applicability of UAV surveying to such fluvial monitoring.

6.2.1. Cross-sectional Analyses

Seven cross section sample transects were applied to the data (CS1-7), approximately every 200m along Wooler Water's channel. These cross sections include elevation data from every UAV survey (2016-2018) as well as LiDAR data from 2009. It should be noted that the not every cross-section is able to completely display both banks of the river channel due to tree occlusion, the river's bed is clear in all cases however. An overview map of the plotted cross section transects is shown in Figure 6.1.



Figure 6.1 – Locations of cross sections CS1-7 at the Wooler Water field site.

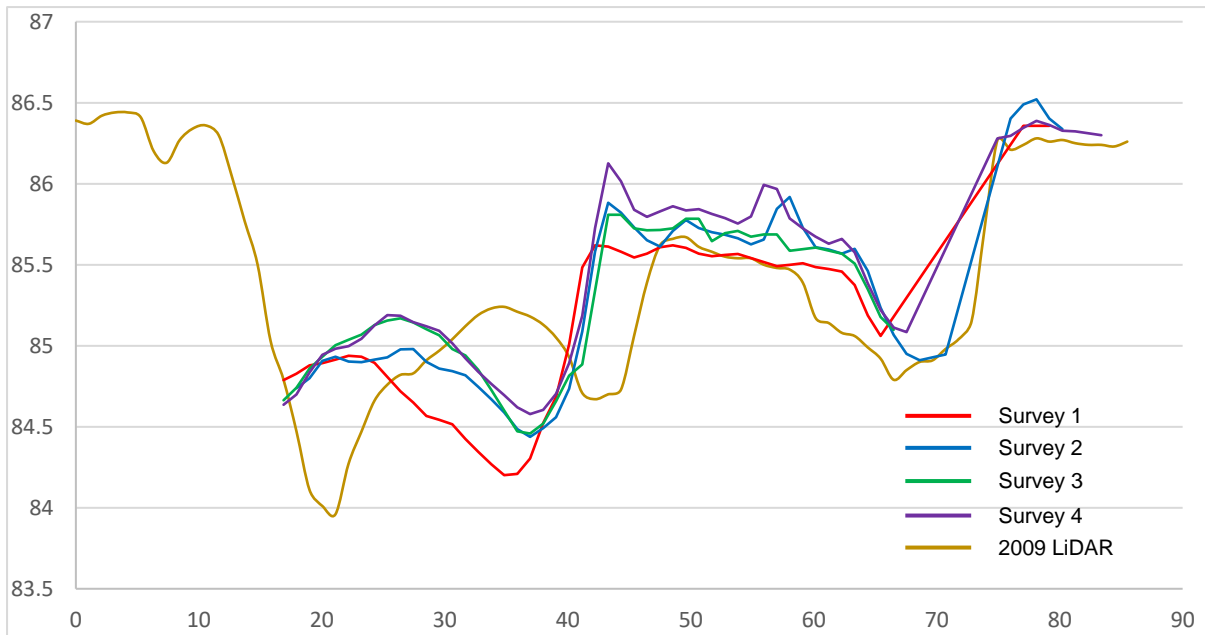


Figure 6.2 – Cross sectional profile CS1

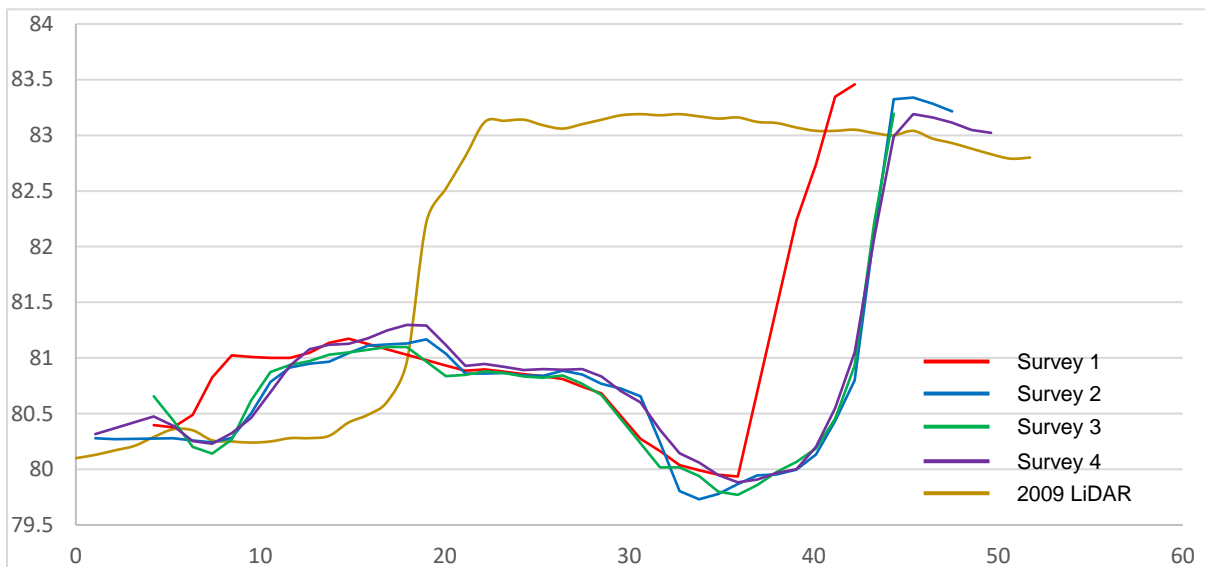


Figure 6.3 – Cross sectional profile CS2

Figure 6.2 displays the cross-sectional profile CS1, which is situated across the first bend of the study area. This section is characterised by three vertically disparate sub-channels. Included within the cross-section profile are all four UAV surveys to date and an additional 2009 LiDAR dataset. Due to occlusion by tree cover the left-most sub-channel is not modelled by UAV data but is mapped approximately 25m downstream where it is un-occluded. Important cross-sectional evolutions since 2009 include the shifting of the

two of river's sub-channels approximately 15m toward the left side of the incised margin. Widening and shallowing of the central inset channel is also recorded. This pattern of change persists within the contemporary data, particularly in the left sub-channel, where depth-reduction is observed between Survey 1 and 4 (2016-2018). In-contrast to the 2009-2016 pattern however is the relative channel contraction seen onwards from Survey 1. The shallowing of this sub-channel may be attributable to bar construction, which is visible by comparison of UAV acquired imagery.

CS2, shown in Figure 6.3 is situated approximately 1 meander wavelength downstream from CS1 (Figure 6.2). This section is dominated by two channels, separated by a partially vegetated bar. The right of the two sub-channels extends up to the steep bank of the incised margin. The left bank of the left sub-channel is occluded by tree-cover in the UAV data. Between 2009 and 2016, the right bank has undergone significant retreat, laterally eroding 15m. This paradigm is consistent during the course of this project's field campaign (2016-2018), where approximately 4m of bank retreat is recorded by UAV observations (Survey 1-2 epoch). The vegetated bar, (approx. 10-30m across CS2) remains static throughout the field campaign, however some erosion into its left margin is noted after Survey 1. Contrastingly to CS1, little vertical change is observed at the channel bed, which is static in CS2. The pattern of vertical stability extends to cross-sections CS3-5, profiled in Figure 6.4. The river's bed appears to have remained static since 2009 at CS3 and CS5, however some vertical change is clear at CS4 between 2009 and the commencement of this project's field campaign in 2016. This vertical evolution is symptomatic of the leftward migration of the 2009 channel rather than downward scour under flood conditions. There is also evidence of erosion to the left side of the channel in CS4, scouring 20 centimetres between 2016 and 2018. The river bed at CS3 and CS5 has contrastingly remained stable since 2009.

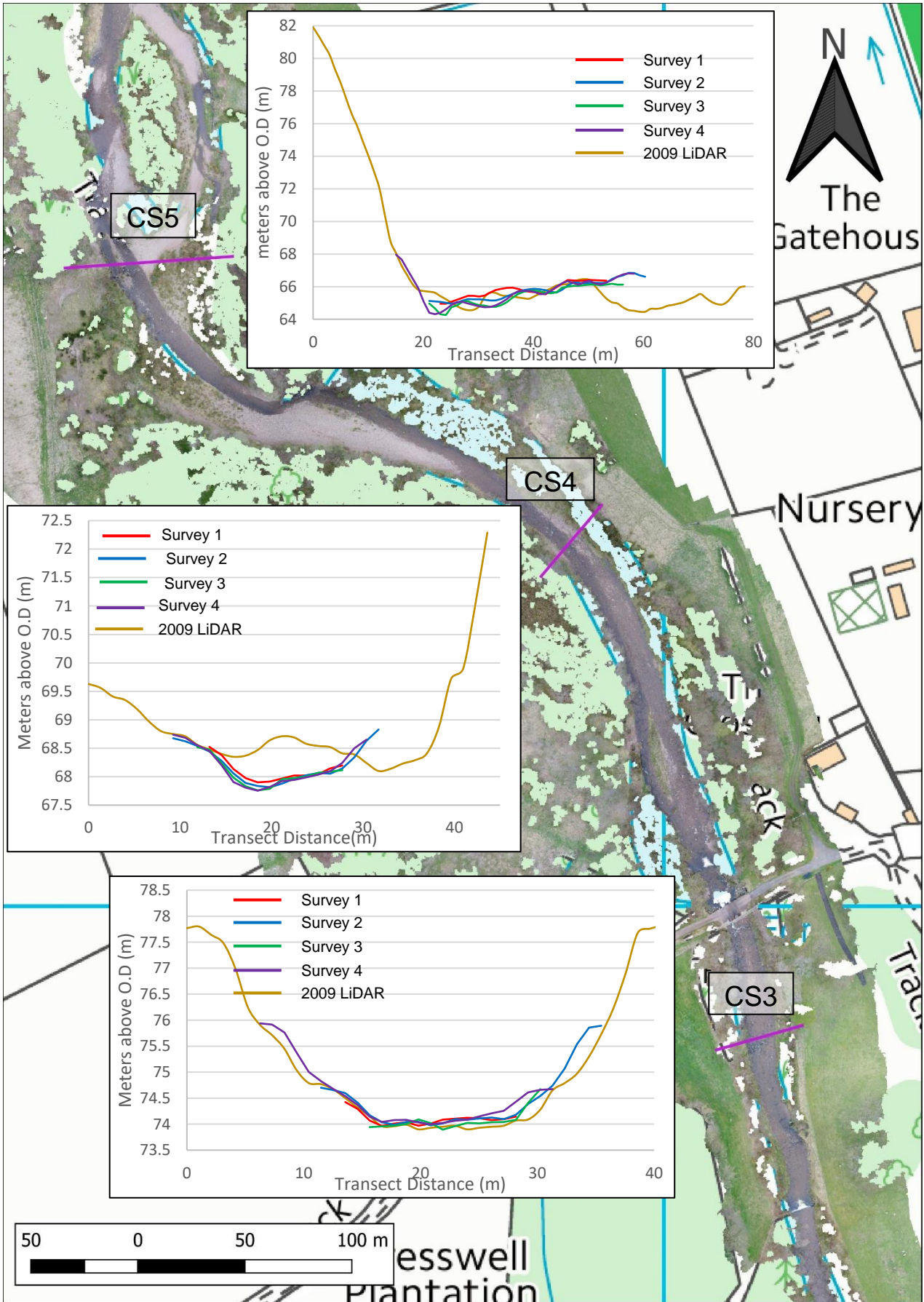


Figure 6.4 – Cross sectional profiles CS3 - 5

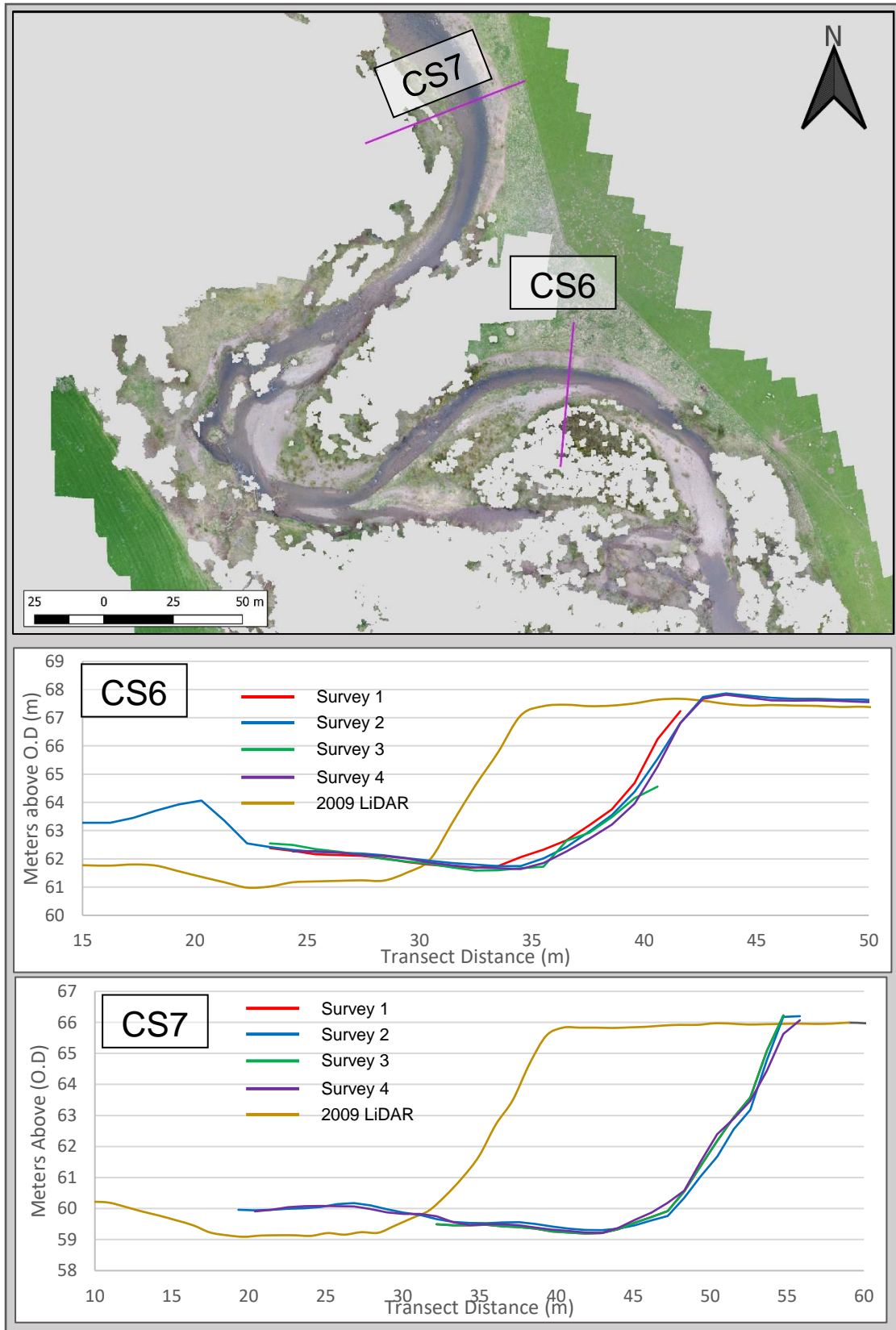


Figure 6.5 – Cross sectional profiles CS6 and CS7

Cross sections CS6 and CS7 are situated in a sinuous section at the downstream end of the study reach and are separated by approximately 1 meander wavelength. The left bank

of the main river channel is occluded by trees and therefore not modelled by UAV data. The steep right bank is however well captured. Consistent with CS2, significant bank retreat is recorded between 2009 and 2016. Approximately 10m at CS6 and 7m at CS7. In contrast to CS2 however is the relative stability of the banks recorded by this project's UAV observations. Only 10cm of bank retreat is detected between Survey 1 and 4 at CS6. The cross sections presented in Figure 6.2Figure 6.5 suggest a general pattern of lateral instability but comparative stability at the river's bed. Lateral evolution is particularly prevalent in zones of high sinuosity, such as in the extreme upstream and downstream ends of the field site. Vertical stability is more consistently recorded throughout the study reach. Vertical evolutions, particularly those recorded between 2009 and Survey 1 (2016) in CS1 and CS4, are the result of lateral migrations of channels, not downcutting. This is validated by the presence of channels in the 2009 data which are not vertically distant from the channel configuration seen from 2016 onwards, and is also supported by comparison of 2009 and 2016 aerial imagery Figure 6.12Figure 6.17.

6.2.2. Planform Evolution

Planform evolutions at Wooler Water manifest primarily as bank adjustment to the incised margin, however there are also internal migrations of sediment bars. Lateral expansion since 2009 has been most prevalent in the upper sections of the study reach, as illustrated by Figure 6.6 and Figure 6.7 and outline the bank extents within the most mobile section, as traced from aerial imagery. A maximum expansion of 23.7m is observed between 2009 and 2018. Also displayed in Figure 6.6 is a cross section (CS2) corresponding to the bank outlines shown. The planform expansion seen between 2009 and 2016 is consistent with a regression toward the historic channel configuration observed pre-1970, as shown by Figure 4.9. The rightward and downstream (northward)

expansion of the incised margin is also synonymous with an attempt by the river to increase sinuosity as a result of an artificial increase to gradient. The section displayed in Figure 6.6 may be considered to show the formation of a proto-meander bend, and as such, a counter bend may be expected to develop immediately downstream. It is predicted that this will manifest as bank erosion to the left bank within the straightened section immediately downstream of point B, where the two sub-channels reconnect. The left bank within this section is however heavily forested and likely stabilised by a dense root network and there is no mapped course since 1860 (Figure 4.8) which extends further left (west) than the present configuration. As such, a leftward expansion may not be expected in the short-term.

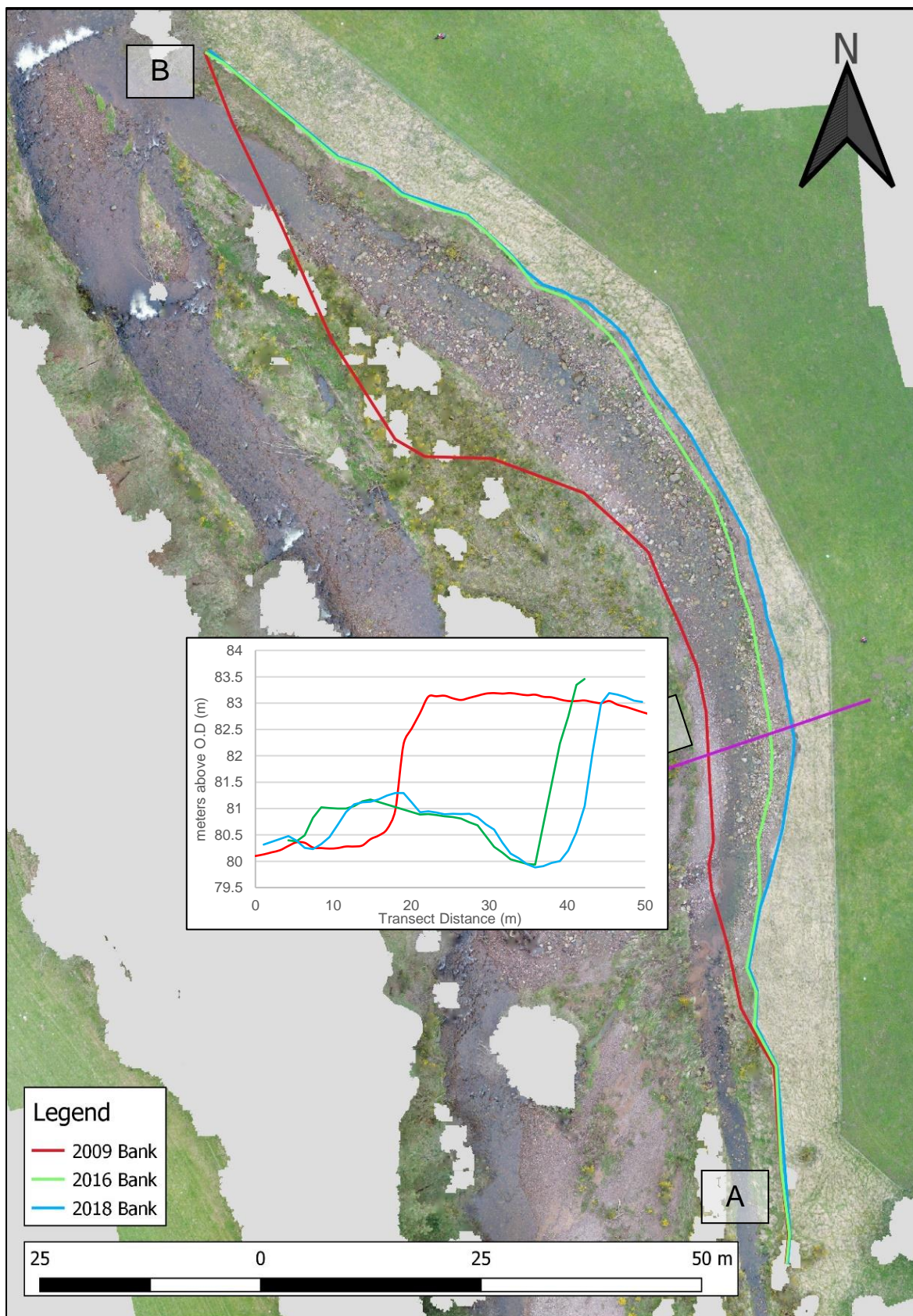


Figure 6.6 – Planform adjustment to the right bank in the proximity of CS2.

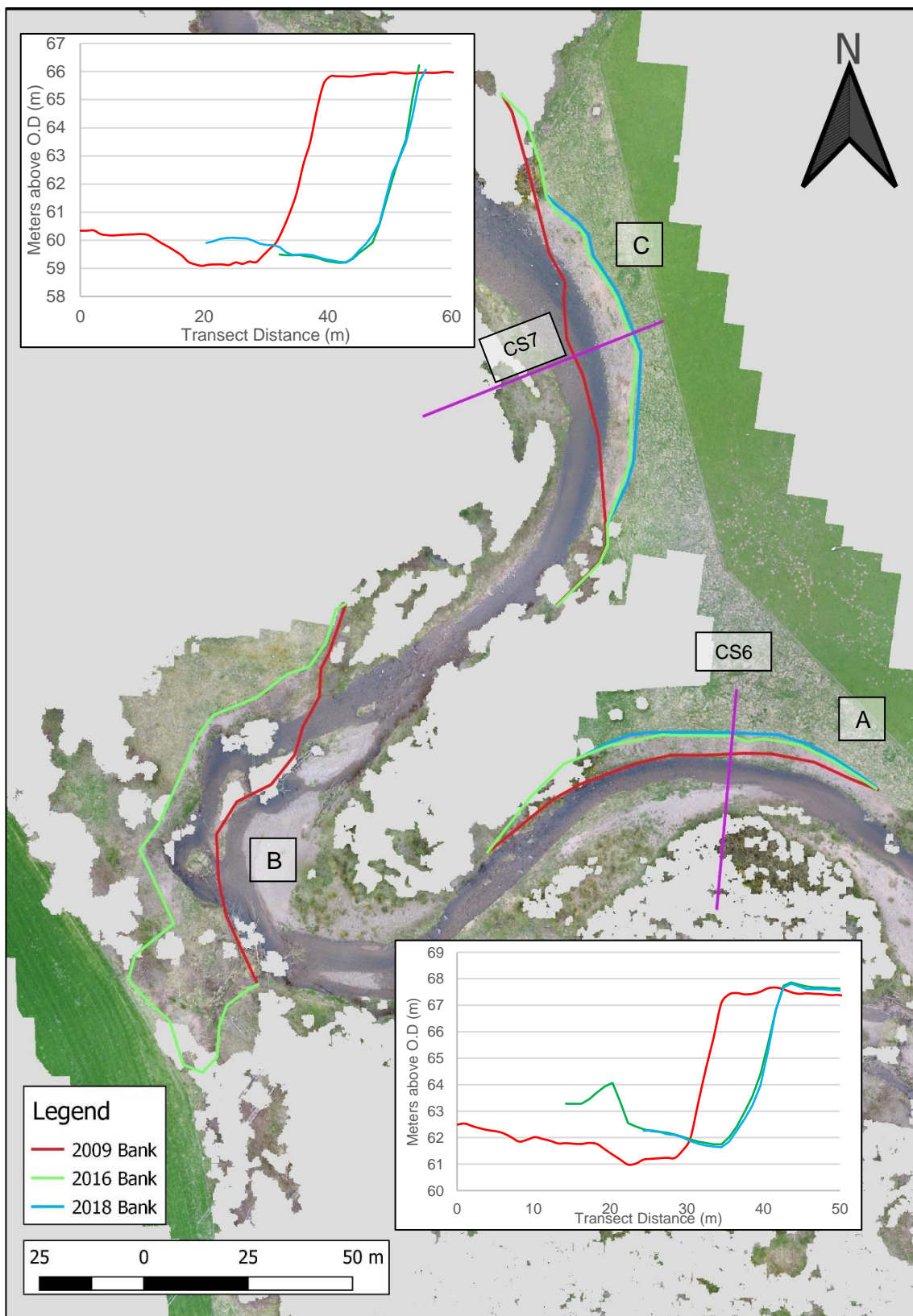


Figure 6.7 – Planform adjustments and bank collapse in the downstream end of the Study Site.

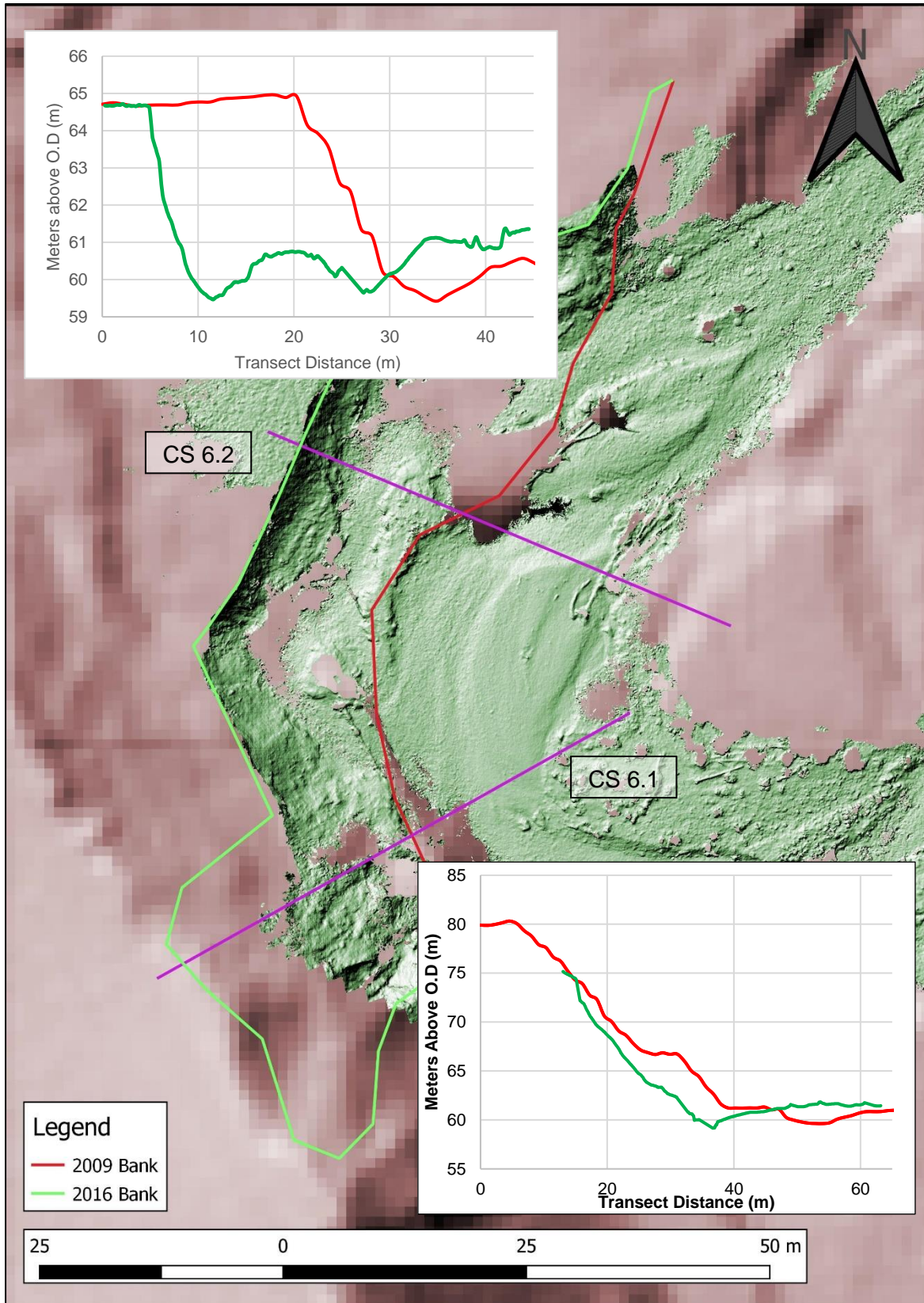


Figure 6.8 – Shaded relief closeup of left bank in the proximity of CS6.

Additional planform adjustment has taken place within the extreme downstream section of the study reach which similarly to the section examined by Figure 6.6, is considerably more sinuous than the rest of the site. These evolutions are examined in Figure 6.7, which includes in-set cross sections for CS6 and CS7. The majority of change is observed to have occurred during the 2009-2016 epoch, where significant lateral expansions via bank collapse have served to increase sinuosity even further. Of particular note is the large bank collapse at the leftmost (west) bend, designated B in Figure 6.7. A more in-depth analysis of this area is given in Figure 6.8, which displays hillshaded DEMs of 2009 LiDAR (red) and 2016 UAV photogrammetry (green). Included in Figure 6.8 are additional cross section profiles; CS 6.1 and CS 6.2. It should be noted that the traced bank extent for 2016 does not match the extent of the 2016 UAV data due to occlusion by trees. The high ground immediately adjacent to the river's left flank is considerably eaten into by the channel resulting in large sections of collapse, likely by undercutting and mass failure. This is particularly evident within the cross sections; CS 6.1 and CS 6.2. The former recording a significant landslip style failure and the later capturing a bank retreat of approximately 15m.

Planform adjustments A and C seen in Figure 6.7 are lesser in magnitude than that observed at the upstream end of the study site. They are however similarly consistent with an attempt by the system to increase in sinuosity. The section examined by Figure 6.7 has no recent mapped history of such a sinuous course. 1860 mapping indicates a relatively straight course which persists until at-least 1970. The significant planform changes post 1970 are coincidental with termination of gravel mining works, which are known to have caused incision and increased gradient (Sear and Archer, 1998).

6.2.3. Gradient Adjustments

Significant longitudinal changes to Wooler Water are recorded by Sear and Archer (1998), who reveal the effect of incision due to gravel extraction upon the river's bed.

Figure 6.9 is a map and long profile of the section immediately upstream from Haugh Head Ford, which was artificially channelized sometime after 1950. A series of 10 weirs

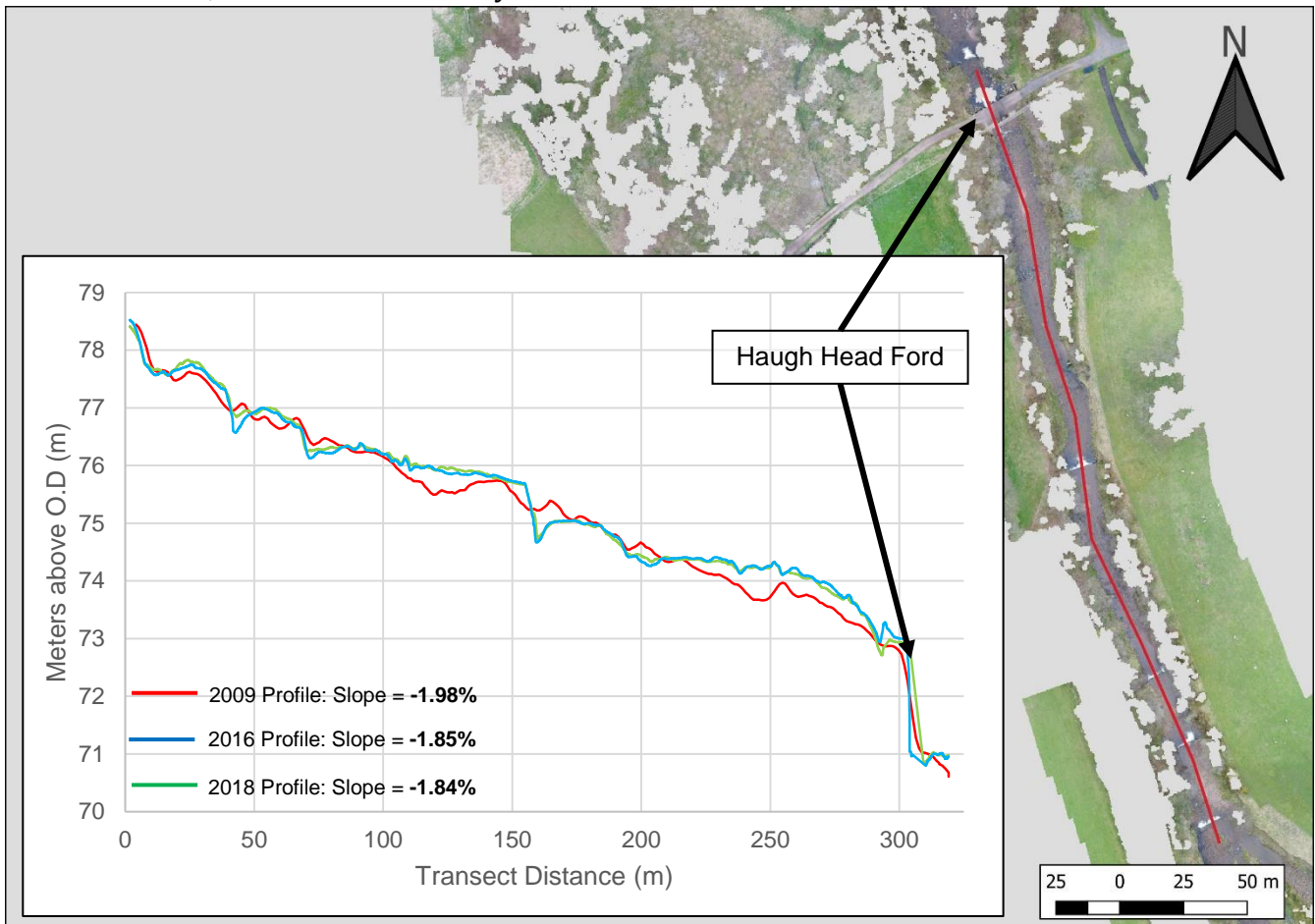


Figure 6.9 – Map and longitudinal profile of the river section leading up to Haugh Head Ford

were installed as part of this work to maintain the straightened course, although many have been buried or destroyed. Four remain visible in Figure 6.9. Overall gradient across the long-profile in Figure 6.9 has decreased by approximately 7% between 2009 and 2018. The majority of this change is observed to occur via aggradation immediately upstream of Haugh Head Ford and approximately midway along the longitudinal profile. Minimal vertical change is observed to occur between 2016 and 2018 (Survey 1 – Survey 4).

6.3. Geomorphic Evolution – Reach Scale Analyses

For analysis at the sub-reach level, clipping was applied to the processed full-scale point clouds to split each Survey into the respective sections illustrated in Figure 6.11. The locations of the splits were chosen based on a compromise between sub-reach size and morphological regime heterogeneity. This aims to minimise the number of sub-sections, and thus processing load, as well as the total level of error variability within respective sub-sections. This produced a total of 24 point-clouds ready for application of the experimental POET correction workflow. In order to gauge the necessary offset factor required, CloudCompare’s “cloud 2 cloud” (C2C) distance tool was employed. This utility functions in a similar way to standard DEM to DEM subtraction for DoD production but is more suited to point cloud data. This produces a scalar field present on the later survey cloud for C2C distance and is represented as a histogram within the program’s interface. C2C additionally was able to detect some points which had been missed during cloud

Table 6.1 – Respective offset factors for each sub-reach when compared to the respective preceding survey.

Applied Translations	A	B	C	D	E	F	Mean
Survey 2	-0.042	0.101	0.140	0.339	0.031	-0.008	0.093
Survey 3	-0.018	0.000	0.051	-0.008	0.117	0.103	0.041
Survey 4	-0.049	-0.050	-0.074	0.010	0.004	-0.037	-0.033

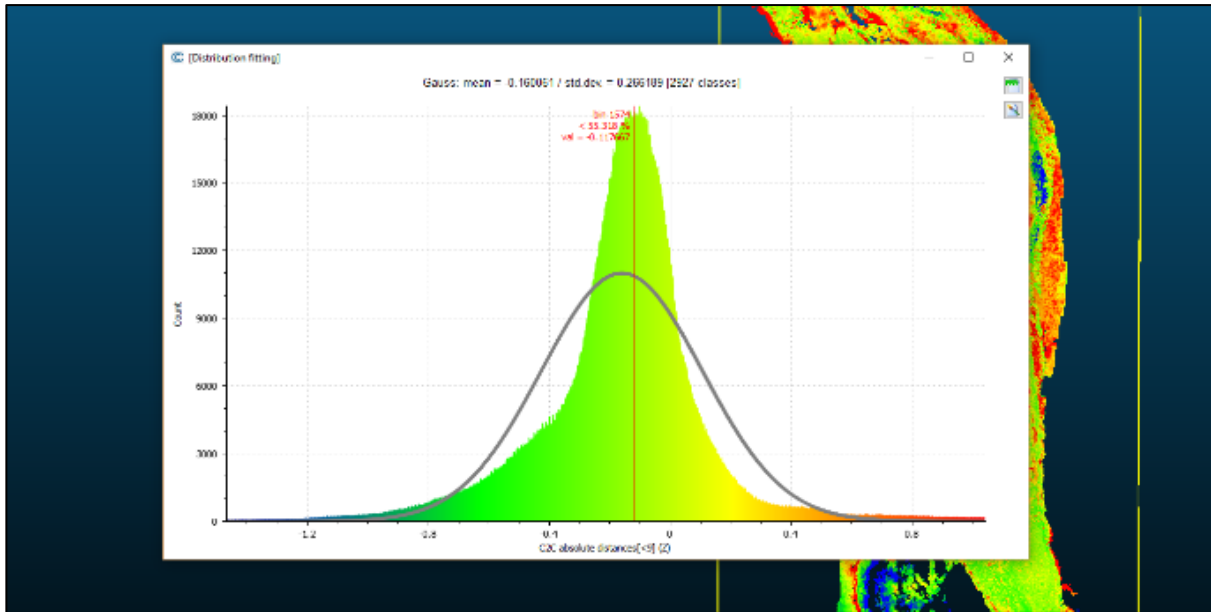


Figure 6.10 – CloudCompare screenshot displaying “cloud of difference” histogram offset.

Reclassification in Agisoft Photoscan and by subsequent SQR filtering in CloudCompare. These detections were characterised by overly extended histogram limbs, with very low frequency, extreme values at the upper and lower numerical extents cloud of difference. These are filtered according to adjustment of the maximum and minimum values within C2C scalar field. Histogram data for clouds of difference is accessible in CloudCompare, whose in-built viewing utility enables quick checking of the peak frequency offset from zero (Figure 6.10). This value is noted, and the inverse applied as a vertical translation to the later Survey’s point cloud. All translation offsets are displayed in Table 6.1

Translative corrections are always applied to the later of the two-point clouds being compared, hence why Survey 1 is not present within Table 6.1. The surface of the earlier of the two surveys always remains. This does however increase the volume of files within the processing archive, requiring a high-level of discipline surrounding folder and file naming and branching. The magnitude of translations is quite variable. A maximum offset translation of +33cm was applied for Sub-reach D when correcting Survey 2 relative to Survey 1. Conversely, Sub-reach B for Survey 3 required no translation.

Figure 6.11 displays the extents of each named sub-reach within the context of the full study site. Each red box outlines the viewport for each sub-reach change map. The viewport for each grouping of maps for each sub-reach have identical coordinate extents. Displayed data possesses similar symbology as in the preceding full site maps, semi-transparent green shading indicating DoD pixels within the limits of the set detection threshold ($\pm 0.1\text{m}$). Blue and red indicative of deposition and erosion respectively. Histogram colouring is unrelated to this shading and is used only for ease of differentiation between Survey lines. Volumetric and areal statistics are presented similarly to the preceding section. Graphical comparisons of volume are presented in Section 6.2.5. It should be noted that for all volumetric comparisons, bed/bank segregation is integrated as it was for the full-scale change analysis. This is intended to provide more intricate data and better insight to geomorphological mechanics at the site.

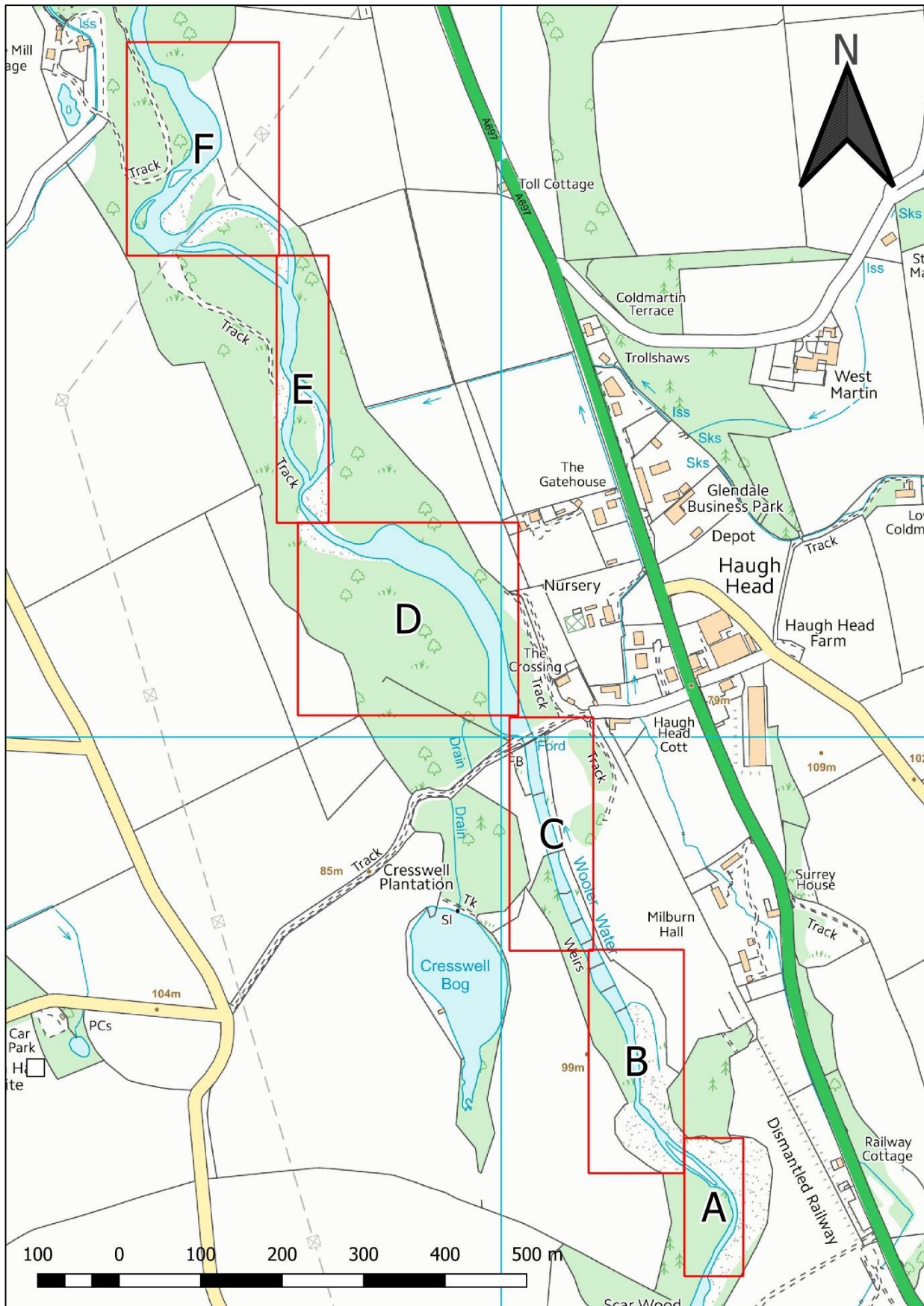


Figure 6.11 – Locations of sub-reach splitting, based on a compromise between size and morphological continuity.

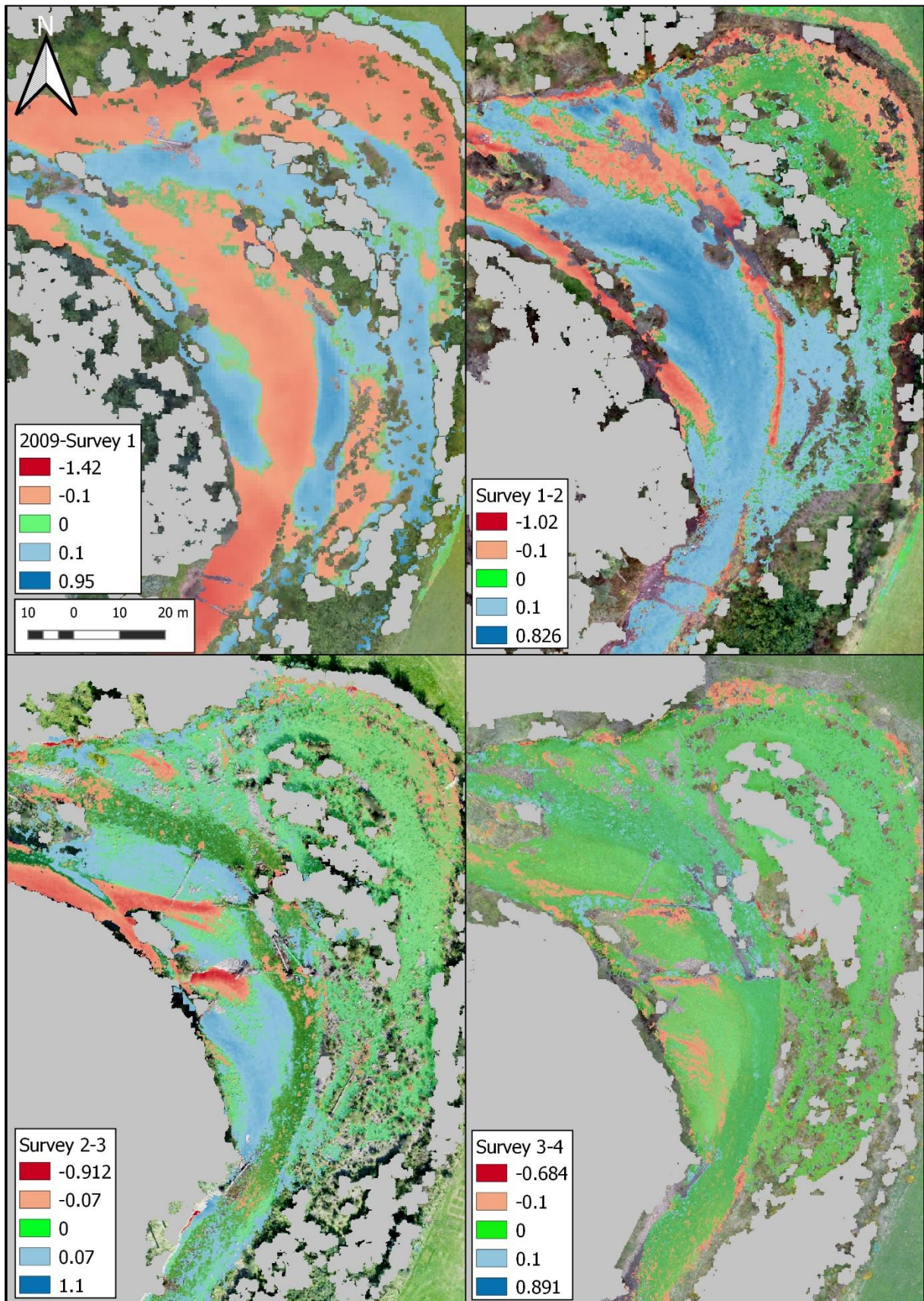


Figure 6.12 – Geomorphic change analyses for Sub-reach A.

Figure 6.12 displays DoD shading for all inter-survey epochs and 2009 LiDAR data vs 2016 UAV data (Survey 1) within Sub-reach A. Important geomorphic developments between 2009 and Survey 1 include the scour within the central channel and outer section of the bend (right bank). Deposition is seen to occur between these two areas of scour, attributable to bar construction. By 2016, this bar is vegetated and seen to be stabilised. Significant deposition is recorded between Survey 1 and 2 in the form of a bar which extends into the main channel previously excavated during the 2009-2016 epoch. A degree of deepening is seen within the main sub-channel is seen, but perhaps not as much as might be expected, considering the relative narrowing caused by extension of the bar. This may be explained by the appearance of a secondary relief channel near the left bank, diverting energy from the aforementioned channel. This constructed bar is then actioned upon by woody debris mechanics between Surveys 2 and 3, when a number of tree trunks are deposited. 6 tree sized logs are present, spread between the primary wetted channel and atop the gravel bar. At least two of the logs are orientated perpendicular to the flow. The DoD records scour just upstream of these LWD well. A deepening of approximately 70-90cm is seen. Not all LWD items are observed to have caused significant scour however, revealing the possible timescale over which they were deposited. The LWD associated scour observed is consistent with Bilby and Ward, (1989). These debris are seen to cause scour on their upstream side, potentially triggering the formation of a chute or cut-off channel adjacent to the left bank. For Survey3-4 geomorphic change is less extensive; the constructed bar appears fairly static, however a slight amount of action is present surround LWD. Common to all DoD of sub-reach A is the relative stability of the area near the right bank, which is vegetated primarily by gorse bushes. This area is somewhat vertically disconnected, thus requires exceedingly high flow to be worked upon.

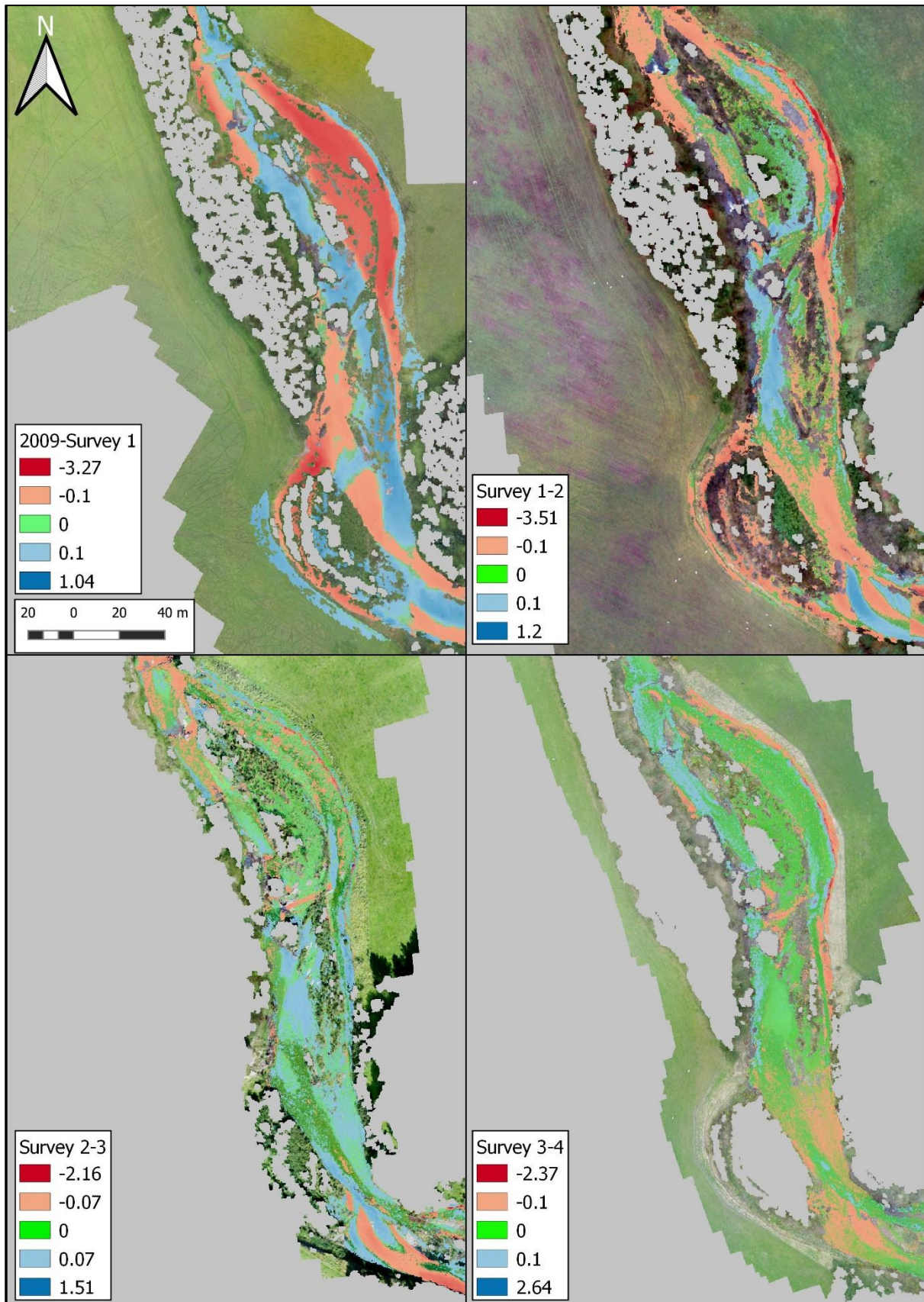


Figure 6.13– Geomorphic change analyses for Sub-reach B.

Figure 6.13 illustrates geomorphic changes between 2009 and 2016, and for all inter-survey epochs at Sub-reach B. The most significant changes seen between 2009 and 2016 include the departure of the river channel from its straight course to a more sinuous pattern. Large sections of the left and right banks are eroded, widening the main incised margin by approximately 20m. This occurs in tandem with aggradation within the straighter section of the channel. Sub-reach B represents one of the most active sections of the study site. The incised channel margins within this section are intermediately sinuous ($SI=1.29$), indicative of embryonic meander formation. The primary wetted channel runs centrally however, with minimal lateral deviation. Auxiliary channels are present at the margins of the incised channel, one within the upstream half of the sub-reach, and the other in the downstream half. The upstream sub-channel is vertically disparate from the primary wetted channel, being above and set into the naturally higher ground that dominates the left floodplain in this section. The sub-channel within the downstream half of this section however is vertically below the central channel by approximately 0.3m. This channel is initiated near the upstream limits of sub-reach B practically adjacent to the right bank. It is segregated from the primary wetted channel by a fairly well vegetated gravel bar, approximately 3m in width. This leads to a lower discharge within the auxiliary channel despite being vertically lower than the main.

The pre-2016 pattern of bank erosion is mirrored between Surveys 1 and 2, albeit at a lesser magnitude. A vegetated bar now separates two sub-channels, the left occupying the river's pre-2009 course, the right extending up to the right bank of the incised margin. Some bar construction is recorded near the left bank, approximately central within subsection B, as well as at the southern extent of Figure 6.13. These bars are seen to migrate or be reworked between Survey 2 and 3. Additional construction to the "central" bar is

also recorded. Bank erosion is more limited for this epoch, although some widening is recorded near the northern extent of the right bank. Increased bank erosion is however recorded between Survey 3 and 4. In addition, some bed scour is captured within the southern section of the reach. Mild deposition is seen to occur within the left channel near the northern extent of sub-reach B. The general pattern of evolution of this section may be described by slight deposition within the central channel, limited vertical scour within the auxiliary channel, and aggressive lateral action on the right bank of the incised margin. The main and auxiliary channels are punctuated by vegetated areas, which mostly persist throughout the field campaign, indicating vertical stability in-between the two channels.

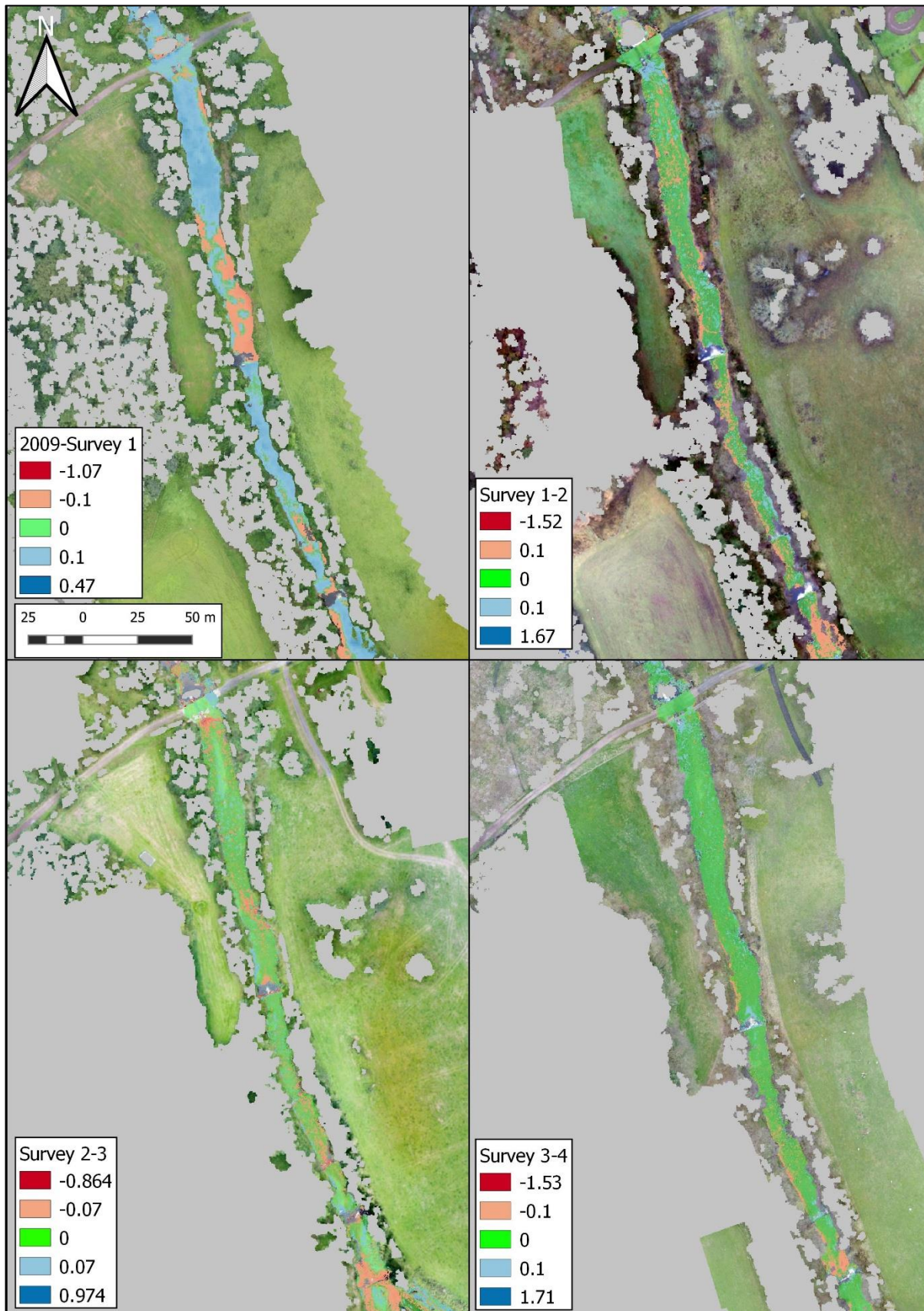


Figure 6.14– Geomorphic change analyses for Sub-reach C.

The maps within Figure 6.14 (Sub-reach C) show less geomorphic evolution than previous sub-reaches due to the straight nature of the river in this section. An amount of vertical change is however recorded between 2009 and Survey 1 (2016). Such change primarily consists of deposition of depth up to 0.47m, however some scour is recorded immediately downstream of one of the weirs. Sub-reach C is the most stable section of the study site, containing several weirs. These structures were installed circa. 1950 (Ordnance Survey, 2018) for course maintenance following channelization to halt encroachment on a nearby rail line, now disused. The weirs are no longer maintained and are becoming either degraded, outflanked, or buried as is the case for those within Sub-reach B (Figure 4.7). Geomorphic activity within this sub-reach is limited to movement of specific large clasts and boulders, rather than channel mobility. The relative stability within this sub-reach is reflected within all inter-survey DoD section. Approximately 80-90% of the entire channel area remains stable for this Sub-reach.

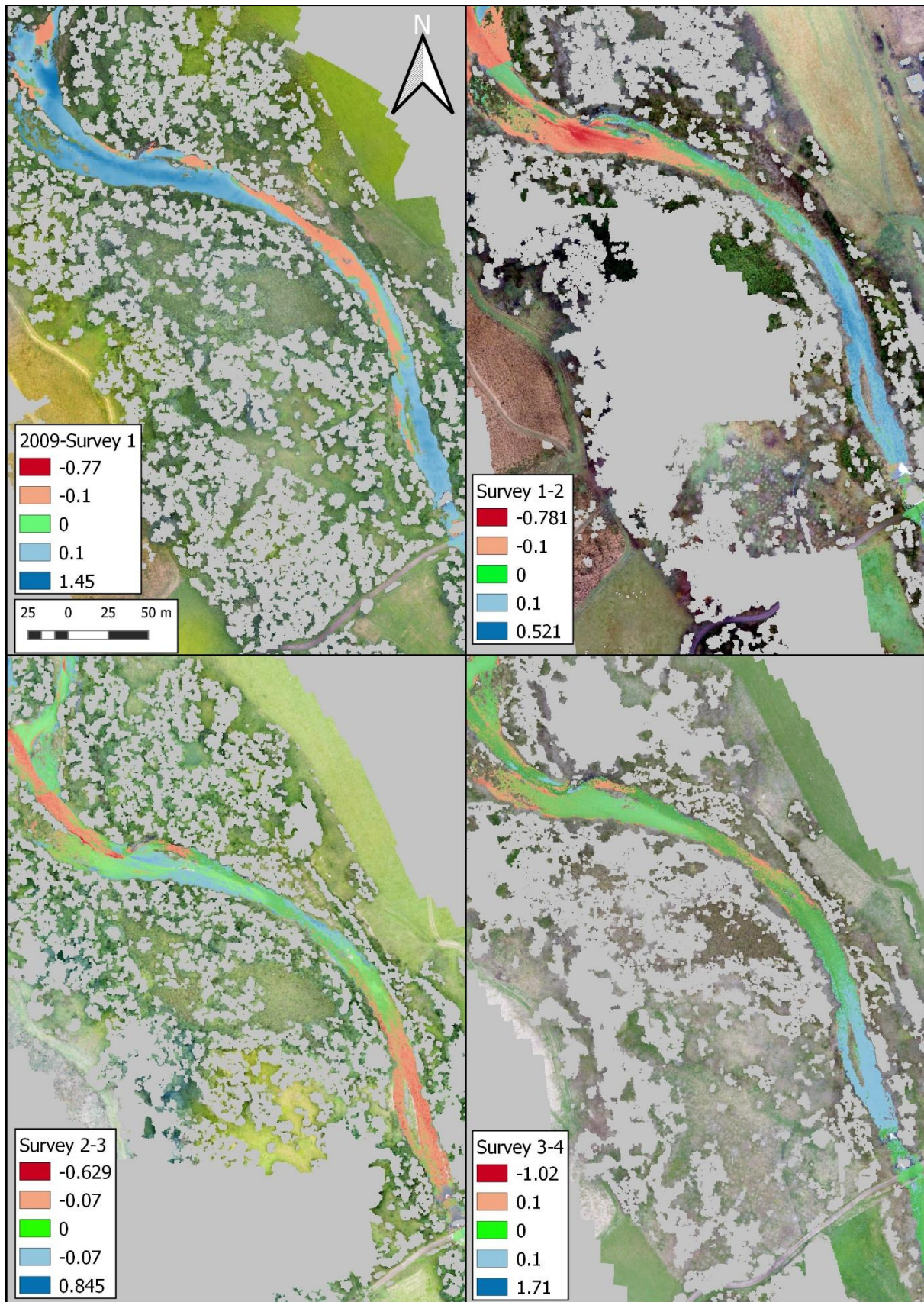


Figure 6.15 – Geomorphic change analyses for Sub-reach D.

Geomorphic changes within Sub-reach D (shown in Figure 6.15) between 2009 and 2016 include significant deposition to the main channel, which takes a single threaded form in Sub-reach D. This deposition is then largely “undone” between UAV survey’s 1 and 2, where erosive action appears to occur. This is however countered by additional depositional activity at the upstream (southern) end of the reach, immediately downstream of Haugh Head Ford. Further alternations of erosion and deposition are recorded between Survey 2 and 4 within this section of Sub-reach D. The rest of the reach remains relatively stable, except for some erosion a near the downstream limits of Figure 6.15 between Survey 2 and 3.

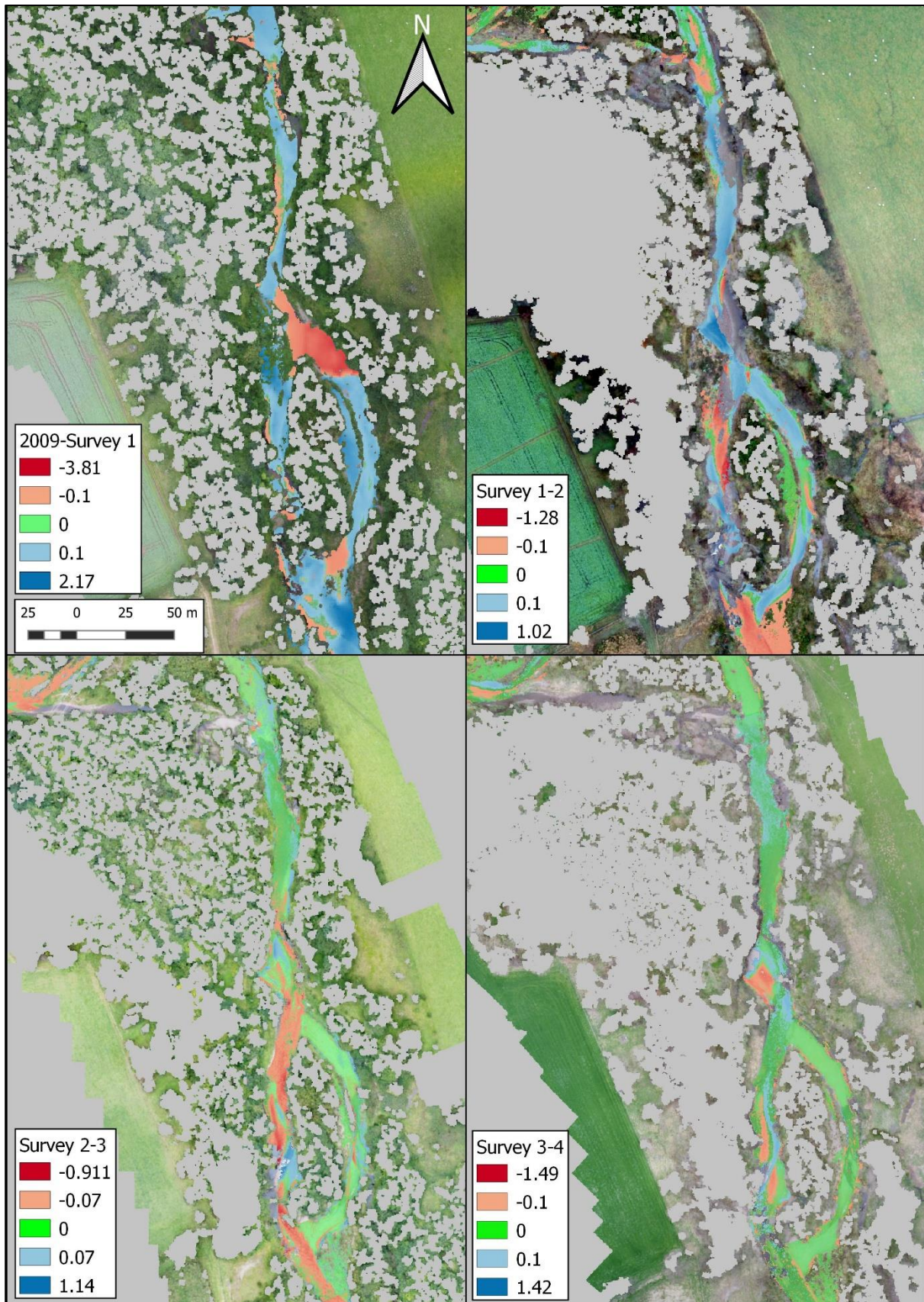


Figure 6.16 – Geomorphic change analyses for Sub-reach E.

Figure 6.16 maps geomorphic changes in Sub-reach E. 2009 to 2016 (Survey 1) is characterised by extensive deposition within the channel, however an amount of erosion reflecting channel avulsion is present. The erosion detected records the widening of the incised margin, possibly due to bank collapse under high flow conditions. The full extent of the bank collapse cannot be directly compared as the UAV survey methodology cannot penetrate the vegetation canopy which dominates this sub-reach of the field site. The twin channels created by this widening persist throughout this projects field observations, however there is a degree of re-working and internal action. Erosion and deposition, attributable to bar migration are observed between survey 1 and 2, erosive conditions dominating in the left channel and deposition occurring primarily in the right. The right channel remains stable for the remainder of this study's field observations however the left channel continues to undergo bed scouring. Bar migration patterns are observed in the left channel between Survey 3 and 4. Sub-reaches D and E represent a transition to a more stable state than upstream sections, being primarily single threaded with densely vegetated margins. Channel divergence is seen in places, punctuated by well vegetated bars/islands. Geomorphic patterns within these sub-reaches include deposition just downstream of Haugh Head Ford, accompanied by proximal erosion downstream. In sub-reach E, preference for flow within the left-hand channel where divergence occurs appears, likely attributable to the creation of a gravel bar at the mouth of the right channel, potentially restricting flow.

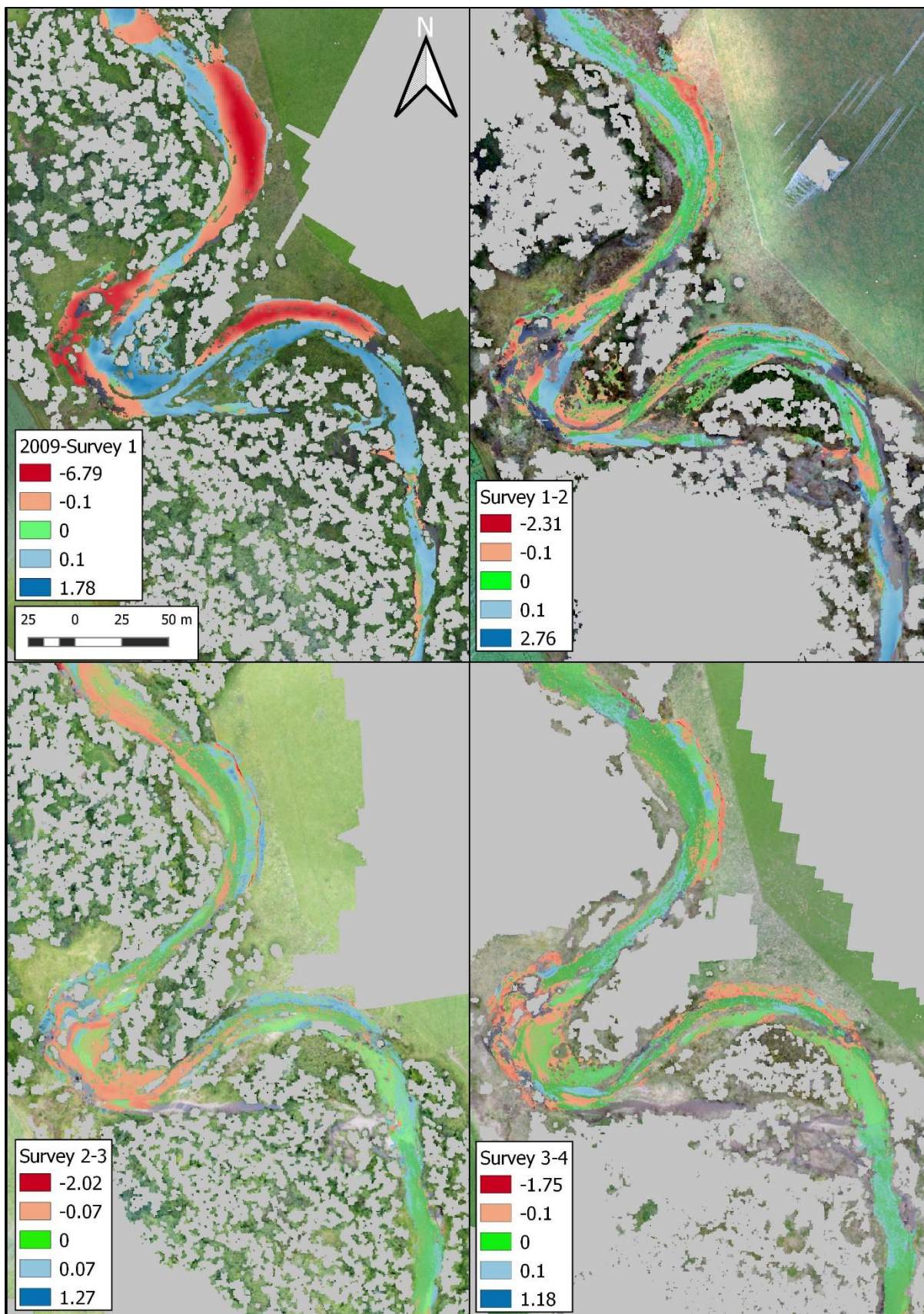


Figure 6.17 – Geomorphic change analyses for Sub-reach F.

Figure 6.17 illustrates geomorphic changes within Sub-reach F, which is the downstream extent of this project's data collection. The 2009 – Survey 1 epoch is characterised by significant bank erosion and widening of the incised margin. These widening actions are additionally analysed in Figure 6.7 and Figure 6.8. This is coupled with extensive deposition on the river's bed. Widening action between Survey 1 and 2 is more modest but still underway. The river bed is mostly stable during this epoch, however some bar mechanics manifesting as patterns of erosion and deposition are present within the westmost bend of Sub-reach F. This bend continues to see the majority of geomorphic change for the rest of this project's observations. Bars constructed during the Survey 1-2 epoch are reworked between Survey 2 and 3, whilst some bank collapse and material storage is observed in the Survey 3-4 epoch. Sub-reach F is the downstream extent of the UAV survey and sees conditions more similar to the sinuous upstream reaches. Bank gradients within sub-reach F are less extreme, unlike in Sub-Reach B where banks are vertical or overhang. This shallower gradient enables material failing under gravity at the very top of the bank to remain and "sit" partway up. This is visible within the DoD figures, as red at the extreme margins of the bank and blue adjacent to the wetted channel.

6.3.1. Error Considerations and implications

Geomorphic change detection analyses are sensitive to survey errors, thus careful consideration must be given to ensure reliability of volumetric calculations and change maps. Minimum level of detection (LOD) thresholding is used by this project's DEM comparisons. The threshold of detection is defined by the square root of the sum of each survey's maximum Z error (given in Table 4.1) squared:

Equation 6.1

$$LOD_{(min)} = \sqrt{\delta Z_1^2 + \delta Z_2^2}$$

Table 6.2 - LODs and net propagated error in volume calculations for inter-survey epochs.

Inter-survey epoch	Minimum LOD Threshold (m)	Propagated Erosion Volume Error	Propagated Deposition Volume Error
Survey 1-2	0.106	24%	35%
Survey 2-3	0.072	31%	32%
Survey 3-4	0.098	36%	63%

The minimum LOD values given by Table 6.2 define the threshold for detection of geomorphic changes differentiating between vertical differences which can be ruled out due to DEM error and those which reflect valid geomorphic evolution. DoD cells which do not exceed the minimum LOD are not used in volumetric analyses for sediment budgeting and are not displayed as erosion or deposition on geomorphic change maps (Figure 6.12 Figure 6.17). For inter-survey epochs 1-2 and 2-3 an LOD of approximately ± 10 cm calculated, for Survey 2-3, a threshold of approximately ± 7 cm is used. The scale of these thresholds is low enough that moderate bed adjustments, bar evolutions and bank erosion are capturable. Margins of bar formations and the mobility of individual clasts smaller than the threshold are however undetectable through DEM comparison. The implication that the edges of bars or material movement might not be detected is an apparent drawback of the UAV surveying methodology. The loss of fine scale geomorphic change to noise is unavoidable if minimum LOD thresholding is used, however this is only the case for elevation data. The provision of secondary data outputs such as high resolution orthmosaic imagery aid detection and interpretation of geomorphic changes. It should also be noted that survey timing may affect the amount of detectable changes. In the event of a scour or fill event which is then neutralised by countering deposition or erosion, recorded volumetric change would be zero, despite geomorphic evolution

having occurred. Such action is however likely to be limited to special cases, such as LWD inclusions.

Table 6.2 also includes the calculated propagated error within volumetric calculations for sediment budgeting. The values are calculated by multiplication of the propagated error (also minimum LOD threshold) with the total area of DoD cells which exceed that value (positively in the case of deposition, negatively in the case of erosion) to attain an error volume for erosion and deposition components. The final propagated volume error is the propagation of either the erosion or depositional error volume as a percentage of the complete volume for the negative or positive component respectively. These propagated errors are manifested as error bars on sediment budget graphs, reflecting the percentage of volume which may or may not be attributable to survey error. The variable nature of the propagated error is attributable to the large range of change volumes observed between surveys. Volumetric error is higher for epoch 3-4 than 1-2 despite the LOD being lower since the average depth of change is significantly smaller relative to the detection threshold. This is an example of the one of the drawbacks of the UAV surveying methodology, that for even for surveys of decent accuracy, signal cannot be differentiated from noise below a certain threshold. Such a disadvantage is however common to all landscape surveying methods and can be mitigated by improvements to instruments and processing techniques.

6.3.2. Budget Segregation

Raw change alone limits the amount of spatial intricacy accessible to users. Understanding the geomorphic origins and contexts of sedimentary flux is particularly important when analysing fluvial systems at the scales utilised here. The near vertical 5m high banks at the site, particularly those in sub-reach B and F present an enormous potential source of sediment if laterally eroded. The high-resolution data afforded by the

UAV enables precise volumetric segregation of material lost from the rivers banks vs that which is eroded from the bed of the river. Significant ($\pm 0.2\text{m}$) erosion is spatially segregated into that which occurs from the banks of the incised margin and that which occurs within the riverbed itself. This was done by applying a masking polygon to the specific banks identified to be undergoing mass wasting, namely within sub-reach B and F. The masking polygons were then used to query the DoD pixel values, allowing for calculation of volumetric statistics, independent of the rest of the model. Segregation results are presented within the volumetric and areal statistics section pertaining to the analysis of geomorphic change at the full reach scale.

6.3.3. Sediment Budget - Volumetric Statistics

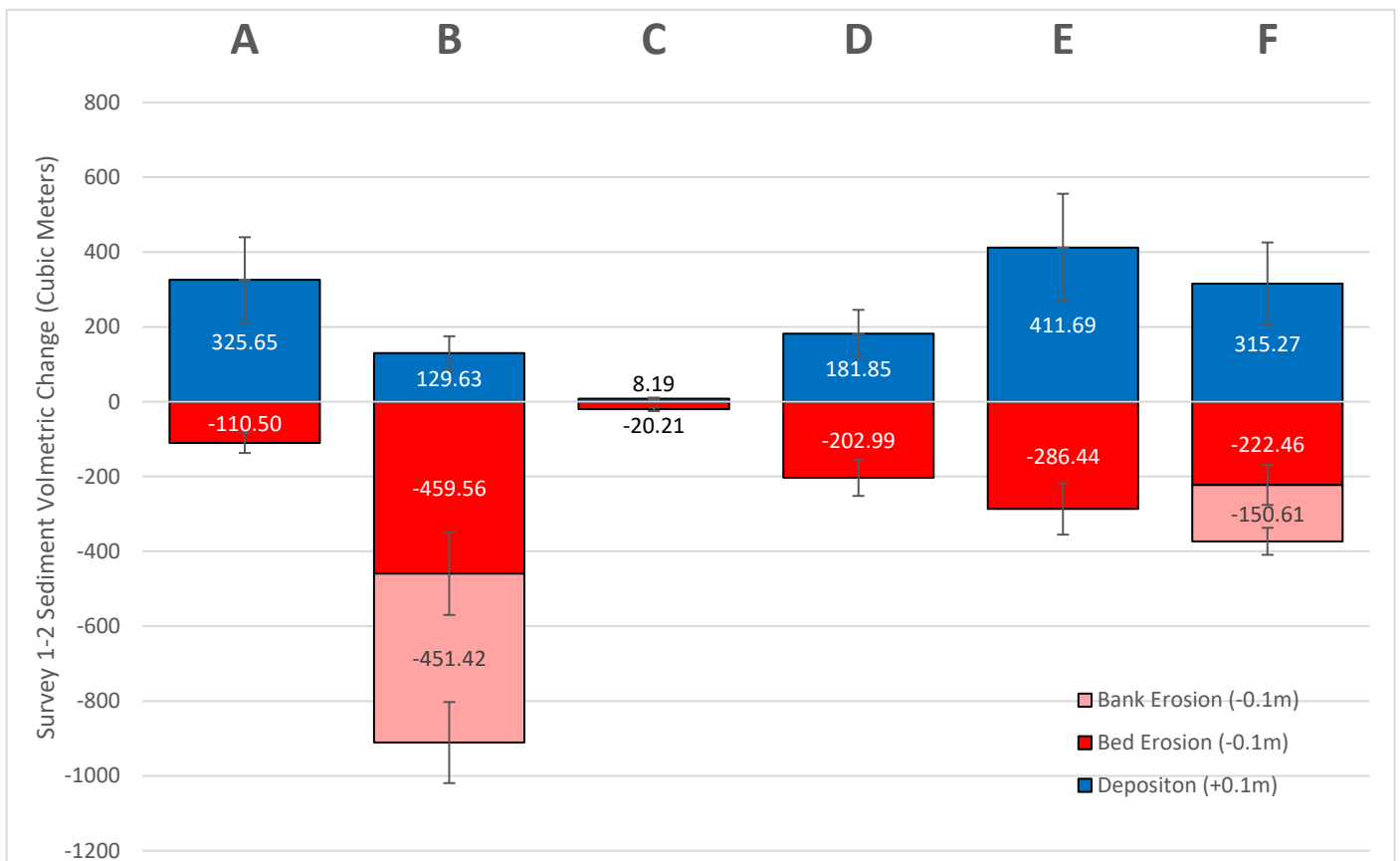


Figure 6.18 - Bed/bank segregated volumetric statistics for Survey 1-2.

Figure 6.18 - Bed/bank segregated volumetric statistics for Survey 1-2. displays volumetric change for the Survey 1-2 epoch. Most erosion is seen to occur within sub-

reach B, where bank material loss accounts for nearly half of all negative volume loss. Erosion in other reaches is more equal to deposition, however sub-reach A has a dominantly positive sediment budget. Inspection of Figure 6.12 reveals this is likely due to the creation of a large bar which extends into the channel. Minimal volumetric change activity is observed in sub-reach C, which is consistent with change mapping. Sub-reaches D-F are more balanced in terms of volumetric change; however, bank collapse does make a significant contribution to erosion in sub-reach F, ultimately tipping the budget to a negative regime.

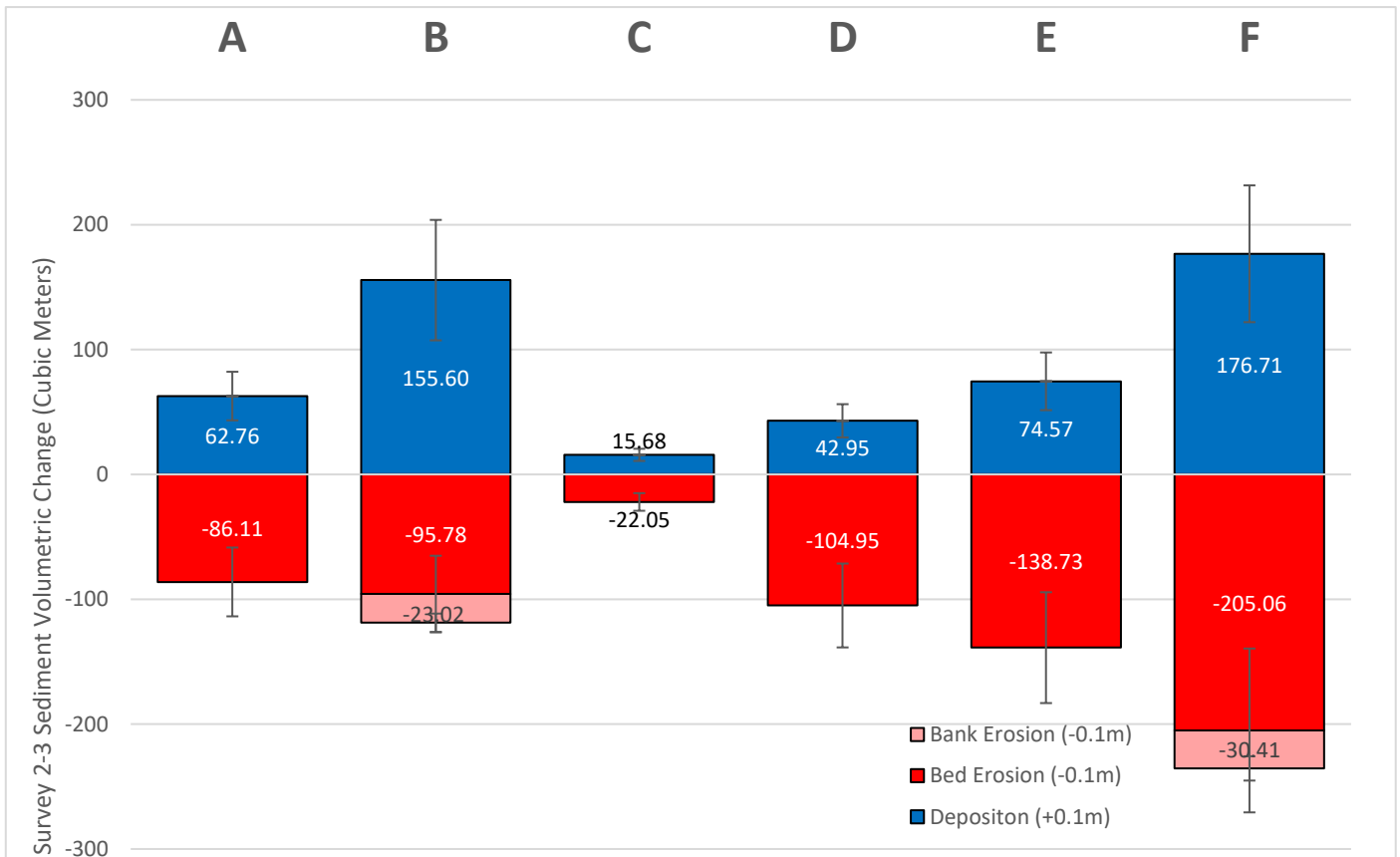


Figure 6.19 - Bed/bank segregated volumetric statistics for Survey 2-3.

Volumetric change presented in Figure 6.19 (Survey 2-3) is overall more conservative than that in Figure 6.18. The previously most negative sub-reach, (sub-reach B) is now net-positive. Bar construction and reduced bank collapse activity observed in Figure 6.13 are the cause of this. Much of the erosion in sub-reach A is attributable to scour activity

triggered by introduction of woody debris atop the bar constructed during the Survey 1-2 epoch. Erosion appears to dominate in sub-reaches D-E and there is evidence for some bed scouring in change mapping. Bank losses are significantly reduced in sub-reach F however.

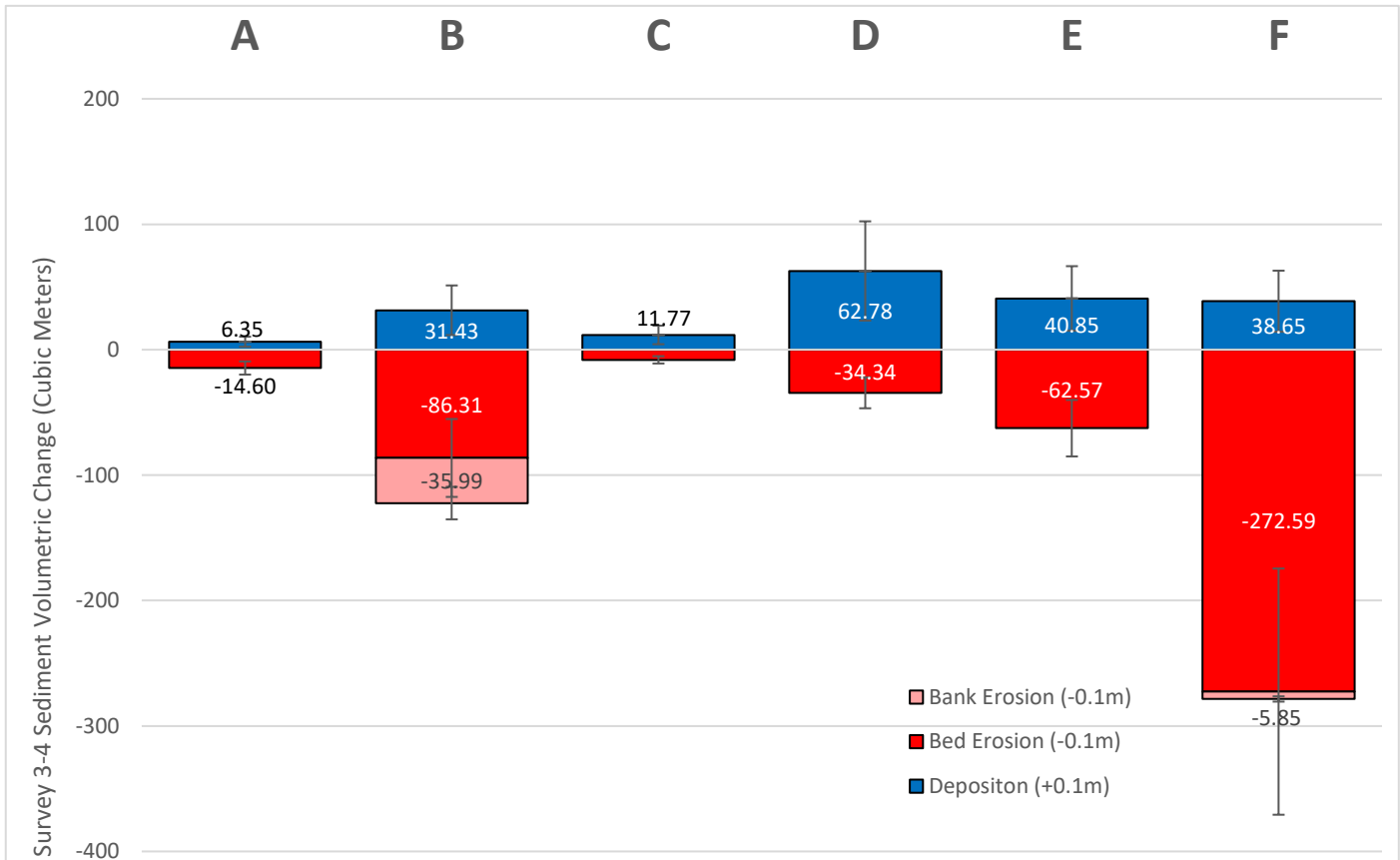


Figure 6.20 - Bed/bank segregated volumetric statistics for Survey 3-4.

Figure 6.20 outlines volumetric changes for the Survey 3-4 epoch. The overall magnitude of change is lower than shown by Figure 6.18 and Figure 6.19. Sub-reach A is particularly static. Similarly, sub-reach C also seen to undergo relatively little volumetric change. The negative budget of sub-reach B is attributable to the reworking of bed material and some bank collapse activity. Such bank collapse may be due to sub-areal processes, particularly if previous flows have served to undercut and destabilize the margins of the incised channel. The largely negative sediment budget of sub-reach F may be attributed to the

loss of material from the bed by scour induced by woody debris falling into the channel.

A portion of erosion in sub-reach F may be linked to bank losses by sub-areal processes.

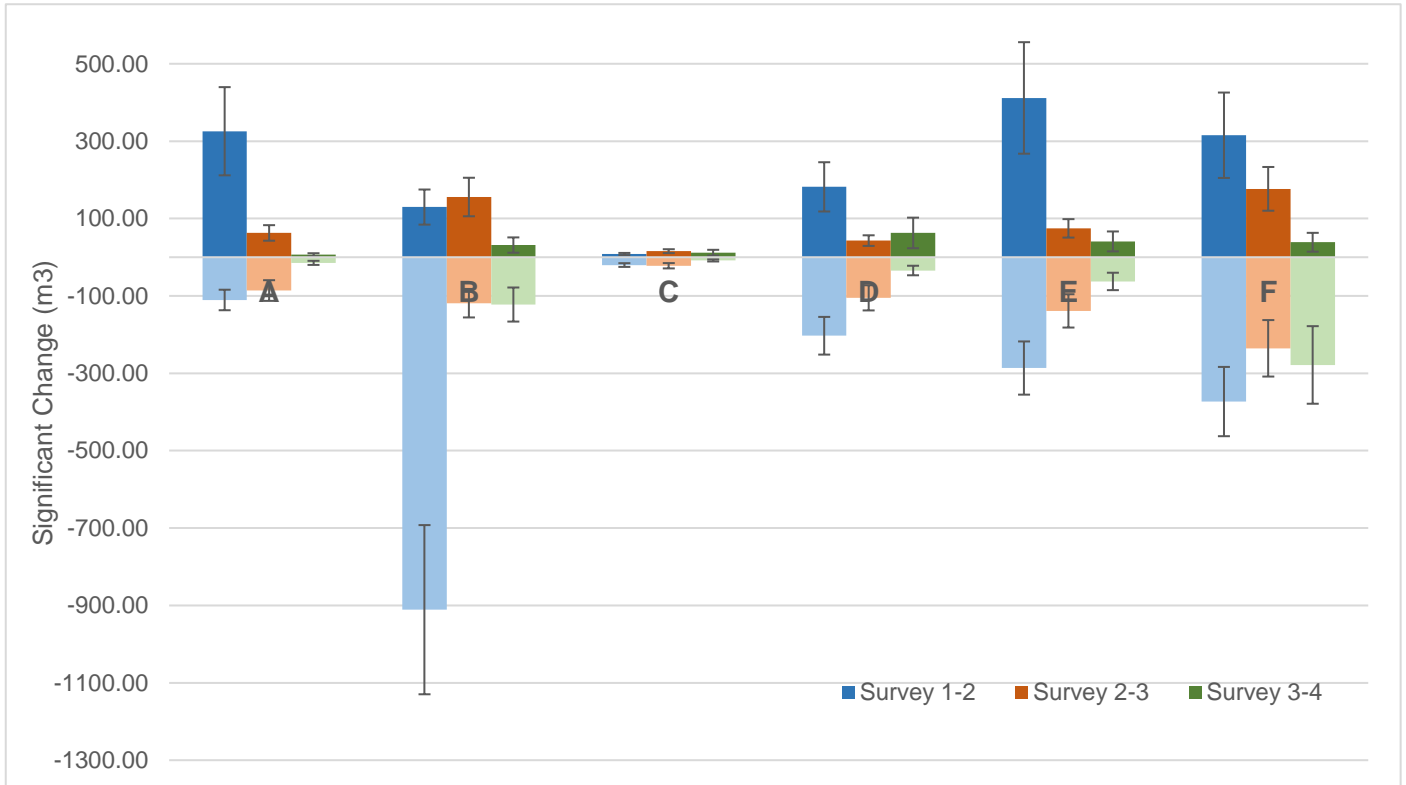


Figure 6.21 – Total volumetric comparison for all inter-survey periods. Lighter shading represents erosion.

Overall comparison of sediment budgets for all sub-reaches and epochs reveal the variability of geomorphic change over both time and space. Sub-reach B most prevalently losing mass between Surveys 1 and 2 at a scale unlike the other sections of the study site. Figure 6.13 maps significant bank collapse and widening at the right bank and Figure 6.18 accounts for nearly half of all eroded material being sourced from that bank. This strongly suggests that the incised margin of the river is responsible for much of the geomorphic dynamism at Wooler Water, especially in its upper section. Significant depositional activity is also revealed during the survey 1-2 epoch, especially in sub-reaches A and B.

6.3.4. Sediment Budget - Area Statistics

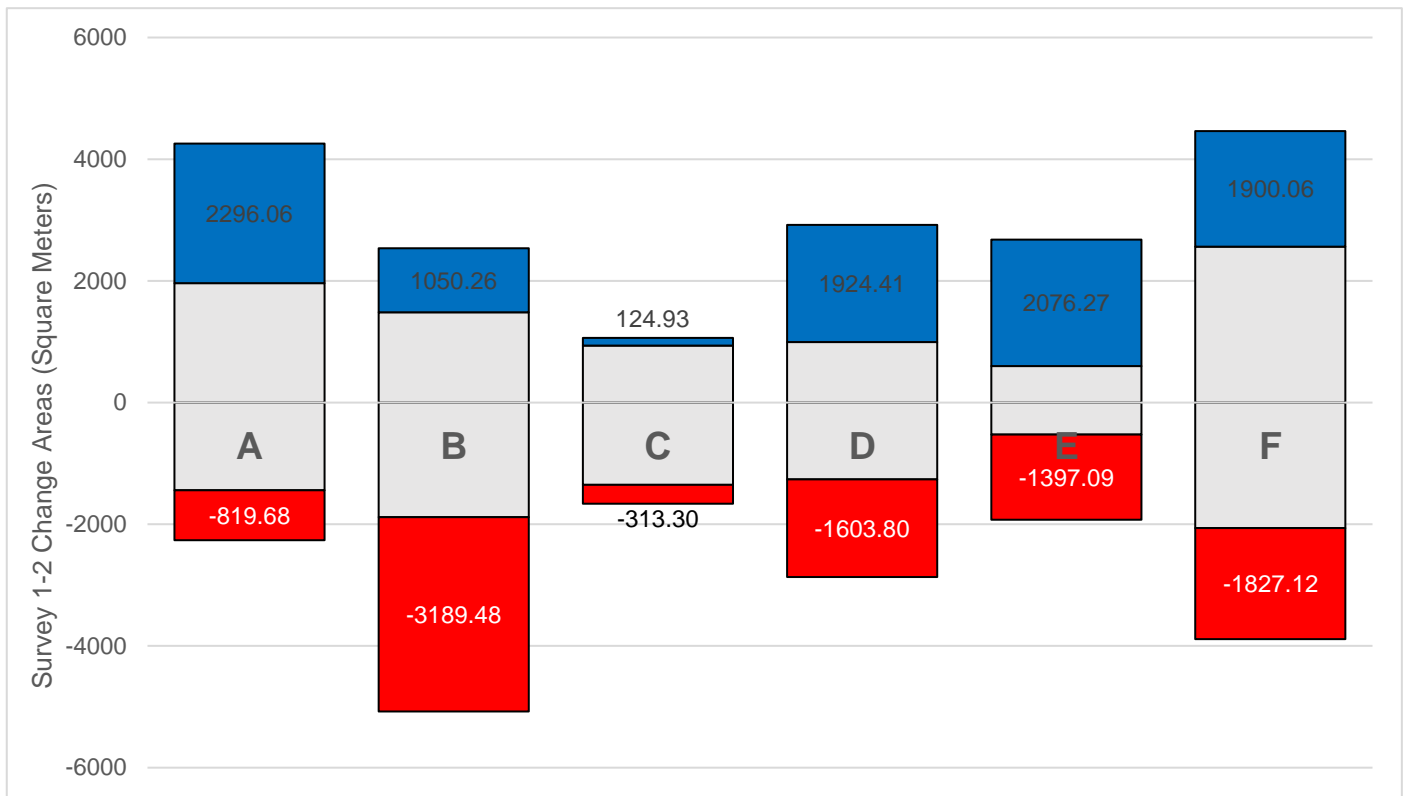


Figure 6.22 – Area statistics for erosion (red), stability (grey) and deposition (blue) between Surveys 1 and 2.

Figure 6.22 graphically compares the total area of ground within each sub-reach which is subject to deposition, erosion, or no detectable change between Surveys 1 and 2. By area, the largest portion of erosion is seen to occur in sub-reach B. This reach also sees the largest volume loss as supported by Figure 6.18. The majority of cells compared for sub-reaches A, D and E are seen to be depositional in nature, however the depth of this deposition varies. In sub-reach A, the majority of depositional area is attributable to the construction of a large bar. However, for sub-reaches D and E, general bed deposition appears to be more the cause. Sub-reach F is the most stable by area for the Survey 1-2 epoch, however it is the second most erosive by volume, as indicated by Figure 6.18. Erosion within this sub-reach must therefore be relatively deep, indicative of bank collapse activity.

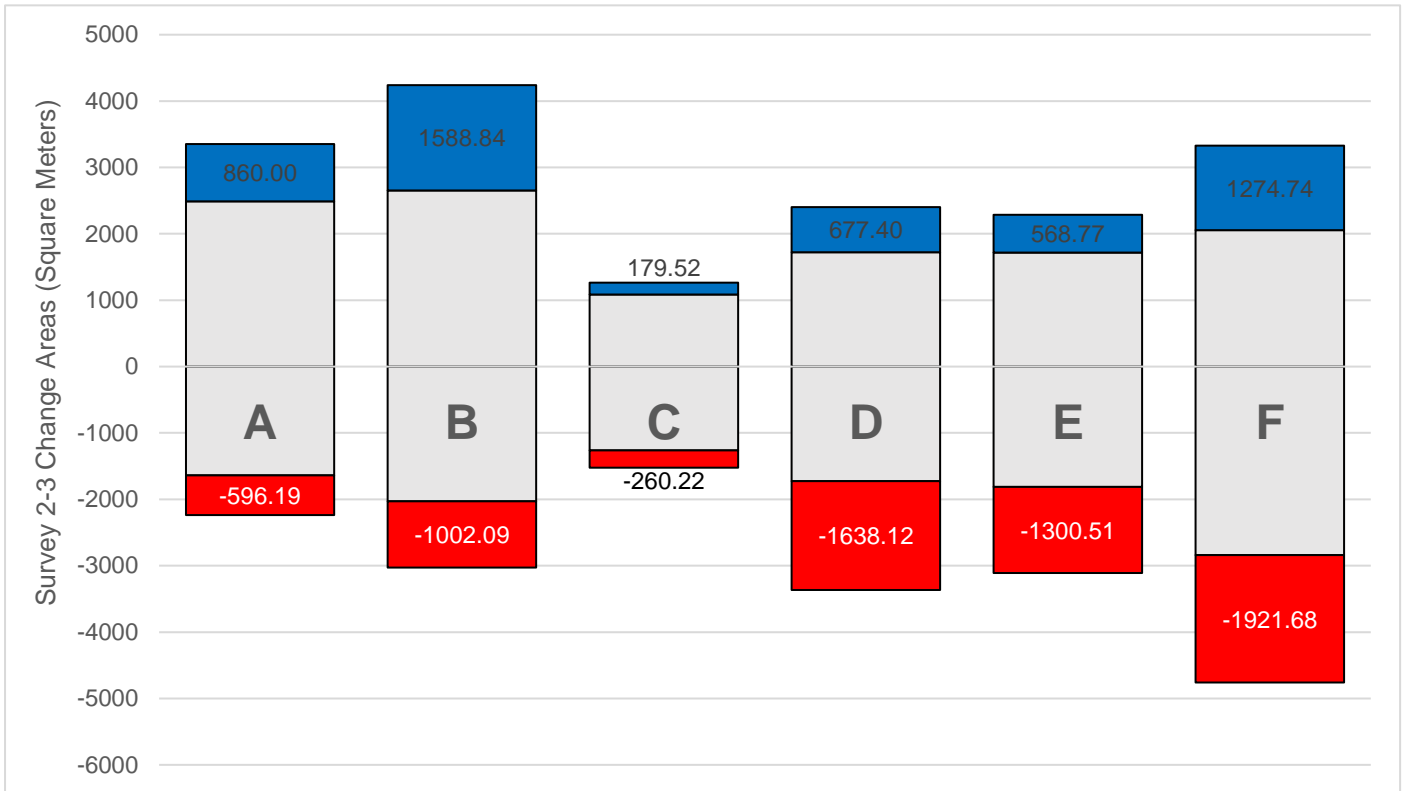


Figure 6.23 - Area statistics for erosion (red), stability (grey) and deposition (blue) between Surveys 2 and 3.

Figure 6.23 compares the areas of positive, negative and neutral geomorphic change between Surveys 2 and 3. Stability is more dominant than in Figure 6.22 (survey 1-2) which agrees with the more conservative rate of geomorphic change for this period. For sub-reach A, deposition is seen to occur over a larger area than erosion, despite the section having a net-negative sediment budget. This is attributable to the role of woody debris which had been deposited following Survey 2, causing acute scour. Bar construction continues as normal just upstream however, thus accounting for the larger area of deposition. Sub-reach B deposition dominant by area, as well as by volume in-contrast to sub-reach A. Bed aggradation and limited bank collapse are similarly the cause of this. Erosional area outweighs depositional area for sub-reaches D to F.

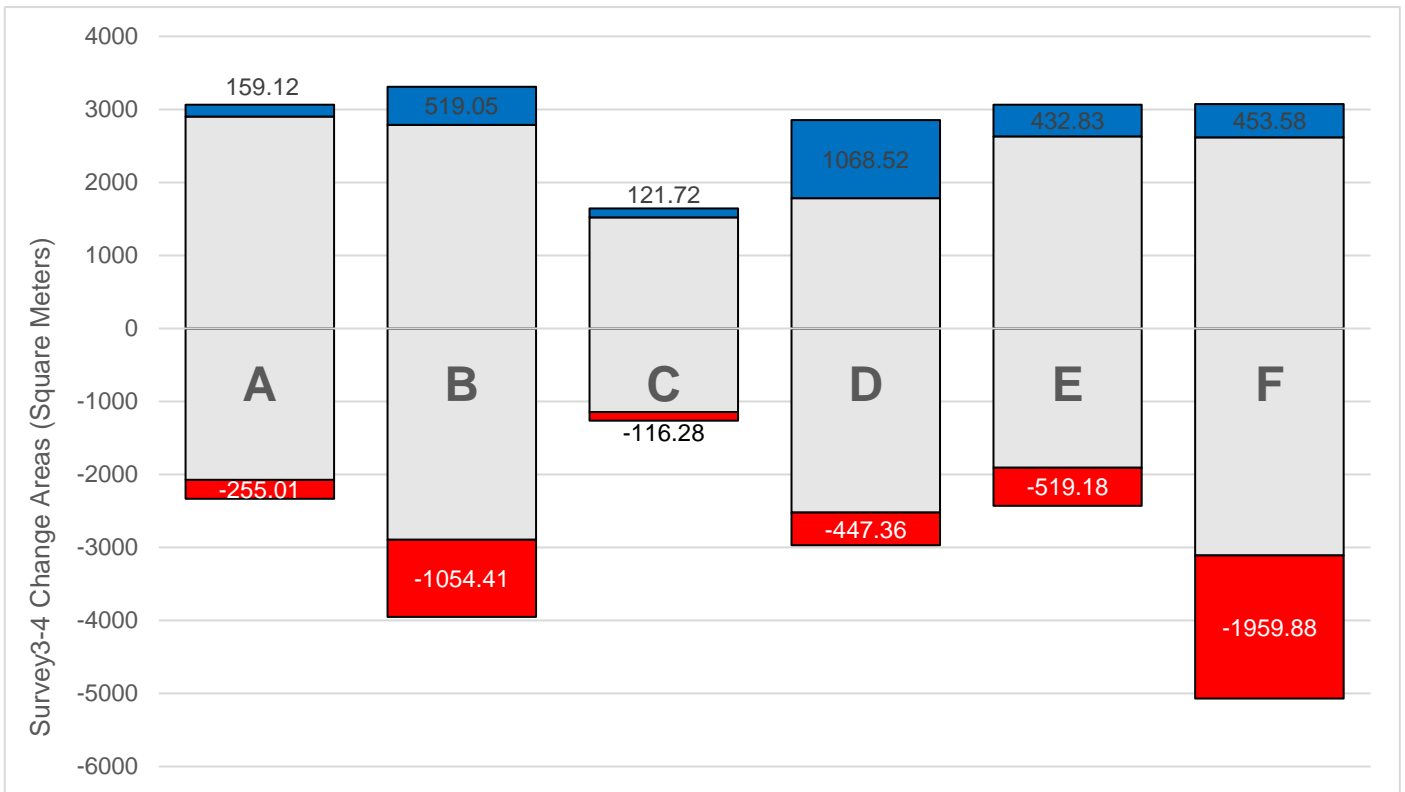


Figure 6.24 - - Area statistics for erosion (red), stability (grey) and deposition (blue) between Surveys 3 and 4.

Area statistics given by Figure 6.24 refer to changes which occur between Surveys 3 and 4. A further increase in overall stability is observed relative to previous inter-survey periods. Minimal geomorphic evolution is seen to occur in sub-reaches A and C, which is reflected in Figure 6.12Figure 6.14. More prevalent change activity is reflected in sub-reaches B and F, which are both seen to undergo moderate erosion, both in the form of bank collapse and bed scour. The largest area of deposition is seen in sub-reach D, which also contains the most positive geomorphic change by volume. This deposition is seen in Figure 6.15 to occur in the upstream extent of the sub-reach and is reflective of bed aggradation as the channel widens downstream of Haugh Head ford.

6.4. Internal Bed Dynamics and Inter-reach Geomorphic Change

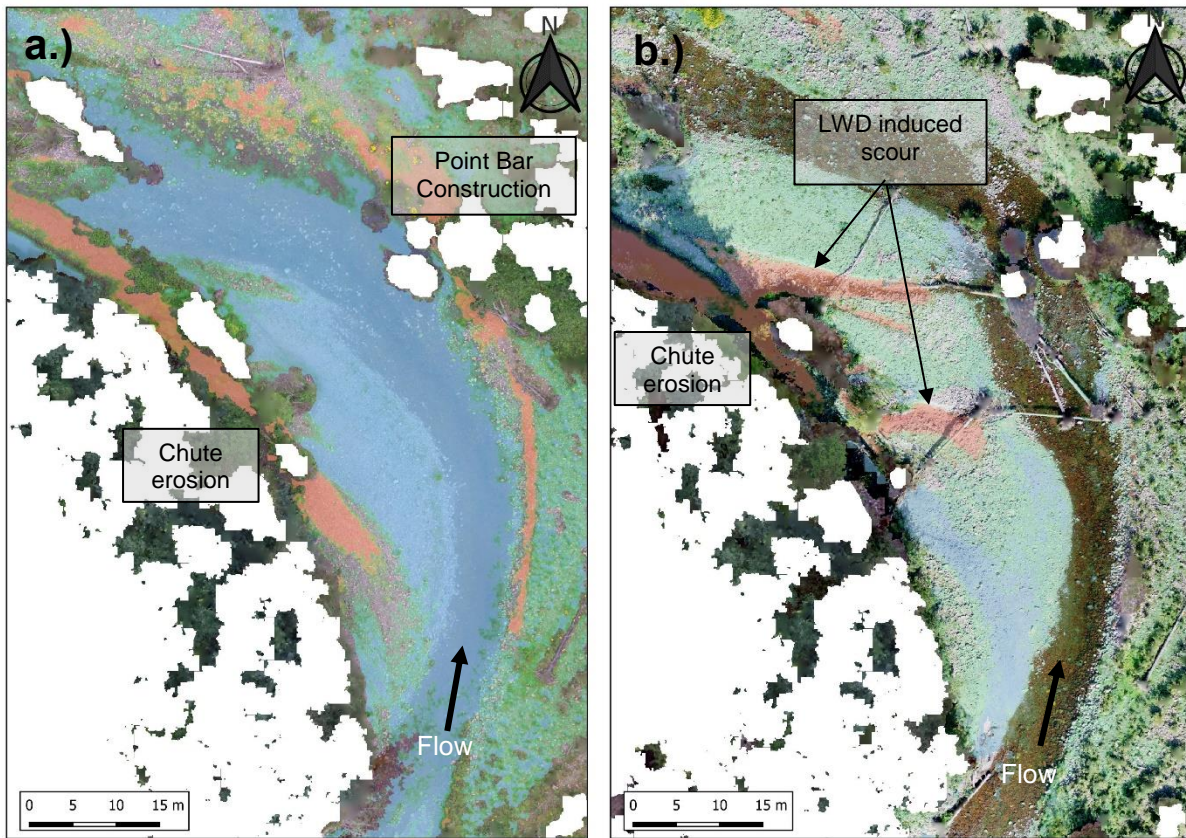


Figure 6.25 – Internal Bed dynamics occurring in Sub-reach A.

Gravel bed rivers are defined by the nature of their channel bottoms, where facies are subject to constant reconfiguration, even at relatively low flow conditions. Vegetation and in-channel features are very often the drivers of lateral erosion (Rodrigues *et al.*, 2006). The heterogeneity of biotopes created by gravel features additionally lends ecological value to such rivers (Karaus *et al.*, 2005). Bed evolution at Wooler Water, in light of the now ceased gravel mining operations, is particularly reflective of the very transitional phase the system is presently experiencing. Sub-reach A and B see extensive construction, destruction and reconfiguration of channel features, often catalysed by woody debris.

Figure 6.25a and b display orthomosaic imagery and semi-transparent DoD layers for inter-survey 1-2 and 2-3 epochs respectively. Prevalent bar construction is seen, leading to some erosion into the terrace which comprises the right bank of the confined sub-channel. Also of note is the opening of a new channel near the left bank to accommodate the reduction of depth within the primary wetted channel. Development of this cut-off

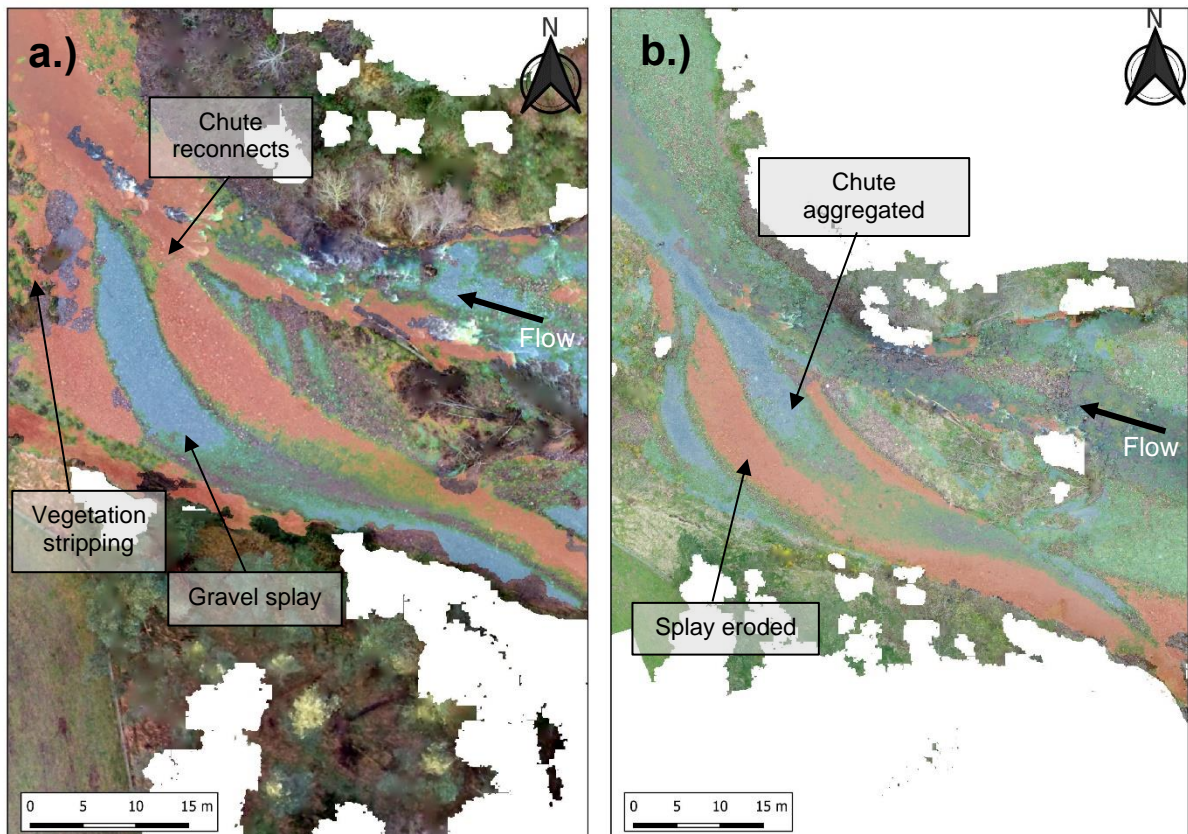


Figure 6.26 – Continuation of chute channel in Figure 6.25

channel is further catalysed by the introduction of large woody debris (LWD) atop the newly constructed bar, which scours a pool area perpendicular to the bar's a-axis. This pool then connects to the previously scoured chute channel, increasing throughput. The continuation of this chute channel is visible in Figure 6.26a and b, again showing orthomosaic imagery and vertical change detection mapping between Surveys 1-2 and 2-3. Imagery for inter-survey epoch 3-4 is not included as this section remains stable.

Figure 6.26a reveals continued bed erosion following reconnection of the chute channel to the primary course. In addition, a gravel splay lobe is created when flow velocity is lost at the “mouth” of the secondary channel upon convergence. Reworking of these features during the intermediate flows which occur between Survey 2 and 3 appears to have a levelling effect; the previously constructed gravel splay is eroded, and aggradation occurs at the convergence between the main channel and the mouth of the chute channel. The appearance of a chute cut off channel observed at this section of the study site is mechanically similar (Hooke, 1995; Fuller *et al.*, 2003; van Dijk *et al.*, 2014), albeit at a somewhat smaller scale. Maintenance of chute cut-offs is dependent on continued throughput (Micheli and Larsen, 2011), however construction of bars or other depositional features at their upstream end may choke these channels. The prevalent bar visible in Figure 6.25b could be considered large enough to vertically disconnect the chute cut-off from the main channel, however dissection of the bar by LWD associated scour offers a secondary flow supply. Coincidental if approximate alignment of the scour created by the LWD enables continued use of the cut-off channel.

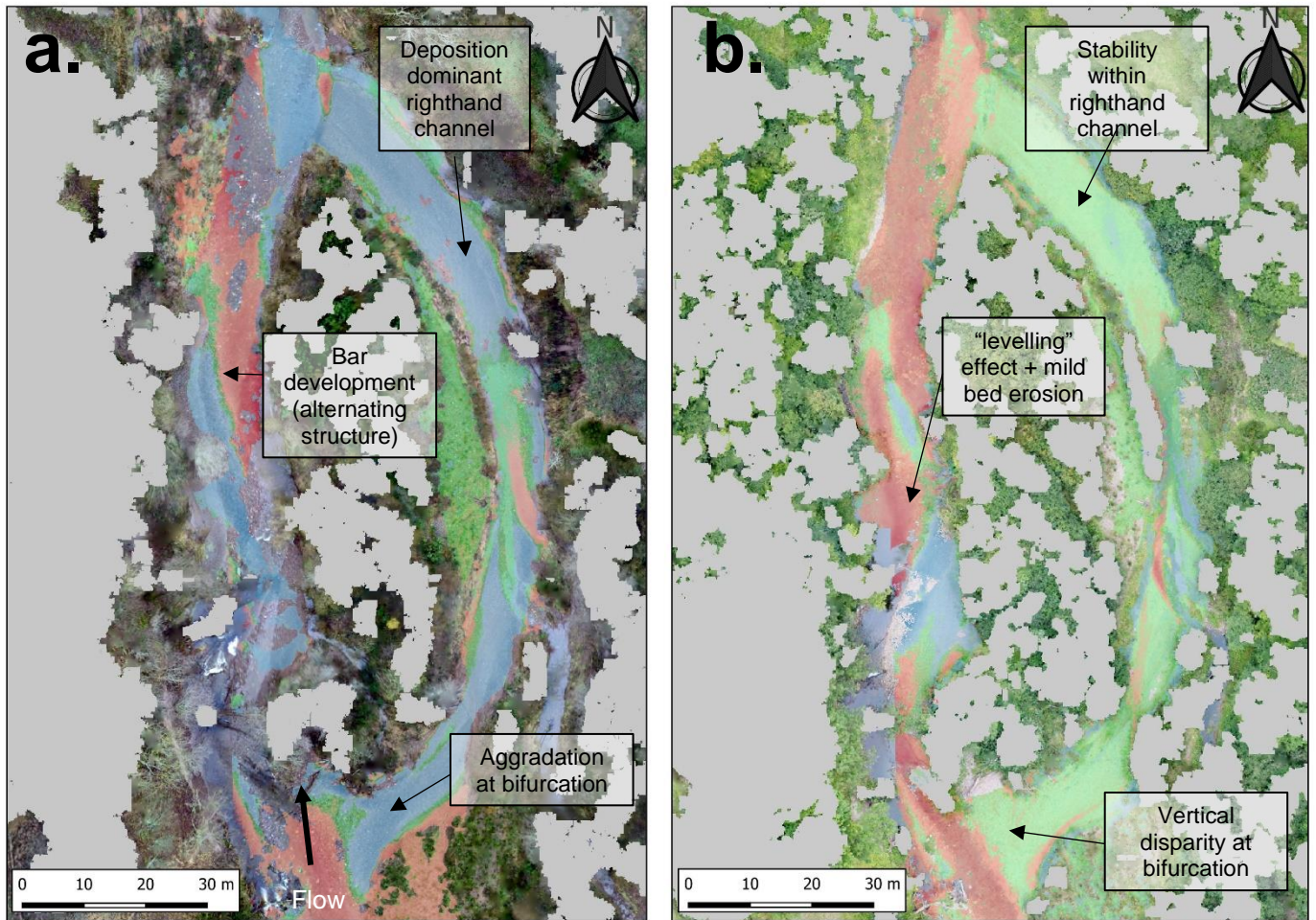


Figure 6.27 - Internal Bed dynamics occurring in Sub-reach E.

Figure 6.27a and b display DoD change maps and orthomosaic imagery of sub-reach D for inter-survey epochs 1-2 and 2-3 respectively. The channel in this sub-reach diverges into two channels of approximately equal width but with a degree of vertical contrast. The left-hand channel being the deeper of the two. Dense tree canopy and vegetation gives the underlain orthophoto images patchy coverage of the medial island which punctuates the channels, however the continued presence of vegetation on this island throughout the field campaign is indicative that no inter-survey flows were large enough to rework material atop it. Inclusive in the left channel are a pair of gravel bars, their initial state shown in Figure 6.28a. Imagery of the upstream bar on the left side of the channel (Bar 1) is limited due to occlusion by dense vegetation, however the head and tail of the feature are visible. Just downstream on the right bank, is a second bar (Bar 2), which extends

from the vegetated island that separates the twin channels. Reworking under the high flow conditions (approx. $32 \text{ m}^3/\text{s}^{-1}$) configures the channel such that Bar 1 and Bar 2 appear to swap their respective lateral positions and move upstream approximately 20m. The bars appear to be configured in an alternating fashion, potentially symptomatic of an attempted increase in sinuosity or embryonic meander development by the channel at this otherwise relatively straight section. Whilst material continuity cannot be verified between Figure 6.28a and b, comparison of Figure 6.28b and c clearly indicate the downstream growth of both Bar 1, which appears point-bar like, and Bar 2, which is more morphologically alike a mid-channel bar or sediment slug. Vertical contrast is also reduced between the riverbed and both sediment features, as verified by Figure 6.27b. This levelling effect is also similar to that observed in Figure 6.26b.

This equalisation of surface features appears to occur during periods of medium flow conditions ($<15 \text{ m}^3/\text{s}$), such as that seen between Survey's 2, 3, and 4 (peak estimated discharge $14.6 \text{ m}^3/\text{s}$ and $7.9 \text{ m}^3/\text{s}$ respectively). The reduction in height of gravel bars and mild aggradation within adjacent channels is attributable to the surface structure of each

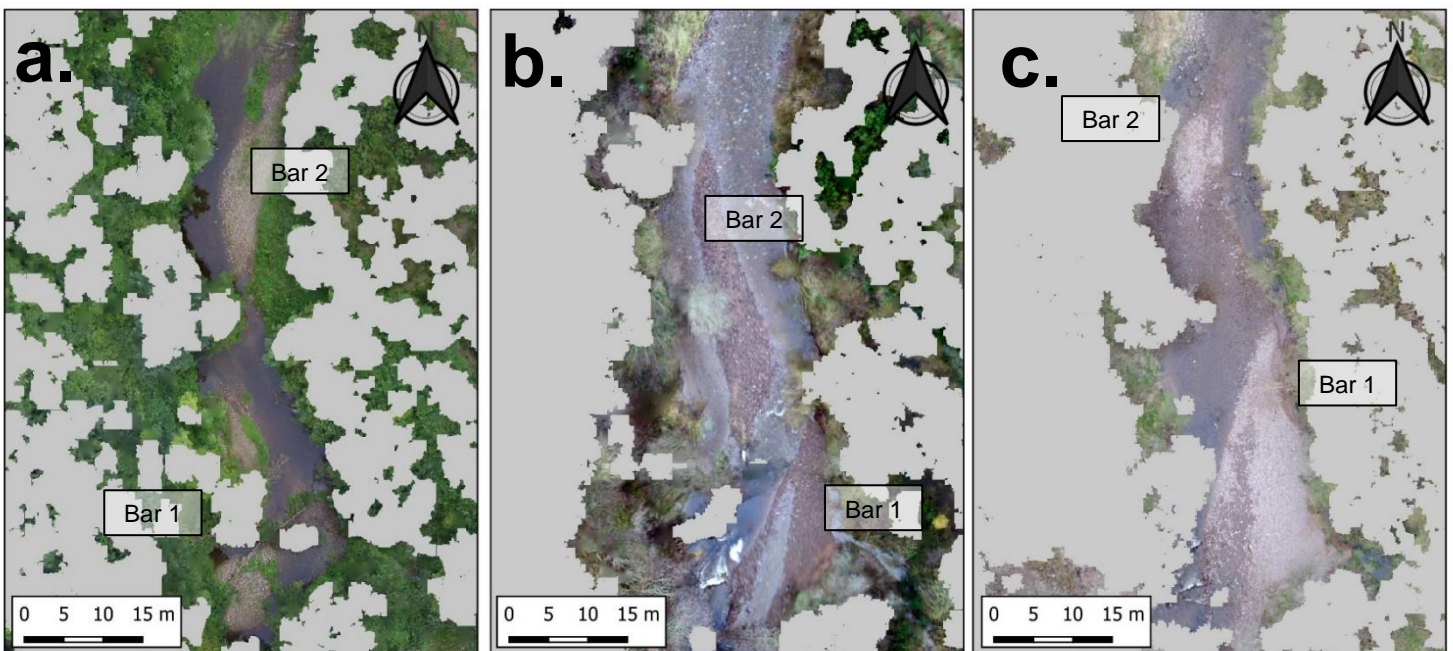


Figure 6.28 – Detail view of bar formation and migration in Sub-reach E.

respective feature. For protruding features, such as bars, shear stresses are generally higher resulting in mobilisation of some material (Rice *et al.*, 2009). Conversely the relatively reduced velocity within deeper sections will cause deposition. High magnitude flows, if not already carrying sufficient sediment, will universally cause scour to the bed; the difference in velocity between flow over bar features and deep channels being minimal. However, for intermediate flow conditions, the disparity in velocity between these locations is larger, due in part to the vertical contrast between bar and bed being a larger fraction of the water depth. This results in more limited erosion of bar forms whilst permitting aggradation to occur within adjacent channels (Hassan and Church, 2000).

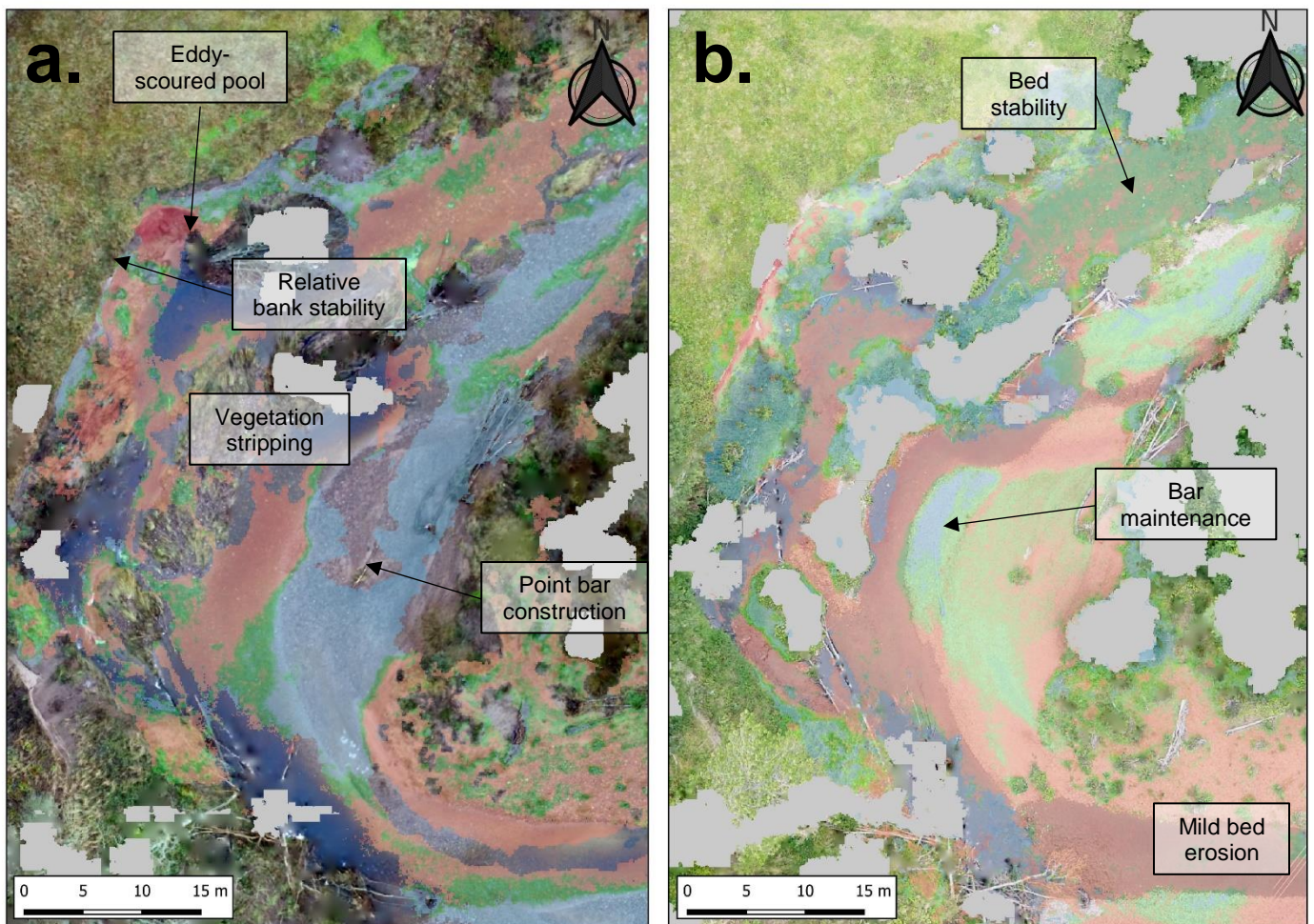


Figure 6.29 – Detail view of the left bank within Sub-reach F. DoDs for Survey 1-2 and 2-3.

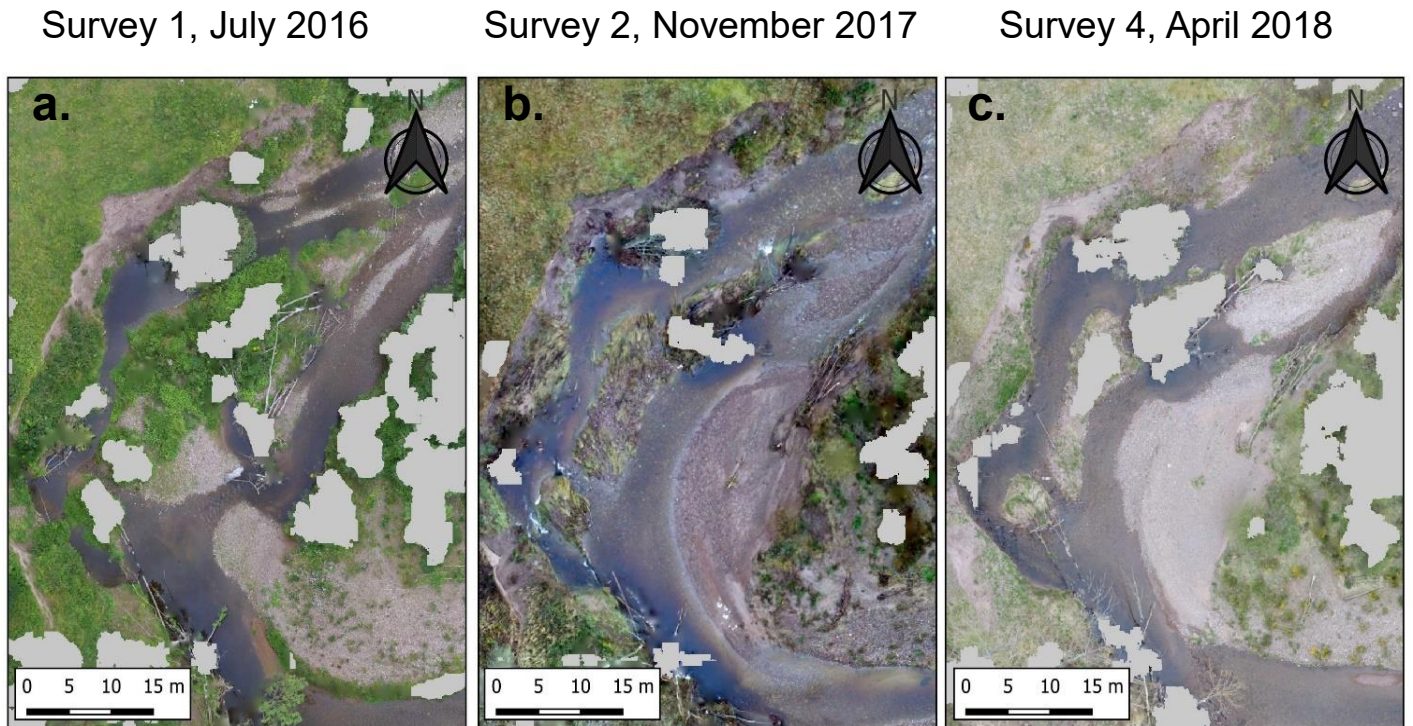


Figure 6.30 – Orthomosaic images for Survey 1, 2 and 4 of the left bank within Sub-reach F.

Figure 6.29 and Figure 6.30 display the left-hand bank within the sinuous section of Sub-reach F. This area sees geomorphic evolution in the form of gravel bar construction and maintenance, as well as vegetation stripping and some localized scouring. The banks within this section however see comparatively little erosion. This is more clearly illustrated by Figure 6.30 which shows aerial imagery only. The contour of the bank lip is seen to be approximately the same between surveys, indicating no collapses from the top have occurred. More erosion is however present upon the face and at the base of the bank. Erosion visible at the base of the bank in Figure 6.29a indicates a partial collapse. A close-up view of this section is shown by Figure 6.31. The very top of the bank appears stable and to even have partially re-vegetated during the two years between this project's first and most-recent survey of Wooler Water. Noticeable however in Figure 6.31b is the failure plane of a large section of this bank. This mass failure is likely due to lateral erosion at the base of the bank, however this is not continuous for the whole bank. The blurred

portion of Figure 6.31a is due to the presence of LWD; one large deciduous tree which has retained its smaller branches, very likely deposited in-situ following bank erosion during a much higher flow, such as that in 2013. This vegetation was filtered out during post-processing so as to prevent it contributing to volumetric calculations. This LWD persists between all surveys. Scour on the upstream side of LWD is universally observed (Triska, 1984), however in this special case the proximity of the bank introduces added complexity. The natural scour caused by eddy recirculation on the upstream side of the debris in this case contributes to bank erosion, however very minimal bank erosion is observed immediately downstream. This a result of a “shielding” effect by the LWD which lies approximately parallel to the bank.

The retention of smaller branches and limbs has the effect of lowering velocity and reducing shear stress. Unfortunately, ground elevation data is unavailable underneath

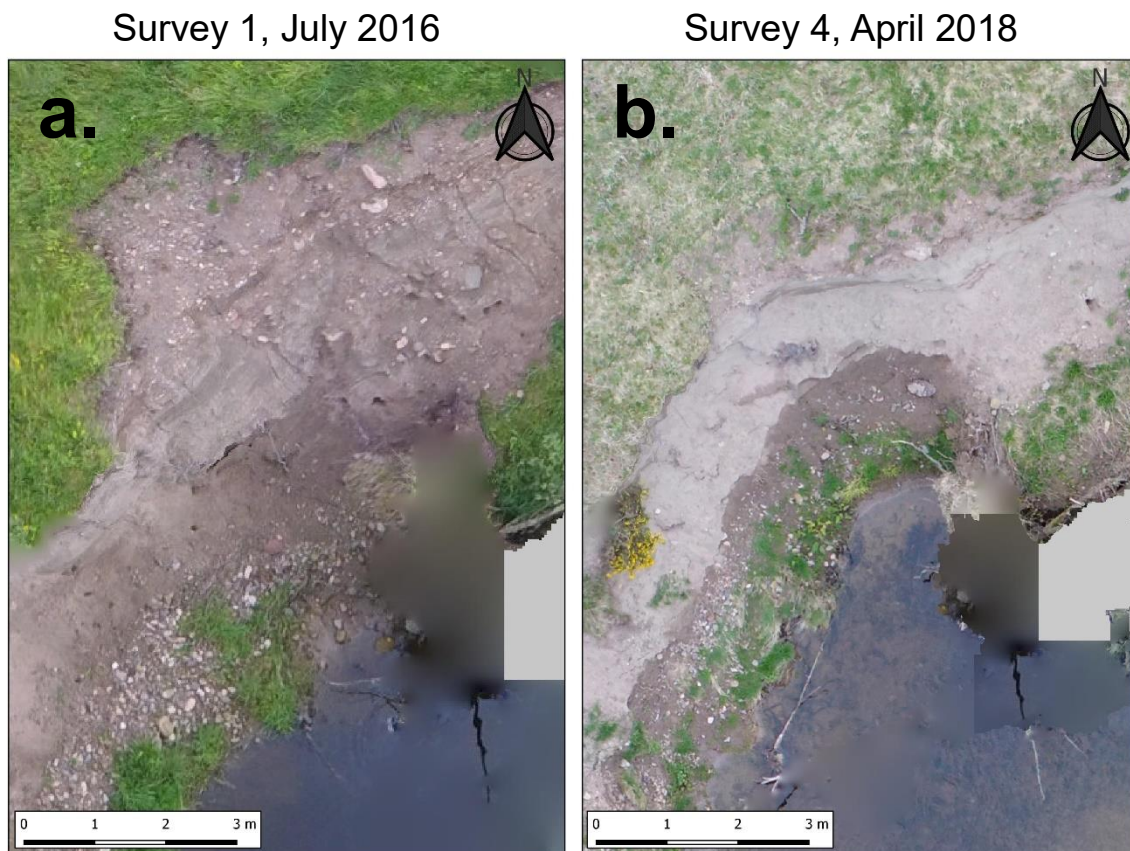


Figure 6.31 – Close up of left bank within Sub-reach F. Mass failure and bed scour visible

this LWD feature due to the density of the branches which obscure SfM data collection, however it may be expected that aggradation of finer material is occurring. This may eventually lead to the LWD becoming buried which may decrease its shielding effect of the adjacent bank. Alternatively, this may effectively result in construction of a bank “extension”, where deposited material appears to augment the existing bank. Further investigation is required however, perhaps by a more subject specific surveying tool such as LiDAR, since vegetation penetration is a known drawback of the UAV-SfM method. On the other hand, detection of novel geomorphic processes requires extensive datasets which enable a good level of detail across wide scales, to which low-cost drone surveying is well suited.

D

6.5. Clast Scale Geomorphic Change Analysis

Besides capture and reconstruction of landscape geometries, characterisation and classification of the bedload present within fluvial systems is one of the most prevalent means of analysis undertaken by geomorphologists. Grain size one of the main controllers of fluvial form (Dade and Friend, 1998) and a key input parameter to hydrological models. Quantification that is accurate and extensive is therefore crucial to understanding what form a river will naturally take, information highly valuable to planners and for implementation of management strategies. Grainsize ratios are also able to inform regarding flow regime, a relative fining or coarsening load may be indicative of changes upstream (Bagnold, 1966). Distributions and variability of grainsize is known to be considerably heterogenous at the reach scale, although usually present in homogenous “patches” (Dietrich *et al.*, 2005). This inherently makes attaining a representative measure of grainsize distributions within a river reach a difficult task if using contact sampling methods. Traditional methods for attaining grainsize data such as the Wolman

Pebble Count (Wolman, 1954) are manually intensive, invasive, and require access directly to sample areas. Additionally they may be susceptible to bias (Kondolf and Li, 1992). Additionally, such surveys must be carried out twice if geomorphic change results are sought, making the process doubly intensive. The ability to remotely sense grainsize data is thus invaluable to river scientists.

Numerous works surrounding the remote quantification of river bedload grainsize exist. LiDAR systems have demonstrated their power and suitability for such applications (Entwistle and Fuller, 2009; Heritage and Milan, 2009; Hodge *et al.*, 2009; Brasington *et al.*, 2012), however their bulk and cost restrict their coverage. The survey reach of this project represents too large an area for continuous data to be collected with terrestrial LiDAR scanning. Characterisation of grainsize with LiDAR primarily relies upon surface roughness. Optical methods are similarly present within the literature field. These studies primarily utilize RGB imagery and associated SfM processing DEMs, and may be sub-classified into those which quantify grainsize based on image texture (Carbonneau *et al.*, 2004, 2005a; Verdú *et al.*, 2005a; Woodget and Austrums, 2017), and those which use spectral variability and frequency to detect individual clasts (Buscombe, 2008, 2013; Buscombe and Masselink, 2009; Buscombe *et al.*, 2010). Limited work to apply such methodologies to scales beyond individual sediment patches exists. Absent from the literature is a demonstration of the application of remotely sensed grainsize distribution mapping for the purpose geomorphic evolution and at the macro/kilometric scale. This may be distinguished by the need for wide coverage, very high-resolution data, that must be precisely spatially referenced for data validation purposes.

Analysis of grainsize distribution is complicated for the UAV surveying methodology, as the minimum resolvable grainsize is linked to the GSD of an image. Despite the ability of

UAV systems to attain very high resolutions (~1cm/pixel) the resolution of this project’s dataset cannot fully resolve the smallest grainsizes present within the Wooler Water system. Whilst it is possible to gauge what clasts are resolved by eye, for reliable estimation of grainsize a GSD 2-3 times smaller than the median grainsize must be used (Buscombe *et al.*, 2010).

Table 6.3 – Ground sampling distances and minimum resolvable grainsized for all surveys.

Survey Number	Resolution (cm/pixel)	Minimum Resolvable Grainsize (cm)
Survey 1	1.75	5.25
Survey 2	2.17	6.51
Survey 3	1.50	4.50
Survey 4	1.31	3.93

Table 6.3 gives the resolutions and minimum resolvable grainsizes (3 x GSD) for each respective UAV survey. A D₅₀ of 15.2cm from Sear and Archer (1998) does place the median grainsize above the GSD for all surveys, however a portion of the clasts at Wooler Water cannot be quantified.

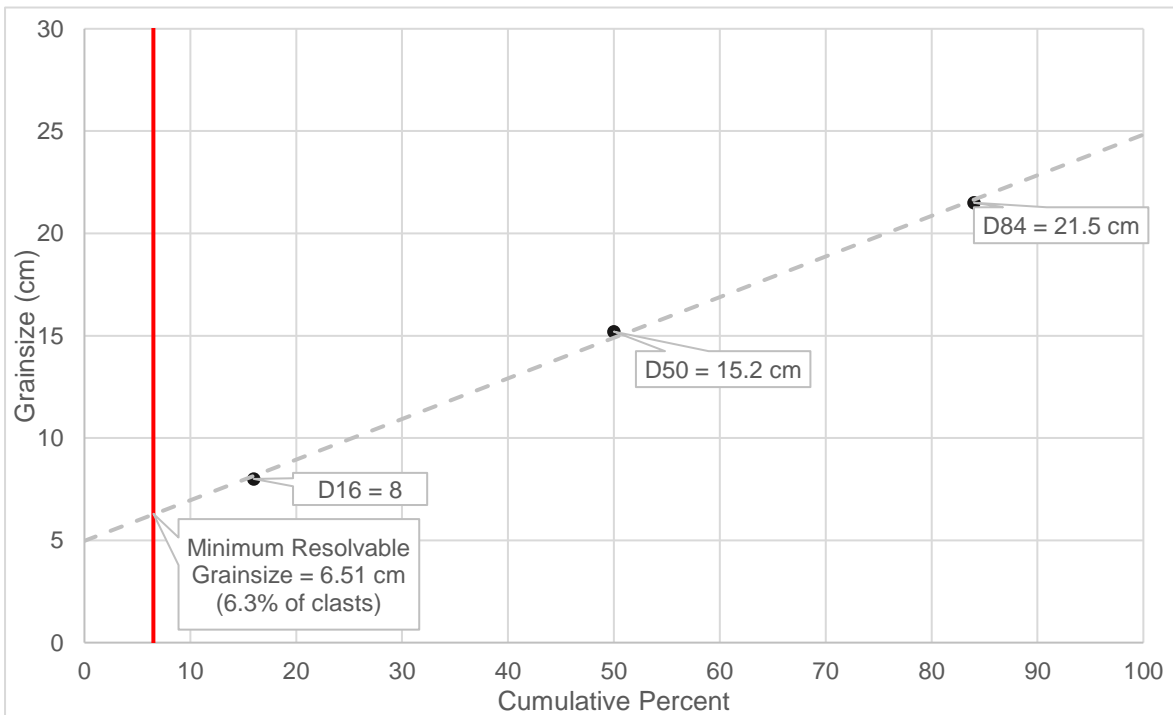


Figure 6.32 - Estimated portion of grains unable to be sized by image based analysis methods (6.3%) based on reported D₁₆, D₅₀, and D₈₄ from Sear and Archer (1994).

Figure 6.32 makes use of grainsize data provided by Sear and Archer (1994) to estimate the fraction of clasts at Wooler Water that cannot be resolved by aerial imagery. For the coarsest imagery (Survey 2) this is 6.3%. This figure is likely to be conservative however, since in reality lighting conditions, sediment contrast and other factors such as submergence can further reduce resolving ability. This places an inherent limit upon the amount of information which can be retrieved from such aerial imagery when compared to conventional field sampling. Coarse clast detection, mapping and change analysis still presents a potential insight to fluvial dynamics at Wooler Water however.

Figure 6.33 displays an area within sub-reach B which is seen to undergo significant reworking during the course of the field campaign, particularly during the Survey 1-2 epoch. Channel scour and bank collapse are observable in comparison DoDs, however there is evidence of deposition at the channel margins. This area is suitable for experimental application of a clast detection methodology which utilizes image intensity sieving to differentiate coarse material from the fine-grain matrix upon which such clasts

rest. The contrast between the surface of a stone and the apparent dark boundary around it (also known as the “pore”) permits this (Buscombe *et al.*, 2010).

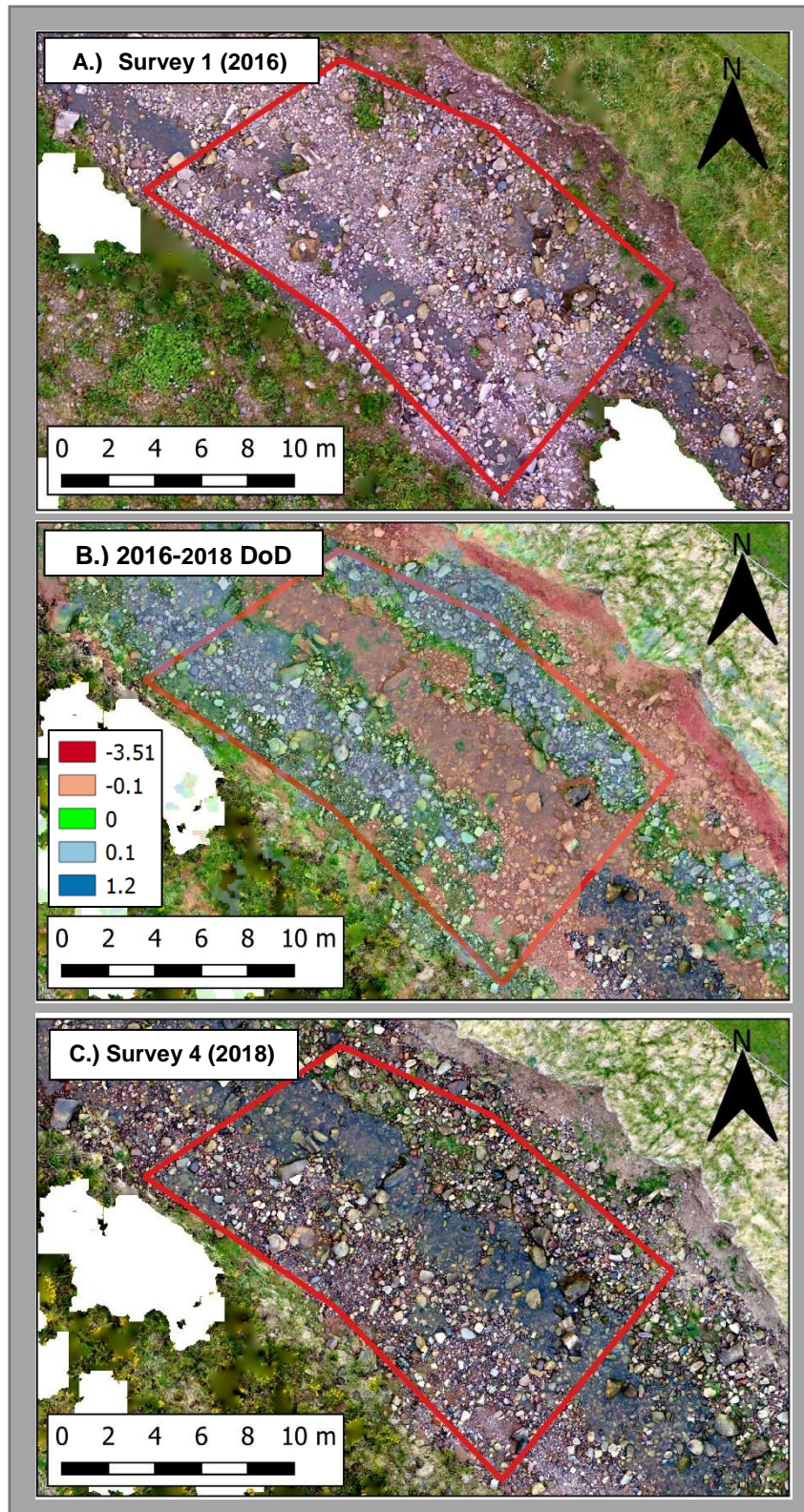


Figure 6.33 – Area of Interest for coarse clast analysis (sub-reach B)

For detection of sediment clasts, the RGB orthophotos were clipped to the extent of the area of interest and then converted from multiband RGB to single-band greyscale (intensity) raster files by addition of each colour bands 0-255 integer. The intensity histograms for these images were individually tweaked by clipping their maximum and minimum extents so that only the spectral signatures of bed material remained. The maximum and minimum intensity values are noted at this point and utilised for re-classification of the raster file to a binary image. Pixels with intensity values outside the identified spectral threshold are reassigned as 0 (no data), whereas those which lie within the threshold receive 1, indicating the presence of a contiguous sediment quanta. The binary raster is converted to vector data by applying the minimum bounding convex hull to each individual group of contiguous pixels. All polygons whose minor axis does not exceed the minimum resolvable grainsize of 6.51 cm are deleted. For clast sampling, a random selection of 500 clasts was extracted from the remaining shape data.

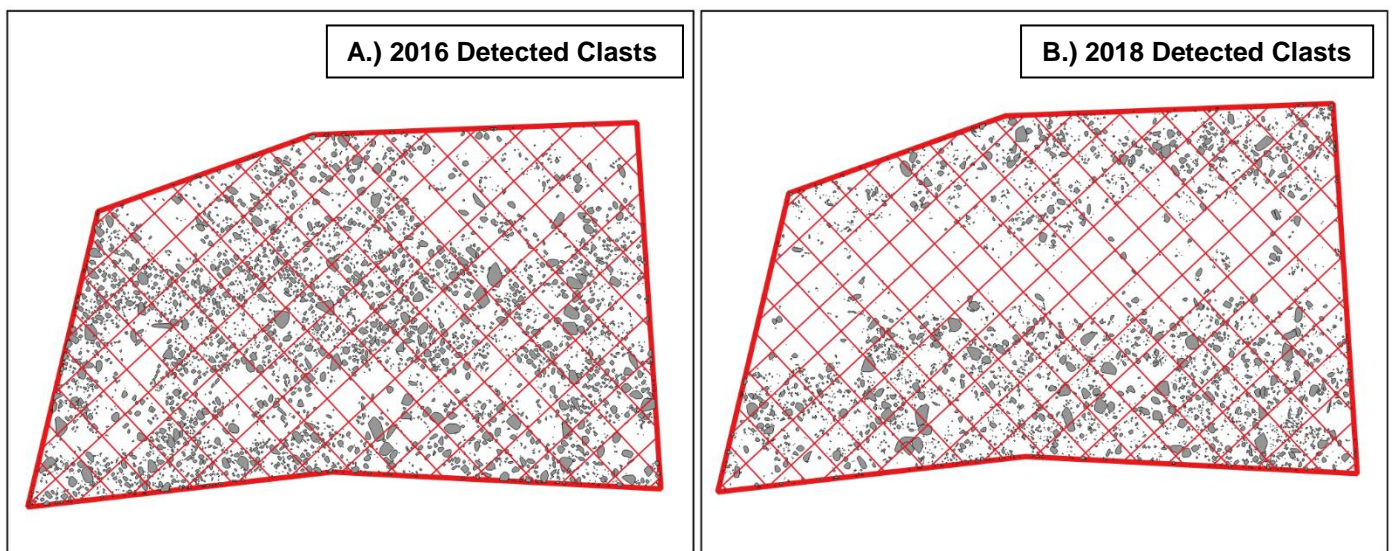


Figure 6.34 - Detected clasts (grey) for 2016 and 2018 based upon clast/pore contrast definition

The boundaries of the shapefiles produced approximate the “pore” boundaries of each individual clast. Conversion of the ellipsoid envelopes to oriented minimum bounding boxes permits measurement of the major and minor axes of the approximate enclosing

polygon. It is unreasonable to assume that all measured minor axis lengths correspond to the b axis of the real-world stone, since factors such as clast orientation, occlusion, and imbrication may not present the entire axis to the camera. In the absence of cohesion or clast occlusion, stones can be expected to naturally settle with their c (shortest) axis orientated upwards (Wolman, 1954), thus presenting the a and b axes parallel to the ground and thus visible from the air. For a large sample size (>300) the presented minor axis of most stones will thus be representative of the clast's b axis.

For acquisition of a validation dataset, the minor axes of clasts in aerial imagery were manually measured using a digital ruler. 636 for 2016 and 802 for 2018 data. Randomisation was ensured in this step by use of a grid-wise selection process. A 1x1m grid was imposed over the area of interest and all resolvable clasts which touched the

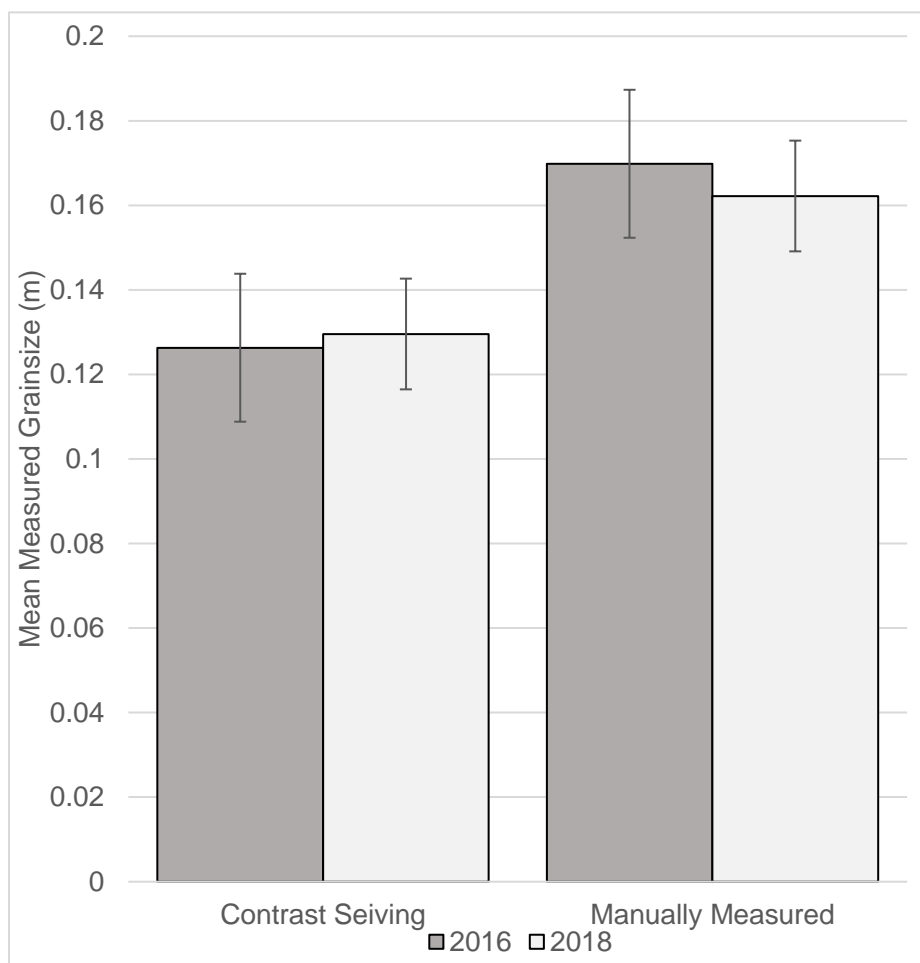


Figure 6.36 – Comparison of image sieving methodology against manual measurement of resolved clasts from aerial imagery. The former underestimates grainsize by approximately 23%.

gridlines at any point were measured. A random sample of 500 of these clasts (from each year) makes up the validation dataset.

Figure 6.36 graphically displays the comparison in mean measured grainsize between the image intensity sieving methodology. Error bars represent the GSD of each respective survey (1.75 cm for 2016, 1.31 cm for 2018). The image analysis methodology underestimated mean grainsizes by an average of 23% when compared to the manual digital measurement of clasts. The underestimation is more pronounced for large clasts, evidenced by Figure 6.37. Clasts over 0.4m are more likely to be significantly underestimated in size by the method (> 50%). This places a limitation on the upper size limit of clasts the image analysis technique can quantify.

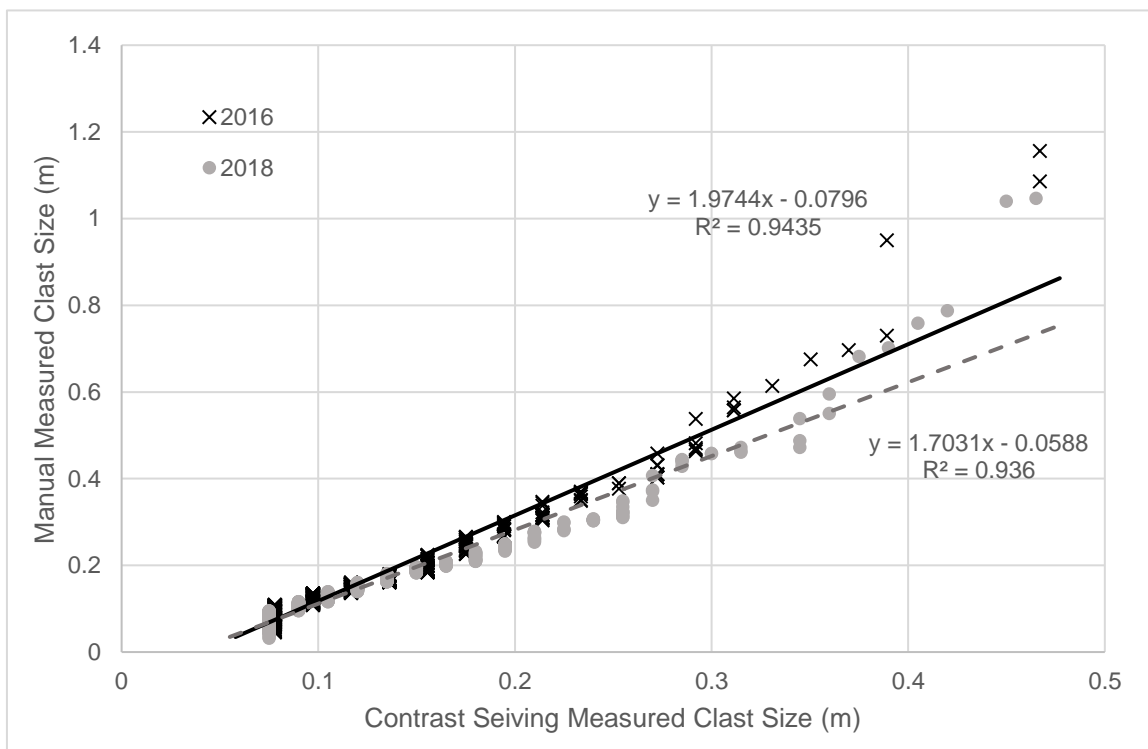


Figure 6.37 – Linear regression between manual and image analysis clast measurements

6.5.1. Critical Evaluation and Limitations

The clast detection and measurement methodology presented here cannot be considered comprehensive enough to be used for routine grainsize quantification, since inherent limits to the minimum and maximum grainsizes that can be discerned exist. The lower limit of detection is controlled by the resolution of the imagery. Clasts which are smaller than 3 x GSD cannot be resolved and thus are not detectable. The maximum limit of detection, approximately 0.4m in this case, is likely attributable to the mis-classification of large clasts as multiple smaller ones. Above a certain size, visible variations in light and colour occur across the surface of a stone. This effect is illustrated in Figure 6.38 where particularly large clasts have been mis-represented as multiple smaller stones by the contrast sieving methodology.

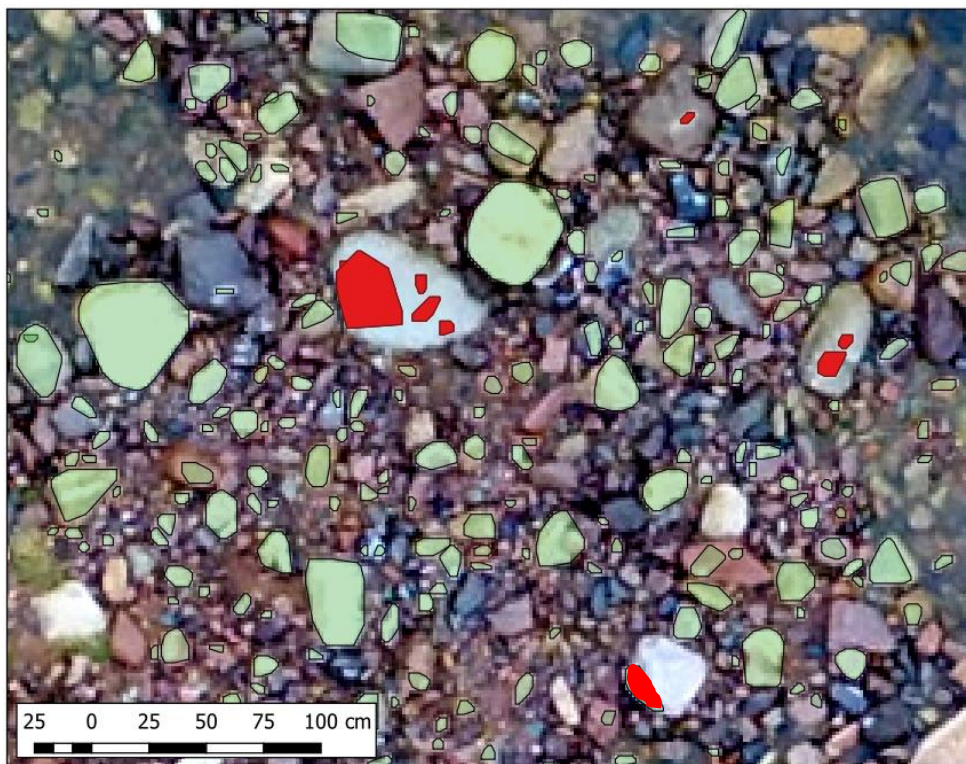


Figure 6.38 – Mis-classifications (red) of individual clasts as multiple due to surface contrast variations

A degree of aliasing is also present in the data. Although smoothed so as to more closely envelope each clast, the bounding polygons are “snapped” to the pixels of the image, thus

their measurement of clast size is only as precise as the image resolution. This may result in clasts at the smallest resolvable scale (3xGSD) being mis-measured by up to 33%. The inherent limitations of this method suit it to a specific range of clast sizes. The range of clasts detectable by this method (6.51cm – 40cm) remain a significant fraction of the grainsize distribution at Wooler Water however (Sear and Archer, 1998). The implications of the underestimation of clast size by the image analysis method are that the technique cannot be utilised as a direct quantification of grainsize distribution but rather as a proxy measurement potentially suitable for classification of morphological units. For areas of sediment, such as fine gravels, cohesive material or boulder-fields, unclassifiable by the method, the grainsize within such zones may be reasonably assumed to be at least below or above the detection limits of the methodology.

6.5.2. Grainsize evolution at Wooler Water

For examination of grainsize changes at Wooler Water, the contrast sieving clast detection methodology was applied to a larger area shown in Figure 6.39. An identical methodology was used as when analysing the smaller area of interest in Section 6.5.0, except a larger random sample of 3000 clasts was instead extracted for each year of analysis (2016 and 2018).



Figure 6.39 – Region of interest for grainsize change analysis and detected clasts for 2016 and 2018.

Table 6.4 – Reported grainsizes (cm) from Sear and Archer 1998, and estimated distributions for 2016 and 2018 by this study. (2016 error $\pm 1.75\text{cm}$, 2018 error $\pm 1.31\text{cm}$)

	D ₁₆	D ₁₆ +23%	D ₅₀	D ₅₀ +23%	D ₈₄	D ₈₄ + 23%
1998	8.0	-	15.2	-	21.5	-
2016	7.8	9.6	11.7	14.4	17.5	21.5
2018	7.5	9.2	10.1	12.9	18.0	22.1

The results of clast sizing analysis are given by Table 6.4. 1998 data is provided by Sear and Archer (1998). Based on findings in the previous section that the automatic clast detection methodology underestimated grainsizes by an average of 23%, an offset was added to each respective grainsize proportion. Doing so appears to bring the

approximated values for 2016 and 2018 much more closely in-line with that reported by Sear and Archer (1998), actually matching it in the case of D_{84} in 2016. Data for 2016 and 2018 are however subject to the same errors reported by Section 6.3.0 and displayed in Figure 6.36 ($\pm 1.75\text{cm}$ for 2016 and $\pm 1.31\text{cm}$ for 2018 data). The findings within the region of interest do not appear to suggest a discernible change in grainsize in the past decade. Figure 6.40 indicates 1998 values for D_{16} , D_{50} , and D_{84} lie within the error range of this study's data.

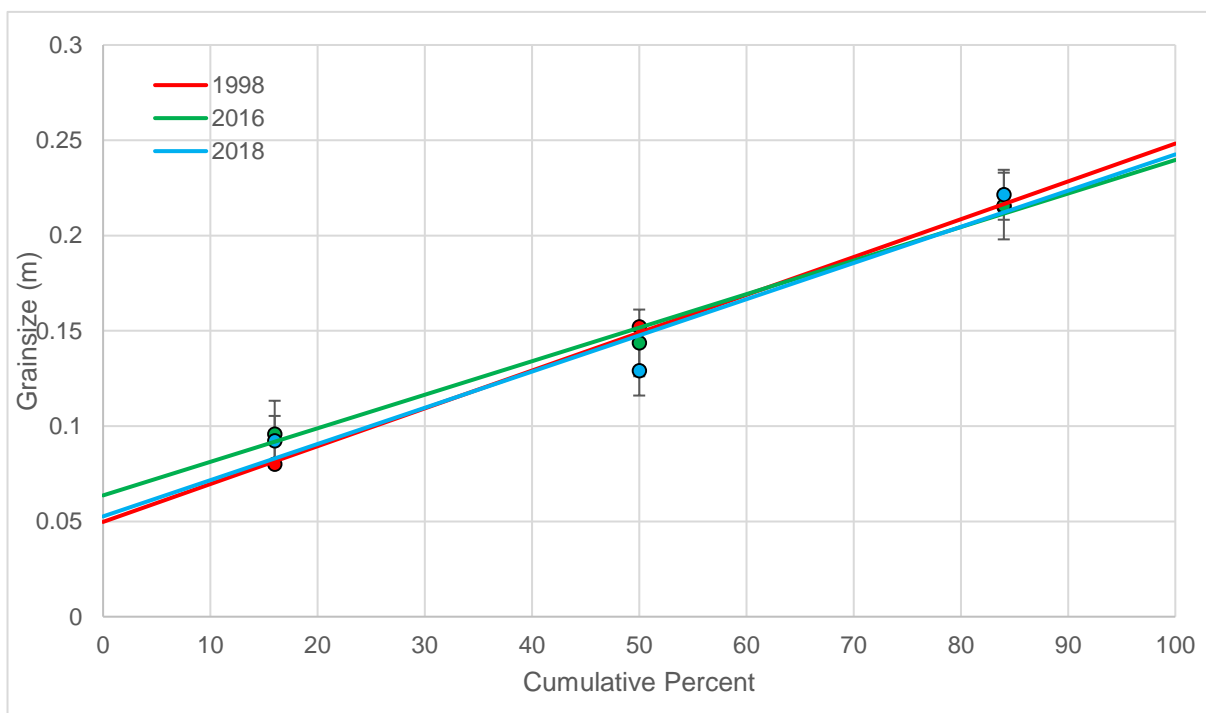


Figure 6.40 – Grainsize distributions for 1998 (Sear and Archer, 1998), and error corrected (+23%) data for 2016 and 2018.

Chapter 7: Discussion & Conclusions

7.1. Sediment Budget and Flow Regime

The evolutionary trajectory of Wooler Water modelled here within the context of its artificially modified past presents some contrary findings to what may be expected from standard river re-naturalization models. Most notably, the persistently negative net sediment budget. Previous analyses of the site by Sear and Archer (1994) recount phased extraction volumes from various in-channel gravel mines. Volumes approximating 32,000 m³/year are recorded. An estimated annual natural sediment yield of 145 m³/year places the Wooler Water at an obvious deficit (Sear and Archer, 1998). Associated degradation results in the modern paradigm of a confined channel, set within a highly incised (4-9m) margin. Summarily, the very high and steep banks delivered by this degradation represent an enormous supply of material, mobilizable by modest widening action. This is particularly the case within Sub-reach B. This does not particularly contradict existing models of channel adjustment, however more contrary is the very little comparative deposition is seen within the bed of the confined channel, despite cessation of gravel mining works. This section relates the temporal variability of sedimentary mobility throughout the course of the field campaign to Wooler Water's local flow regime and the role of large flood pulses. Data provided by a gauging station at Coldgate Mill, approximately 500m upstream of the Study Site's upper extent grants insight to Wooler Water's flow regime within the context of the recent survey carried out by this project.

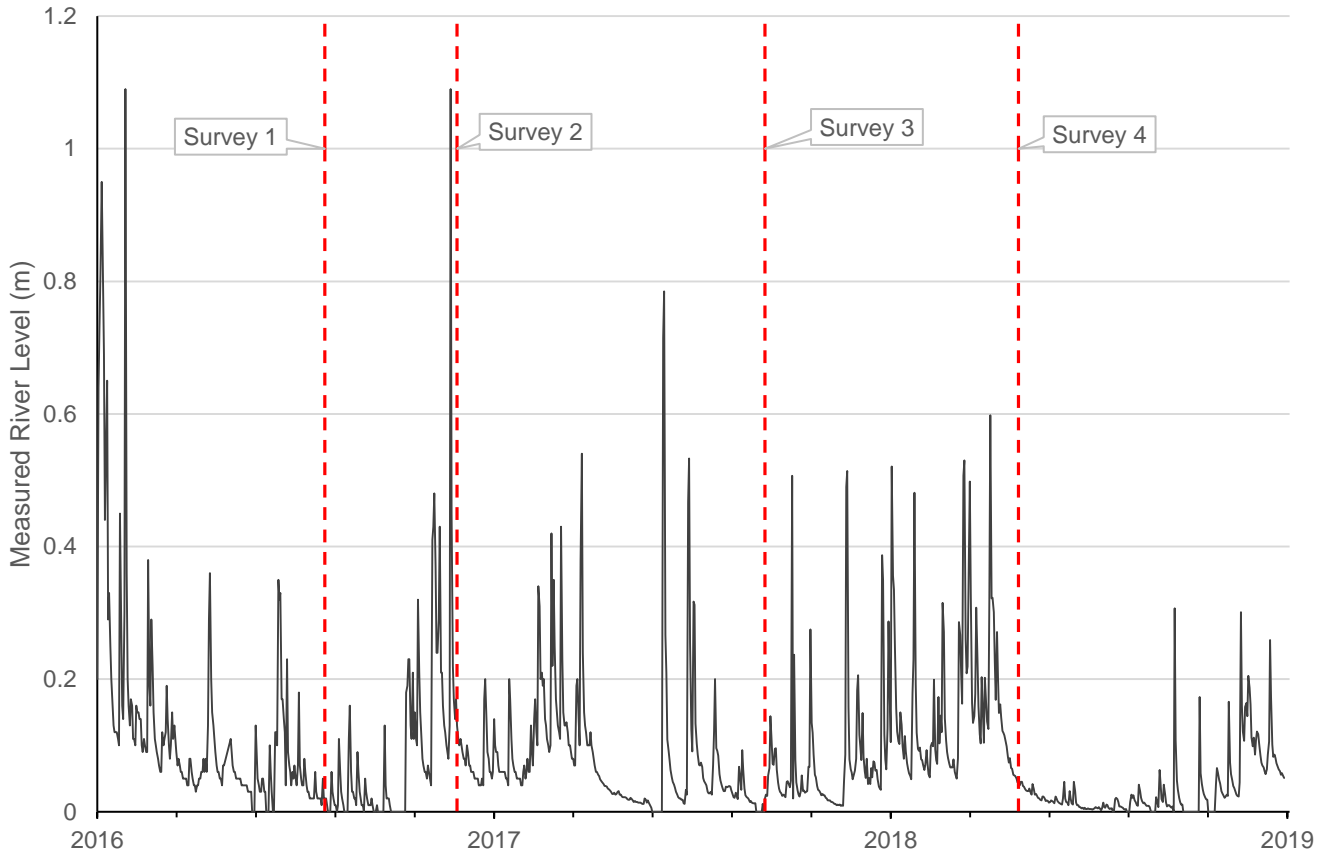


Figure 7.1 - Daily River level record at Coldgate Mill.

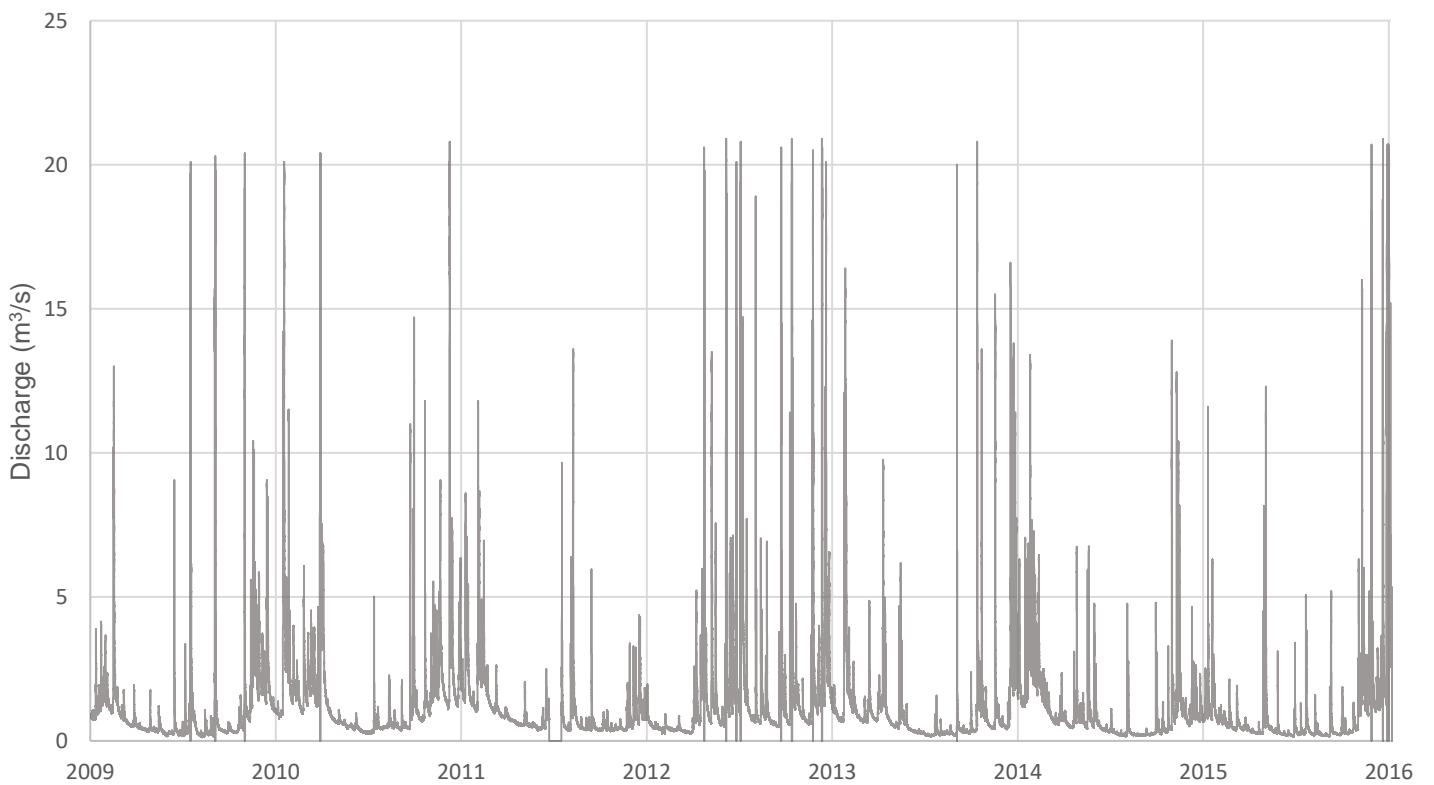


Figure 7.2 - Gauged flow record 2009-2016 from Coldgate Mill gauging station. Maximum

Figure 7.1 and Figure 7.2 represent the measured flow at the Coldgate Mill station. Figure 7.1 provides mean daily river level in meters between 2016 and 2018. Of particular note are the high flows recorded in early and late 2016, as well as in mid-2017. Figure 7.2 gives longer term data available as discharge in m^3/s . The apparent “cutoff” at approximately $20 \text{ m}^3/\text{s}$ represents the upper limit of the gauging station’s recording ability. Figure 7.2 is therefore more useful as a measure of flood-pulse frequency than absolute discharge over

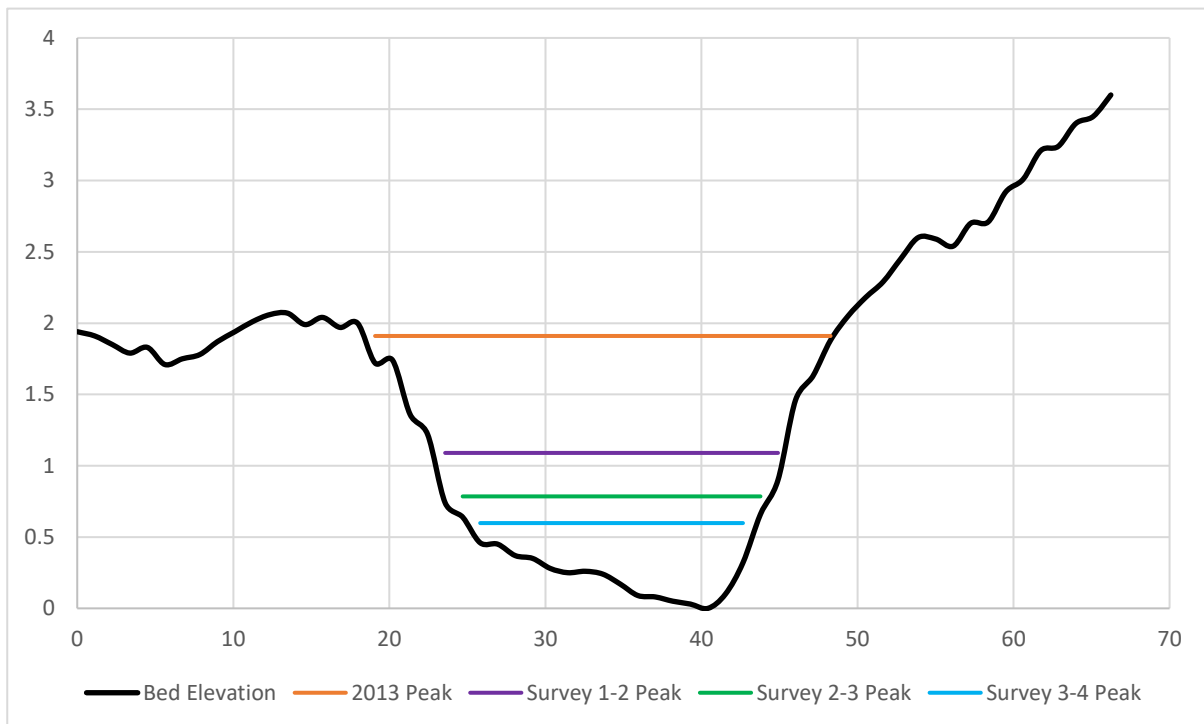


Figure 7.3 – Flow levels within cross section at Coldgate Mill.

a given time period. Recurrence of $>20 \text{ m}^3/\text{s}$ flows was very common in 2012 when at least 7 pulses of such magnitude are recorded. Conversely, only 7 flows that exceed $20 \text{ m}^3/\text{s}$ are present for the multiple years of this project’s field campaign (2016-2018). Figure 7.3 illustrates the cross-sectional topographic profile at the Coldgate Mill gauging station based off 1m resolution aerial LiDAR collected in 2009 by the UK Environment Agency. These datasets are openly available, for a range of resolutions and with good national coverage. Imposed upon this cross section are level lines, taken from Figure 7.3 and a historical data from 2013 (riverlevels.uk, 2019), corresponding to peak flow events

during and before this study's surveys. Trapezoidal fitting to calculate cross-sectional area was used in combination with velocity calculated with Manning's equation ($n=0.055$) to estimate discharge. Included in Figure 7.3 is the highest recorded flow in the past decade, which occurred in October 2013.

Table 7.1 – Comparison of inter-survey peak flows and respective volumetric change.

	Maximum inter-survey river level (m)	Estimated Discharge (m^3/s)	Inter-survey Erosion (m^3)	Inter-survey Deposition (m^3)	System Sediment Loss (m^3)
2009-2016	1.91	99.51	-19373.60	7020.58	-12353.01
Survey 1 - 2	1.09	32.20	-1904.18	1372.28	-531.9
Survey 2 - 3	0.785	14.63	-706.12	528.27	-177.85
Survey 3 - 4	0.598	7.945	-520.35	191.83	-328.52

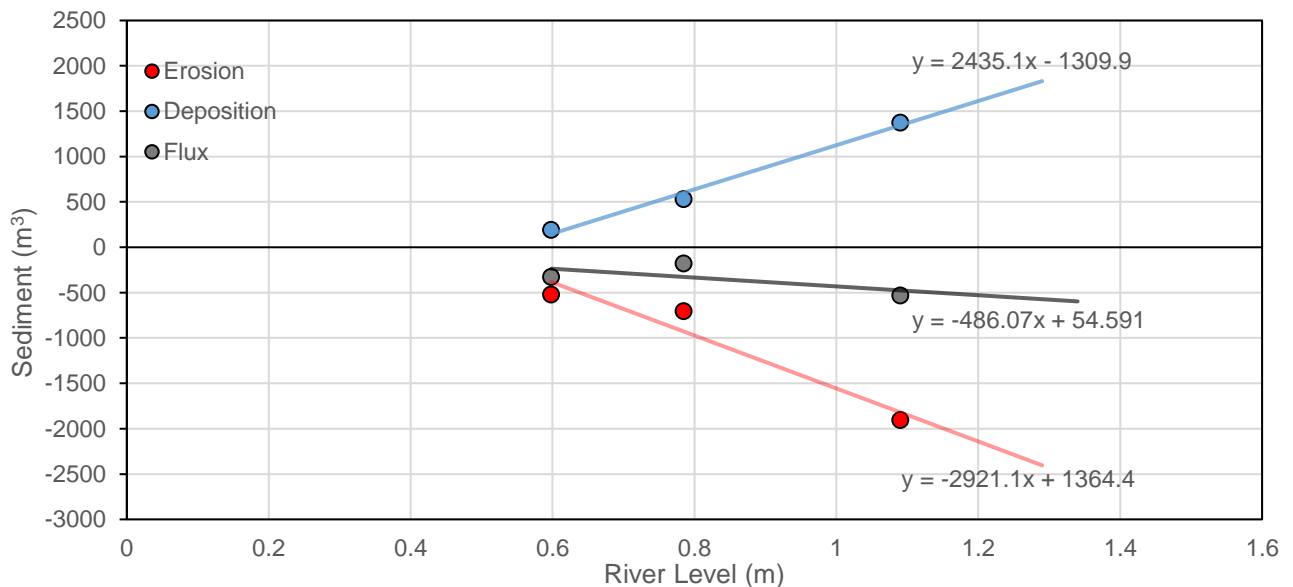


Figure 7.4 – Scatter graph of sedimentary response to different flow magnitudes.

Table 7.1 displays the maximum recorded river level, amount of erosion and deposition, as well as the net sediment loss for each inter-survey epoch. This data is graphically displayed by Figure 7.4 with linear best-fit lines applied. It should be noted that “negative” sediment on the Y axis refers to erosive action or “loss” of material and not

negative quantities. Flow magnitude thus positively correlates with erosion. Deposition also strongly correlates to flow magnitude. Subtle variance within the gradients of each linear trendline suggest these two variables are not correlated to flow magnitude with the same strength. The sediment budget appears to trend negatively as a result, indicative of that higher magnitude flood pulses will create a sediment deficit. The data presented here is however limited to three inter-survey epochs, thus net sedimentary flux cannot be confidently considered to be negatively correlated with flow magnitude.

7.1.1. Planform Response

Termination of gravel extraction works within Wooler Water should be synonymous with a return to a net-positive sediment regime however the data presented suggest such a transition is yet to fully occur. Chang, (1986) describes the general response of river systems to variability in flow magnitude and sediment input. An increase in material from upstream that exceeds the carrying capacity should be expected to cause bed aggradation. This reduction in depth constricts the channel, resulting in responsive widening. This is not the case for channels such as that of Wooler Water, which exists partly as an in-set channel within an incised margin. In such a scenario, widening of the wetted sub-channel does not occur under the same mechanics. Figure 7.5 shows a diagrammatic representation of bed aggradation (Figure 7.5a) in an incised context. Flow in aggregated sub-channels will overtop and instead occupy the considerably wider incised margin (Figure 7.5b). This constitutes a huge reduction in velocity and aids further deposition. Resultant aggradation within the wider incised margin to continues to reduce depth, however the now confined flow causes the associated widening response to affect the very high banks (Figure 7.5c). Even limited lateral erosion to steep

banks can translate to a disproportionately big mobilization of material, as hydraulic work is augmented by mass failure under gravity (Figure 7.5d).

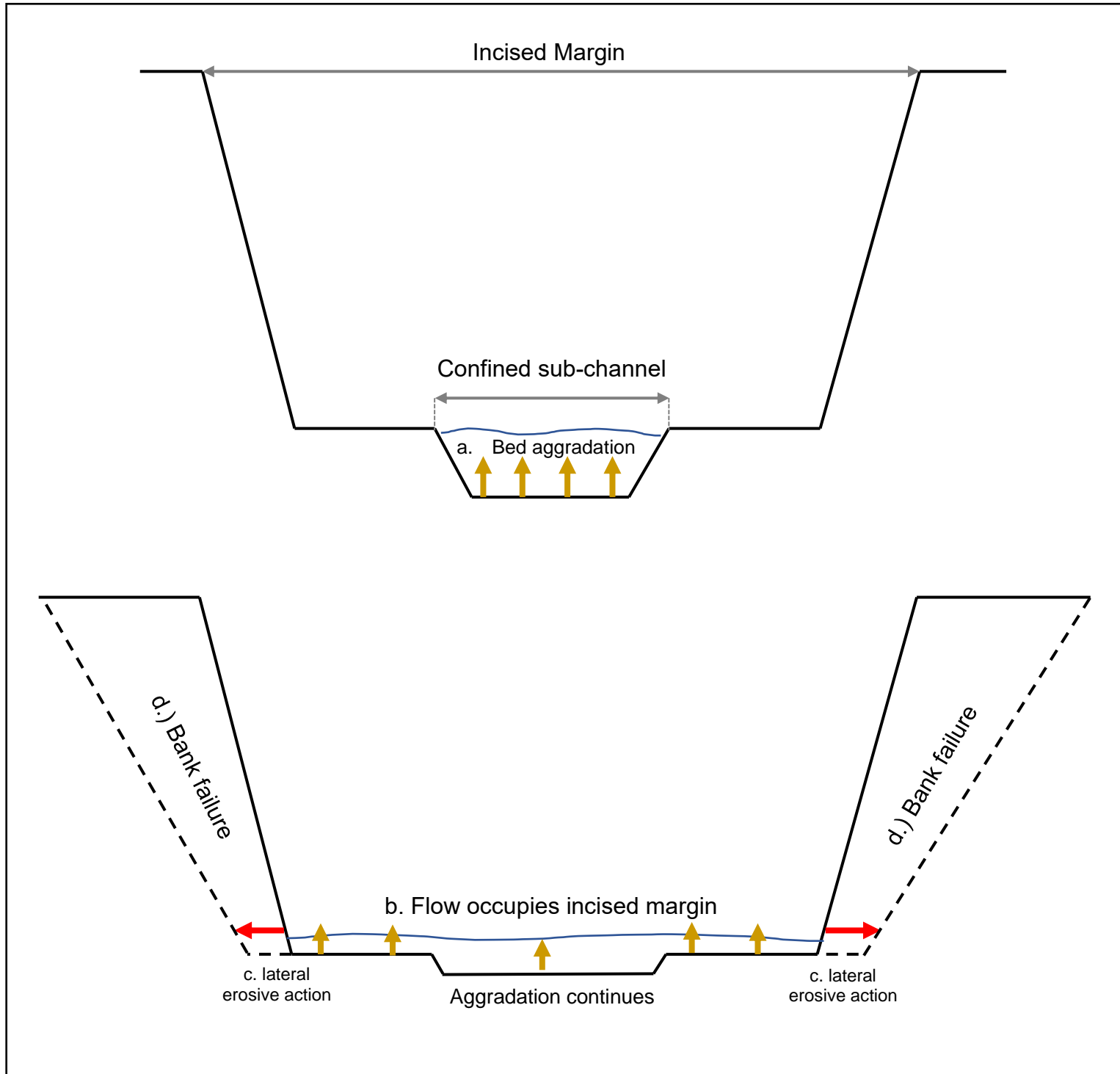


Figure 7.5 – Diagrammatic representation of a widening mechanism in an incised river.

This model of development is somewhat replicated at the right bank of sub-reach B of the Wooler Water Study Site. Figure 7.7 is a cross sectional profile of the right bank of the incised margin in sub-reach B which includes two sub-channels which diverge

approximately 30m upstream (south) of the transect line. The location of the cross section transect is shown in Figure 7.6, overlaid by orthomosaic imagery for Survey 1 (2016) and Survey 4 (2018).

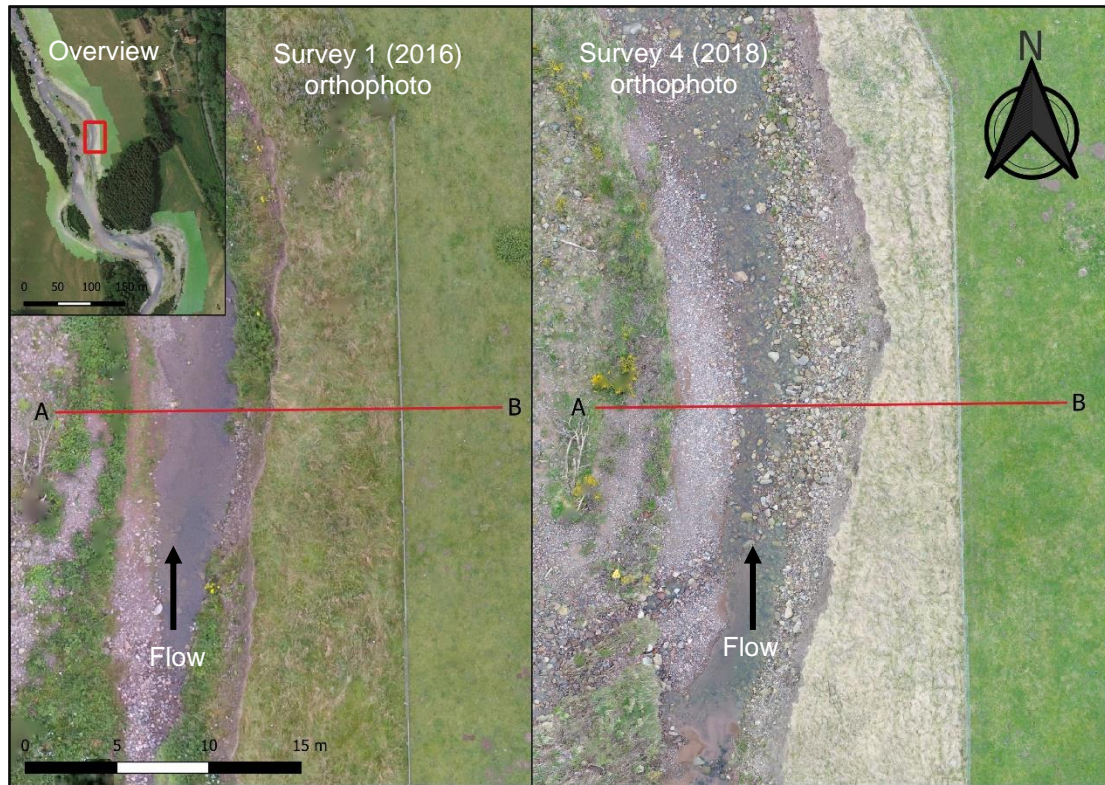


Figure 7.6 – Cross sectional transect location.

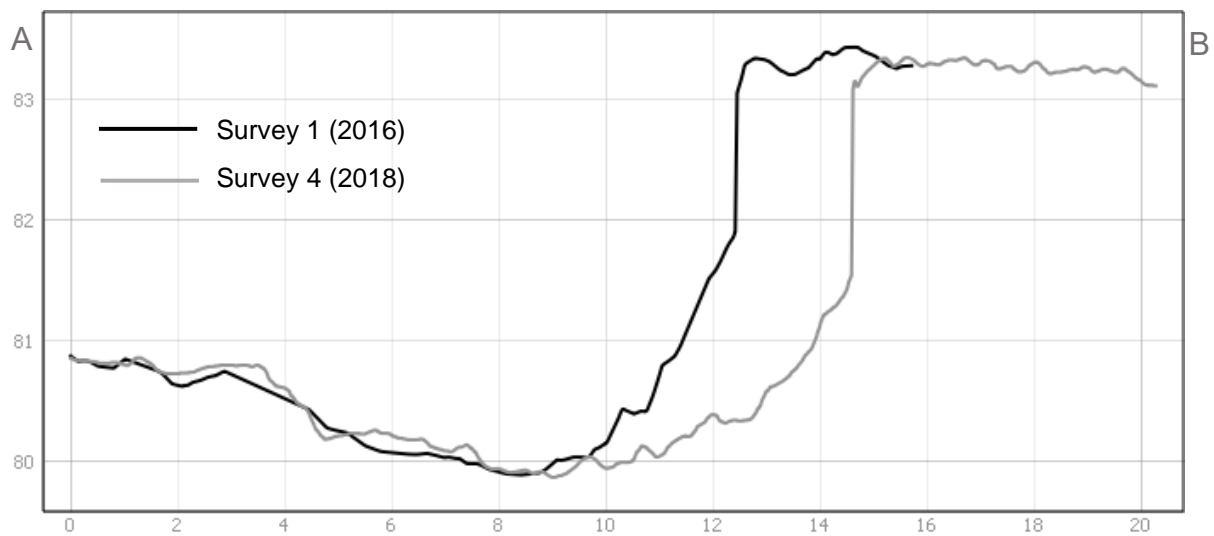


Figure 7.7 – Cross sectional profile of right bank in Sub-reach B.

Inspection of Figure 7.7 indicates minimal vertical change to the river bed, in this case the lowest point of the cross section, which is validated by inspection of the associated DoD map presented in Chapter 6 (Figure 6.13). Vertical stability is more compromised downstream within this sub-channel as erosion becomes more prevalent on the inner (left) bank but does not exceed 0.25m until convergence of the two sub-channels. Bank erosion is very dominant within this section. Figure 7.7 illustrates a bank retreat of approximately 2m, for the outer 100m stretch of right bank in Sub-reach B. Collapse of this right bank accounts for nearly half (451m³) of all erosion within Sub-reach B between Surveys 1 and 2. This coincides with the maximum recorded flow during the field campaign, which occurred on the 22nd of November 2016 during Storm Angus. If bank eroded material is excluded from budgetary calculations for this inter-survey epoch the sediment budget of the entire survey site becomes almost neutral, from -531m³ to just -80m³. Additional but more minor bank erosion is seen to occur within the highly sinuous Sub-reach F. Bank losses here approximate 150m³, however bed stability is fairly consistent.

Table 7.2 – Source: Janes *et al.*, (2018), modelled bank retreat rates for UK rivers.

	Mean Bank retreat rate per year (m/yr)	Mean Bank retreat as a percentage of mean channel width (%)
Exe	0.114	0.78
Avon	0.117	0.82
Itchen	0.09	0.59
Stour	0.075	0.91
Wye	0.074	0.39
Eye	0.086	0.72
Ouse	0.105	0.49
Wooler Water (This Study)	0.830	4.10

For the case of sub-reach B the rate of bank retreat is considerably higher than other UK rivers. These UK values presented in Spiekermann *et al.*, (2017) and Janes *et al.*, (2018)

are more conservative than the global mean of 0.86 m/yr and 1.6% channel width/yr as measured by Walker and Rutherford, (1999) which is more comparable to the data presented by this study. Whilst data for Wooler Water is more localised, the sub-reach in question shows to be undergoing significant planform adjustment characteristic of meander development. Large flood pulse flows are a necessary driver of this planform adjustment. High discharge events have been shown to be important forcers of riverbank erosion, particularly for cohesive margins (Wolman, 1959; Julian and Torres, 2006). Subaerial processes do contribute to sediment mobilization (Henshaw *et al.*, 2013), threshold exceedance by flood pulse flows is what drives bank erosion (Palmer *et al.*, 2014). This agrees with observations at Wooler Water. The majority (>60%) of bank erosion takes place between Survey's 1 and 2 during which the peak flow of level of 1.1m is recorded at Coldgate Mill. Other inter-survey peaks are measured at 0.8m and 0.6m for Survey 2-3 and 3-4 respectively. Bank erosion is seen to occur during these times, however a larger portion of lost material may be attributed to subaerial processes.

In terms of the evolutionary trajectory that is implied by the significant bank erosion at sub-reach B, an indirectly proportional increase in channel sinuosity is to be expected following particularly high (>1m) level flows. The most recent flow of such magnitude was in November of 2016, however such flood pulse events have been observed to occur multiple times per year, as in 2012. Continuation at the current estimated rate of 0.83 m/yr will see outflanking of the remaining legacy weirs within sub-reach C in the short-term (1-5 years.) In the long term, a counter-bending meander channel may be expected to form downstream of the present area of most aggressive lateral erosion (Walker and Rutherford, 1999). Such a course would be consistent with the natural evolution of wandering gravel bed rivers and contrary to the straightened course which currently exists (Desloges and Church, 1989; Fuller *et al.*, 2003). Erosion to the left bank within

Sub-reach C has potential to reveal another, even larger source of material for fluvial transport, due to the natural rise in the landscape there. Vertical separations of nearly 15m exist between the current river-bed, and the land adjacent to its left bank. Furthermore, this steep slope is forested, thus bank collapses will certainly introduce woody debris that will further serve to deflect flows and introduce bed dynamism. Lateral vs Vertical Stability

The general geomorphic findings of this thesis may be summarised by the observed widening due to bank erosion within sub-reach B and F, which are currently the most sinuous sections. The material mobilised by this action is a significant fraction of all sediment that is being lost from the study reach. If lateral erosion is ignored, the negative sediment budget is effectively neutralised, becoming positive in the case of inter-survey period 1-2. Such a sediment regime is reflective of a system undergoing slow aggradation, as might be expected during following in-channel gravel extraction. Large flows, such as that which occurred in 2013 and 2016 may be expected to cause significant vertical and lateral expansion given their increased stream power, however for the case of Wooler Water the observed erosion is limited to the horizontal dimension. Large scale vertical adjustment is not comparable to the lateral changes seen, nor is it proportional to the magnitude of flows between each survey. Internal bed dynamics are present in the form of gravel feature creation, but no generalized vertical adjustment can be detected by the data presented here.

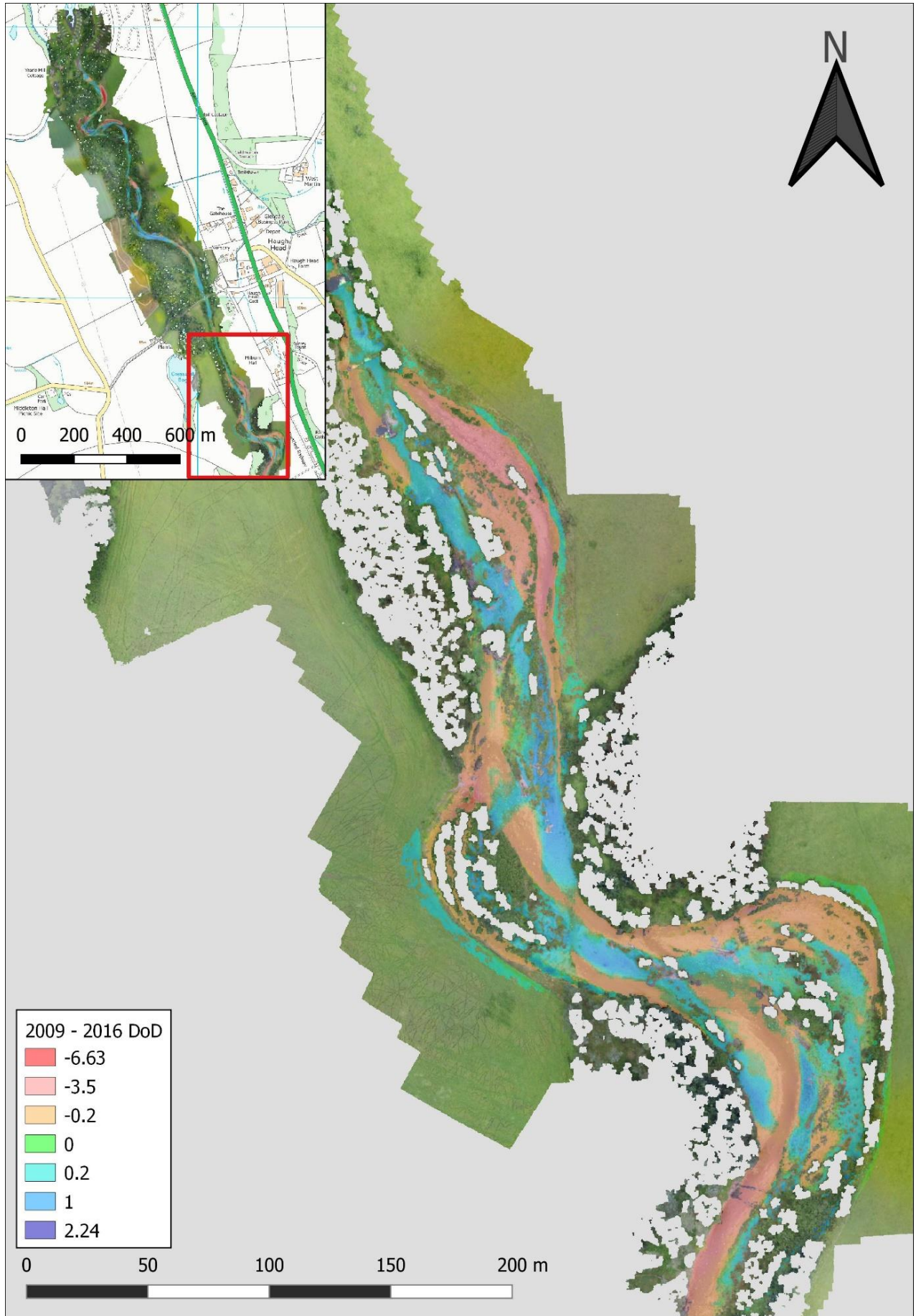


Figure 7.8 – Upstream half of full-scale DoD for 2009 LiDAR against 2016 UAV Dataset.

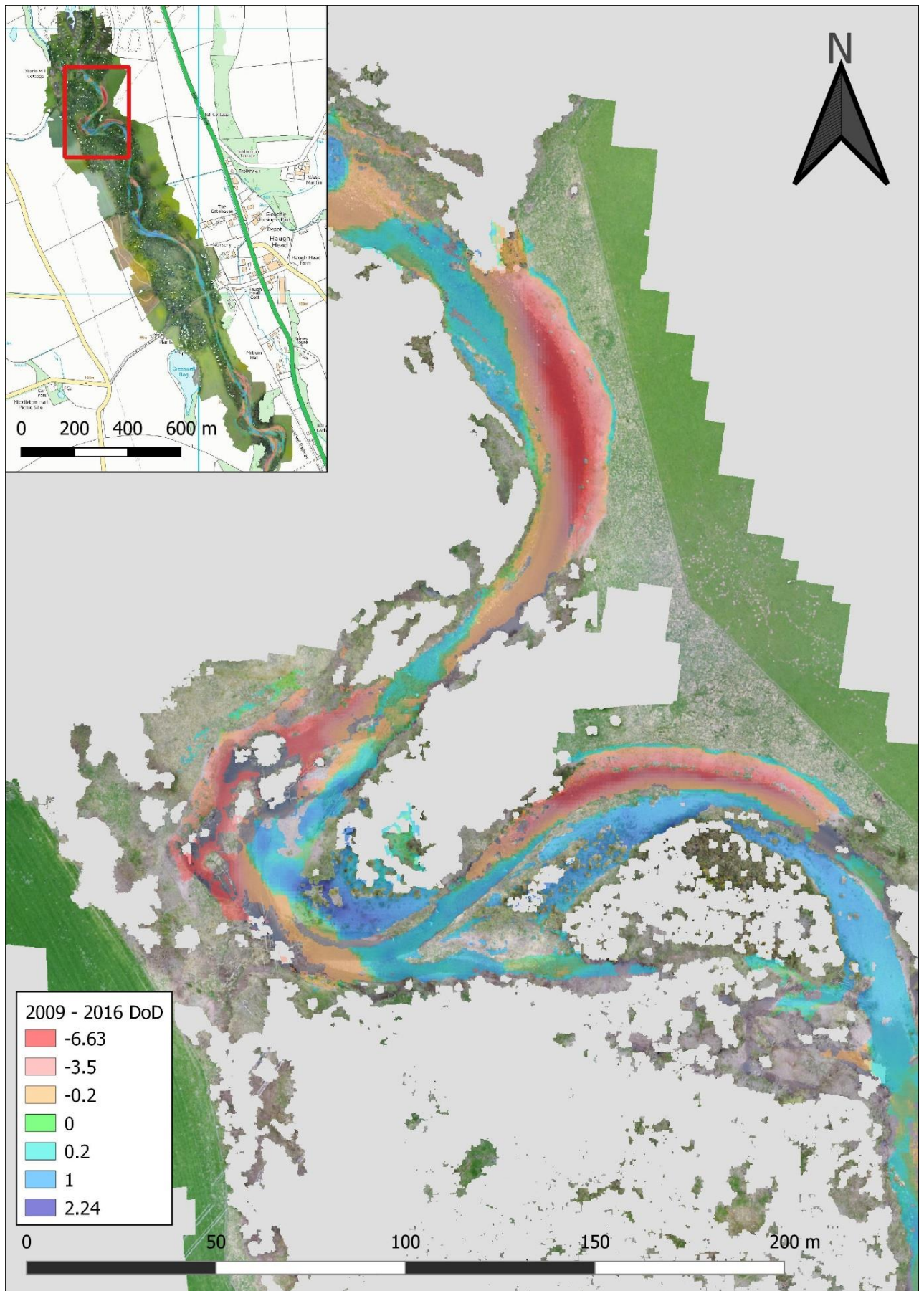


Figure 7.9 - Downstream half of full-scale DoD for 2009 LiDAR against 2016 UAV Dataset.

For a 32 m³/s flow (2016 Peak) the reflected mean retreat of the right bank in sub-reach B approximates 3.5m. Comparison of the UAV data acquired by Survey 1 to the open LiDAR dataset from 2009, it is evident that maximum bank retreat of 34m in Sub-reach B and 19m in Sub-reach F have occurred between 2009 and 2016. Figure 7.8 and Figure 7.9 are DoD change maps for the 2009 LiDAR and 2016 Drone DEMs. Volumetric change data is included within Table 7.1. The pattern of geomorphic change remains similar to that seen during this project's field campaign, lateral expansion accompanied by relatively vertical stability or accretion in places. It is known that some flows which occurred between 2009 and 2016 are considerably larger than peak discharge events recorded during the course of this thesis. A recorded river level of 1.91 in October 2013, translates to an estimated discharge of approx. 100 m³/s is the maximum between 2009 and 2016. Figure 7.10 shows a cross section spanning the same transect as in Figure 7.6 and Figure 7.7. A bank retreat of approximately 20m is observed between 2009 and 2016. Whilst the precise amount of widening caused by the 2013 peak cannot be known, it is possible to ascertain what effect this flow might have had upon the river's bed by relating known discharge values to the median size of clasts which are not moved between surveys. Since peak flow river level data is not known for Sub-reach B, data from the Coldgate Mill

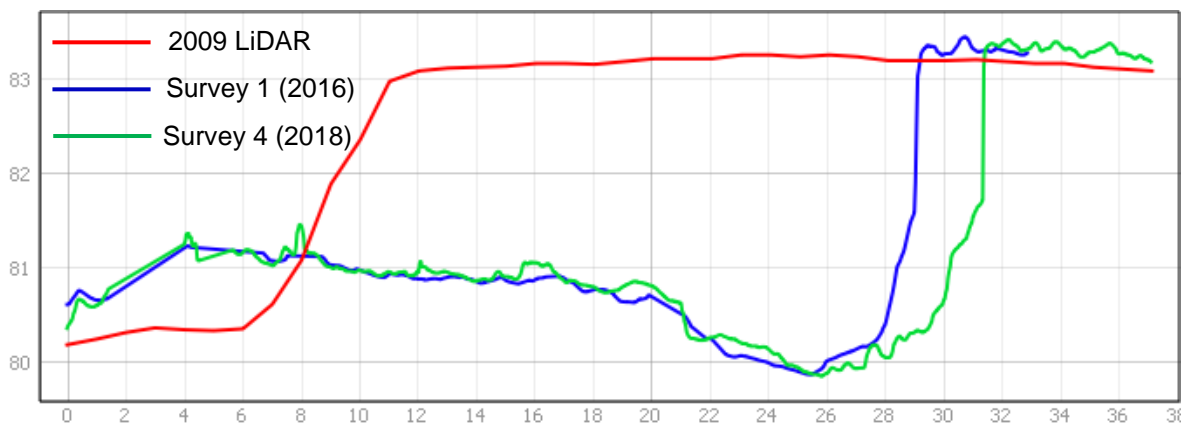


Figure 7.10 – Cross sectional profile along the same transect as in Figure 7.6, including LiDAR DEM gauging station will be used to approximate the mean flow velocity of the 2013 maximum

at this location. Estimated velocity during the peak flow within the 30m wide channel at the gauging station was 2.1 m/s^{-1} , based upon a slope of 0.015 and roughness coefficient of 0.055. A mean water depth of 1.26m was calculated for the 2013 flow at the gauging station based on the trapezoidal fitting applied to Figure 7.3. Assuming a channel width of 30m at that location, this translates to a mean depth within the right-hand channel of Sub-reach B of 0.95m. Special consideration must be taken however due to the dual nature of the channels within this section. Calculations were made based on the full 50m width of the incised margin and then adjusted (divided by two) to account for the splitting of the sub-reach into two channels, approximately 25m wide, separated by a 5m wide vegetated island. This estimates the velocity within right channel of Sub-reach B to be at

least 1.8 m/s^{-1} . Visual inspection of high-resolution imagery between surveys reveals a large number of recognisably static clasts. Figure 7.11 shows a selection of the some of the most easily identifiable boulder sized clasts which are seen to persist throughout the field campaign. This example shows only 9, however the effect is noticeable throughout the right-hand channel of Sub-reach B. The 9 identified clasts do not represent the median size of material observed to persist. Smaller clasts are seen to persist between 2016 and



Figure 7.11 – Example selection of easily identifyable clasts which remain immobile throughout the field campaign.

2018 due to imbrication and hiding of by larger clasts. The generally very coarse material seen within sub-reach B following this flow is a likely cause of the relatively high vertical stability which is seen at Wooler Water.

The sedimentary makeup of Wooler Water's floodplain can be considered to be very heterogenous as the channel currently presides within a river terrace formation of coarse material and sand, identified to have been laid down between 3900 – 4200 years ago (Tipping, 1994; Sear and Archer, 1998). The river bed in Sub-reach B reflects this fact, containing boulders larger than could have been deposited from upstream, that instead have been laid down in-situ as the right bank of the river has retreated and in doing so, exposed them. A diagrammatic representation of this process is illustrated by Figure 7.12. The selective sorting of material liberated from the banks by lateral erosion is the main reason for the lack of obvious vertical scour during the particularly high flow events since

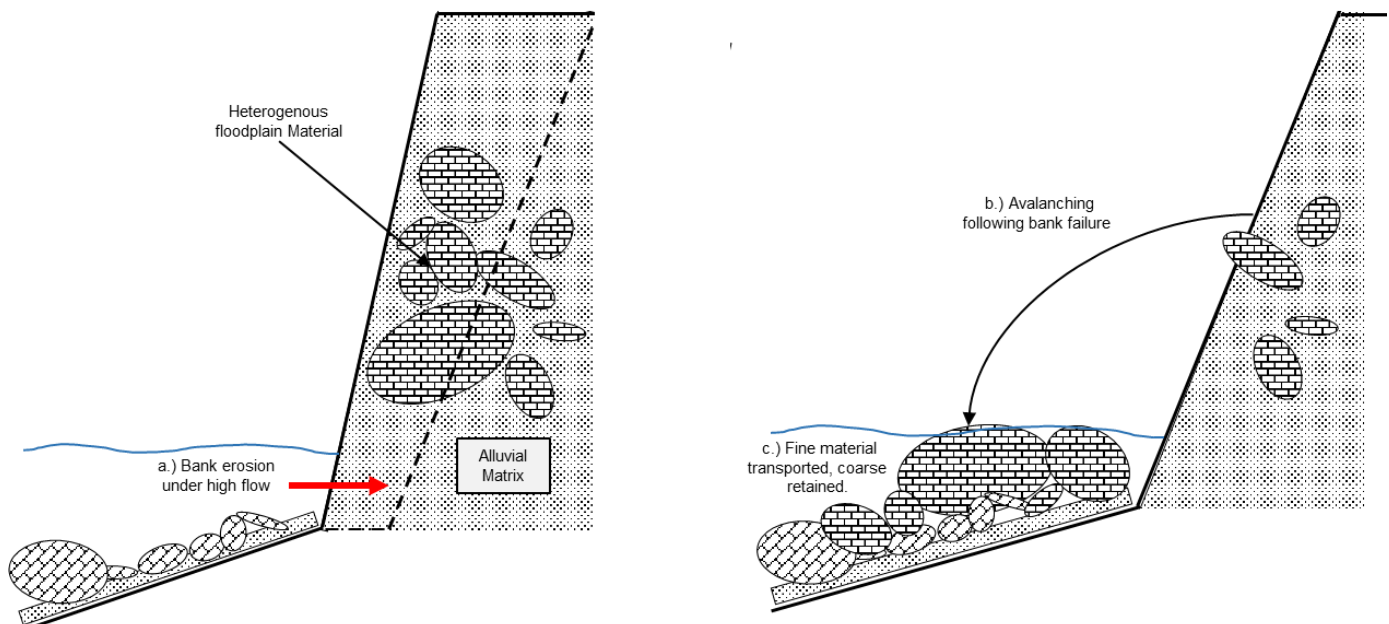


Figure 7.12 – A mechanism for in-situ construction of a bed armour layer by lateral expansion.

armouring of the bed would not be possible if such coarse material were not present. This links the vertical and horizontal components of geomorphic evolution within this section

of the case study; lateral instability and bank erosion permit vertical stabilisation of the river's bed. The process as outlined here is similar to that observed by Erskine, (1992) where the preferential erosion of fine material leaves behind a densely packed layer of coarse clasts that protects underlying sands and gravels. In contrast to this study Erskine, (1992) examines the process in a laterally stable setting. Here, the process is revealed to actually be augmented by lateral erosion, due to the liberation of floodplain facies during bank collapse. Increase re-occurrence of a larger flows, such as that in 2013 (approx. 100 m³/s), may cause a partial breakup of the armour layer (Vericat *et al.*, 2006), however a general increase in water throughput will include a higher frequency of low-medium sized floods (30 m³/s) which are responsible for construction of the armour layer by selective transport and clast liberation from bank avalanches.

7.2. Error Considerations and Limitations

The error for each survey DEM given by Table 4.1 and the associated minimum levels of change detection in Table 6.2 represent the smallest scale of geomorphic change which can be detected by the comparative analyses undertaken by this study. For the purpose of detecting large scale changes such as bank collapse, bar construction and migration, LWD dynamics, a threshold of 10cm is highly conservative as such geomorphic actions usually manifest as vertical change well in-excess of 10cm. Fine scale geomorphic action, such as individual clast mobility or sand bar construction, is harder to detect as the error propagated error of the comparison surface must be below that of size of change occurring. In the case of gravel bed rivers, especially coarse clast dominated systems, this may be of less concern since the minimum "unit" of change (1 clast) may itself be larger than the detection threshold. The size of detection threshold achievable also has implications for detection of the actual X/Y extents (planform extent) of geomorphic

processes such as bars. The edges of such features may be below the detection threshold and thus their size may be slightly underestimated on change maps. This may be mitigated by increasing survey resolution however, such that more cells describe the margins of a geomorphic feature. Comparative analysis of UAV-SfM DEMs, even if completely errorless, is not enough to be able to describe every level of geomorphic evolution in a fluvial system. Secondary data products provided by the UAV methodology, such as high-resolution orthomosaic imagery, do however aid in interpretation of changes and are useful in their own right. Providing RGB data and a more accessible visualisation of site evolution.

7.3. Conclusions

The work of this thesis joins the fields of remote sensing and fluvial geomorphology. The need for accurate, vegetation free, high-resolution topographic data is facilitated by workflows and processing methods which optimise the UAV methodology. Data collection is optimised through careful flight planning according to the users' requirements for coverage and resolution. Planning out the placement GCPs ahead of fieldwork is advised; placement in or as close as possible to the river channel will limit vertical uncertainty in error sensitive sections. Data quality is improved further by application of vegetation and noise filtering tools to the SfM generated point-cloud. These steps may be carried out in both Agisoft Photoscan and in free software, like CloudCompare. Correction for geo-referencing error may be applied by vertically translating one model by a probabilistically determined distance such that it aligns more closely with a compared model. This removes the usefulness of the model as an "absolutely" referenced surface but increases the reliability of volumetric change calculations.

The general geomorphic regime at the Wooler Water field site is vertically static, but laterally unstable. Peak flows lead to lateral erosion, particularly in Sub-reach B and F, where bank collapse events liberate coarse clasts that serve to limit vertical scour of the river's bed. Intermediate level flows (~10-15 m³/s) are seen to also cause more limited lateral erosion whilst permitting retention of finer material on the bed. Incised and sediment starved rivers may be rejuvenated by artificial replenishment of gravels (Kondolf, 1997; Merz & Ochikubo Chan, 2005), however such strategies are very costly and require import of gravels extracted elsewhere. Replication of the bed armouring effect seen at Wooler Water by dumping a lower mass of much coarser clasts into channel may be more efficient. An armoured bed layer benefits the restoration of an incised river channel by preventing further scour and catalysing the transition to a more wandering and laterally mobile system via natural bed aggradation. The reconnection of a previously incised channel to its floodplain holds benefits for flood management and ecological conservation (Heritage et al., 2016).

7.3.1. Research Question 1

1. How are existing channel and bed morphologies influenced by the current flow regime and how might they be affected by future variability?

The current evolutionary trajectory of Wooler Water is dependent upon a varied flow regime, where occasional large flood pulses drive lateral expansion and medium to low flows serve to resupply the bed with more fine material. These medium flow events between that exceed 20 m³/s may occur multiple times per year. The aggradation caused by such flows is most common within Sub-reaches A, B and F. Lateral erosion to the steep banks leads to mass failure and collapse events, avalanching material onto the bed. Bed aggradation in the presence of lateral erosion is afforded by relatively moderate flow events (~30 m³/s), which retain enough energy to erode the banks, but lack the velocity

to strip anything but the finest bed material. Fining of bed material is detected within orthomosaic imagery of sub-reach B following such a flow. High magnitude flow events are responsible for more aggressive lateral erosion and removal of fine bed material. The increased rate of bank erosion is however responsible for creating a self-armouring effect, where coarse floodplain facies are deposited on the riverbed, thereby shielding underlying fine material. The amount of very coarse material liberated is proportional to the amount of bank erosion which occurs, thus higher magnitude flows serve to augment the process. Imbrication and occlusion of intermediate material additionally serves to increase bed resilience. Although limited by the armouring effect, some vertical scour may be expected under very high flows ($\sim 100 \text{ m}^3/\text{s}$). The UK's precipitation regime may see an increased occurrence of extreme rainfall events in the coming decades due to climate change (Ekström *et al.*, 2005). This could in-turn increase the frequency of high magnitude flood events, particularly in for small catchments (Prudhomme *et al.*, 2003) which are more sensitive to highly localised rainfall. Such regime change could lead to an increased rate of vertical scour at Wooler Water however the lateral expansion caused by such pulses may serve to limit bed erosion to a degree. Conversely, a reduction in the return frequency of large flood events will see a decreased rate of bank erosion, offset by increased aggradation. The inability of the river to continue its de-constriction could prevent the formation of ecologically valuable features; pools, riffles and gravel bars.

7.3.2. Research Question 2

2. What present evolutionary trajectories exist for the channel and bed morphology of Wooler Water.

The geomorphic evolution of Wooler Water following the termination of gravel extraction works generally is reflective of an attempt by the system to revert the changes introduced during these works, including vertical incision and channelization. Gentle aggradation of

the bed during medium size flow events ($\sim 10\text{-}15\text{ m}^3/\text{s}$), is observed between Surveys 2-3 and Surveys 3-4 of this study. This is accentuated in more sinuous sections of the study site, such as Sub-reach B and F. Flow events of high magnitude ($>30\text{ m}^3/\text{s}$) are seen to cause lateral erosion, which has the effect of liberating large amounts of extremely coarse material from the steep banks. The release of such clasts results in their concentration on the river bed which limits the ability of flood pulses to cause any further scour. As lateral expansion progresses, bed aggradation may be expected to accelerate as the channel takes on a more wandering form. As channel widening and aggradation take place, high magnitude flood pulses may be expected to overtop the banks of the incised margin. If allowed to do so repeatedly, a transition to an anastomosing system would result. The reconnection of the main channel to its floodplain may constitute the completion of the recovery of Wooler Water's restoration to its pre-extraction layout.

Construction of in-channel features such as gravel bars, chute cut-offs, and channel bifurcations serve to add complexity and diversity to the system. The additional space granted by lateral expansion will permit continued development of these features, which themselves are able to catalyse other geomorphic developments. LWD is seen to be particularly important for providing the initial disturbance required for features such as chute cut-off channels to form. Lateral expansion within the heavily wooded Sub-reaches D and E is more limited. Bank collapses here could lead to inclusions of large amounts of LWD items. The more laterally active Sub-reach F may see further development of in-channel bars or channel bifurcations as a result. Addition of LWD from upstream of the study site can also be expected to contribute to dynamism within Sub-reaches A and B, where lateral expansion is most prevalent.

7.3.3. Research Question 3

2. How extensively and effectively can UAV photogrammetry be applied for multi-scale (kilometric to centimetric) fluvial surveying?

The use of low-cost UAV surveying to acquire the data presented by this study has permitted highly detailed insight of geomorphic processes across a wide scale, although there are several aspects which require increased workload on the part of the user to ensure end data products are fit for purpose. The high-resolution imagery provided by the UAV allows rapid and easy inspection of bed and channel morphologies, enabling users to detect areas and features of geomorphic interest. Compared to traditional field observations on the ground, the aerial perspective gives users a unique viewpoint from which to observe fluvial features at practically any scale. Topographic data generated via SfM provides users with a true digital reconstruction of their river of study. The cost barrier to such surveying methods is fractional when compared to other methods of topographic data collection like LiDAR. Such data must have the highest possible level of accuracy to acquire reliable sediment budget calculations. As survey scale increases, so too does the spatial variability of error within the end elevation model. Without post-processing, wholesale surface comparison of kilometre scale river DEMs produced by UAV-SfM is not reliable enough for practical application.

In order for large DEM surfaces generated by UAV-SfM to be competitive with those produced by LiDAR, their accuracy and resolution must be at least as good if not better. Acquisition of centimetric resolutions is routine for UAV surveying and has been demonstrated by numerous studies (Bhandari *et al.*, 2015; Nolan *et al.*, 2015; Jay *et al.*, 2019). The photogrammetric aspect of the UAV methodology however can increase the error within end-data products. Camera calibration, lens distortion and subject features (shape, illumination, occlusion etc.) all contribute to point-cloud error. This error may be

limited by inclusion of independent ground control points (GCPs), whose known position allows for fine point cloud geo-referencing. The scale of site being surveyed is thus proportional to the number of GCPs required. The placement and referencing of these points remain the most laborious part of the methodology. Even for surveys undertaken to strict methodological standards, resultant surfaces should be subject to full error analysis and validated for quality assurance against independent data if available.

Besides management of vertical error, users must additionally ensure that final DEMs are representative of the ground surface and do not include vegetation and other irrelevant data. Spatial filtering and DEM creation tools are included within photogrammetry software such as Agisoft Photoscan and Pix4D. The default settings for ground point classification may often be sufficient to remove non-ground data if the terrain slope and undulation is limited for the site. For subjects with more variable ground conditions and vegetation types (as in the case of this study) multiple iterations of filtering may be required. The needed parameters for filtering are specific to the site and users should experiment to gauge which settings best detect vegetation whilst not mis-classifying ground points as irrelevant data. The success of point-cloud filtering is visually obvious, especially at the margins of vegetation areas. Isolated viewing of solely ground points or non-ground points is the best way to check for possible classification inaccuracies, as such points will be noticeably disconnected from their neighbours. If desired, users may simply select and manually re-classify point's as necessary, rather than apply another filtering pass.

The maximum scale at which UAV-SfM can be applied is more-so a question of the time available in which to work in field and what final DEM resolution is required. GCP placement and referencing being the most time-consuming step of the data collection process. Resolution and image quantity most strongly define the duration of processing

required. For dedicated workstations with excess RAM and powerful GPU cards, wholesale processing may be feasible. For more standard machines, splitting of the survey site into sections to be joined later may be necessary due to memory limitations. Under best circumstances, the processing machine will have as many GB of RAM as GBs of images which can be processed in one go.

For detection and mapping of centimetric scale geomorphic change, such as sediment size change, the very-high resolution photography provided by the UAV enables visual detection of changes in bed character, quantifiable by application of image-analysis techniques. The methods applied by this thesis for such a purpose are not exhaustive however, and many other methods to precisely measure bedload size exist for aerial imagery and topographic data (Carbonneau *et al.*, 2005b; Verdú *et al.*, 2005b; Woodget *et al.*, 2016). This project demonstrates the applicability of “image-sieving” for detection of individual clasts, albeit at a limited scale, fractional to that of the entire survey extent. The method used here is most suitable to targeted application, however other methods, such as those which quantify roughness as a proxy for sediment size (Vázquez-Tarrío *et al.*, 2017) may be suitable for wholesale application.

The UAV-SfM method requires careful tailoring to the specific river being surveyed, from data collection to post-processing. Subject scale, survey conditions, in-channel vegetation and accessibility to GCP placement locations all affect the level and type of post-processing methods which must be applied to ensure the quality of data outputs. The benefits provided by the UAV-SfM workflow, namely low-cost and easy deployment, when compared to other topographic survey methods, make the method extremely attractive to geomorphic researcher without large capital resources. Such users should however be aware of the need for the relatively large amount of post-processing required to produce competitive data-products. The usefulness of a single UAV-SfM dataset to

multiple scales and types of geomorphic study is dependent foremost upon the GSD to coverage ratio attainable by the surveyor. Smaller ratios will increase required field time and processing resources, thus maximising resolution may not always be feasible. Users should consider the scale of their study and select resolution and flight height accordingly using a workflow such as that suggested by Figure 4.4.

7.3.4. Future Works

This Thesis reveals that a diverse flow regime of both high and low-magnitude flood pulses is needed to recover Wooler Water from its incised state. The geomorphic development of the system is balanced by lateral erosion from high-magnitude flows and by bed aggradation during medium-low flood events. The potential for a flow event larger than $100 \text{ m}^3/\text{s}$ to occur presents an opportunity to observe the resilience of the armoured bed during such a flow and how it may be affected by lateral expansion. If such a flow were to occur, a UAV survey could rapidly capture the resulting developments. A continuous or regular monitoring of Wooler Water will continue to improve knowledge of the self-armouring effect. Wooler Water is highly unique in its mechanism of bed-armouring, however incised channels exist all over the world. Global demand for aggregate and sand is unlikely to see deceleration and present production cannot keep pace (Torres *et al.*, 2017). Exploitation of river and floodplain sediments will additionally place strain on water resources through pollution and channel incision. Any means to limit these effects must be considered, particularly in developing part of the world, where vulnerability is higher (Vörösmarty *et al.*, 2000). For this reason, the continuation of study that seeks to improve and recover the state of gravel-bed river systems is imperative.

The growth of the field will be aided by the continued development of cheap and easy-to-use UAV systems, as well as open source SfM processing package. Such technology will

improve proficiency of current workers whilst opening up the fields of geomorphology and river restoration to a new generation of scientists. Further streamlining of the UAV-SfM workflow will be facilitated by the inclusion of highly accurate real time kinematic (RTK) GPS to drone systems. Presently such platforms are relatively expensive, however as the technology proliferates, cost will decrease. This may eventually negate the need for ground control point placement during fieldwork, which remains the most laborious part of the survey process. This will permit truly remote analysis of rivers, where data collection may be essentially automated.

References

- Agisoft (2011) *Algorithms Used in Photoscan*. Available at: <https://www.agisoft.com/forum/index.php?topic=89.0>.
- Agisoft (2018) *Agisoft PhotoScan User Manual Professional Edition, Version 1.4*. Available at: www.agisoft.com/pdf/photoscan-pro_1_4_en.pdf.
- Ahrens, S., Levine, D., Andrews, G. and How, J. P. (2009) 'Vision-based guidance and control of a hovering vehicle in unknown, GPS-denied environments', in *Robotics and Automation, 2009. ICRA'09. IEEE International Conference*. IEEE, pp. 2643–2648.
- Altmaier, A. and Kany, C. (2002) 'Digital surface model generation from CORONA satellite images', *ISPRS Journal of Photogrammetry and Remote Sensing*, 56(4), pp. 221–235.
- Amici, S., Turci, M., Giammanco, S., Spampinato, L. and Giulietti, F. (2013) 'UAV thermal infrared remote sensing of an Italian mud volcano', *Advances in Remote Sensing*, 2013.
- Andersen, H.-E., McGaughey, R. J. and Reutebuch, S. E. (2005) 'Estimating forest canopy fuel parameters using LIDAR data', *Remote Sensing of Environment*, 94(4), pp. 441–449.
- Anthony, D., Elbaum, S., Lorenz, A. and Detweiler, C. (2014) 'On crop height estimation with UAVs', in *2014 IEEE/RSJ International Conference on Intelligent Robots and Systems*. IEEE, pp. 4805–4812.
- Arnot, M. J., Good, T. R. and Lewis, J. J. M. (1997) 'Photogeological and Image-analysis Techniques for Collection of Large-Scale Outcrop Data: RESEARCH METHOD PAPER', *Journal of sedimentary research*, 67(5).
- Arvor, D., Durieux, L., Andrés, S. and Laporte, M. A. (2013) 'Advances in Geographic Object-Based Image Analysis with ontologies: A review of main contributions and limitations from a remote sensing perspective', *ISPRS Journal of Photogrammetry and Remote Sensing*. Elsevier, pp. 125–137. doi: 10.1016/j.isprsjprs.2013.05.003.
- Ashmore, P. E. and Church, M. (1998) 'Sediment transport and river morphology: a paradigm for study', *Gravel-bed Rivers in the Environment*. Water Resources

-
- Publications: Highlands Ranch, Colorado, pp. 115–148.
- Bagheri, O., Ghodsian, M. and Saadatseresht, M. (2015) 'Reach Scale Application of UAV+ SFM Method in Shallow Rivers Hyperspatial Bathymetry', *The International Archives of Photogrammetry, Remote Sensing and Spatial Information Sciences*, 40(1), p. 77.
- Bagnold, R. A. (1966) *An approach to the sediment transport problem from general physics*. US government printing office.
- Baillard, C. and Maitre, H. (1999) '3-D reconstruction of urban scenes from aerial stereo imagery: a focusing strategy', *Computer Vision and Image Understanding*, 76(3), pp. 244–258.
- Baluja, J., Diago, M. P., Balda, P., Zorer, R., Meggio, F., Morales, F. and Tardaguila, J. (2012) 'Assessment of vineyard water status variability by thermal and multispectral imagery using an unmanned aerial vehicle (UAV)', *Irrigation Science*, 30(6), pp. 511–522.
- Bangen, S. G., Wheaton, J. M., Bouwes, N., Bouwes, B. and Jordan, C. (2014) 'A methodological intercomparison of topographic survey techniques for characterizing wadeable streams and rivers', *Geomorphology*, 206, pp. 343–361. doi: <http://dx.doi.org/10.1016/j.geomorph.2013.10.010>.
- Barclay, J. S. (1980) *Impact of stream alterations on riparian communities in Southcentral Oklahoma*.
- Barnard, J. (2010) 'Use of unmanned air vehicles in oil, gas and mineral exploration activities', in *AUVSI Unmanned Syst. North America Conf., Denver, CO, USA*.
- Barnard, S. T. and Fischler, M. A. (1982) 'Computational stereo', *ACM Computing Surveys (CSUR)*, 14(4), pp. 553–572.
- Barrett, J. S. (1978) 'Instant electronic camera'. Google Patents.
- Barry, P. and Coakley, R. (2013) 'Field Accuracy Test of Rpas Photogrammetry', *Uav-G2013*, pp. 27–31.
- Bellian, J. A., Kerans, C. and Jennette, D. C. (2005) 'Digital outcrop models: applications of terrestrial scanning lidar technology in stratigraphic modeling', *Journal of sedimentary research*, 75(2), pp. 166–176.

- Bendig, J., Yu, K., Aasen, H., Bolten, A., Bennertz, S., Broscheit, J., Gnyp, M. L. and Bareth, G. (2015) 'Combining UAV-based plant height from crop surface models, visible, and near infrared vegetation indices for biomass monitoring in barley', *International Journal of Applied Earth Observation and Geoinformation*, 39, pp. 79–87.
- Bendig, J., Bolten, A. and Bareth, G. (2013) 'UAV-based Imaging for Multi-Temporal, very high Resolution Crop Surface Models to monitor Crop Growth Variability Monitoring des Pflanzenwachstums mit Hilfe multitemporaler und hoch auflösender Oberflächenmodelle von Getreidebeständen auf Basis von Bildern', *Photogrammetrie-Fernerkundung-Geoinformation*, 2013(6), pp. 551–562.
- Berni, J A J, Zarco-Tejada, P. J., Suárez, L., González-Dugo, V. and Fereres, E. (2009) 'Remote sensing of vegetation from UAV platforms using lightweight multispectral and thermal imaging sensors', *Int. Arch. Photogramm. Remote Sens. Spatial Inform. Sci*, 38(6).
- Berni, Jose A J, Zarco-Tejada, P. J., Suárez, L. and Fereres, E. (2009) 'Thermal and narrowband multispectral remote sensing for vegetation monitoring from an unmanned aerial vehicle', *IEEE Transactions on Geoscience and Remote Sensing*, 47(3), pp. 722–738.
- Bhandari, B., Oli, U., Pudasaini, U. and Panta, N. (2015) 'Generation of high resolution DSM using UAV images', in *FIG Working Week*, pp. 17–21.
- Blaschke, T. (2010) 'Object based image analysis for remote sensing', *ISPRS Journal of Photogrammetry and Remote Sensing*, 65(1), pp. 2–16. doi: <http://dx.doi.org/10.1016/j.isprsjprs.2009.06.004>.
- Bond, G., Broecker, W., Johnsen, S., McManus, J., Labeyrie, L., Jouzel, J. and Bonani, G. (1993) 'Correlations between climate records from North Atlantic sediments and Greenland ice', *Nature*, 365(6442), pp. 143–147.
- Booth, D. B. (1990) 'STREAM-CHANNEL INCISION FOLLOWING DRAINAGE-BASIN URBANIZATION 1', *JAWRA Journal of the American Water Resources Association*. Wiley Online Library, 26(3), pp. 407–417.
- Brandtberg, T., Warner, T. A., Landenberger, R. E. and McGraw, J. B. (2003) 'Detection and analysis of individual leaf-off tree crowns in small footprint, high sampling density lidar data from the eastern deciduous forest in North America', *Remote Sensing of*

-
- Environment*, 85(3), pp. 290–303.
- Brasington, J., Rumsby, B. T. and McVey, R. A. (2000) 'Monitoring and modelling morphological change in a braided gravel-bed river using high resolution GPS-based survey', *Earth Surface Processes and Landforms: The Journal of the British Geomorphological Research Group*. Wiley Online Library, 25(9), pp. 973–990.
- Brasington, J., Vericat, D. and Rychkov, I. (2012) 'Modeling river bed morphology, roughness, and surface sedimentology using high resolution terrestrial laser scanning', *Water Resources Research*. John Wiley & Sons, Ltd, 48(11). doi: 10.1029/2012WR012223.
- Bristow, C. S. and Best, J. L. (1993) 'Braided rivers: perspectives and problems', *Geological Society, London, Special Publications*. Geological Society of London, 75(1), pp. 1–11. doi: 10.1144/GSL.SP.1993.075.01.01.
- Brizga, S. O. and Finlayson, B. L. (1990) 'Channel avulsion and river metamorphosis: the case of the Thomson River, Victoria, Australia', *Earth Surface Processes and Landforms*. Wiley Online Library, 15(5), pp. 391–404.
- Brookes, A. (1987) 'River channel adjustments downstream from channelization works in England and Wales', *Earth Surface Processes and Landforms*. Wiley Online Library, 12(4), pp. 337–351.
- Brookes, A. (1990) 'Restoration and enhancement of engineered river channels: some European experiences', *Regulated Rivers: Research & Management*. Wiley Online Library, 5(1), pp. 45–56.
- Brown, L. G. (1992) 'A survey of image registration techniques', *ACM computing surveys (CSUR)*. ACM, 24(4), pp. 325–376.
- Brunier, G., Fleury, J., Anthony, E. J., Gardel, A. and Dussouillez, P. (2016) 'Close-range airborne Structure-from-Motion Photogrammetry for high-resolution beach morphometric surveys: Examples from an embayed rotating beach', *Geomorphology*. Elsevier, 261, pp. 76–88.
- Buckley, S. J., Vallet, J., Braathen, A. and Wheeler, W. (2008) 'Oblique helicopter-based laser scanning for digital terrain modelling and visualisation of geological outcrops', *International Archives of the Photogrammetry, Remote Sensing and Spatial*
-

-
- Information Sciences*, 37(Part B4).
- Buckley, S. J., Enge, H. D., Carlsson, C. and Howell, J. A. (2010) 'Terrestrial laser scanning for use in virtual outcrop geology', *The Photogrammetric Record*, 25(131), pp. 225–239.
- Burke, E. (2009) 'Islam at the Center: Technological Complexes and the Roots of Modernity', *Journal of World History*. University of Hawai'i Press, 20(2), pp. 165–186. Available at: <http://www.jstor.org/stable/40542756>.
- Burton, D., Dunlap, D. B., Wood, L. J. and Flaig, P. P. (2011) 'Lidar intensity as a remote sensor of rock properties', *Journal of sedimentary research*, 81(5), pp. 339–347.
- Buscombe, D. (2008) 'Estimation of grain-size distributions and associated parameters from digital images of sediment', *Sedimentary Geology*, 210(1), pp. 1–10. doi: <https://doi.org/10.1016/j.sedgeo.2008.06.007>.
- Buscombe, D. (2013) 'Transferable wavelet method for grain-size distribution from images of sediment surfaces and thin sections, and other natural granular patterns', *Sedimentology*. John Wiley & Sons, Ltd (10.1111), 60(7), pp. 1709–1732. doi: 10.1111/sed.12049.
- Buscombe, D. and Masselink, G. (2009) 'Grain-size information from the statistical properties of digital images of sediment', *Sedimentology*. John Wiley & Sons, Ltd (10.1111), 56(2), pp. 421–438. doi: 10.1111/j.1365-3091.2008.00977.x.
- Buscombe, D., Rubin, D. M. and Warrick, J. A. (2010) 'A universal approximation of grain size from images of noncohesive sediment', *Journal of Geophysical Research: Earth Surface*. John Wiley & Sons, Ltd, 115(F2). doi: 10.1029/2009JF001477.
- Business Insider (2015) 'The Drones Report: Market forecasts, regulatory barriers, top vendors, and leading commercial applications', *Business Insider*, 27.
- Cai, G., Lum, K.-Y., Chen, B. M. and Lee, T. H. (2010) 'A brief overview on miniature fixed-wing unmanned aerial vehicles', in *Control and Automation (ICCA), 2010 8th IEEE International Conference on*. IEEE, pp. 285–290.
- Caltabiano, D., Muscato, G., Orlando, A., Federico, C., Giudice, G. and Guerrieri, S. (2005) 'Architecture of a UAV for volcanic gas sampling', in *2005 IEEE Conference on Emerging Technologies and Factory Automation*. IEEE, pp. 6 pp. – 744.
-

- Campa, G., Fravolini, M. L., Ficola, A., Napolitano, M. R., Seanor, B. and Perhinschi, M. G. (2004) 'Autonomous aerial refueling for UAVs using a combined GPS-machine vision guidance', in *Proceedings of the AIAA Guidance, Navigation, and Control Conference and Exhibit*, pp. 1–11.
- Campbell, W. (2011) *Introduction to Remote Sensing*. 5th edn. New York: The Guilford Press.
- Canis, B. (2015) *Unmanned aircraft systems (UAS): Commercial outlook for a new industry*. Congressional Research Service Washington.
- Carbonneau, P. E., Bergeron, N. E. and Lane, S. N. (2005a) 'Texture-based image segmentation applied to the quantification of superficial sand in salmonid river gravels', *Earth Surface Processes and Landforms*. John Wiley & Sons, Ltd, 30(1), pp. 121–127. doi: 10.1002/esp.1140.
- Carbonneau, P. E., Bergeron, N. E. and Lane, S. N. (2005b) 'Texture-based image segmentation applied to the quantification of superficial sand in salmonid river gravels', *Earth Surface Processes and Landforms*. John Wiley & Sons, Ltd, 30(1), pp. 121–127. doi: 10.1002/esp.1140.
- Carbonneau, P. E., Lane, S. N. and Bergeron, N. E. (2004) 'Catchment-scale mapping of surface grain size in gravel bed rivers using airborne digital imagery', *Water Resources Research*. John Wiley & Sons, Ltd, 40(7). doi: 10.1029/2003WR002759.
- Carlisle, B. H. (2005) 'Modelling the Spatial Distribution of DEM Error', *Transactions in GIS*. John Wiley & Sons, Ltd (10.1111), 9(4), pp. 521–540. doi: 10.1111/j.1467-9671.2005.00233.x.
- Caroti, G., Martínez-Espejo Zaragoza, I. and Piemonte, A. (2015) 'Accuracy assessment in structure from motion 3D reconstruction from UAV-born images: the influence of the data processing methods.', *International Archives of the Photogrammetry, Remote Sensing & Spatial Information Sciences*, 40.
- Casana, J. and Cothren, J. (2008) 'Stereo analysis, DEM extraction and orthorectification of CORONA satellite imagery: archaeological applications from the Near East', *Antiquity*, 82(317), pp. 732–749.
- Cesetti, A., Frontoni, E., Mancini, A., Zingaretti, P. and Longhi, S. (2009) 'A vision-based

- guidance system for UAV navigation and safe landing using natural landmarks', in *Selected papers from the 2nd International Symposium on UAVs, Reno, Nevada, USA June 8–10, 2009*. Springer, pp. 233–257.
- Chang, H. H. (1986) 'River channel changes: adjustments of equilibrium', *Journal of Hydraulic Engineering*. American Society of Civil Engineers, 112(1), pp. 43–55.
- Chasmer, L., Hopkinson, C. and Treitz, P. (2006) 'Investigating laser pulse penetration through a conifer canopy by integrating airborne and terrestrial lidar', *Canadian Journal of Remote Sensing*. Taylor & Francis, 32(2), pp. 116–125.
- Chisholm, R. A., Cui, J., Lum, S. K. Y. and Chen, B. M. (2013) 'UAV LiDAR for below-canopy forest surveys', *Journal of Unmanned Vehicle Systems*. NRC Research Press, 01(01), pp. 61–68. doi: 10.1139/juvs-2013-0017.
- Clapuyt, F., Vanacker, V. and Van Oost, K. (2016) 'Reproducibility of UAV-based earth topography reconstructions based on Structure-from-Motion algorithms', *Geomorphology*, 260, pp. 4–15.
- Cobby, D. M., Mason, D. C. and Davenport, I. J. (2001) 'Image processing of airborne scanning laser altimetry data for improved river flood modelling', *ISPRS Journal of Photogrammetry and Remote Sensing*. Elsevier, 56(2), pp. 121–138.
- Colomina, I. and Molina, P. (2014) 'Unmanned aerial systems for photogrammetry and remote sensing: A review', *ISPRS Journal of Photogrammetry and Remote Sensing*, 92, pp. 79–97. doi: <http://dx.doi.org/10.1016/j.isprsjprs.2014.02.013>.
- Cook, K. L. (2017) 'An evaluation of the effectiveness of low-cost UAVs and structure from motion for geomorphic change detection', *Geomorphology*, 278, pp. 195–208. doi: <https://doi.org/10.1016/j.geomorph.2016.11.009>.
- Dade, W. B. and Friend, P. F. (1998) 'Grain-Size, Sediment-Transport Regime, and Channel Slope in Alluvial Rivers', *The Journal of Geology*. The University of Chicago Press, 106(6), pp. 661–676. doi: 10.1086/516052.
- Derrien, M., Farki, B., Harang, L., LeGleau, H., Noyalet, A., Pochic, D. and Sairouni, A. (1993) 'Automatic cloud detection applied to NOAA-11/AVHRR imagery', *Remote Sensing of Environment*, 46(3), pp. 246–267.
- Desloges, J. R. and Church, M. A. (1989) 'WANDERING GRAVEL-BED RIVERS', *The*

-
- Canadian Geographer / Le Géographe canadien*. John Wiley & Sons, Ltd (10.1111), 33(4), pp. 360–364. doi: 10.1111/j.1541-0064.1989.tb00922.x.
- Deurloo, R., Bastos, L. and Bos, M. (2012) 'On the use of UAVs for strapdown airborne gravimetry', in *Geodesy for Planet Earth*. Springer, pp. 255–261.
- Dietrich, W. E., Nelson, P. A., Yager, E., Venditti, J. G., Lamb, M. P. and Collins, L. (2005) 'Sediment patches, sediment supply, and channel morphology', *River Coastal and Estuarine Morphodynamics*. Taylor and Francis Philadelphia, Pa., pp. 79–90.
- van Dijk, W. M., Schuurman, F., van de Lageweg, W. I. and Kleinhans, M. G. (2014) 'Bifurcation instability and chute cutoff development in meandering gravel-bed rivers', *Geomorphology*, 213, pp. 277–291. doi: <https://doi.org/10.1016/j.geomorph.2014.01.018>.
- Doeglas, D. J. (1962) 'the Structure of Sedimentary Deposits of Braided Rivers', *Sedimentology*. John Wiley & Sons, Ltd, 1(3), pp. 167–190. doi: 10.1111/j.1365-3091.1962.tb00453.x.
- Dozier, J. (1984) 'Snow reflectance from Landsat-4 thematic mapper', *IEEE Transactions on Geoscience and Remote Sensing*, (3), pp. 323–328.
- Dozier, J. (1989) 'Spectral signature of alpine snow cover from the Landsat Thematic Mapper', *Remote Sensing of Environment*, 28, pp. 9–22.
- Drake, J. B., Dubayah, R. O., Clark, D. B., Knox, R. G., Blair, J. B., Hofton, M. A., Chazdon, R. L., Weishampel, J. F. and Prince, S. (2002) 'Estimation of tropical forest structural characteristics using large-footprint lidar', *Remote Sensing of Environment*, 79(2), pp. 305–319.
- Dreimanis, A. (1977) 'Late Wisconsin glacial retreat in the Great Lakes region, North America', *Annals of the New York Academy of Sciences*, 288(1), pp. 70–89.
- Dubayah, R. O. and Drake, J. B. (2000) 'Lidar remote sensing for forestry', *Journal of Forestry*, 98(6), pp. 44–46.
- Ebert, E. (1987) 'A pattern recognition technique for distinguishing surface and cloud types in the polar regions', *Journal of Climate and Applied Meteorology*, 26(10), pp. 1412–1427.
- Edwards, M. B. (1975) 'Glacial retreat sedimentation in the Smalfjord Formation, late
-

- Precambrian, north Norway', *Sedimentology*, 22(1), pp. 75–94.
- Ekström, M., Fowler, H. J., Kilsby, C. G. and Jones, P. D. (2005) 'New estimates of future changes in extreme rainfall across the UK using regional climate model integrations. 2. Future estimates and use in impact studies', *Journal of Hydrology*, 300(1), pp. 234–251. Available at: http://ac.els-cdn.com/S0022169404002823/1-s2.0-S0022169404002823-main.pdf?_tid=f0e511f6-c055-11e6-9478-00000aacb361&acdnat=1481538782_834e1762bb0182dfdf7d414ff0c3c515.
- Entwistle, N. S. and Fuller, I. C. (2009) 'Terrestrial Laser Scanning to Derive Surface Grain Size Facies Character of Gravel Bars', *Laser Scanning for the Environmental Sciences*. (Wiley Online Books). doi: doi:10.1002/9781444311952.ch7.
- Erskine, W. D. (1986) 'River metamorphosis and environmental change in the Macdonald Valley, New South Wales, since 1949', *Australian Geographical Studies*. John Wiley & Sons, Ltd, 24(1), pp. 88–107. doi: 10.1111/j.1467-8470.1986.tb00513.x.
- Erskine, W. D. (1990) 'Environmental impacts of sand and gravel extraction on river systems', *The Brisbane River: a source book for the future*, Australian Littoral Society, Moorooka, pp. 295–302.
- Erskine, W. D. (1992) 'Channel response to large-scale river training works: hunter river, Australia', *Regulated Rivers: Research & Management*. John Wiley & Sons, Ltd, 7(3), pp. 261–278. doi: 10.1002/rrr.3450070305.
- Erskine, W. D. and White, L. J. (1996) 'Historical river metamorphosis of the Cann River, East Gippsland, Victoria', in *First National Conference on Stream Management in Australia, Merrijig, Cooperative Research Centre for Catchment Hydrology, Melbourne*, pp. 277–282.
- FAA (2004) *Handbook, Airplane Flying*. Edited by F. S. S. US Department of Transportation.
- Ferguson, R. I. (1993) 'Understanding braiding processes in gravel-bed rivers: progress and unsolved problems', *Geological Society, London, Special Publications*. Geological Society of London, 75(1), pp. 73–87.
- Feurer, D., Bailly, J.-S., Puech, C., Le Coarer, Y. and Viau, A. A. (2008) 'Very-high-resolution mapping of river-immersed topography by remote sensing', *Progress in Physical Geography*, 32(4), pp. 403–419. doi: 10.1177/0309133308096030.

-
- Flener, C. *et al.* (2013) 'Seamless mapping of river channels at high resolution using mobile LiDAR and UAV-photography', *Remote Sensing*. Multidisciplinary Digital Publishing Institute, 5(12), pp. 6382–6407.
- Flynn, K. and Chapra, S. (2014) 'Remote Sensing of Submerged Aquatic Vegetation in a Shallow Non-Turbid River Using an Unmanned Aerial Vehicle', *Remote Sensing*, 6(12), p. 12815. Available at: <http://www.mdpi.com/2072-4292/6/12/12815>.
- Fonstad, Mark A, Dietrich, J. T., Courville, B. C., Jensen, J. L. and Carbonneau, P. E. (2013) 'Topographic structure from motion: a new development in photogrammetric measurement', *Earth Surface Processes and Landforms*, 38(4), pp. 421–430. doi: 10.1002/esp.3366.
- Fonstad, Mark A., Dietrich, J. T., Courville, B. C., Jensen, J.-2013-E. pdf. L. and Carbonneau, P. E. (2013) 'Topographic structure from motion: A new development in photogrammetric measurement', *Earth Surface Processes and Landforms*. doi: 10.1002/esp.3366.
- Fraser, C. and Ravanbakhsh, M. (2009) 'Georeferencing performance of Geoeye-1', *Photogrammetric engineering & remote sensing*, 75(6), pp. 634–638.
- Fuller, I. C., Large, A. R. G. and Milan, D. J. (2003) 'Quantifying channel development and sediment transfer following chute cutoff in a wandering gravel-bed river', *Geomorphology*, 54(3), pp. 307–323. doi: [https://doi.org/10.1016/S0169-555X\(02\)00374-4](https://doi.org/10.1016/S0169-555X(02)00374-4).
- Funaki, M. and Hirasawa, N. (2008) 'Outline of a small unmanned aerial vehicle (Ant-Plane) designed for Antarctic research', *Polar Science*, 2(2), pp. 129–142. doi: <http://dx.doi.org/10.1016/j.polar.2008.05.002>.
- Galay, V. J. (1983) 'Causes of river bed degradation', *Water resources research*. Wiley Online Library, 19(5), pp. 1057–1090.
- George, E. A., Tiwari, G., Yadav, R. N., Peters, E. and Sadana, S. (2013) 'UAV systems for parameter identification in agriculture', in *Global Humanitarian Technology Conference: South Asia Satellite (GHTC-SAS), 2013 IEEE*. IEEE, pp. 270–273.
- Gitelson, A. A. (2004) 'Wide Dynamic Range Vegetation Index for Remote Quantification of Biophysical Characteristics of Vegetation', *Journal of Plant Physiology*, 161(2), pp.

- 165–173. doi: <http://dx.doi.org/10.1078/0176-1617-01176>.
- Goldhagen, P., Clem, J. M. and Wilson, J. W. (2003) 'Recent results from measurements of the energy spectrum of cosmic-ray induced neutrons aboard an ER-2 airplane and on the ground', *Advances in Space Research*, 32(1), pp. 35–40. doi: [http://dx.doi.org/10.1016/S0273-1177\(03\)90367-X](http://dx.doi.org/10.1016/S0273-1177(03)90367-X).
- Gregory, K. J., Davis, R. J. and Downs, P. W. (1992) 'Identification of river channel change to due to urbanization', *Applied Geography*. Elsevier, 12(4), pp. 299–318.
- Gunasekaran, S. (1996) 'Computer vision technology for food quality assurance', *Trends in Food Science and Technology*. Elsevier, pp. 245–256. doi: 10.1016/0924-2244(96)10028-5.
- Gutman, G., Tarpley, D. and Ohring, G. (1987) 'Cloud screening for determination of land surface characteristics in a reduced resolution satellite data set', *International Journal of Remote Sensing*, 8(6), pp. 859–870.
- Hall, D. K., Ormsby, J. P., Bindschadler, R. A. and Siddalingaiah, H. (1987) 'Characterization of snow and ice reflectance zones on glaciers using Landsat Thematic Mapper data', *Annals of glaciology*, 9, pp. 104–108.
- Hall, D. K., Chang, A. T. C., Foster, J. L., Benson, C. S. and Kovalick, W. M. (1989) 'Comparison of in situ and Landsat derived reflectance of Alaskan glaciers', *Remote Sensing of Environment*, 28, pp. 23–31.
- Hall, D. K., Riggs, G. A. and Salomonson, V. V (1995) 'Development of methods for mapping global snow cover using moderate resolution imaging spectroradiometer data', *Remote Sensing of Environment*, 54(2), pp. 127–140.
- Hamilton, P. M. (1969) 'The application of a pulsed-light rangefinder (lidar) to the study of chimney plumes', *Philosophical Transactions of the Royal Society of London A: Mathematical, Physical and Engineering Sciences*, 265(1161), pp. 153–172.
- Harvey, M. D. and Smith, T. W. (1998) 'Gravel mining impacts on San Benito River, California', in *Stream Stability and Scour at Highway Bridges: Compendium of Stream Stability and Scour Papers Presented at Conferences Sponsored by the Water Resources Engineering (Hydraulics) Division of the American Society of Civil Engineers*. ASCE, p. 80.

- Harwin, S. and Lucieer, A. (2012) 'Assessing the accuracy of georeferenced point clouds produced via multi-view stereopsis from unmanned aerial vehicle (UAV) imagery', *Remote Sensing*. Molecular Diversity Preservation International, 4(6), pp. 1573–1599.
- Hassan, M. A. and Church, M. (2000) 'Experiments on surface structure and partial sediment transport on a gravel bed', *Water Resources Research*. John Wiley & Sons, Ltd, 36(7), pp. 1885–1895. doi: 10.1029/2000WR900055.
- Henshaw, A. J., Thorne, C. R. and Clifford, N. J. (2013) 'Identifying causes and controls of river bank erosion in a British upland catchment', *CATENA*, 100, pp. 107–119. doi: <https://doi.org/10.1016/j.catena.2012.07.015>.
- Heritage, G., Entwistle, N. and Bentley, S. (2016) *Floodplains: the forgotten and abused component of the fluvial system*, *E3S Web of Conferences*. doi: 10.1051/e3sconf/20160713007.
- Heritage, G. L., Milan, D. J., Large, A. R. G. and Fuller, I. C. (2009) 'Influence of survey strategy and interpolation model on DEM quality', *Geomorphology*, 112(3–4), pp. 334–344. doi: 10.1016/j.geomorph.2009.06.024.
- Heritage, G. L. and Milan, D. J. (2009) 'Terrestrial Laser Scanning of grain roughness in a gravel-bed river', *Geomorphology*, 113(1), pp. 4–11. doi: <https://doi.org/10.1016/j.geomorph.2009.03.021>.
- Hernandez-Lopez, D., Felipe-Garcia, B., Gonzalez-Aguilera, D. and Arias-Perez, B. (2013) 'An automatic approach to UAV flight planning and control for photogrammetric applications', *Photogrammetric Engineering & Remote Sensing*. American Society for Photogrammetry and Remote Sensing, 79(1), pp. 87–98.
- Hodge, R., Brasington, J. and Richards, K. (2009) 'In situ characterization of grain-scale fluvial morphology using Terrestrial Laser Scanning', *Earth Surface Processes and Landforms*. John Wiley & Sons, Ltd, 34(7), pp. 954–968. doi: 10.1002/esp.1780.
- Hodgson, D. M. (2013) 'Laser scanning and digital outcrop geology in the petroleum industry: A review', *Marine and Petroleum Geology*. doi: 10.1016/j.marpetgeo.2013.02.014.
- Hooke, J. M. (1995) 'River channel adjustment to meander cutoffs on the River Bollin and

-
- River Dane, northwest England', *Geomorphology*, 14(3), pp. 235–253. doi: [https://doi.org/10.1016/0169-555X\(95\)00110-Q](https://doi.org/10.1016/0169-555X(95)00110-Q).
- Hooke, J. and Perry, R. A. (1976) 'The planimetric accuracy of tithe maps', *The Cartographic Journal*. Taylor & Francis, 13(2), pp. 177–183.
- Howat, I. M., Joughin, I. and Scambos, T. A. (2007) 'Rapid changes in ice discharge from Greenland outlet glaciers', *Science*, 315(5818), pp. 1559–1561.
- Hummel, S., Hudak, A. T., Uebler, E. H., Falkowski, M. J. and Megown, K. A. (2011) 'A comparison of accuracy and cost of LiDAR versus stand exam data for landscape management on the Malheur National Forest', *Journal of forestry*. Oxford University Press, 109(5), pp. 267–273.
- Huntingford, C., Jones, R. G., Prudhomme, C., Lamb, R., Gash, J. H. C. and Jones, D. A. (2003) 'Regional climate-model predictions of extreme rainfall for a changing climate', *Quarterly Journal of the Royal Meteorological Society*, 129(590), pp. 1607–1621.
- Hussain, M., Chen, D., Cheng, A., Wei, H. and Stanley, D. (2013) 'Change detection from remotely sensed images: From pixel-based to object-based approaches', *ISPRS Journal of Photogrammetry and Remote Sensing*. Elsevier, pp. 91–106. doi: [10.1016/j.isprsjprs.2013.03.006](https://doi.org/10.1016/j.isprsjprs.2013.03.006).
- Van Iersel, W. K., Straatsma, M. W., Addink, E. A. and Middelkoop, H. (2016) 'Monitoring phenology of floodplain grassland and herbaceous vegetation with UAV imagery', in *XXIII ISPRS Congress, Commission VII, 12–19 July 2016, Prague, Czech Republic*. International Society for Photogrammetry and Remote Sensing, pp. 569–571.
- Immerzeel, W. W., Kraaijenbrink, P. D. A., Shea, J. M., Shrestha, A. B., Pellicciotti, F., Bierkens, M. F. P. and de Jong, S. M. (2014) 'High-resolution monitoring of Himalayan glacier dynamics using unmanned aerial vehicles', *Remote Sensing of Environment*, 150, pp. 93–103. doi: [10.1016/j.rse.2014.04.025](https://doi.org/10.1016/j.rse.2014.04.025).
- James, L. A., Hodgson, M. E., Ghoshal, S. and Latiolais, M. M. (2012) 'Geomorphic change detection using historic maps and DEM differencing: The temporal dimension of geospatial analysis', *Geomorphology*, 137(1), pp. 181–198. doi: <https://doi.org/10.1016/j.geomorph.2010.10.039>.
- James, M. R., Robson, S., d'Oleire-Oltmanns, S. and Niethammer, U. (2017) 'Optimising
-

- UAV topographic surveys processed with structure-from-motion: Ground control quality, quantity and bundle adjustment', *Geomorphology*, 280, pp. 51–66. doi: <https://doi.org/10.1016/j.geomorph.2016.11.021>.
- James, M. R. and Robson, S. (2012) 'Straightforward reconstruction of 3D surfaces and topography with a camera: Accuracy and geoscience application', *Journal of Geophysical Research: Earth Surface*. John Wiley & Sons, Ltd, 117(F3). doi: 10.1029/2011JF002289.
- Janes, V., Holman, I., Birkinshaw, S., O'Donnell, G. and Kilsby, C. (2018) 'Improving bank erosion modelling at catchment scale by incorporating temporal and spatial variability', *Earth Surface Processes and Landforms*. John Wiley & Sons, Ltd, 43(1), pp. 124–133. doi: 10.1002/esp.4149.
- Jaud, M., Passot, S., Le Bivic, R., Delacourt, C., Grandjean, P. and Le Dantec, N. (2016) 'Assessing the accuracy of high resolution digital surface models computed by PhotoScan® and MicMac® in sub-optimal survey conditions', *Remote Sensing*. Multidisciplinary Digital Publishing Institute, 8(6), p. 465.
- Javernick, L., Brasington, J. and Caruso, B. (2014) 'Modeling the topography of shallow braided rivers using Structure-from-Motion photogrammetry', *Geomorphology*, 213, pp. 166–182. doi: <http://dx.doi.org/10.1016/j.geomorph.2014.01.006>.
- Jay, S., Baret, F., Dutartre, D., Malatesta, G., Héno, S., Comar, A., Weiss, M. and Maupas, F. (2019) 'Exploiting the centimeter resolution of UAV multispectral imagery to improve remote-sensing estimates of canopy structure and biochemistry in sugar beet crops', *Remote Sensing of Environment*. Elsevier, 231, p. 110898.
- Jensen, A. M., Hardy, T., McKee, M. and Chen, Y. (2011) 'Using a multispectral autonomous unmanned aerial remote sensing platform (AggieAir) for riparian and wetlands applications', in *Geoscience and Remote Sensing Symposium (IGARSS), 2011 IEEE International*. IEEE, pp. 3413–3416.
- Joughin, I., Das, S. B., King, M. A., Smith, B. E., Howat, I. M. and Moon, T. (2008) 'Seasonal speedup along the western flank of the Greenland Ice Sheet', *Science*, 320(5877), pp. 781–783.
- Julian, J. P. and Torres, R. (2006) 'Hydraulic erosion of cohesive riverbanks', *Geomorphology*, 76(1), pp. 193–206. doi:

<https://doi.org/10.1016/j.geomorph.2005.11.003>.

- Kaminer, I., Pascoal, A., Hallberg, E. and Silvestre, C. (1998) 'Trajectory Tracking for Autonomous Vehicles: An Integrated Approach to Guidance and Control', *Journal of guidance, control, and dynamics*. American Institute of Aeronautics and Astronautics, 21(1), pp. 29–38. doi: 10.2514/2.4229.
- Kaneko, K. and Nohara, S. (2014) 'Review of effective vegetation mapping using the UAV (Unmanned Aerial Vehicle) method', *Journal of Geographic Information System*, 6(06), p. 733.
- Karaus, U., Alder, L. and Tockner, K. (2005) "'Concave islands": Habitat heterogeneity of parafluvial ponds in a gravel-bed river', *Wetlands*. Springer, 25(1), pp. 26–37.
- Kay, A. L., Jones, R. G. and Reynard, N. S. (2006) 'RCM rainfall for UK flood frequency estimation. II. Climate change results', *Journal of Hydrology*, 318(1), pp. 163–172. Available at: http://ac.els-cdn.com/S002216940500301X/1-s2.0-S002216940500301X-main.pdf?_tid=f5ae6c96-c055-11e6-beee-00000aab0f6b&acdnat=1481538790_1bd5dcbef2cf44b001db34c5c7047da7.
- Kim, J.-H., Sukkarieh, S. and Wishart, S. (2006) 'Real-Time Navigation, Guidance, and Control of a UAV Using Low-Cost Sensors', in Yuta, S. et al. (eds) *Field and Service Robotics: Recent Advances in Reserch and Applications*. Berlin, Heidelberg: Springer Berlin Heidelberg, pp. 299–309. doi: 10.1007/10991459_29.
- Klingeman, P. C. (1998) *Gravel-bed Rivers in the Environment*. Water Resources Publication.
- Kondolf, G. M. (1997) 'PROFILE: Hungry Water: Effects of Dams and Gravel Mining on River Channels', *Environmental Management*, 21(4), pp. 533–551. doi: 10.1007/s002679900048.
- Kondolf, G. M. (1998) 'Environmental effects of aggregate extraction from river channels and floodplains', *Department of Landscape Architecture and Environmental Planning, University of California, Berkeley, USA*.
- Kondolf, G. M. and Li, S. (1992) 'The pebble count technique for quantifying surface bed material size in instream flow studies', *Rivers*, 3(2), pp. 80–87.
- Kondolf, M. (1994) 'Geomorphic and environmental effects of instream gravel mining',

-
- Landscape and Urban Planning*, 28(2), pp. 225–243. doi: [https://doi.org/10.1016/0169-2046\(94\)90010-8](https://doi.org/10.1016/0169-2046(94)90010-8).
- Krabill, W. B., Collins, J. G., Link, L. E., Swift, R. N. and Butler, M. L. (1984) 'Airborne laser topographic mapping results'.
- Kulkarni, A. V, Bahuguna, I. M., Rathore, B. P., Singh, S. K., Randhawa, S. S., Sood, R. K. and Dhar, S. (2007) 'Glacial retreat in Himalaya using Indian Remote Sensing satellite data', *Current science*, 92(1), pp. 69–74.
- Kümmerlen, B., Dauwe, S., Schmundt, D. and Schurr, U. (1999) *Handbook of computer vision and applications, Handbook of computer vision and applications: systems and applications (Vol. 3)*. doi: 10.1007/s00138-006-0021-7.
- Lane, S. N., Richards, K. S. and Chandler, J. H. (1998) *Landform monitoring, modelling and analysis*. John Wiley and Sons Ltd.
- Lane, S. N., Westaway, R. M. and Murray Hicks, D. (2003) 'Estimation of erosion and deposition volumes in a large, gravel-bed, braided river using synoptic remote sensing', *Earth Surface Processes and Landforms*. John Wiley & Sons, Ltd, 28(3), pp. 249–271. doi: 10.1002/esp.483.
- Lange, S., Sunderhauf, N. and Protzel, P. (2009) 'A vision based onboard approach for landing and position control of an autonomous multirotor UAV in GPS-denied environments', in *Advanced Robotics, 2009. ICAR 2009. International Conference on*. IEEE, pp. 1–6.
- Langhammer, J., Bernsteinová, J. and Miřijovský, J. (2017) 'Building a high-precision 2D hydrodynamic flood model using UAV photogrammetry and sensor network monitoring', *Water*. Multidisciplinary Digital Publishing Institute, 9(11), p. 861.
- Lato, M. J., Diederichs, M. S. and Hutchinson, D. J. (2010) 'Bias correction for view-limited Lidar scanning of rock outcrops for structural characterization', *Rock mechanics and rock engineering*, 43(5), pp. 615–628.
- Latrubesse, E. M. (2008) 'Patterns of anabranching channels: The ultimate end-member adjustment of mega rivers', *Geomorphology*, 101(1), pp. 130–145. doi: <https://doi.org/10.1016/j.geomorph.2008.05.035>.
- van Leeuwen, M. and Nieuwenhuis, M. (2010) 'Retrieval of forest structural parameters
-

- using LiDAR remote sensing', *European Journal of Forest Research*, 129(4), pp. 749–770. doi: 10.1007/s10342-010-0381-4.
- Leitao, J. P., de Vitry, M. M., Scheidegger, A. and Rieckermann, J. (2016) 'Assessing the quality of digital elevation models obtained from mini unmanned aerial vehicles for overland flow modelling in urban areas', *Hydrology and Earth System Sciences*, 20(4), pp. 1637–1653. doi: 10.5194/hess-20-1637-2016.
- Lelong, C. C. D., Burger, P., Jubelin, G., Roux, B., Labbé, S. and Baret, F. (2008) 'Assessment of unmanned aerial vehicles imagery for quantitative monitoring of wheat crop in small plots', *Sensors (Switzerland)*, 8(5), pp. 3557–3585.
- Leopold, L. B. and Wolman, M. G. (1957) *River channel patterns: Braided, meandering, and straight, Professional Paper*. Washington, D.C. doi: 10.3133/pp282B.
- Lim, K., Treitz, P., Wulder, M., St-Onge, B. and Flood, M. (2003) 'LiDAR remote sensing of forest structure', *Progress in Physical Geography*, 27(1), pp. 88–106.
- Lin, Y., Hyyppä, J. and Jaakkola, A. (2011) 'Mini-UAV-Borne LIDAR for Fine-Scale Mapping', *IEEE Geoscience and Remote Sensing Letters*, 8(3), pp. 426–430. doi: 10.1109/LGRS.2010.2079913.
- Lopes, L. and Thomas, O. (1973) 'Digital camera'. Google Patents.
- Lucas, B. D. and Kanade, T. (1981) 'An iterative image registration technique with an application to stereo vision'. Vancouver, BC, Canada.
- Maas, H.-G. (1995) 'New developments in Multimedia Photogrammetry', *Symposium A Quarterly Journal In Modern Foreign Literatures*, 8(3), pp. 150–5. Available at: https://tu-dresden.de/bu/umwelt/geo/ipf/photogrammetrie/ressourcen/dateien/forschung/publikationen/pubdocs/1999-und-aelter/1995_Maas_multimed.pdf?lang=en (Accessed: 21 November 2017).
- Malos, J., Beamish, B., Munday, L., Reid, P. and James, C. (2013) 'Remote monitoring of subsurface heatings in opencut coal mines'.
- Mancini, A., Frontoni, E., Zingaretti, P. and Longhi, S. (2015) 'High-resolution mapping of river and estuary areas by using unmanned aerial and surface platforms', in *Unmanned Aircraft Systems (ICUAS), 2015 International Conference on*, pp. 534–542.

- doi: 10.1109/ICUAS.2015.7152333.
- Marshall, G. J., Rees, W. G. and Dowdeswell, J. A. (1993) 'Limitations imposed by cloud cover on multitemporal visible band satellite data sets from polar regions', *Annals of glaciology*, 17(1), pp. 113–120.
- Marston, R. A., Girel, J., Pautou, G., Piegay, H., Bravard, J.-P. and Arneson, C. (1995) 'Channel metamorphosis, floodplain disturbance, and vegetation development: Ain River, France', in *Biogeomorphology, Terrestrial and Freshwater Systems*. Elsevier, pp. 121–131.
- Mathews, A. J. and Jensen, J. L. R. (2013) 'Visualizing and quantifying vineyard canopy LAI using an unmanned aerial vehicle (UAV) collected high density structure from motion point cloud', *Remote Sensing*. doi: 10.3390/rs5052164.
- Maxwell, E. L. (1976) 'Multivariate system analysis of multispectral imagery', *Photogrammetric Engineering and Remote Sensing*, 42(9).
- McDonald, J. K. (1995) 'CORONA, America's First Satellite Program'. Washington DC: Central Intelligence Agency, pp. 316–362. Available at: <https://www.cia.gov/library/center-for-the-study-of-intelligence/csi-publications/books-and-monographs/corona.pdf>.
- McGonigle, A. J. S., Aiuppa, A., Giudice, G., Tamburello, G., Hodson, A. J. and Gurrieri, S. (2008) 'Unmanned aerial vehicle measurements of volcanic carbon dioxide fluxes', *Geophysical Research Letters*, 35(6).
- McKeown, D. M., Harvey, W. A. and Wixson, L. E. (1989) 'Automating knowledge acquisition for aerial image interpretation', *Computer Vision, Graphics, and Image Processing*. Elsevier, 46(1), pp. 37–81.
- Merz, J. E. and Ochikubo Chan, L. K. (2005) 'Effects of gravel augmentation on macroinvertebrate assemblages in a regulated California River', *River Research and Applications*. John Wiley & Sons, Ltd, 21(1), pp. 61–74. doi: 10.1002/rra.819.
- Met Office (2018) *UK Storm Season 2017/18 - Met Office*. Available at: <https://www.metoffice.gov.uk/weather/warnings-and-advice/uk-storm-centre/uk-storm-season-2017-18> (Accessed: 5 August 2018).
- Meyer, G. E. and Neto, J. C. (2008) 'Verification of color vegetation indices for automated

-
- crop imaging applications', *Computers and Electronics in Agriculture*, 63(2), pp. 282–293. doi: <http://dx.doi.org/10.1016/j.compag.2008.03.009>.
- Micheli, E. R. and Larsen, E. W. (2011) 'River channel cutoff dynamics, Sacramento river, California, USA', *River Research and Applications*. Wiley Online Library, 27(3), pp. 328–344.
- Milan, D. J., Heritage, G. L., Large, A. R. G. and Fuller, I. C. (2011) 'Filtering spatial error from DEMs: Implications for morphological change estimation', *Geomorphology*, 125(1), pp. 160–171. doi: <https://doi.org/10.1016/j.geomorph.2010.09.012>.
- Miller, J. B. (1988) *Unmanned Air Vehicles-Real Time Intelligence Without the Risk*. DTIC Document.
- Moran, M. S., Inoue, Y. and Barnes, E. M. (1997) 'Opportunities and limitations for image-based remote sensing in precision crop management', *Remote Sensing of Environment*, 61(3), pp. 319–346.
- Mossa, J. and Marks, S. R. (2011) 'Pit avulsions and planform change on a mined river floodplain: Tangipahoa River, Louisiana', *Physical Geography*. Taylor & Francis, 32(6), pp. 512–532.
- Mulkey, S. S., Chazdon, R. L. and Smith, A. P. (2012) *Tropical forest plant ecophysiology*. Springer Science & Business Media.
- Murray, A. B. and Paola, C. (1994) 'A cellular model of braided rivers', *Nature*. Nature Publishing Group, 371(6492), p. 54.
- Myint, S. W., Gober, P., Brazel, A., Grossman-Clarke, S. and Weng, Q. (2011) 'Per-pixel vs. object-based classification of urban land cover extraction using high spatial resolution imagery', *Remote Sensing of Environment*. Elsevier, 115(5), pp. 1145–1161. doi: [10.1016/j.rse.2010.12.017](https://doi.org/10.1016/j.rse.2010.12.017).
- Nakano, T., Kamiya, I., Tobita, M., Iwahashi, J. and Nakajima, H. (2014) 'Landform monitoring in active volcano by UAV and SfM-MVS technique', *The International Archives of Photogrammetry, Remote Sensing and Spatial Information Sciences*, 40(8), p. 71.
- Nanson, G. C. and Knighton, A. D. (1996) 'Anabranching rivers: their cause, character and classification', *Earth surface processes and landforms*. Wiley Online Library, 21(3),
-

pp. 217–239.

- Neitzel, F. and Klonowski, J. (2011) 'Mobile 3D mapping with a low-cost UAV system', *Int.Arch.Photogramm.Remote Sens.Spat.Inf.Sci.* doi: doi:10.5194/isprsarchives-XXXVIII-1-C22-39-2011, 2011.
- Nex, F. and Remondino, F. (2014) 'UAV for 3D mapping applications: A review', *Applied Geomatics*. doi: 10.1007/s12518-013-0120-x.
- Nolan, M., Larsen, C. F. and Sturm, M. (2015) 'Mapping snow-depth from manned-aircraft on landscape scales at centimeter resolution using Structure-from-Motion photogrammetry.', *Cryosphere Discussions*. Citeseer, 9(1).
- Ouédraogo, M. M., Degré, A., Debouche, C. and Lisein, J. (2014) 'The evaluation of unmanned aerial system-based photogrammetry and terrestrial laser scanning to generate DEMs of agricultural watersheds', *Geomorphology*. Elsevier, 214, pp. 339–355.
- Padmore, C. L. (1997) 'Physical biotopes in representative river channels: identification, hydraulic characterisation and application'. Newcastle University.
- Palmer, J. A., Schilling, K. E., Isenhardt, T. M., Schultz, R. C. and Tomer, M. D. (2014) 'Streambank erosion rates and loads within a single watershed: Bridging the gap between temporal and spatial scales', *Geomorphology*, 209, pp. 66–78. doi: <https://doi.org/10.1016/j.geomorph.2013.11.027>.
- Patenaude, G., Hill, R. A., Milne, R., Gaveau, D. L. A., Briggs, B. B. J. and Dawson, T. P. (2004) 'Quantifying forest above ground carbon content using LiDAR remote sensing', *Remote Sensing of Environment*, 93(3), pp. 368–380.
- Patterson, M. C. L., Mulligan, A., Douglas, J., Robinson, J., Wardell, L. and Pallister, J. (2005) 'Volcano surveillance by ACR silver fox', *Infotech@ Aerospace*, pp. 26–29.
- Petit, F., Poinart, D. and Bravard, J.-P. (1996) 'Channel incision, gravel mining and bedload transport in the Rhône river upstream of Lyon, France ("canal de Miribel")', *CATENA*, 26(3), pp. 209–226. doi: [https://doi.org/10.1016/0341-8162\(95\)00047-X](https://doi.org/10.1016/0341-8162(95)00047-X).
- Piermattei, L., Carturan, L. and Guarnieri, A. (2015) 'Use of terrestrial photogrammetry based on structure-from-motion for mass balance estimation of a small glacier in

- the Italian alps', *Earth Surface Processes and Landforms*, 40(13), pp. 1791–1802.
- Polmar, N. (2013) 'THE PIONEERING PIONEER', *Naval History*, 27(5), p. 14.
- Popescu, S. C., Wynne, R. H. and Nelson, R. F. (2003) 'Measuring individual tree crown diameter with lidar and assessing its influence on estimating forest volume and biomass', *Canadian journal of remote sensing*, 29(5), pp. 564–577.
- Prosdocimi, M., Calligaro, S., Sofia, G., Dalla Fontana, G. and Tarolli, P. (2015) 'Bank erosion in agricultural drainage networks: new challenges from structure-from-motion photogrammetry for post-event analysis', *Earth Surface Processes and Landforms*. John Wiley & Sons, Ltd, 40(14), pp. 1891–1906. doi: 10.1002/esp.3767.
- Prudhomme, C., Jakob, D. and Svensson, C. (2003) 'Uncertainty and climate change impact on the flood regime of small UK catchments', *Journal of hydrology*. Elsevier, 277(1–2), pp. 1–23.
- Restrepo, J. D., Kettner, A. J. and Syvitski, J. P. M. (2015) 'Recent deforestation causes rapid increase in river sediment load in the Colombian Andes', *Anthropocene*, 10, pp. 13–28. doi: <https://doi.org/10.1016/j.ancene.2015.09.001>.
- Rice, S. P., Church, M., Wooldridge, C. L. and Hickin, E. J. (2009) 'Morphology and evolution of bars in a wandering gravel-bed river; lower Fraser river, British Columbia, Canada', *Sedimentology*. Wiley Online Library, 56(3), pp. 709–736.
- Richards, K. (1987) 'Fluvial geomorphology', *Progress in Physical Geography*. Sage Publications Sage CA: Thousand Oaks, CA, 11(3), pp. 432–457.
- Richter, R. (1996) 'Atmospheric correction of satellite data with haze removal including a haze/clear transition region', *Computers & Geosciences*, 22(6), pp. 675–681.
- riverlevels.uk (2019) *RiverLevels.uk*. Available at: Daily River level record from Coldgate Mill.
- Rodrigues, S., Br  h  ret, J.-G., Macaire, J.-J., Moatar, F., Nistoran, D. and Jug  , P. (2006) 'Flow and sediment dynamics in the vegetated secondary channels of an anabranching river: The Loire River (France)', *Sedimentary Geology*, 186(1), pp. 89–109. doi: <https://doi.org/10.1016/j.sedgeo.2005.11.011>.
- Rosgen, D. L. (1994) 'A classification of natural rivers', *Catena*, 22(3), pp. 169–199.

-
- Ruiz, J. J., Diaz-Mas, L., Perez, F. and Viguria, A. (2013) 'Evaluating the Accuracy of Dem Generation Algorithms from Uav Imagery', *Uav-G2013*, pp. 333–337.
- Rundquist, D. C., Collins, S. C., Barnes, R. B., Bussom, D. E., Samson, S. A. and Peake, J. S. (1980) 'The use of Landsat digital information for assessing glacier inventory parameters', *International Association of Hydrological Sciences*, 126, pp. 321–331.
- Rundquist, L. A. (1980) 'Effects of gravel removal on river hydrology and hydraulics', *Fish Wildl. Serv*, 80(08), pp. 67–140.
- Rupnik, E., Daakir, M. and Deseilligny, M. P. (2017) 'MicMac—a free, open-source solution for photogrammetry', *Open Geospatial Data, Software and Standards*. Nature Publishing Group, 2(1), p. 14.
- Ryan, J. C., Hubbard, A. L., Todd, J., Carr, J. R., Box, J. E., Christoffersen, P., Holt, T. O. and Snooke, N. (2014) 'Repeat UAV photogrammetry to assess calving front dynamics at a large outlet glacier draining the Greenland Ice Sheet', *The Cryosphere Discuss*, 8(2), pp. 2243–2275.
- Ryan, J. C., Hubbard, A. L., Box, J. E., Todd, J., Christoffersen, P., Carr, J. R., Holt, T. O. and Snooke, N. A. (2015) 'UAV photogrammetry and structure from motion to assess calving dynamics at Store Glacier, a large outlet draining the Greenland ice sheet'.
- Saggiani, G. *et al.* (2007) 'A UAV system for observing volcanoes and natural hazards', in *AGU Fall Meeting Abstracts*, p. 5.
- Saiki, K. and Ohba, T. (2010) 'Development of an unmanned observation aerial vehicle (UAV) as a tool for volcano survey', *Bull. Volcanol. Soc. Jpn*, 55, pp. 137–146.
- Sanz-Ablanedo, E., Chandler, J., Rodríguez-Pérez, J. and Ordóñez, C. (2018) *Accuracy of Unmanned Aerial Vehicle (UAV) and SfM Photogrammetry Survey as a Function of the Number and Location of Ground Control Points Used*, *Remote Sensing*. doi: 10.3390/rs10101606.
- Saunders, R. W. and Kriebel, K. T. (1988) 'An improved method for detecting clear sky and cloudy radiances from AVHRR data', *International Journal of Remote Sensing*, 9(1), pp. 123–150.
- Scambos, T. A., Dutkiewicz, M. J., Wilson, J. C. and Bindshadler, R. A. (1992) 'Application of image cross-correlation to the measurement of glacier velocity using satellite

- image data', *Remote Sensing of Environment*, 42(3), pp. 177–186.
- Schenk, T. (1994) 'Concepts and algorithms in digital photogrammetry', *ISPRS Journal of Photogrammetry and Remote Sensing*, 49(6), pp. 2–8. doi: 10.1016/0924-2716(94)90009-4.
- Schenk, T. (2005) 'Introduction to Photogrammetry'. Available at: <http://www.mat.uc.pt/~gil/downloads/IntroPhoto.pdf> (Accessed: 21 November 2017).
- Schindler, K. (2015) 'Mathematical foundations of photogrammetry', in *Handbook of Geomathematics: Second Edition*, pp. 3087–3103. doi: 10.1007/978-3-642-54551-1_63.
- Schmidt, M., Goossens, R., Menz, G., Altmaier, A. and Devriendt, D. (2001) 'The use of CORONA satellite images for generating a high resolution digital elevation model', in *Geoscience and Remote Sensing Symposium, 2001. IGARSS'01. IEEE 2001 International*. IEEE, pp. 3123–3125.
- Schowengerdt, R. A. (2007) 'Remote sensing : models and methods for image processing'. Burlington, MA: Burlington, MA : Academic Press.
- Schumm, S. A. (1969) 'River metamorphosis', *Journal of the Hydraulics division*. ASCE, 95(1), pp. 255–274.
- Schumm, S. A. (1985) 'Patterns of alluvial rivers', *Annual Review of Earth and Planetary Sciences*. Annual Reviews 4139 El Camino Way, PO Box 10139, Palo Alto, CA 94303-0139, USA, 13(1), pp. 5–27.
- Schumm, S. A. (1993) 'River response to baselevel change: implications for sequence stratigraphy', *The Journal of Geology*. University of Chicago Press, 101(2), pp. 279–294.
- Schumm, S. and Lichty, R. (1963) 'Channel widening and flood-plain construction along Cimarron River in southwestern Kansas', *Geological Survey Professional Paper*. doi: 0-8493-6348-9.
- Sear, D. A. and Archer, D. (1998) 'Effects of gravel extraction on stability of gravel-bed rivers: the Wooler Water, Northumberland, UK', *Gravel-bed rivers in the environment*. Edited by RL Beschta, PD Komar, and JB Bradley. *Water Resources*

-
- Publications, Highlands Ranch, Colo*, pp. 415–432.
- Shima, T., Idan, M. and Golan, O. M. (2006) 'Sliding-mode control for integrated missile autopilot guidance', *Journal of guidance, control, and dynamics*, 29(2), pp. 250–260.
- Siebert, S. and Teizer, J. (2014) 'Mobile 3D mapping for surveying earthwork projects using an Unmanned Aerial Vehicle (UAV) system', *Automation in Construction*, 41, pp. 1–14. doi: <http://dx.doi.org/10.1016/j.autcon.2014.01.004>.
- Smith, N. D. and Smith, D. G. (1984) 'William River: an outstanding example of channel widening and braiding caused by bed-load addition (Saskatchewan, Canada).', *Geology*. doi: 10.1130/0091-7613(1984)12<78:WRAOEO>2.0.CO;2.
- Spiekermann, R., Betts, H., Dymond, J. and Basher, L. (2017) 'Volumetric measurement of river bank erosion from sequential historical aerial photography', *Geomorphology*, 296, pp. 193–208. doi: <https://doi.org/10.1016/j.geomorph.2017.08.047>.
- Stickley, C. M. and Gingrande, A. (1967) *A Bibliography of Laser Applications*. DTIC Document.
- Storlazzi, C. D., Dartnell, P., Hatcher, G. A. and Gibbs, A. E. (2016) 'End of the chain? Rugosity and fine-scale bathymetry from existing underwater digital imagery using structure-from-motion (SfM) technology', *Coral Reefs*, 35(3), pp. 889–894. doi: 10.1007/s00338-016-1462-8.
- Stumpf, A., Malet, J.-P., Allemand, P., Pierrot-Deseilligny, M. and Skupinski, G. (2015) 'Ground-based multi-view photogrammetry for the monitoring of landslide deformation and erosion', *Geomorphology*. Elsevier, 231, pp. 130–145.
- Tahar, K. N. (2013) 'An Evaluation on Different Number of Ground Control Points in Unmanned Aerial Vehicle Photogrammetric Block', *Isprs 8th 3d Geoinfo Conference & Wg li/2 Workshop*, 40-2-W2, pp. 93–98.
- Tavares, J. M. R. S., Jorge, R. M. N., Lima, R., Nakamura, M., Omori, T., Ishikawa, T., Wada, S. and Yamaguchi, T. (2009) *Advances in Computational Vision and Medical Image Processing, Environ Sci Pollut Res Int*. Edited by J. M. R. S. Tavares and R. M. N. Jorge. Dordrecht: Springer Netherlands. doi: 10.1007/978-1-4020-9086-8.
- Terasmae, J. and Hughes, O. L. (1960) 'Glacial retreat in the North Bay area, Ontario', *Science*, 131(3411), pp. 1444–1446.
-

-
- Tesla, N. (1905) 'The transmission of electrical energy without wires as a means for furthering peace', *Electrical World and Engineer*, 7, p. 21.
- Thomas, J. I. and Oliensis, J. (1999) 'Dealing with Noise in Multiframe Structure from Motion', *Computer Vision and Image Understanding*, 76(2), pp. 109–124. doi: <https://doi.org/10.1006/cviu.1999.0779>.
- Tipping, R. (1994) 'Fluvial chronology and valley floor evolution of the upper bowmont valley, borders region, Scotland', *Earth Surface Processes and Landforms*, 19(7), pp. 641–657. doi: 10.1002/esp.3290190705.
- Tonkin, T. N., Midgley, N. G., Graham, D. J. and Labadz, J. C. (2014) 'The potential of small unmanned aircraft systems and structure-from-motion for topographic surveys: A test of emerging integrated approaches at Cwm Idwal, North Wales', *Geomorphology*. Elsevier, 226, pp. 35–43.
- Tooth, S. and Nanson, G. C. (1999) 'Anabranching rivers on the Northern Plains of arid central Australia', *Geomorphology*, 29(3), pp. 211–233. doi: [https://doi.org/10.1016/S0169-555X\(99\)00021-5](https://doi.org/10.1016/S0169-555X(99)00021-5).
- Torres-Sánchez, J., López-Granados, F. and Peña, J. M. (2015) 'An automatic object-based method for optimal thresholding in UAV images: Application for vegetation detection in herbaceous crops', *Computers and Electronics in Agriculture*, 114, pp. 43–52. doi: <http://dx.doi.org/10.1016/j.compag.2015.03.019>.
- Torres, A., Brandt, J., Lear, K. and Liu, J. (2017) 'A looming tragedy of the sand commons', *Science*, 357(6355), pp. 970 LP – 971. doi: 10.1126/science.aao0503.
- Triska, F. J. (1984) 'Role of wood debris in modifying channel geomorphology and riparian areas of a large lowland river under pristine conditions: A historical case study: With 7 figures and 4 tables in the text', *Internationale Vereinigung für theoretische und angewandte Limnologie: Verhandlungen*. Taylor & Francis, 22(3), pp. 1876–1892.
- Turner, D., Lucieer, A. and Watson, C. (2011) 'Development of an Unmanned Aerial Vehicle (UAV) for hyper resolution vineyard mapping based on visible, multispectral, and thermal imagery', in *Proceedings of 34th International symposium on remote sensing of environment*, p. 4.
-

- Turner, D., Lucieer, A. and Watson, C. (2012) 'An automated technique for generating georectified mosaics from ultra-high resolution Unmanned Aerial Vehicle (UAV) imagery, based on Structure from Motion (SfM) point clouds', *Remote Sensing*. doi: 10.3390/rs4051392.
- Turner, W., Spector, S., Gardiner, N., Fladeland, M., Sterling, E. and Steininger, M. (2003) 'Remote sensing for biodiversity science and conservation', *Trends in Ecology & Evolution*, 18(6), pp. 306–314. doi: [http://dx.doi.org/10.1016/S0169-5347\(03\)00070-3](http://dx.doi.org/10.1016/S0169-5347(03)00070-3).
- UAVGLOBAL (2016) *Commercial UAV Manufacturers*. Available at: <http://www.uavglobal.com/commercial-uav-manufacturers/> (Accessed: 15 May 2016).
- Vasterling, M., Schloemer, S., Fischer, C. and Ehrler, C. (2010) 'Thermal Imaging of Subsurface Coal Fires by means of an Unmanned Aerial Vehicle (UAV) in the Autonomous Province Xinjiang, PRC', in *EGU General Assembly Conference Abstracts*, p. 8664.
- Vázquez-Tarrío, D., Borgniet, L., Liébault, F. and Recking, A. (2017) 'Using UAS optical imagery and SfM photogrammetry to characterize the surface grain size of gravel bars in a braided river (Vénéon River, French Alps)', *Geomorphology*. Elsevier, 285, pp. 94–105.
- Verdú, J. M., Batalla, R. J. and Martínez-Casasnovas, J. A. (2005a) 'High-resolution grain-size characterisation of gravel bars using imagery analysis and geo-statistics', *Geomorphology*, 72(1), pp. 73–93. doi: <https://doi.org/10.1016/j.geomorph.2005.04.015>.
- Verdú, J. M., Batalla, R. J. and Martínez-Casasnovas, J. A. (2005b) 'High-resolution grain-size characterisation of gravel bars using imagery analysis and geo-statistics', *Geomorphology*, 72(1), pp. 73–93. doi: <https://doi.org/10.1016/j.geomorph.2005.04.015>.
- Vericat, D., Batalla, R. J. and Garcia, C. (2006) 'Breakup and reestablishment of the armour layer in a large gravel-bed river below dams: The lower Ebro', *Geomorphology*, 76(1), pp. 122–136. doi: <https://doi.org/10.1016/j.geomorph.2005.10.005>.
- Verma, V., Kumar, R. and Hsu, S. (2006) '3D building detection and modeling from aerial

-
- LIDAR data', in *2006 IEEE Computer Society Conference on Computer Vision and Pattern Recognition (CVPR'06)*. IEEE, pp. 2213–2220.
- Vernon, D. (1991) 'Machine vision-Automated visual inspection and robot vision', *NASA STI/Recon Technical Report A*, 92.
- Versteeg, R., McKay, M., Anderson, M., Johnson, R., Selfridge, B. and Bennett, J. (2007) *Feasibility study for an Autonomous UAV-Magnetometer system*. DTIC Document.
- Vita-Finzi, C. and Schumm, S. A. (1992) 'To Interpret the Earth: Ten Ways to be Wrong', *The Geographical Journal*, p. 231. doi: 10.2307/3059801.
- Vörösmarty, C. J., Green, P., Salisbury, J. and Lammers, R. B. (2000) 'Global Water Resources: Vulnerability from Climate Change and Population Growth', *Science*, 289(5477), pp. 284 LP – 288. doi: 10.1126/science.289.5477.284.
- Walker, M. and Rutherford, I. (1999) 'An approach to predicting rates of bend migration in meandering alluvial streams', in *Proceedings of the Second Australian Stream Management Conference, Adelaide, Australia*. Cooperative Research Centre for Catchment Hydrology Clayton, Victoria, Australia, pp. 659–665.
- Wallace, L., Lucieer, A. and Watson, C. (2012) 'Assessing the feasibility of UAV-based LiDAR for high resolution forest change detection', *Proc. ISPRS, Int. Archives Photogramm., Remote Sens. Spatial Inf. Sci*, 38, p. B7.
- Watts, A. C., Ambrosia, V. G. and Hinkley, E. A. (2012) 'Unmanned Aircraft Systems in Remote Sensing and Scientific Research: Classification and Considerations of Use', *Remote Sensing*, 4(6), pp. 1671–1692. doi: 10.3390/rs4061671.
- Westoby, M. J., Dunning, S. A., Woodward, J., Hein, A. S., Marrero, S. M., Winter, K. and Sugden, D. E. (2015) 'Sedimentological characterization of Antarctic moraines using UAVs and Structure-from-Motion photogrammetry', *Journal of Glaciology*, 61(230), pp. 1088–1102. doi: 10.3189/2015JoG15J086.
- Whiting, P. J. and Dietrich, W. E. (1993) 'Experimental constraints on bar migration through bends: Implications for meander wavelength selection', *Water Resources Research*. Wiley Online Library, 29(4), pp. 1091–1102.
- Wickliff, G. A. (1997) 'Geology, Photography, and Environmental Rhetoric in the American West of 1860-1890', *Technical Communication Quarterly*. Routledge, 6(1), pp. 41–
-

75. doi: 10.1207/s15427625tcq0601_4.
- Wilson, S. (2010) 'Level 1 Strategic Flood Risk Assessment'. Edited by N. C. Council. Middlesbrough: Scott Wilson Group. Available at: [http://www.northumberland.gov.uk/NorthumberlandCountyCouncil/media/Planning-and-Building/planning policy/Studies and Evidence Reports/Flood Water Studies/1. SFRA Level 1/Level-1-SFRA-September-2010.pdf](http://www.northumberland.gov.uk/NorthumberlandCountyCouncil/media/Planning-and-Building/planning_policy/Studies_and_Evidence_Reports/Flood_Water_Studies/1_SFRA_Level_1/Level-1-SFRA-September-2010.pdf).
- Wolman, M. G. (1954) 'A method of sampling coarse river-bed material', *Eos, Transactions American Geophysical Union*. John Wiley & Sons, Ltd, 35(6), pp. 951–956. doi: 10.1029/TR035i006p00951.
- Wolman, M. G. (1959) 'Factors influencing erosion of a cohesive river bank', *American Journal of Science*. American Journal of Science, 257(3), pp. 204–216.
- Woodget, A., Visser, F., Maddock, I. and Carbonneau, P. (2016) 'Quantifying fluvial substrate size using hyperspatial resolution UAS imagery and SfM-photogrammetry', *11th ISE 2016, Melbourne, Australia*.
- Woodget, A. S. and Austrums, R. (2017) 'Subaerial gravel size measurement using topographic data derived from a UAV-SfM approach', *Earth Surface Processes and Landforms*. John Wiley & Sons, Ltd, 42(9), pp. 1434–1443. doi: 10.1002/esp.4139.
- Wright, S. J. and Van Schaik, C. P. (1994) 'Light and the phenology of tropical trees', *American Naturalist*, pp. 192–199.
- Young, A. P., Olsen, M. J., Driscoll, N., Flick, R. E., Gutierrez, R., Guza, R. T., Johnstone, E. and Kuester, F. (2010) 'Comparison of airborne and terrestrial lidar estimates of seacliff erosion in southern California', *Photogrammetric engineering & remote sensing*, 76(4), pp. 421–427.
- Yu, Q., Gong, P., Clinton, N., Biging, G., Kelly, M. and Schirokauer, D. (2006) 'Object-based Detailed Vegetation Classification with Airborne High Spatial Resolution Remote Sensing Imagery', *Photogrammetric Engineering & Remote Sensing*, 72(7), pp. 799–811. doi: 10.14358/PERS.72.7.799.
- Zanter, K. (2016) 'Landsat 8 (L8) Data Users Handbook'. Edited by USGS. Sioux Falls, South Dakota: USGS.
- Zwally, H. J., Abdalati, W., Herring, T., Larson, K., Saba, J. and Steffen, K. (2002) 'Surface

melt-induced acceleration of Greenland ice-sheet flow', *Science*, 297(5579), pp. 218–222.

Appendix 1 – Final Data Products



Figure A1.1 – Survey 1 Channel DEM result.



Figure A1.2 – Survey 1 Orthomosaic Result



Figure A1.3 - Survey 2 Channel DEM result.



Figure A1.4 - Survey 2 Orthomosaic Result



Figure A1.5 - Survey 3 Channel DEM result.



Figure A1.6 - Survey 3 Orthomosaic Result



Figure A1.7 - Survey 4 Channel DEM result.

1 Appendix 2 – Geomorphic change Tables

2

3 *Table A2.1 - Reported volumetric statistics for sub-reach scale analyses between Surveys 1 and 2.*

4

Survey 1-2 Volumetric Statistics	A	B	C	D	E	F	Total
Total Volume Gain	643.5	300.1	52.9	421.4	647.8	627.6	2693.4
Total Volume Loss	-247.7	-1322.8	-106.4	-425.6	-448.4	-649.3	-3200.0
Significant (+0.1m) Deposition	325.7	129.6	8.2	181.9	411.7	315.3	1372.3
Significant (-0.1m) Erosion	-110.5	-911.0	-20.2	-203.0	-286.4	-373.1	-1904.2
Sub-threshold Volume Gain	317.9	170.5	44.7	239.5	236.2	312.4	1321.1
Sub-threshold Volume Loss	-137.2	-411.8	-86.2	-222.6	-161.9	-276.2	-1295.9
Net Sedimentary Change	215.2	-781.4	-12.0	-21.1	125.3	-57.8	-531.9
Bank Erosion (-0.1m)	N/A	-451.4	N/A	N/A	N/A	-150.6	-602.0
Bed Erosion (-0.1m)	-110.5	-459.6	-20.2	-203.0	-286.4	-222.5	-1302.2

1 *Table A2.2 - Reported volumetric statistics for sub-reach scale analyses between Surveys 2 and 3.*

Survey 2-3 Volumetric Statistics	A	B	C	D	E	F	Total
Total Volume Gain	257.6	437.7	72.3	191.2	196.2	388.6	1543.6
Total Volume Loss	-203.8	-301.6	-96.7	-353.1	-340.9	-558.6	-1854.7
Significant (+0.1m) Deposition	62.8	155.6	15.7	43.0	74.6	176.7	528.3
Significant (-0.1m) Erosion	-86.1	-118.8	-22.1	-105.0	-138.7	-235.5	-706.1
Sub-threshold Volume Gain	194.8	282.1	56.7	148.2	121.7	211.9	1015.3
Sub-threshold Volume Loss	-117.7	-182.8	-74.6	-248.1	-202.2	-323.1	-1148.6
Net Sedimentary Change	-23.4	36.8	-6.4	-62.0	-64.2	-58.8	-177.9
Bank Erosion (-0.1m)	N/A	-23.0	N/A	N/A	N/A	-30.4	-53.4
Bed Erosion (-0.1m)	-86.1	-95.8	-22.1	-105.0	-138.7	-205.1	-652.7

2

3 *Table A2.3 - Reported volumetric statistics for sub-reach scale analyses between Surveys 3 and 4.*

Survey 3-4 Volumetric Statistics	A	B	C	D	E	F	Total
Total Volume Gain	108.6	186.6	68.2	234.4	182.9	174.7	955.3
Total Volume Loss	-101.3	-358.4	-52.5	-177.1	-172.0	-601.7	-1462.9
Significant (+0.1m) Deposition	6.4	31.4	11.8	62.8	40.9	38.7	191.8
Significant (-0.1m) Erosion	-14.6	-122.3	-8.1	-34.3	-62.6	-278.5	-520.4
Sub-threshold Volume Gain	102.3	155.1	56.4	171.6	142.1	136.0	763.5
Sub-threshold Volume Loss	-86.7	-236.1	-44.4	-142.7	-109.4	-323.2	-942.5
Net Sedimentary Change	-8.3	-90.9	3.7	28.4	-21.7	-239.8	-328.5
Bank Erosion (-0.1m)	N/A	-36.0	N/A	N/A	N/A	-5.9	-41.8
Bed Erosion (-0.1m)	-14.6	-86.3	-8.1	-34.3	-62.6	-272.6	-478.5

4

1 *Table A2.4 - Reported area statistics for sub-reach scale analyses between Surveys 1 and 2.*

Survey 1-2 Area Statistics	A	B	C	D	E	F	Total
Total Surveyed Area	6521.5	7610.1	2724.6	5785.1	4603.8	8352.7	35597.8
Significant (+0.1m) Deposition Area	2296.1	1050.3	124.9	1924.4	2076.3	1900.1	9372.0
Significant (-0.1m) Erosion Area	819.7	3189.5	313.3	1603.8	1397.1	1827.1	9150.5
Sub-threshold (stable) Area	3405.7	3370.4	2286.4	2256.9	1130.4	4625.5	17075.4
% Survey Area Stable	52.2	44.3	83.9	39.0	24.6	55.4	48.0
% Survey Area Deposition	35.2	13.8	4.6	33.3	45.1	22.8	26.3
% Survey Area Erosion	12.6	41.9	11.5	27.7	30.4	21.9	25.7

2

3 *Table A2.5 - Reported area statistics for sub-reach scale analyses between Surveys 2 and 3.*

Survey 2-3 Area Statistics	A	B	C	D	E	F	Total
Total Surveyed Area	5587.5	7271.8	2787.3	5766.9	5397.0	8089.4	34899.8
Significant (+0.1m) Deposition Area	860.0	1588.8	179.5	677.4	568.8	1274.7	5149.3
Significant (-0.1m) Erosion Area	596.2	1002.1	260.2	1638.1	1300.5	1921.7	6718.8
Sub-threshold (stable) Area	4131.3	4680.9	2347.5	3451.4	3527.7	4893.0	23031.7
% Survey Area Stable	73.9	64.4	84.2	59.9	65.4	60.5	66.0
% Survey Area Deposition	15.4	21.9	6.4	11.8	10.5	15.8	14.8
% Survey Area Erosion	10.7	13.8	9.3	28.4	24.1	23.8	19.3

4

1 *Table A2.6 - Reported area statistics for sub-reach scale analyses between Surveys 3 and 4.*

Survey 3-4 Areal Statistics	A	B	C	D	E	F	Total
Total Surveyed Area	5393.3	7257.5	2904.3	5823.6	5490.3	8141.5	35010.5
Significant (+0.1m) Deposition Area	159.1	519.1	121.7	1068.5	432.8	453.6	2754.8
Significant (-0.1m) Erosion Area	255.0	1054.4	116.3	447.4	519.2	1959.9	4352.1
Sub-threshold (stable) Area	4979.2	5684.0	2666.3	4307.7	4538.3	5728.1	27903.6
% Survey Area Stable	92.3	78.3	91.8	74.0	82.7	70.4	79.7
% Survey Area Deposition	3.0	7.2	4.2	18.4	7.9	5.6	7.9
% Survey Area Erosion	4.7	14.5	4.0	7.7	9.5	24.1	12.4

2

1 Appendix 3 – Agisoft Photoscan® Processing Reports
2

JulyChannel

Processing Report
28 August 2018



Survey Data

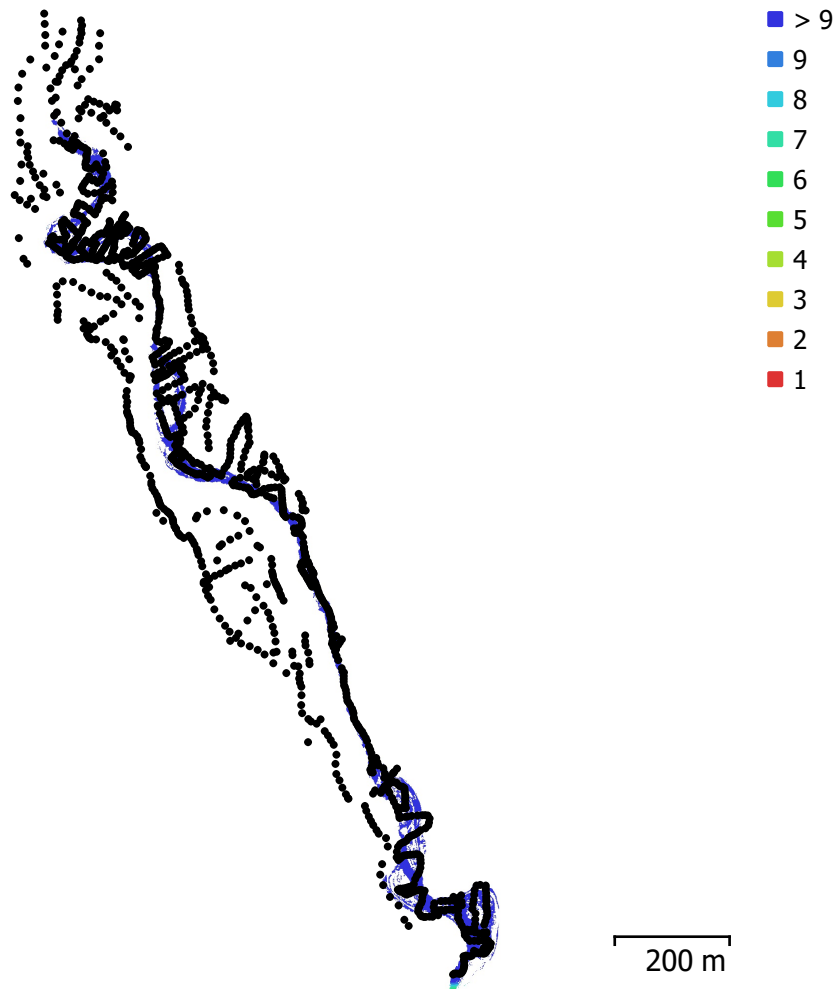


Fig. 1. Camera locations and image overlap.

Number of images:	1,296	Camera stations:	1,283
Flying altitude:	56 m	Tie points:	432,030
Ground resolution:	1.75 cm/pix	Projections:	2,192,557
Coverage area:	0.037 km ²	Reprojection error:	0.813 pix

Camera Model	Resolution	Focal Length	Pixel Size	Precalibrated
FC300X (3.61 mm)	4000 x 3000	3.61 mm	1.56 x 1.56 μ m	No
FC300X (3.61 mm)	4000 x 3000	3.61 mm	1.56 x 1.56 μ m	No
FC300X (3.61 mm)	4000 x 3000	3.61 mm	1.56 x 1.56 μ m	No
FC300X (3.61 mm)	4000 x 3000	3.61 mm	1.56 x 1.56 μ m	No
FC300X (3.61 mm)	4000 x 3000	3.61 mm	1.56 x 1.56 μ m	No

Camera Model	Resolution	Focal Length	Pixel Size	Precalibrated
FC300X (3.61 mm)	4000 x 3000	3.61 mm	1.56 x 1.56 μm	No

Table 1. Cameras.

Camera Calibration

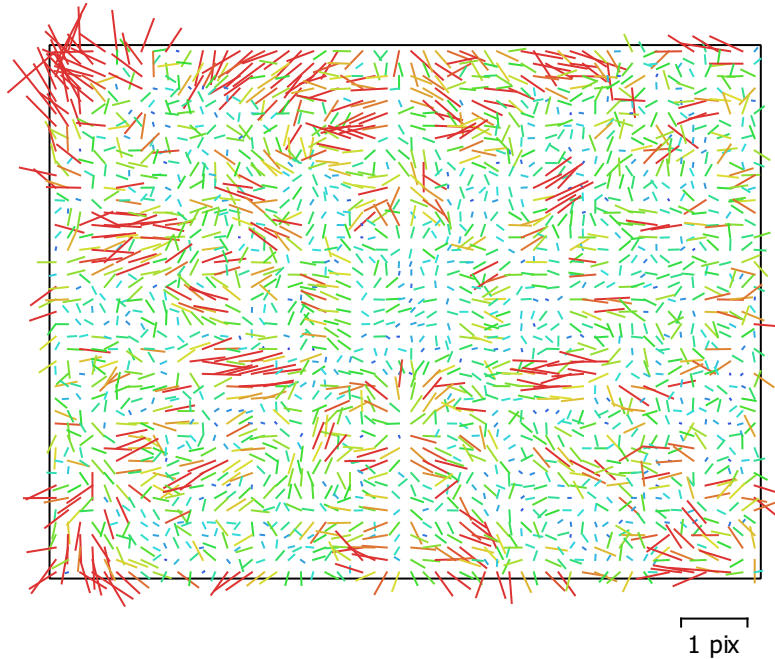


Fig. 2. Image residuals for FC300X (3.61 mm).

FC300X (3.61 mm)

96 images

Type	Resolution	Focal Length	Pixel Size
Frame	4000 x 3000	3.61 mm	1.56 x 1.56 μm

	Value	Error	F	Cx	Cy	B1	B2	K1	K2	K3	K4	P1	P2
F	2262.35	0.55	1.00	0.20	-0.26	-0.10	0.01	-0.06	0.01	0.05	-0.07	0.12	0.01
Cx	-8.09623	0.32		1.00	0.04	0.11	0.25	-0.01	-0.02	0.03	-0.03	0.30	0.04
Cy	0.13555	0.22			1.00	-0.13	0.24	0.00	0.01	-0.03	0.03	0.01	0.23
B1	-0.471491	0.042				1.00	0.06	-0.01	-0.00	-0.00	0.00	-0.18	-0.02
B2	1.27485	0.047					1.00	0.00	-0.01	0.01	-0.01	-0.03	0.54
K1	-0.00658869	0.00013						1.00	-0.95	0.90	-0.84	-0.00	-0.01
K2	-0.00978929	0.00041							1.00	-0.98	0.95	-0.01	-0.00
K3	0.0305971	0.00054								1.00	-0.99	0.02	0.00
K4	-0.0131595	0.00024									1.00	-0.02	-0.00
P1	0.00235771	1.1e-05										1.00	0.03
P2	4.32426e-05	9.2e-06											1.00

Table 2. Calibration coefficients and correlation matrix.

Camera Calibration

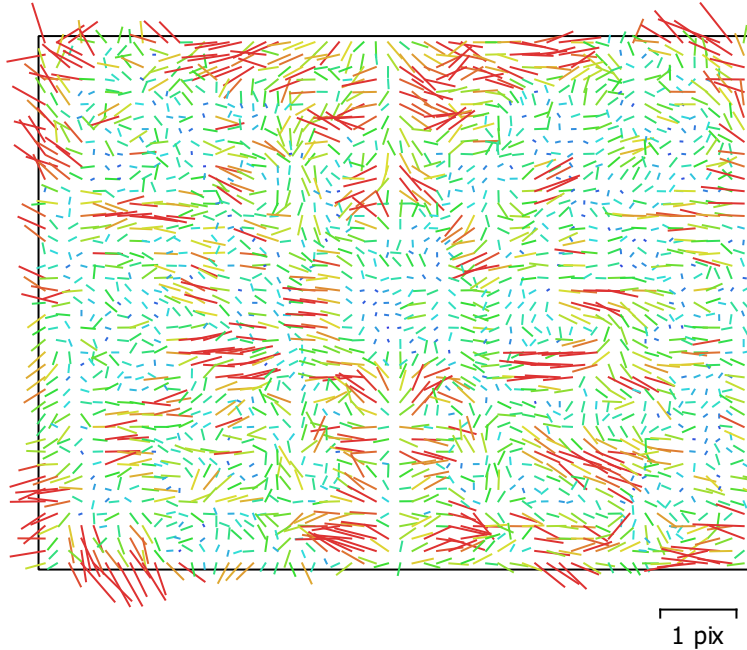


Fig. 3. Image residuals for FC300X (3.61 mm).

FC300X (3.61 mm)

236 images

Type
Frame

Resolution
4000 x 3000

Focal Length
3.61 mm

Pixel Size
1.56 x 1.56 μm

	Value	Error	F	Cx	Cy	B1	B2	K1	K2	K3	K4	P1	P2
F	2262.49	0.4	1.00	0.10	-0.08	0.05	0.05	-0.06	-0.01	0.10	-0.15	0.17	-0.03
Cx	7.67665	0.1		1.00	-0.07	-0.08	0.06	-0.02	0.01	0.01	-0.02	0.20	-0.00
Cy	-0.734073	0.1			1.00	-0.12	-0.02	-0.00	0.01	-0.02	0.03	-0.07	0.19
B1	-0.027196	0.014				1.00	-0.00	0.01	-0.02	0.02	-0.02	-0.01	0.07
B2	0.411406	0.014					1.00	-0.01	0.01	-0.00	0.00	-0.02	0.00
K1	-0.00494467	7e-05						1.00	-0.97	0.91	-0.85	-0.02	0.02
K2	-0.0136919	0.00023							1.00	-0.98	0.95	-0.00	-0.03
K3	0.0377638	0.0003								1.00	-0.99	0.02	0.02
K4	-0.0170475	0.00013									1.00	-0.03	-0.02
P1	0.00341214	3.8e-06										1.00	-0.15
P2	-0.000171743	4.2e-06											1.00

Table 3. Calibration coefficients and correlation matrix.

Camera Calibration

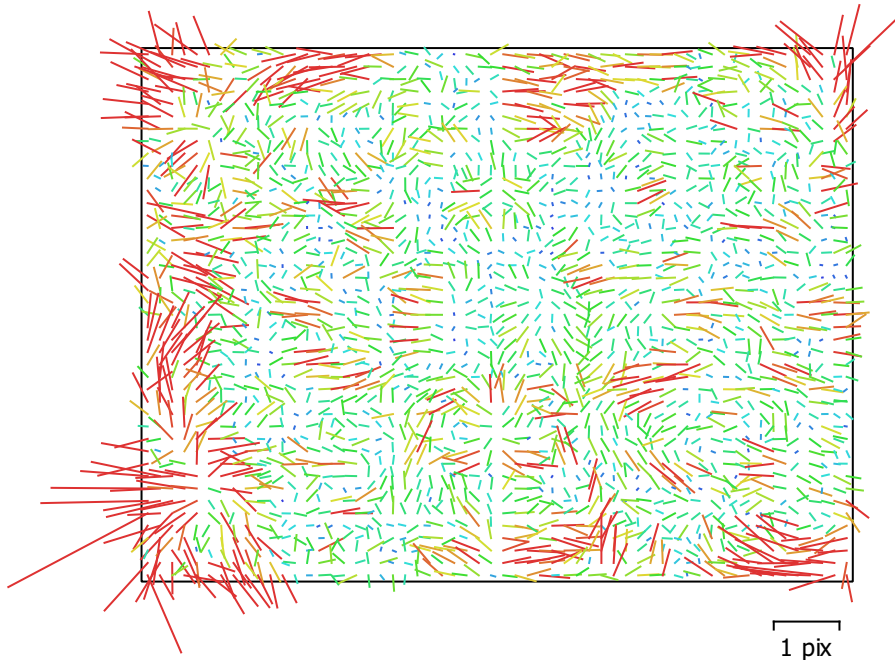


Fig. 4. Image residuals for FC300X (3.61 mm).

FC300X (3.61 mm)

196 images

Type
Frame

Resolution
4000 x 3000

Focal Length
3.61 mm

Pixel Size
1.56 x 1.56 μm

	Value	Error	F	Cx	Cy	B1	B2	K1	K2	K3	K4	P1	P2
F	2264.5	0.38	1.00	0.16	-0.10	0.12	-0.01	-0.06	0.02	0.05	-0.08	0.18	0.01
Cx	13.9891	0.084		1.00	-0.02	-0.16	0.06	-0.01	-0.00	0.01	-0.02	0.32	-0.01
Cy	-2.70165	0.079			1.00	-0.11	-0.13	0.01	-0.00	-0.00	0.01	-0.03	0.28
B1	-0.653622	0.014				1.00	0.01	0.02	-0.03	0.04	-0.04	-0.02	-0.05
B2	-1.2599	0.015					1.00	-0.00	-0.00	0.01	-0.01	-0.08	0.10
K1	-0.00868456	8.2e-05						1.00	-0.97	0.91	-0.86	0.04	-0.02
K2	-0.00318123	0.00027							1.00	-0.98	0.95	-0.04	0.02
K3	0.0251518	0.00034								1.00	-0.99	0.05	-0.02
K4	-0.0116368	0.00015									1.00	-0.05	0.02
P1	0.00394631	4.3e-06										1.00	0.02
P2	-0.000482614	5.1e-06											1.00

Table 4. Calibration coefficients and correlation matrix.

Camera Calibration

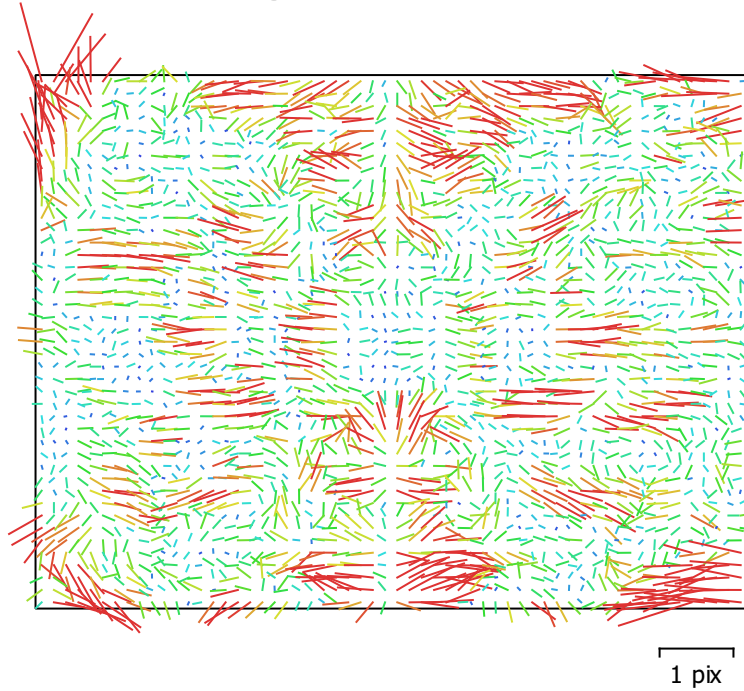


Fig. 5. Image residuals for FC300X (3.61 mm).

FC300X (3.61 mm)

277 images

Type
Frame

Resolution
4000 x 3000

Focal Length
3.61 mm

Pixel Size
1.56 x 1.56 μm

	Value	Error	F	Cx	Cy	B1	B2	K1	K2	K3	K4	P1	P2
F	2270.51	0.39	1.00	0.14	-0.11	0.12	0.00	-0.07	-0.01	0.12	-0.19	0.23	0.04
Cx	3.52545	0.096		1.00	-0.03	-0.04	0.07	0.02	-0.02	0.03	-0.03	0.17	-0.03
Cy	-2.10374	0.097			1.00	-0.11	-0.07	0.01	0.00	-0.02	0.02	-0.05	0.20
B1	-0.0990445	0.013				1.00	-0.03	0.02	-0.03	0.04	-0.05	0.04	-0.02
B2	0.276096	0.013					1.00	0.00	-0.00	0.00	-0.00	-0.07	0.06
K1	-0.00530092	6e-05						1.00	-0.97	0.90	-0.84	0.03	0.01
K2	-0.0131362	0.00019							1.00	-0.98	0.94	-0.02	-0.01
K3	0.0366028	0.00025								1.00	-0.99	0.04	0.01
K4	-0.0166853	0.00011									1.00	-0.05	-0.02
P1	0.00307131	3.2e-06										1.00	-0.03
P2	0.000272974	3.7e-06											1.00

Table 5. Calibration coefficients and correlation matrix.

Camera Calibration

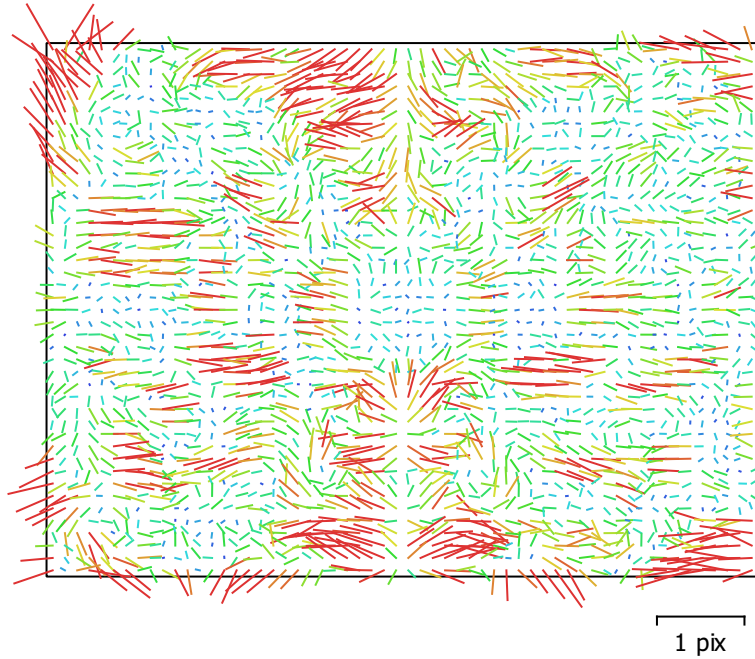


Fig. 6. Image residuals for FC300X (3.61 mm).

FC300X (3.61 mm)

344 images

Type
Frame

Resolution
4000 x 3000

Focal Length
3.61 mm

Pixel Size
1.56 x 1.56 μm

	Value	Error	F	Cx	Cy	B1	B2	K1	K2	K3	K4	P1	P2
F	2283.4	0.45	1.00	0.06	-0.14	0.07	-0.03	-0.03	-0.01	0.13	-0.20	0.13	-0.04
Cx	-4.27363	0.13		1.00	-0.03	0.01	0.20	-0.01	0.01	-0.01	0.01	0.24	0.01
Cy	-0.880186	0.14			1.00	-0.15	-0.05	-0.01	0.01	-0.03	0.04	-0.01	0.13
B1	-1.75829	0.02				1.00	0.03	0.01	-0.02	0.03	-0.03	0.14	-0.10
B2	-0.718503	0.02					1.00	0.02	-0.01	0.00	0.00	0.08	-0.16
K1	-0.00609296	6e-05						1.00	-0.97	0.91	-0.85	0.02	-0.00
K2	-0.00978214	0.00019							1.00	-0.98	0.94	-0.01	0.01
K3	0.0332983	0.00025								1.00	-0.99	0.02	-0.01
K4	-0.0154796	0.00011									1.00	-0.03	0.01
P1	0.00317789	4.1e-06										1.00	-0.07
P2	-0.000284536	4.3e-06											1.00

Table 6. Calibration coefficients and correlation matrix.

Camera Calibration

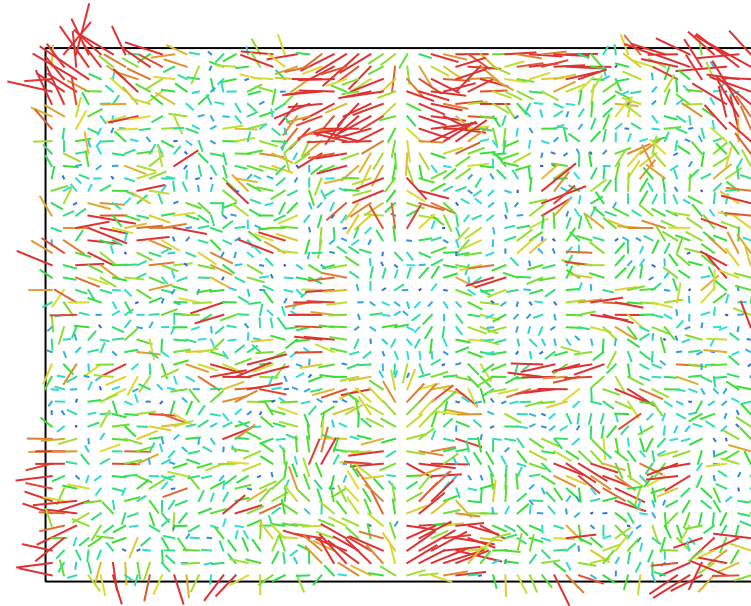


Fig. 7. Image residuals for FC300X (3.61 mm). 1 pix

FC300X (3.61 mm)

135 images

Type
Frame

Resolution
4000 x 3000

Focal Length
3.61 mm

Pixel Size
1.56 x 1.56 μm

	Value	Error	F	Cx	Cy	B1	B2	K1	K2	K3	K4	P1	P2
F	2293.33	0.57	1.00	0.07	-0.19	-0.07	0.09	-0.04	0.01	0.06	-0.09	0.22	-0.13
Cx	15.2324	0.15		1.00	-0.10	-0.03	0.15	0.00	-0.00	0.01	-0.02	0.17	-0.12
Cy	-0.685428	0.13			1.00	-0.03	0.06	-0.00	-0.00	-0.01	0.01	-0.06	0.18
B1	-1.2763	0.016				1.00	0.08	0.03	-0.03	0.01	-0.00	-0.02	0.04
B2	0.549135	0.016					1.00	-0.00	0.00	0.01	-0.01	0.08	-0.03
K1	-0.0070433	0.0001						1.00	-0.97	0.91	-0.86	0.02	0.00
K2	-0.00816853	0.00034							1.00	-0.98	0.95	-0.01	-0.01
K3	0.0323264	0.00046								1.00	-0.99	0.02	-0.01
K4	-0.0151282	0.00021									1.00	-0.03	0.01
P1	0.00317033	6.1e-06										1.00	-0.20
P2	-0.000231974	6.6e-06											1.00

Table 7. Calibration coefficients and correlation matrix.

Ground Control Points

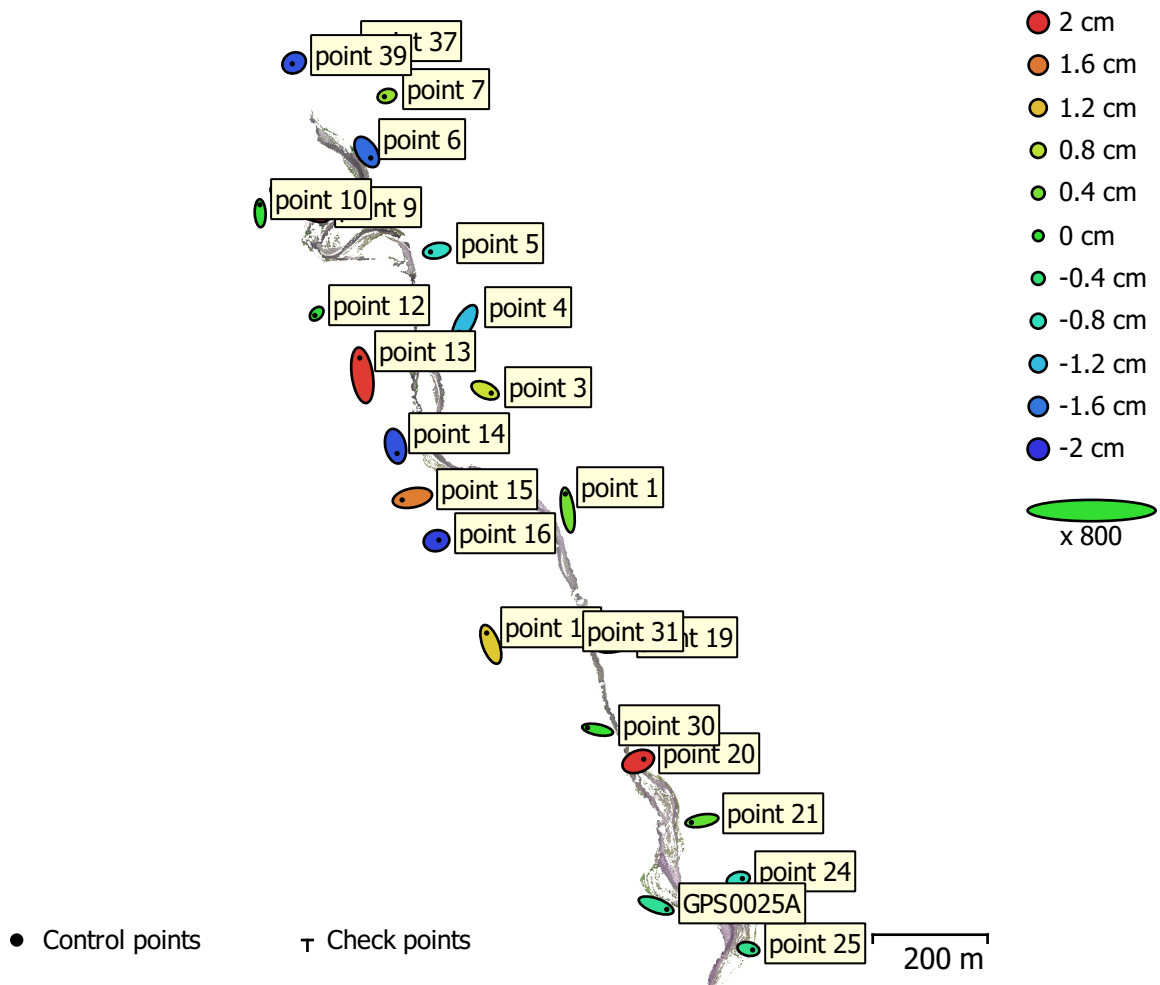


Fig. 8. GCP locations and error estimates.

Z error is represented by ellipse color. X,Y errors are represented by ellipse shape.

Estimated GCP locations are marked with a dot or crossing.

Count	X error (cm)	Y error (cm)	Z error (cm)	XY error (cm)	Total (cm)
24	3.19904	3.13731	1.24908	4.48069	4.65154

Table 8. Control points RMSE.

Label	X error (cm)	Y error (cm)	Z error (cm)	Total (cm)	Image (pix)
point 1	-1.02118	7.00688	0.386127	7.09143	0.258 (5)
point 3	2.69723	-1.21143	0.889696	3.08775	0.495 (9)
point 4	-2.49686	-4.17936	-1.21229	5.01707	0.336 (19)
point 5	-2.69688	-0.527284	-0.85631	2.87828	0.359 (12)
point 6	1.72499	-2.62853	-1.66802	3.55908	0.307 (8)
point 7	-1.12633	-0.310587	0.596774	1.31195	0.242 (9)
point 9	8.36342	-4.6766	1.98274	9.78512	0.672 (15)
point 10	-0.162936	3.71676	-0.0424857	3.72058	0.352 (8)
point 12	-0.7661	-0.769964	-0.0650786	1.08811	0.353 (8)
point 13	-1.1117	7.54383	1.94495	7.86944	0.326 (13)
point 14	0.700667	-3.1629	-1.81466	3.7132	0.346 (10)
point 15	-4.46543	-0.888501	1.56003	4.81281	0.269 (14)
point 16	1.07291	0.248394	-1.91658	2.21046	0.252 (18)
point 17	-1.80264	4.92871	1.12776	5.36782	0.262 (15)
point 19	-4.78158	-0.911311	0.603129	4.90487	0.447 (15)
point 20	2.37672	0.961597	1.98986	3.24546	0.397 (18)
point 21	-4.56968	-0.808674	0.275758	4.64886	0.226 (14)
point 24	1.77813	0.475784	-0.821893	2.01585	0.322 (9)
point 25	1.84604	-0.391047	-0.525217	1.95873	0.213 (22)
point 30	-4.39261	0.857233	0.021075	4.47553	0.222 (11)
point 31	5.02455	-4.72839	-1.09565	6.986	0.301 (25)
point 37	-0.373445	1.8918	1.61333	2.51419	0.187 (12)
point 39	-0.778881	-0.419741	-1.81064	2.01526	0.227 (8)
GPS0025A	4.65446	-1.71479	-0.581408	4.99425	0.230 (14)
Total	3.19904	3.13731	1.24908	4.65154	0.335

Table 9. Control points.

Digital Elevation Model

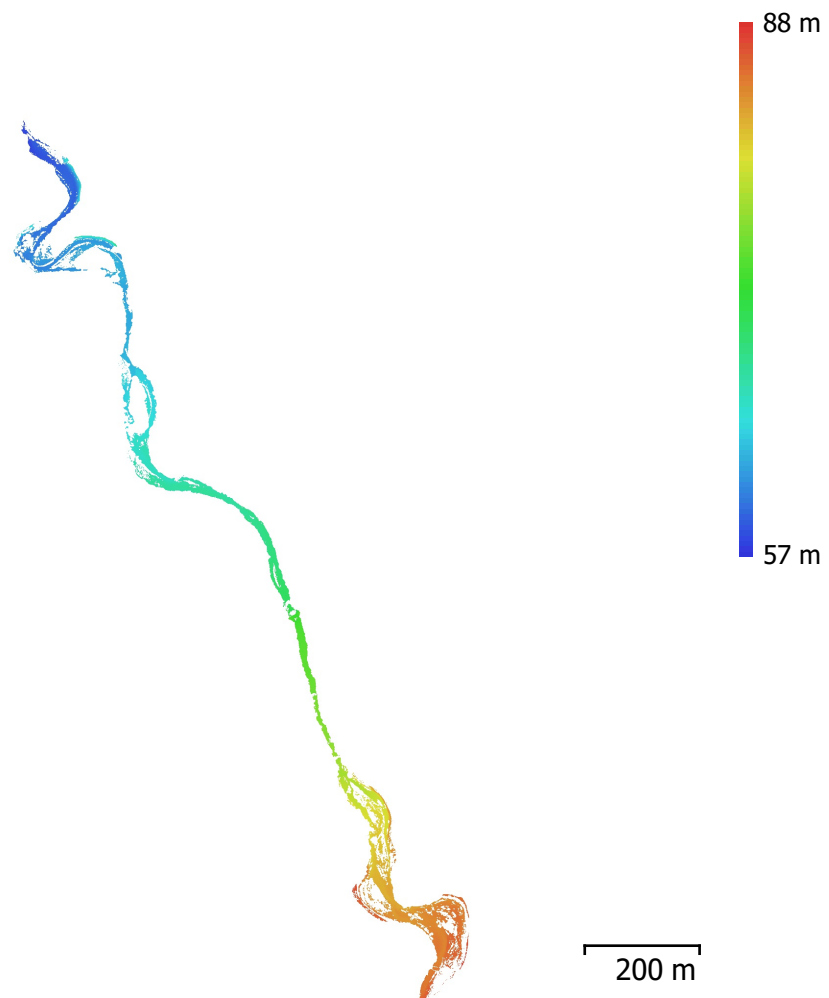


Fig. 9. Reconstructed digital elevation model.

Resolution: 3.51 cm/pix
Point density: 814 points/m²

Processing Parameters

General

Cameras	1296
Aligned cameras	1283
Markers	24

Shapes

Polygons	2
Coordinate system	Local Coordinates (m)
Rotation angles	Yaw, Pitch, Roll

Point Cloud

Points	432,030 of 1,085,614
RMS reprojection error	0.250083 (0.813 pix)
Max reprojection error	3.22572 (38.0237 pix)
Mean key point size	3.1605 pix
Point colors	3 bands, uint8
Key points	No
Average tie point multiplicity	4.67791

Alignment parameters

Accuracy	High
Generic preselection	No
Reference preselection	No
Key point limit	40,000
Tie point limit	4,000
Filter points by mask	No
Adaptive camera model fitting	Yes
Matching time	20 hours 44 minutes
Alignment time	2 hours 42 minutes

Optimization parameters

Parameters	f, b1, b2, cx, cy, k1-k4, p1, p2
Optimization time	4 minutes 22 seconds

Dense Point Cloud

Points	45,562,133
Point colors	3 bands, uint8

Reconstruction parameters

Quality	High
Depth filtering	Aggressive
Depth maps generation time	3 days 5 hours
Dense cloud generation time	4 hours 24 minutes

Model

Faces	1,973,147
Vertices	1,141,761
Vertex colors	3 bands, uint8

Reconstruction parameters

Surface type	Height field
Source data	Dense
Interpolation	Disabled
Quality	High
Depth filtering	Aggressive
Face count	3,037,475
Processing time	3 minutes 9 seconds

DEM

Size	38,512 x 59,734
Coordinate system	Local Coordinates (m)

Reconstruction parameters

Source data	Mesh
Interpolation	Disabled

Processing time	47 seconds
Orthomosaic	
Size	48,167 x 89,732
Coordinate system	Local Coordinates (m)
Colors	3 bands, uint8
Reconstruction parameters	
Blending mode	Mosaic
Surface	DEM
Enable hole filling	Yes
Processing time	34 minutes 59 seconds
Software	
Version	1.4.2 build 6205
Platform	Windows 64

NovemberChannel

Processing Report
28 August 2018



Survey Data

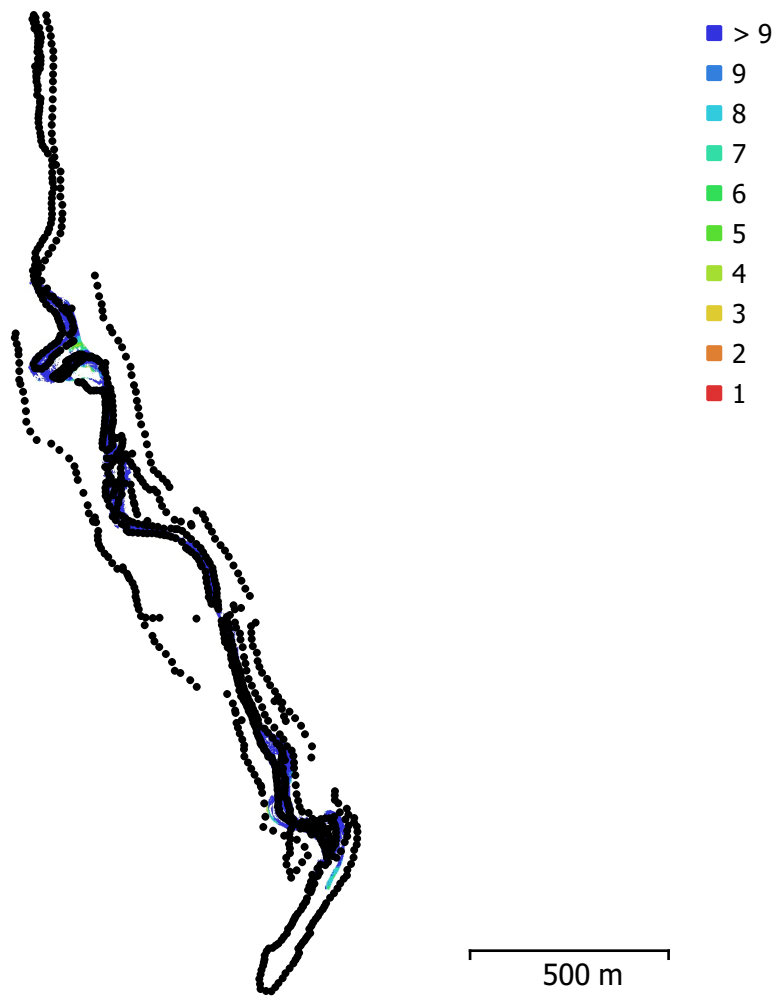


Fig. 1. Camera locations and image overlap.

Number of images:	929	Camera stations:	925
Flying altitude:	58.1 m	Tie points:	680,050
Ground resolution:	2.17 cm/pix	Projections:	2,465,327
Coverage area:	0.0599 km ²	Reprojection error:	0.831 pix

Camera Model	Resolution	Focal Length	Pixel Size	Precalibrated
FC300X (3.61 mm)	4000 x 3000	3.61 mm	1.56 x 1.56 μ m	No
FC300X (3.61 mm)	4000 x 3000	3.61 mm	1.56 x 1.56 μ m	No
FC300X (3.61 mm)	4000 x 3000	3.61 mm	1.56 x 1.56 μ m	No

Table 1. Cameras.

Camera Calibration

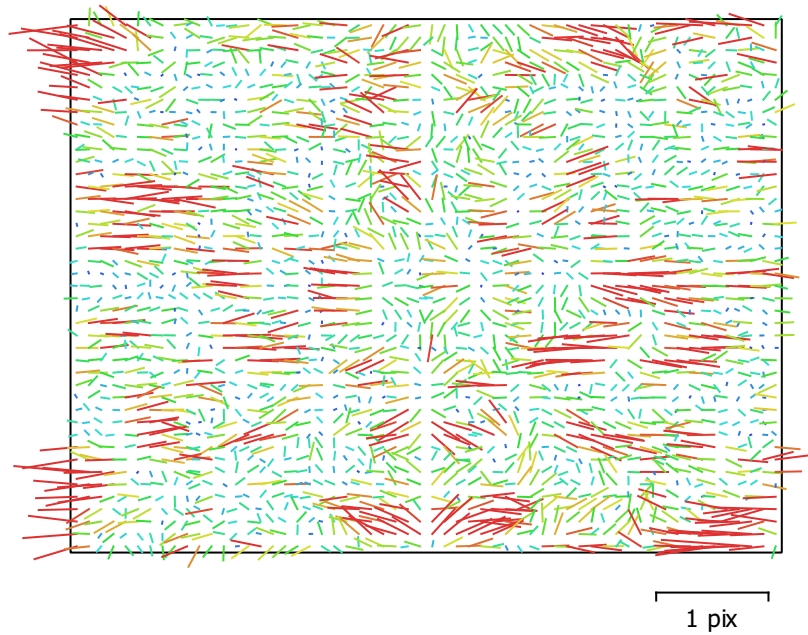


Fig. 2. Image residuals for FC300X (3.61 mm).

FC300X (3.61 mm)

127 images

Type
Frame

Resolution
4000 x 3000

Focal Length
3.61 mm

Pixel Size
1.56 x 1.56 μm

	Value	Error	F	Cx	Cy	B1	B2	K1	K2	K3	K4	P1	P2
F	2296.85	0.98	1.00	0.47	-0.25	0.05	-0.12	-0.14	-0.00	0.22	-0.31	0.20	-0.00
Cx	0.298137	0.18		1.00	-0.12	0.01	0.17	-0.11	0.02	0.10	-0.15	0.39	-0.03
Cy	-4.43826	0.18			1.00	-0.12	-0.00	0.02	0.03	-0.08	0.10	-0.04	0.38
B1	0.109472	0.08				1.00	0.03	-0.01	-0.01	0.03	-0.04	-0.23	0.16
B2	-3.12037	0.072					1.00	0.01	-0.00	-0.02	0.03	0.21	-0.10
K1	-0.0105537	7.1e-05						1.00	-0.94	0.85	-0.77	-0.04	-0.02
K2	-0.00232942	0.00023							1.00	-0.96	0.91	0.01	0.03
K3	0.0273876	0.00031								1.00	-0.99	0.04	-0.02
K4	-0.0131235	0.00014									1.00	-0.06	0.02
P1	0.0030082	6.2e-06										1.00	0.00
P2	-0.00072948	1.1e-05											1.00

Table 2. Calibration coefficients and correlation matrix.

Camera Calibration

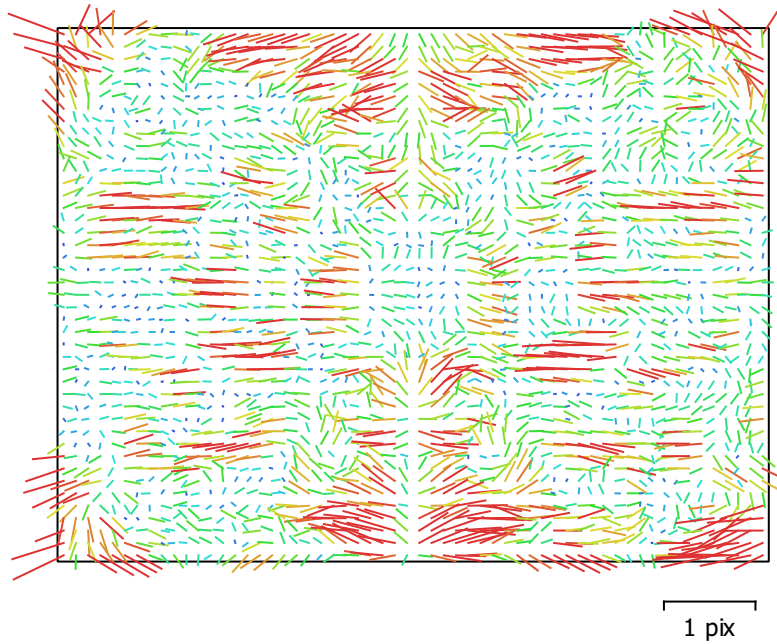


Fig. 3. Image residuals for FC300X (3.61 mm).

FC300X (3.61 mm)

409 images

Type
Frame

Resolution
4000 x 3000

Focal Length
3.61 mm

Pixel Size
1.56 x 1.56 μm

	Value	Error	F	Cx	Cy	B1	B2	K1	K2	K3	K4	P1	P2
F	2329.07	1	1.00	0.07	-0.01	0.01	-0.07	-0.17	-0.09	0.41	-0.53	0.62	-0.06
Cx	-36.9648	0.15		1.00	0.01	0.01	0.32	-0.01	-0.02	0.05	-0.06	0.20	0.01
Cy	-12.7634	0.18			1.00	-0.37	0.04	-0.01	0.02	-0.02	0.02	-0.02	-0.00
B1	-0.719855	0.018				1.00	0.02	0.02	-0.03	0.03	-0.03	0.01	-0.02
B2	-1.90211	0.018					1.00	0.02	-0.01	-0.01	0.02	0.00	-0.02
K1	-0.00782424	4.2e-05						1.00	-0.94	0.76	-0.64	-0.11	0.01
K2	-0.00791869	0.00015							1.00	-0.93	0.85	-0.05	0.00
K3	0.0343654	0.00022								1.00	-0.98	0.26	-0.02
K4	-0.0164392	0.00011									1.00	-0.33	0.03
P1	0.00334246	2.4e-06										1.00	-0.06
P2	-0.000455191	2e-06											1.00

Table 3. Calibration coefficients and correlation matrix.

Camera Calibration

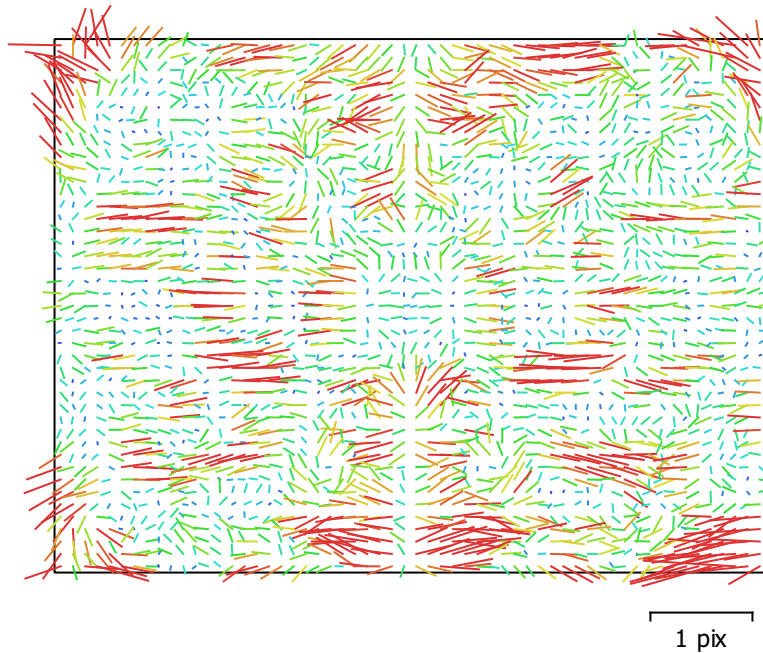


Fig. 4. Image residuals for FC300X (3.61 mm).

FC300X (3.61 mm)

393 images

Type
Frame

Resolution
4000 x 3000

Focal Length
3.61 mm

Pixel Size
1.56 x 1.56 μ m

	Value	Error	F	Cx	Cy	B1	B2	K1	K2	K3	K4	P1	P2
F	2318.86	0.8	1.00	0.00	-0.25	-0.01	-0.18	-0.07	-0.05	0.24	-0.31	0.32	-0.06
Cx	-15.3645	0.18		1.00	-0.13	0.06	0.36	0.01	0.00	-0.00	0.01	0.07	0.04
Cy	-6.88931	0.2			1.00	-0.51	-0.05	0.02	0.01	-0.06	0.08	0.03	0.16
B1	-0.0944111	0.031				1.00	-0.06	-0.00	-0.00	0.01	-0.01	-0.03	-0.02
B2	-2.09069	0.029					1.00	0.01	0.02	-0.05	0.07	-0.08	0.06
K1	-0.0071134	5.7e-05						1.00	-0.96	0.88	-0.80	-0.01	0.00
K2	-0.00836447	0.0002							1.00	-0.97	0.92	-0.03	0.00
K3	0.0337839	0.00029								1.00	-0.99	0.09	-0.01
K4	-0.0159654	0.00014									1.00	-0.11	0.02
P1	0.00333209	3.6e-06										1.00	0.31
P2	-0.00043336	3.5e-06											1.00

Table 4. Calibration coefficients and correlation matrix.

Ground Control Points

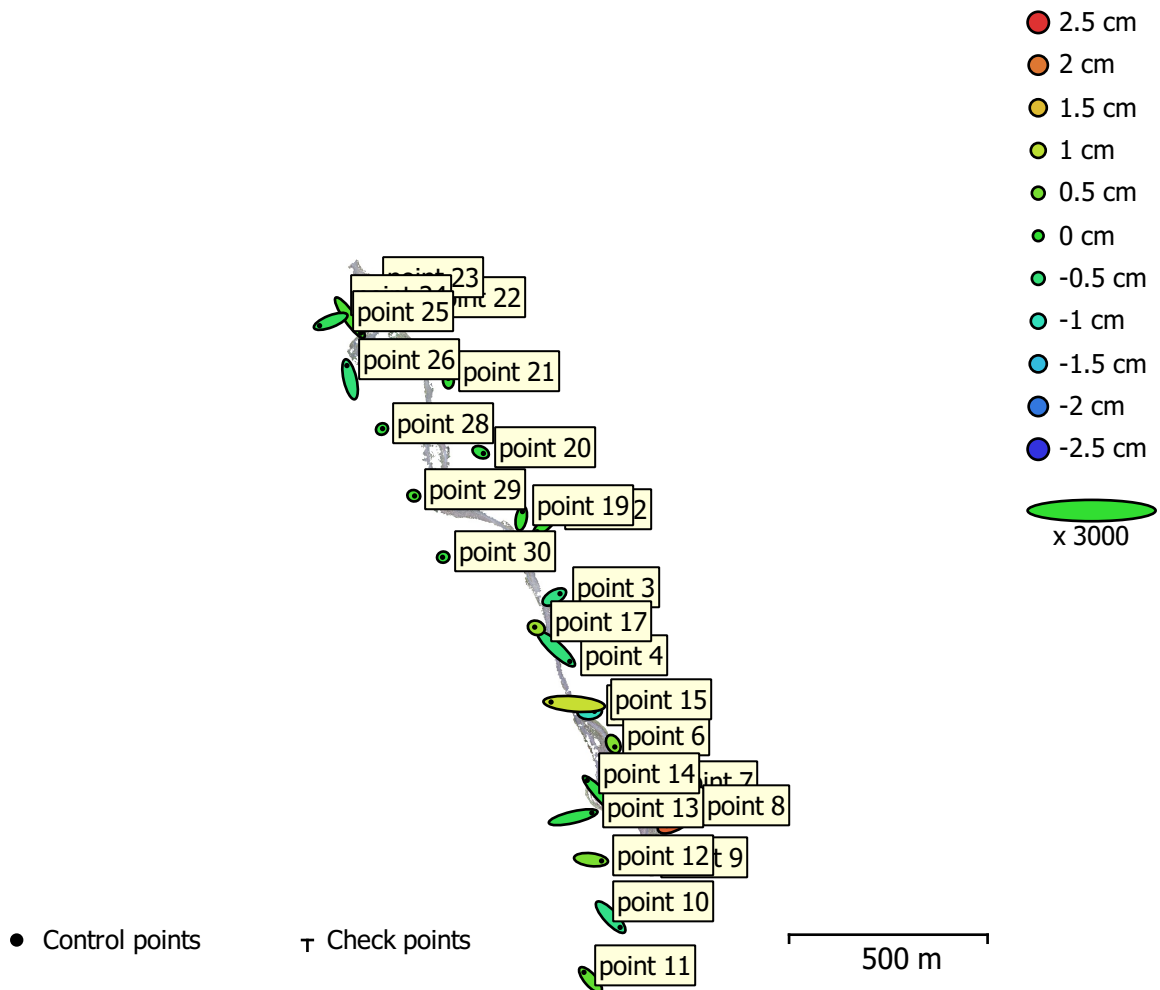


Fig. 5. GCP locations and error estimates.

Z error is represented by ellipse color. X,Y errors are represented by ellipse shape.

Estimated GCP locations are marked with a dot or crossing.

Count	X error (cm)	Y error (cm)	Z error (cm)	XY error (cm)	Total (cm)
26	1.51055	1.1717	0.661951	1.91171	2.02307

Table 5. Control points RMSE.

Label	X error (cm)	Y error (cm)	Z error (cm)	Total (cm)	Image (pix)
point 2	-1.35991	-1.28527	0.065847	1.87233	0.218 (6)
point 3	0.948116	0.552249	-0.589893	1.24574	0.160 (8)
point 4	2.29235	-2.13219	-0.519767	3.17352	0.266 (19)
point 5	0.796261	0.0751387	-1.01685	1.2937	0.289 (13)
point 6	0.24699	-0.473029	0.582068	0.78966	0.221 (7)
point 7	-0.317395	0.780112	-0.937375	1.26015	0.298 (8)
point 8	-1.795	-1.15199	2.16147	3.03662	0.187 (11)
point 9	0.237763	-0.389584	-0.858653	0.972415	0.302 (8)
point 10	1.58928	-1.71737	-0.621724	2.4211	0.300 (11)
point 11	-1.09862	1.26719	0.342638	1.71176	0.202 (8)
point 12	1.76988	-0.204481	0.524225	1.85717	0.047 (4)
point 13	3.13519	0.726239	-0.214617	3.22535	0.236 (5)
point 14	-2.55289	2.6874	-0.154637	3.70989	0.106 (7)
point 15	-3.87983	0.315986	1.08167	4.04016	0.175 (7)
point 17	-0.265864	0.117261	0.764856	0.818193	0.185 (5)
point 19	0.200879	1.13504	0.0509669	1.1538	0.196 (11)
point 20	0.459094	-0.207034	-0.144284	0.523878	0.127 (9)
point 21	-0.0111647	0.383654	-0.0441403	0.386346	0.113 (6)
point 22	-0.892487	0.570686	-0.00786271	1.05938	0.126 (9)
point 23	0.860545	0.326035	-0.217814	0.945663	0.264 (17)
point 24	1.81746	-2.57978	0.204833	3.16234	0.225 (13)
point 25	-1.8699	-0.729517	-0.288167	2.02774	0.167 (5)
point 26	-0.533364	2.30438	-0.511288	2.41993	0.142 (5)
point 28	0.0991325	0.0680515	-0.105655	0.160066	0.023 (3)
point 29	0.137147	-0.0375639	0.153817	0.209476	0.200 (6)
point 30	-0.106107	-0.0229489	-0.107968	0.153109	0.158 (9)
Total	1.51055	1.1717	0.661951	2.02307	0.218

Table 6. Control points.

Digital Elevation Model



Fig. 6. Reconstructed digital elevation model.

Resolution: 4.35 cm/pix
Point density: 529 points/m²

Processing Parameters

General

Cameras	929
Aligned cameras	925
Markers	26
Coordinate system	Local Coordinates (m)
Rotation angles	Yaw, Pitch, Roll

Point Cloud

Points	680,050 of 732,102
RMS reprojection error	0.189151 (0.831269 pix)
Max reprojection error	2.40802 (29.4011 pix)
Mean key point size	4.15552 pix
Point colors	3 bands, uint8
Key points	No
Average tie point multiplicity	3.76511

Alignment parameters

Accuracy	Highest
Generic preselection	Yes
Reference preselection	No
Key point limit	40,000
Tie point limit	3,000
Filter points by mask	No
Adaptive camera model fitting	Yes
Matching time	5 hours 7 minutes
Alignment time	8 minutes 1 seconds

Optimization parameters

Parameters	f, b1, b2, cx, cy, k1-k4, p1, p2
Optimization time	41 seconds

Dense Point Cloud

Points	69,084,263
Point colors	3 bands, uint8

Reconstruction parameters

Quality	High
Depth filtering	Moderate
Depth maps generation time	11 hours 13 minutes
Dense cloud generation time	1 hours 35 minutes

Model

Faces	2,999,347
Vertices	1,682,457
Vertex colors	3 bands, uint8

Reconstruction parameters

Surface type	Height field
Source data	Dense
Interpolation	Disabled
Quality	High
Depth filtering	Moderate
Face count	4,199,611
Processing time	2 minutes 42 seconds

DEM

Size	23,265 x 41,236
Coordinate system	Local Coordinates (m)

Reconstruction parameters

Source data	Mesh
Interpolation	Disabled
Processing time	59 seconds

Orthomosaic

Size	19,838 x 56,132
Coordinate system	Local Coordinates (m)
Colors	3 bands, uint8
Reconstruction parameters	
Blending mode	Mosaic
Surface	DEM
Enable color correction	No
Enable hole filling	Yes
Processing time	13 minutes 4 seconds
Software	
Version	1.4.2 build 6205
Platform	Windows 64

SeptemberChannel

Processing Report
28 August 2018



Survey Data

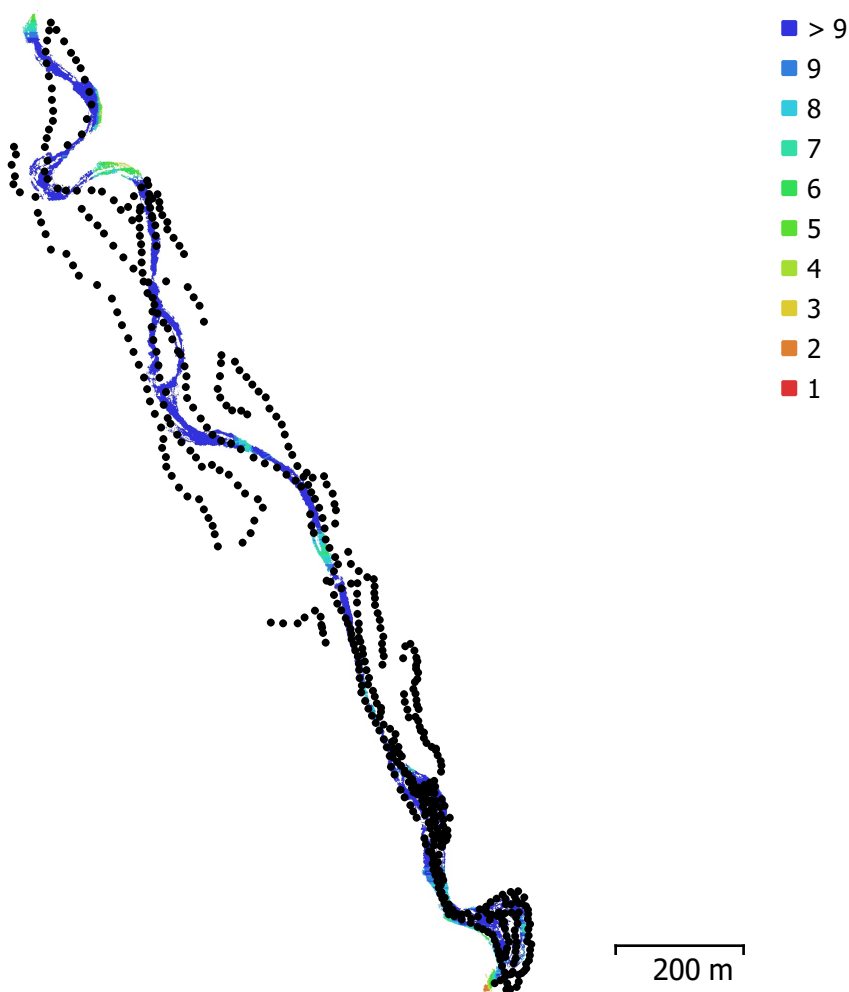


Fig. 1. Camera locations and image overlap.

Number of images:	553	Camera stations:	528
Flying altitude:	63 m	Tie points:	453,776
Ground resolution:	1.5 cm/pix	Projections:	1,569,527
Coverage area:	0.0339 km ²	Reprojection error:	0.541 pix

Camera Model	Resolution	Focal Length	Pixel Size	Precalibrated
FC6310 (8.8 mm)	5472 x 3648	8.8 mm	2.41 x 2.41 μ m	No

Table 1. Cameras.

Camera Calibration

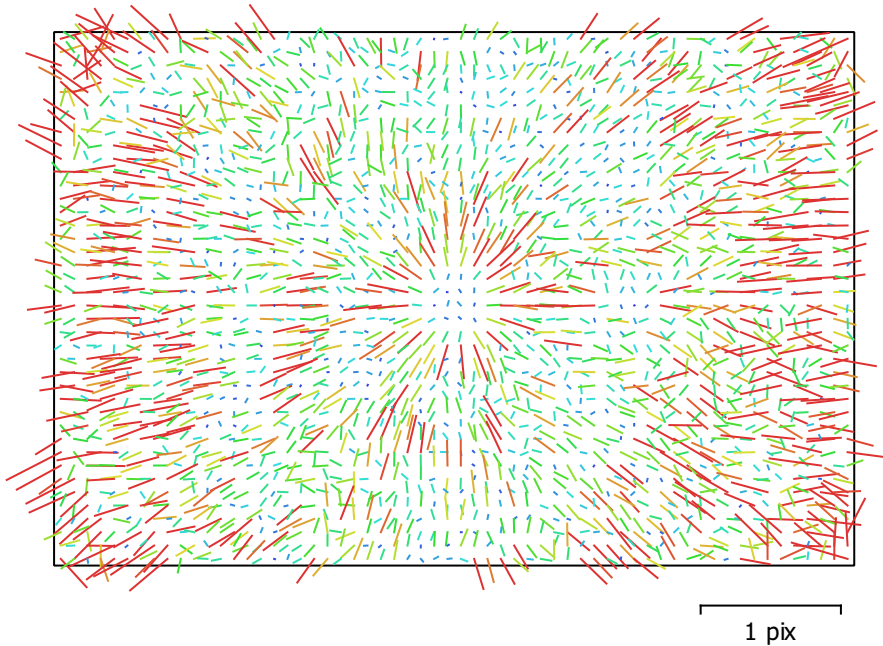


Fig. 2. Image residuals for FC6310 (8.8 mm).

FC6310 (8.8 mm)

553 images

Type
Frame

Resolution
5472 x 3648

Focal Length
8.8 mm

Pixel Size
2.41 x 2.41 μ m

	Value	Error	F	Cx	Cy	B1	B2	K1	K2	K3	K4	P1	P2
F	3674.5	0.26	1.00	-0.27	-0.79	-0.02	-0.23	0.05	-0.08	0.12	-0.16	0.03	-0.06
Cx	5.49789	0.076		1.00	0.17	0.14	0.60	-0.03	0.03	-0.04	0.05	0.25	0.10
Cy	20.2519	0.14			1.00	-0.37	0.32	-0.07	0.09	-0.13	0.15	0.00	0.25
B1	0.0376414	0.015				1.00	-0.00	0.01	-0.01	0.01	-0.01	-0.07	-0.17
B2	1.13794	0.015					1.00	-0.03	0.03	-0.04	0.04	0.03	0.11
K1	0.0145288	3.4e-05						1.00	-0.97	0.92	-0.87	-0.01	-0.01
K2	-0.0584304	0.00017							1.00	-0.99	0.95	-0.01	0.01
K3	0.107812	0.00034								1.00	-0.99	0.01	-0.01
K4	-0.0660677	0.00023									1.00	-0.01	0.02
P1	0.00171385	1.5e-06										1.00	0.15
P2	0.000255027	1.6e-06											1.00

Table 2. Calibration coefficients and correlation matrix.

Ground Control Points

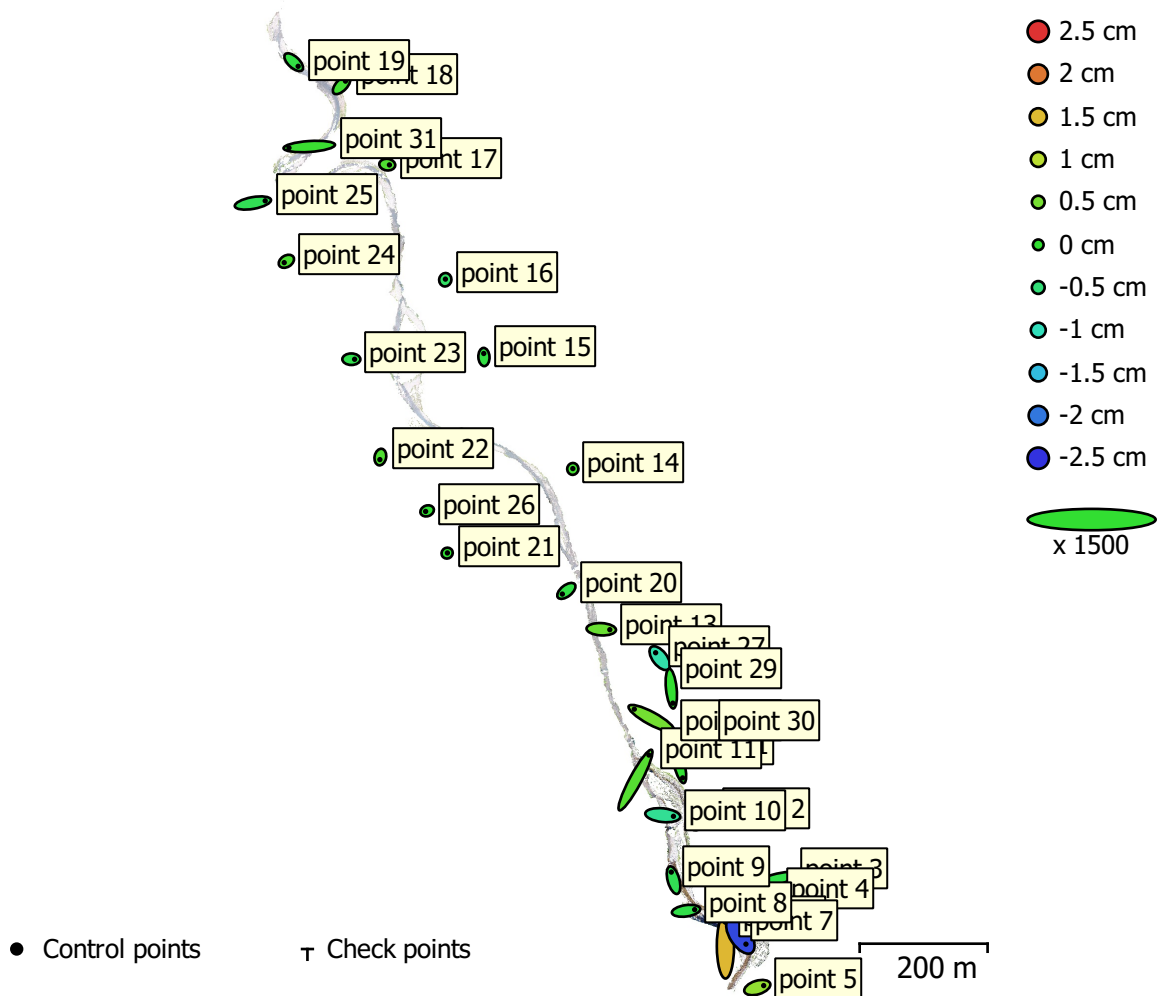


Fig. 3. GCP locations and error estimates.

Z error is represented by ellipse color. X,Y errors are represented by ellipse shape.

Estimated GCP locations are marked with a dot or crossing.

Count	X error (cm)	Y error (cm)	Z error (cm)	XY error (cm)	Total (cm)
30	1.66851	1.83505	0.615891	2.48019	2.55552

Table 3. Control points RMSE.

Label	X error (cm)	Y error (cm)	Z error (cm)	Total (cm)	Image (pix)
point 1	0.744341	-2.93273	-0.000746994	3.02572	0.201 (9)
point 2	-1.44786	-1.13528	0.563384	1.92421	0.326 (8)
point 3	-3.54588	-1.00799	-0.155992	3.68967	0.175 (6)
point 4	0.354546	-3.65866	0.663848	3.73526	0.182 (4)
point 5	1.33374	0.411221	0.695779	1.55951	0.170 (5)
point 6	-0.00972672	4.97481	1.53373	5.20588	0.142 (5)
point 7	1.15746	-1.72826	-2.34244	3.13267	0.419 (13)
point 8	1.78355	0.251346	-0.164563	1.80868	0.246 (10)
point 10	2.22668	-0.233551	-0.715502	2.35045	0.217 (18)
point 11	2.79612	5.21564	0.262089	5.92367	0.156 (11)
point 12	-3.55138	1.92207	0.475254	4.06602	0.199 (13)
point 13	1.78691	-0.093632	0.388431	1.83104	0.190 (14)
point 14	0.0112417	0.0707018	0.120794	0.140415	0.110 (5)
point 15	-0.0378968	0.736704	-0.122084	0.747713	0.072 (5)
point 16	0.0276753	0.128958	-0.36421	0.387356	0.065 (2)
point 17	0.456015	-0.0571622	0.217062	0.508265	0.090 (3)
point 18	0.814307	0.852049	0.122471	1.18494	0.085 (5)
point 19	0.92593	-0.856777	-0.129417	1.26813	0.091 (11)
point 20	-0.837554	-0.661214	-0.138659	1.07607	0.107 (7)
point 21	0.0587744	0.0374776	-0.0105661	0.0705028	0.002 (2)
point 22	-0.103029	-0.530819	0.214008	0.581535	0.101 (4)
point 23	0.677998	-0.00685058	-0.204884	0.708312	0.060 (4)
point 24	-0.450715	-0.279132	0.190938	0.563486	0.067 (3)
point 25	2.5641	0.459614	-0.252877	2.61721	0.160 (8)
point 26	-0.312122	-0.12	-0.00875855	0.33451	0.054 (5)
point 27	-0.867127	1.12086	-0.87261	1.66424	0.350 (8)
point 30	-2.13267	-1.18752	0.128085	2.44436	0.180 (8)
point 9	-0.466017	1.68413	-0.24352	1.7643	0.163 (9)
point 29	0.313413	-3.02751	0.00217663	3.04369	0.197 (10)
point 31	-4.22967	-0.286846	0.0597332	4.23981	0.220 (14)
Total	1.66851	1.83505	0.615891	2.55552	0.208

Table 4. Control points.

Digital Elevation Model

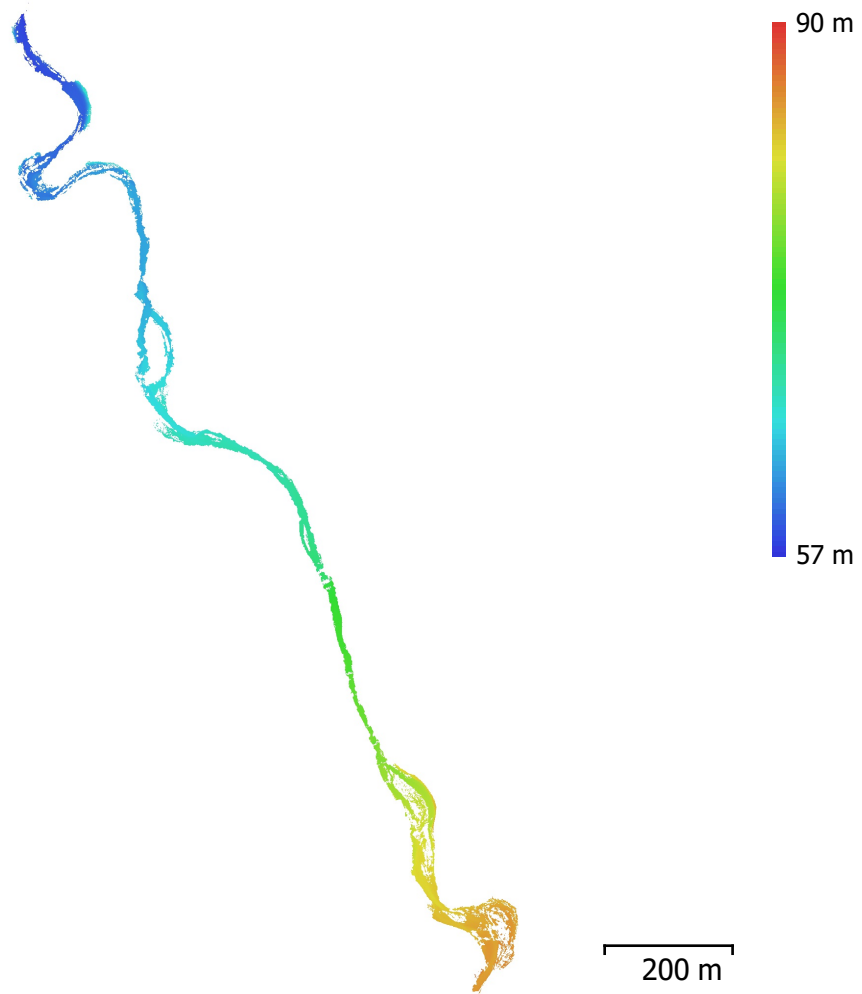


Fig. 4. Reconstructed digital elevation model.

Resolution: 3.01 cm/pix
Point density: 11 points/cm²

Processing Parameters

General

Cameras	553
Aligned cameras	528
Markers	30
Coordinate system	Local Coordinates (m)
Rotation angles	Yaw, Pitch, Roll

Point Cloud

Points	453,776 of 520,132
RMS reprojection error	0.158044 (0.540707 pix)
Max reprojection error	2.43596 (31.5688 pix)
Mean key point size	3.11304 pix
Point colors	3 bands, uint8
Key points	No
Average tie point multiplicity	3.62523

Alignment parameters

Accuracy	High
Generic preselection	No
Reference preselection	No
Key point limit	40,000
Tie point limit	4,000
Filter points by mask	No
Adaptive camera model fitting	Yes
Matching time	3 hours 31 minutes
Alignment time	39 minutes 36 seconds

Optimization parameters

Parameters	f, b1, b2, cx, cy, k1-k4, p1, p2
Optimization time	1 minutes 40 seconds

Dense Point Cloud

Points	82,356,248
Point colors	3 bands, uint8

Reconstruction parameters

Quality	High
Depth filtering	Aggressive
Depth maps generation time	9 hours 10 minutes
Dense cloud generation time	1 hours 36 minutes

Model

Faces	3,671,848
Vertices	2,095,578
Vertex colors	3 bands, uint8

Reconstruction parameters

Surface type	Height field
Source data	Dense
Interpolation	Disabled
Quality	High
Depth filtering	Aggressive
Face count	5,490,416
Processing time	2 minutes 51 seconds

Tiled Model

Texture	3 bands, uint8
---------	----------------

Reconstruction parameters

Source data	Mesh
Tile size	256
Processing time	1 hours 9 minutes

DEM

Size	35,593 x 56,468
------	-----------------

Coordinate system	Local Coordinates (m)
Reconstruction parameters	
Source data	Mesh
Interpolation	Disabled
Processing time	52 seconds
Orthomosaic	
Size	59,975 x 104,225
Coordinate system	Local Coordinates (m)
Colors	3 bands, uint8
Reconstruction parameters	
Blending mode	Mosaic
Surface	DEM
Enable hole filling	Yes
Processing time	20 minutes 33 seconds
Software	
Version	1.4.2 build 6205
Platform	Windows 64

AprilChannel

Processing Report
28 August 2018



Survey Data

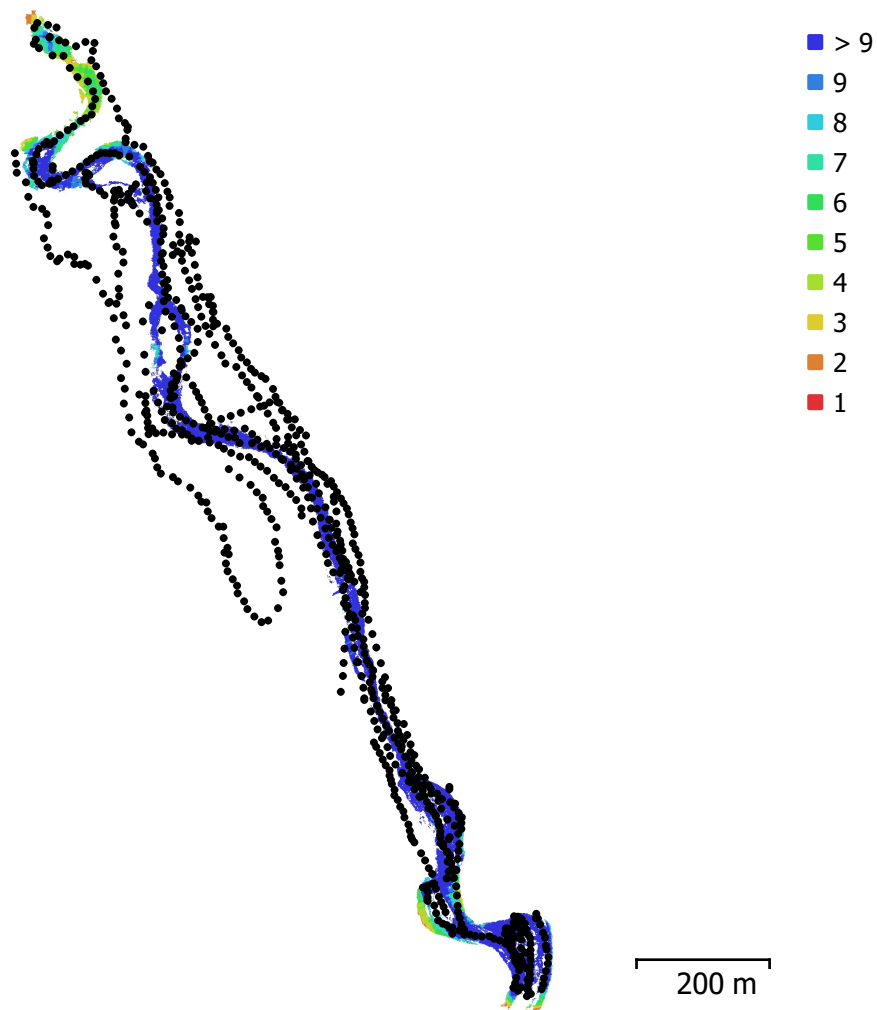


Fig. 1. Camera locations and image overlap.

Number of images:	815	Camera stations:	813
Flying altitude:	53.6 m	Tie points:	974,321
Ground resolution:	1.31 cm/pix	Projections:	3,377,614
Coverage area:	0.054 km ²	Reprojection error:	0.656 pix

Camera Model	Resolution	Focal Length	Pixel Size	Precalibrated
FC6310 (8.8 mm)	4864 x 3648	8.8 mm	2.61 x 2.61 μ m	No

Table 1. Cameras.

Camera Calibration

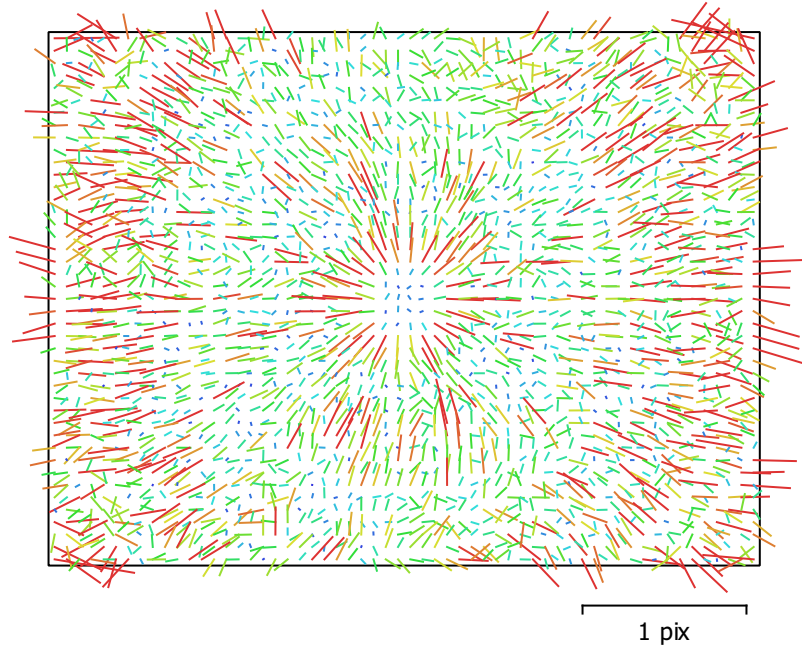


Fig. 2. Image residuals for FC6310 (8.8 mm).

FC6310 (8.8 mm)

815 images

Type
Frame

Resolution
4864 x 3648

Focal Length
8.8 mm

Pixel Size
2.61 x 2.61 μ m

	Value	Error	F	Cx	Cy	B1	B2	K1	K2	K3	K4	P1	P2	P3	P4
F	3695.22	0.067	1.00	0.02	-0.33	-0.38	0.03	-0.07	0.07	-0.05	0.04	-0.01	-0.03	0.00	-0.00
Cx	-4.56705	0.022		1.00	0.00	-0.01	0.30	-0.01	0.00	-0.00	0.00	0.45	-0.10	0.14	-0.09
Cy	1.52036	0.021			1.00	-0.07	-0.01	-0.01	0.01	-0.02	0.02	-0.05	0.41	-0.08	0.06
B1	1.19678	0.007				1.00	0.00	-0.00	0.00	-0.00	0.01	-0.00	0.01	-0.01	0.01
B2	1.35846	0.0066					1.00	-0.00	0.00	-0.00	0.00	-0.01	0.01	-0.02	0.01
K1	0.0196534	4e-05						1.00	-0.97	0.93	-0.88	-0.02	0.01	-0.02	0.02
K2	-0.0862425	0.00024							1.00	-0.99	0.96	0.02	-0.01	0.02	-0.02
K3	0.173228	0.00056								1.00	-0.99	-0.01	0.01	-0.01	0.01
K4	-0.117783	0.00044									1.00	0.01	-0.00	0.01	-0.00
P1	-0.000157436	2.5e-06										1.00	-0.59	0.80	-0.70
P2	8.77063e-05	1.6e-06											1.00	-0.68	0.61
P3	-0.0995827	0.052												1.00	-0.97
P4	0.130293	0.067													1.00

Table 2. Calibration coefficients and correlation matrix.

Ground Control Points

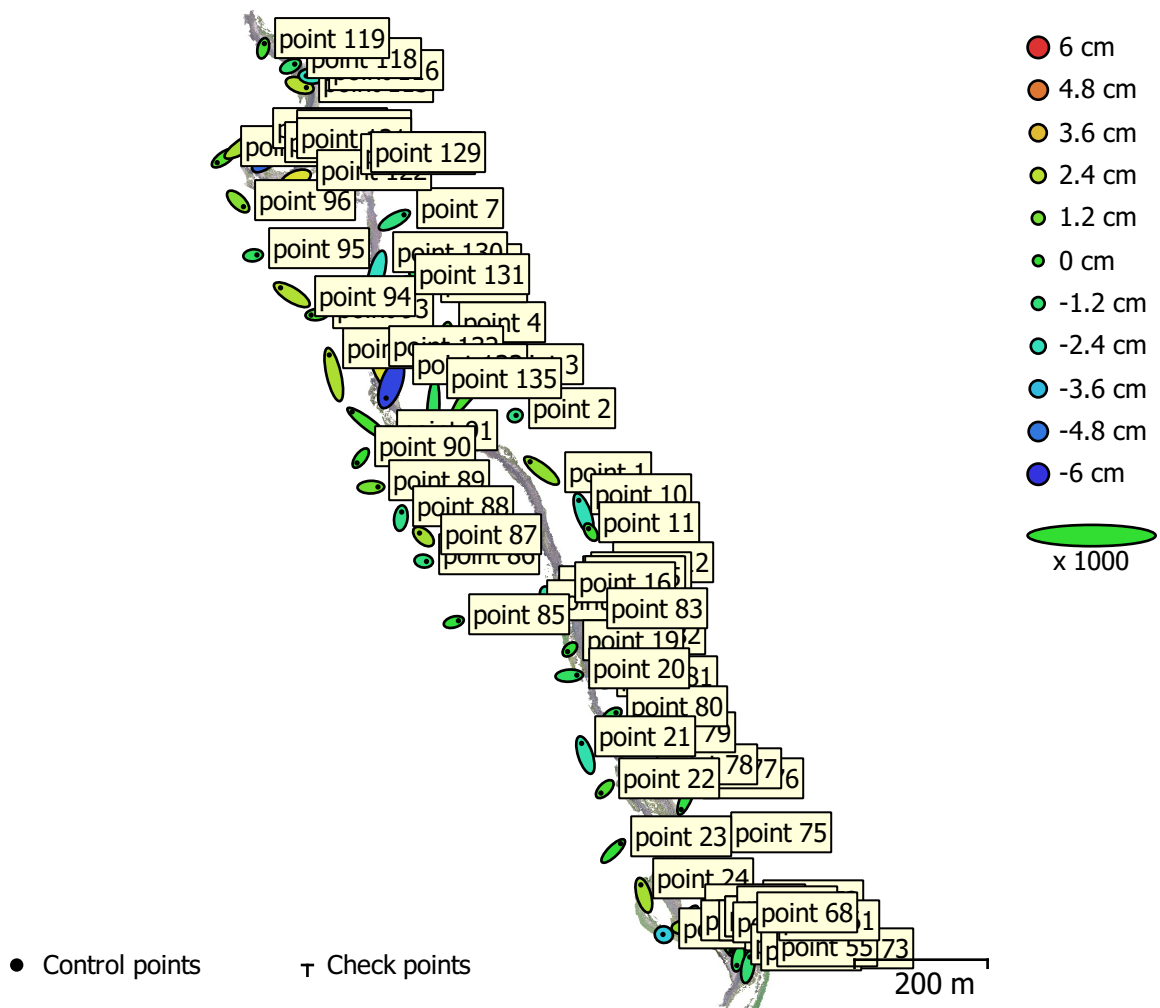


Fig. 3. GCP locations and error estimates.

Z error is represented by ellipse color. X,Y errors are represented by ellipse shape.

Estimated GCP locations are marked with a dot or crossing.

Count	X error (cm)	Y error (cm)	Z error (cm)	XY error (cm)	Total (cm)
80	2.09057	2.30727	1.69542	3.11352	3.5452

Table 3. Control points RMSE.

Label	X error (cm)	Y error (cm)	Z error (cm)	Total (cm)	Image (pix)
point 1	-3.45684	2.65887	1.63127	4.65622	0.259 (14)
point 2	0.293941	0.0776866	-1.36639	1.39981	0.546 (8)
point 3	4.5564	5.97337	0.466651	7.52726	0.484 (4)
point 9	2.70783	1.21268	1.47252	3.31229	0.250 (3)
point 4	0.436307	2.45744	0.706461	2.59393	0.375 (6)
point 5	0.703046	-0.481833	0.838925	1.19592	0.622 (10)
point 6	1.30938	0.275356	-0.559115	1.45014	0.476 (6)
point 7	2.87319	1.60328	-1.31492	3.54327	0.064 (3)
point 8	3.42844	0.255725	0.553967	3.48231	0.229 (8)
point 24	-0.896451	3.12484	2.00476	3.81934	0.342 (9)
point 25	-0.240612	0.0621766	-3.30587	3.3152	0.483 (6)
point 34	-1.50864	-2.3719	3.67624	4.62782	0.750 (24)
point 72	6.83886	-1.89525	-2.65322	7.57638	0.327 (8)
point 73	-4.61094	1.29844	1.2974	4.96286	0.376 (7)
point 75	-5.52505	-0.26698	-0.0111341	5.53151	0.456 (5)
point 76	-1.54058	-3.66622	-0.335688	3.99089	0.538 (11)
point 77	0.0142011	-2.10798	-1.3053	2.47944	0.423 (9)
point 78	1.30737	2.16344	1.04756	2.73626	0.402 (12)
point 79	0.469143	-0.871591	0.197013	1.00925	0.461 (12)
point 81	1.04375	-0.51764	1.15632	1.64147	0.363 (13)
point 80	1.10105	0.693011	-0.646493	1.45276	0.242 (13)
point 82	0.0177082	1.34164	0.312947	1.37777	0.368 (11)
point 17	0.369433	-0.788777	-2.02434	2.20377	0.524 (7)
point 18	2.63509	-2.97385	1.73831	4.33696	0.525 (5)
point 19	-0.702582	-0.659946	-0.0908489	0.968196	0.354 (10)
point 20	2.29968	0.144801	-0.836021	2.4512	0.314 (14)
point 21	-1.14845	3.53135	-2.1211	4.2765	0.011 (2)
point 22	-1.15679	-1.18506	0.487384	1.72629	0.572 (5)
point 23	2.22838	2.21232	-0.0576565	3.1406	0.356 (4)
point 85	1.39526	0.390318	-0.139095	1.45549	0.423 (5)
point 91	-4.97283	3.77571	0.376009	6.25511	0.524 (6)

Label	X error (cm)	Y error (cm)	Z error (cm)	Total (cm)	Image (pix)
point 90	-1.10957	-1.46302	0.0840311	1.8381	0.315 (6)
point 89	2.12669	0.0593432	1.12047	2.40453	0.261 (3)
point 88	0.241266	1.82326	-1.51661	2.38381	0.321 (4)
point 92	-1.35277	5.87989	2.13044	6.39858	0.510 (5)
point 93	-1.66925	-0.151055	0.377437	1.71804	0.481 (6)
point 94	-3.39466	2.08226	2.20989	4.55446	0.254 (7)
point 95	1.14563	0.119276	-0.75926	1.37955	0.121 (4)
point 96	1.60692	-1.55351	1.48556	2.68374	0.097 (3)
point 97	-1.99268	-1.40728	0.671792	2.53032	0.067 (2)
point 10	-1.41549	3.95393	-2.3163	4.79608	0.352 (5)
point 100	4.54583	2.87578	2.06586	5.76216	0.175 (6)
point 101	1.0632	-0.616025	-0.693034	1.41074	0.381 (4)
point 104	0.167869	1.27734	-2.23183	2.57699	0.344 (4)
point 11	-0.67809	1.05415	0.223161	1.27312	0.453 (5)
point 115	2.01667	-0.688692	2.32322	3.15255	0.365 (6)
point 116	-1.46775	0.110933	-2.45172	2.85964	0.225 (5)
point 118	1.277	0.609962	-1.06016	1.76826	0.155 (4)
point 119	0.349573	1.40646	0.326995	1.48569	0.596 (7)
point 12	-1.22181	-0.194375	-0.118362	1.24282	0.445 (7)
point 121	-3.0878	-3.05896	-5.02609	6.64479	0.278 (12)
point 122	-2.18541	-0.905769	2.99452	3.81623	0.384 (9)
point 123	-3.47238	0.607207	-0.0947747	3.52635	0.530 (9)
point 129	0.825405	-3.3331	2.11113	4.03085	0.312 (15)
point 13	-0.627836	0.176274	2.07082	2.17107	0.382 (17)
point 130	-1.204	-4.39888	-2.55218	5.22622	0.345 (15)
point 131	-2.09215	-4.45708	-0.0435933	4.92387	0.343 (14)
point 132	1.85567	-4.39375	2.99373	5.63125	0.556 (18)
point 133	-1.51691	-4.19965	-5.688	7.23128	0.486 (19)
point 135	-0.437468	-7.79025	-0.753251	7.8388	0.460 (9)
point 14	0.18989	-0.0459356	0.690384	0.717494	0.398 (20)
point 15	-1.09391	-0.481337	0.967116	1.53741	0.385 (21)
point 16	-0.784757	0.883564	-2.41282	2.68668	0.416 (19)

Label	X error (cm)	Y error (cm)	Z error (cm)	Total (cm)	Image (pix)
point 26	-1.45234	-2.24661	-0.923806	2.83019	0.391 (13)
point 27	1.65434	0.138733	1.70653	2.38082	0.541 (11)
point 28	-1.88094	-0.810154	-0.0198555	2.04809	0.589 (12)
point 29	-1.35964	-0.474246	-0.800846	1.64769	0.538 (9)
point 30	-0.0508692	-0.203843	0.140826	0.252926	0.636 (14)
point 31	-0.808678	-2.83524	-0.912221	3.08621	0.447 (22)
point 32	-1.02815	-0.71457	1.16744	1.7119	0.598 (27)
point 33	-1.77141	-0.656095	-0.168211	1.89649	0.527 (24)
point 35	1.43909	-3.36025	0.00460609	3.65544	0.490 (31)
point 36	-0.445971	-2.15853	-0.802495	2.34566	0.315 (22)
point 49	0.554297	2.96115	-1.12518	3.21585	0.318 (23)
point 55	-0.762353	0.598557	0.237364	0.997895	0.340 (13)
point 61	-1.38554	-1.44918	2.48317	3.19155	0.547 (15)
point 68	2.07206	-0.679654	-0.78487	2.31763	0.508 (19)
point 83	0.667938	0.987028	1.01797	1.56736	0.487 (5)
point 86	0.838864	-0.109788	-1.26413	1.52111	0.327 (5)
point 87	-1.1869	1.05028	1.99073	2.54457	0.335 (4)
Total	2.09057	2.30727	1.69542	3.5452	0.446

Table 4. Control points.

Digital Elevation Model



Fig. 4. Reconstructed digital elevation model.

Resolution: 2.62 cm/pix
Point density: 14.6 points/cm²

Processing Parameters

General

Cameras	815
Aligned cameras	813
Markers	80
Coordinate system	Local Coordinates (m)
Rotation angles	Yaw, Pitch, Roll

Point Cloud

Points	974,321 of 1,075,286
RMS reprojection error	0.203196 (0.656282 pix)
Max reprojection error	2.22568 (36.2676 pix)
Mean key point size	3.33066 pix
Point colors	3 bands, uint8
Key points	No
Average tie point multiplicity	3.67332

Alignment parameters

Accuracy	High
Generic preselection	No
Reference preselection	No
Key point limit	40,000
Tie point limit	6,000
Filter points by mask	No
Adaptive camera model fitting	No
Matching time	11 hours 21 minutes
Alignment time	1 hours 55 minutes

Optimization parameters

Parameters	f, b1, b2, cx, cy, k1-k4, p1-p4
Optimization time	6 minutes 54 seconds

Dense Point Cloud

Points	116,717,288
Point colors	3 bands, uint8

Reconstruction parameters

Quality	High
Depth filtering	Aggressive
Depth maps generation time	15 hours 44 minutes
Dense cloud generation time	2 hours 41 minutes

Model

Faces	5,855,695
Vertices	3,216,503
Vertex colors	3 bands, uint8

Reconstruction parameters

Surface type	Height field
Source data	Dense
Interpolation	Disabled
Quality	High
Depth filtering	Aggressive
Face count	7,781,152
Processing time	5 minutes 50 seconds

DEM

Size	54,707 x 84,041
Coordinate system	Local Coordinates (m)

Reconstruction parameters

Source data	Dense cloud
Interpolation	Disabled
Processing time	1 minutes 47 seconds

Orthomosaic

Size	66,551 x 115,097
Coordinate system	Local Coordinates (m)
Colors	3 bands, uint8
Reconstruction parameters	
Blending mode	Mosaic
Surface	DEM
Enable color correction	No
Enable hole filling	Yes
Processing time	28 minutes 11 seconds
Software	
Version	1.4.2 build 6205
Platform	Windows 64